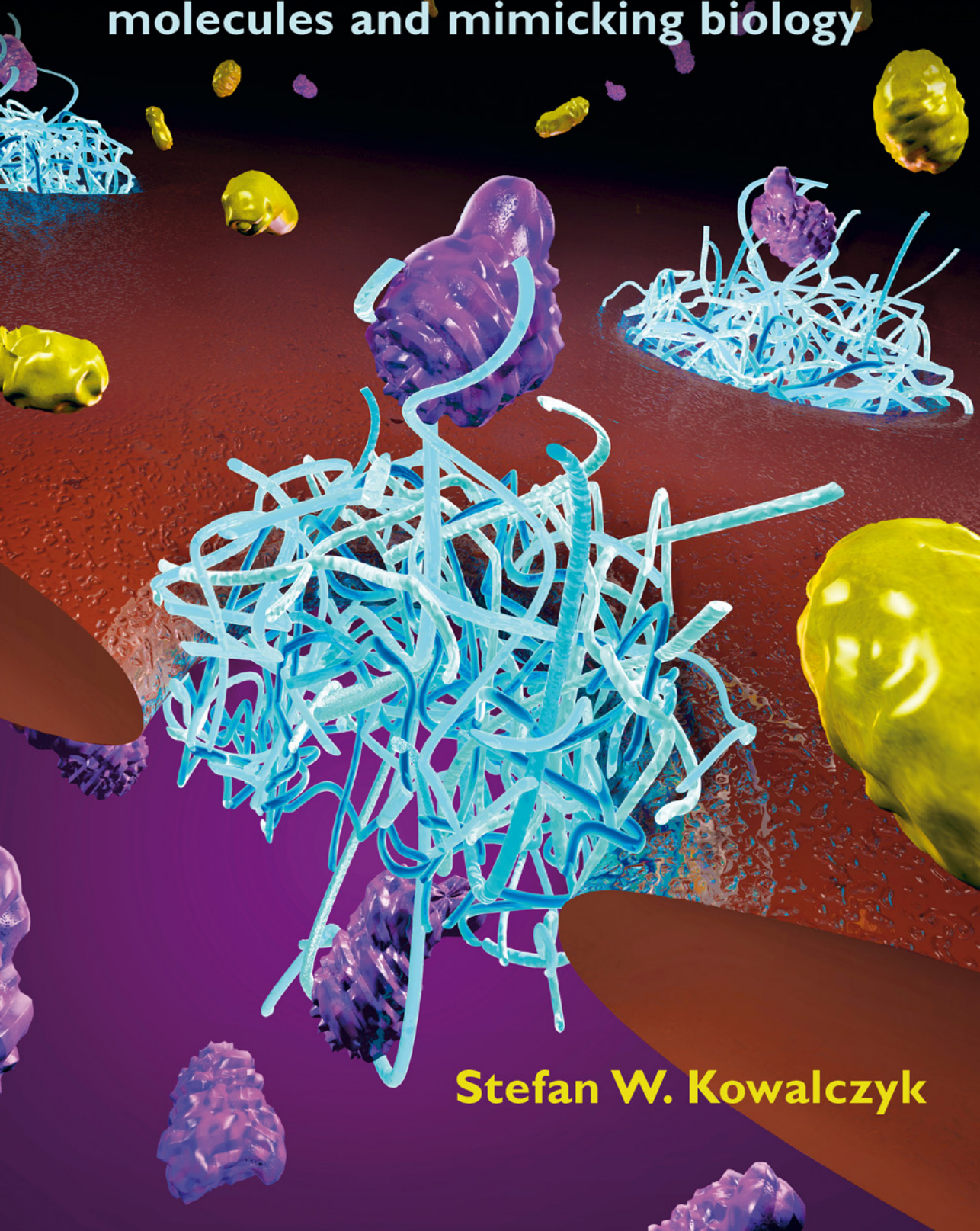


Solid-state nanopores for scanning single molecules and mimicking biology



Stefan W. Kowalczyk

Solid-state nanopores for scanning single molecules and mimicking biology

Proefschrift

ter verkrijging van de graad van doctor
aan de Technische Universiteit Delft,
op gezag van de Rector Magnificus prof. ir. K.C.A.M. Luyben,
voorzitter van het College voor Promoties,
in het openbaar te verdedigen op donderdag 20 oktober 2011 om 15.00 uur

door

**Szczepan (Stefan) Wojciech
KOWALCZYK**

doctorandus in de natuurkunde
geboren te Warschau, Polen.

Dit proefschrift is goedgekeurd door de promotor:

Prof. dr. C. Dekker

Samenstelling van de promotiecommissie:

Rector Magnificus	Voorzitter
Prof. dr. C. Dekker	Technische Universiteit Delft, promotor
Prof. dr. H. Bayley	University of Oxford, United Kingdom
Prof. dr. N. H. Dekker	Technische Universiteit Delft
Prof. dr. Y. Rabin	Bar Ilan University, Israel
Prof. dr. ir. L. M. K. Vandersypen	Technische Universiteit Delft
Dr. U. F. Keyser	University of Cambridge, United Kingdom
Dr. L. M. Veenhoff	Rijksuniversiteit Groningen
Prof. dr. H.W. Zandbergen	Technische Universiteit Delft, reservelid



Bionanoscience Department
Think big about life at the smallest scale

Keywords: nanopores, DNA, protein, translocation, nuclear pore complex, biomimetics, graphene, biosensing, bionanotechnology

Published by: Stefan Kowalczyk

Cover image: Cees Dekker lab TU Delft / Tremani

Printed by: Gildeprint Drukkerijen

The production of this thesis is financially supported by Delft University of Technology and Bratek v.o.f.

An electronic version of this thesis is available at:

<http://www.library.tudelft.nl/dissertations/>

Casimir PhD series, Delft-Leiden, 2011-22

ISBN: 978-90-8593-109-6

Copyright © 2011 by S.W. Kowalczyk

Preface and Acknowledgements

I feel very fortunate to have been part of the molecular biophysics (MB) group – now expanded and better known as the bionanoscience department (BN) – at Delft for the past four years. This journey started when I was assigned to read some papers from a certain Cees Dekker for a class on nanotechnology in Stony Brook. It was Google who introduced me to his polished web page, with all its marvelous images. One day on a visit back to the Netherlands I decided (without any appointment or prior notice) to visit Cees in his office to discuss a possible PhD project. Cees created some time for me in his busy schedule and very enthusiastically told me about the work at MB and showed me around the labs. And so it happened that I decided to apply. It took me some time to convince Cees that I was the right person for the job, given the fact that my background seemed to have no overlap whatsoever with what was awaiting me during my PhD. (Other than the fact that I was studying black holes, and here I would study nano holes.) I have to admit, calculating the entropy of supersymmetric black holes in 26 dimensional string theory is somewhat different than the hands-on experimental biophysics that is happening here. Luckily, in the end Cees did offer me the job, and in retrospect I could not have ended up in a nicer place.

Then a big surprise came: was I supposed to do these measurement all by myself? Not working side by side at the bench with Cees in the lab? (Yes, I was very naïve in those days...) How did that machine work? Why did that software crash all the time when I was using it, but not when others were using it? How did that pipette work? (Here is my advice for starting students: Don't be too enthusiastic and press it all the way to the second level, but only to the first level, as I found out after two weeks...) Fortunately, Ralph Smeets helped me to start up and he patiently explained everything I needed to know about how to run a successful experiment (for example, when to "zap" a pore, when to quickly reverse the voltage, or when to turn it off for a while so that the pore could "relax" a bit). There were not that many hours that we were simultaneously in the lab, Ralph: you were typically not there yet before lunch and I wanted to go home early (with a 1.5 hour trip ahead of me all the way back to Zaandam at that time). Nonetheless, we managed: thanks for the nice times and passing on your masterly nanopore skills, Ralph!

My first year as a PhD student was a time of perseverance as I worked my way through experiments that often did not go as planned. But through the following years I became more convinced that my actual dissertation wasn't just a utopia. Yet research wasn't the only thing keeping me busy, as in July 2010 our beautiful daughter Leora was born. A conference shortly after that in France was a welcome opportunity to catch up on sleep. (My two roommates did worry about my wellbeing as they always found me sleeping very early and in the breaks between sessions.)

There are a lot of people that I'd like to thank. Cees, it was a great time to be a member of your group. I learned a lot from you – not only about science! Your enthusiasm is contagious. Thanks for all the discussions we had, all the red marks you scribbled on our manuscripts, and for your support. You have a sharp eye for details, and even more so for the big picture. It is fun to follow you on twitter nowadays and to witness how many things you take up besides practicing science. It was a privilege to work with you, I'm sure I'll miss it. Nynke, thanks for all your critical comments and ideas in our weekly nanopore meetings. Serge Lemay, thanks also for your input, it's a pity you are not anymore at BN, all the best in Twente. Thanks also to the committee members, for the effort and time that you have invested in order to be here and read my thesis. It is an honor that you are willing to take part in this.

Thanks to all the people who are not mentioned above yet but contributed in one way or another to this thesis. Rod and Larisa, it was fun to collaborate with you on the exciting biomimetic nanopore project. I had a great time in Basel. All the best with your new position as Prof., Rod. And thanks Larisa, for sending freshly prepared proteins again and again. Aleksei and David, it was great to approach a problem together from two sides, merging experiments and simulations. Yitzhak and Shura, it was incredible to see how fast you come up with complex equations (and solutions to them!). Mengyue and Vasili, thanks for drilling all those pores for us. Adam, thanks for your contributions in our joint efforts to detect local structures. Thank you Tim, you were a very welcome help in the TIRF measurements. Greg, our graphene measuring marathon was quite an exercise in patience for both of us, but it was great to get to the finish together. Thanks Serge Donkers for all the hours you spend on making these unfriendly DNA constructs for Maarten and me. You too, Susan and Ilja, thanks for all the help in the biolab. Big thanks also to all the students I had the pleasure of supervising: Maarten, Pauline, Tomás, Rini, and Khin Sam. It was a pleasure to work with each of you. Thanks for all the data you helped to collect. I wish you all the best in the future.

Then my fellow PhD students. Thijn, thanks for allowing me to bother you about RecA on a regular basis, you were always willing to help out. Iddo, you made me believe sharp AFM images can be made in a few minutes, though I ended up spending many hours on it. Martin, I enjoyed the PhD diner at your place just after I started. Too bad we stopped doing that shortly after that. Michiel and Aartjan, it was fun to share an office with you. Michiel, thanks for not taking the piano away for so long: it was of great use to me. Rifka, thanks for the nice conversations we had. Marijn, thanks for selling me your old racing bike almost for free. Good luck with the last bits of your thesis. Felix and Fabai, good luck with squeezing and evolving those bacteria. Calin, I'm sure with your insight and fast work pace cool results will come quickly. Zhuangxiong, all the best at Philips, hope you like it over there. Same goes for Marcel at the Holst centre. To the recently started PhD candidates: Charl, Regis, Jetty, Sriram, Zohreh, Anette, Stanley, Michela, Bojk, Maarten, and Andrew: I wish you good luck and a fun time.

The group trips were great opportunities to chat a bit more with people. Apart from that, playing cricket and punting in Oxford, climbing in Heidelberg, exploring Barcelona, and canyoning in the Pyrenees to name a few was simply great fun! That last point brings me to Jelle. Jelle, 65+ en toch mee gaan met canyoning, je doet het toch maar, respect hoor! En dan die keer dat iemand "goedemorgen Stefan" naar me riep en me hard inhaalde op de fiets, jawel het was.. Jelle. Bedankt voor het maken van de flow cellen. Je hebt in Dimitri een goede opvolger. Jaap, bedankt voor je geduld in het beantwoorden van vele vragen, hulp met computers, randaardes en dergelijke. Jacob, thanks for making that event-fitting algorithm in Matlab, too bad it turned out to be only "just as good" as the old way.

It was fun to do sports with group members as well. Adam, Edgar, Pradyumna, Michiel, Francesco, our weekly squash sessions were very refreshing. Sorry to the new group of squashers that I wasn't able to join often lately, hope to join again soon! Edgar, it was fun to talk a bit of Polish with each other and to cycle in Belgium. I recall our adventures as if they happened yesterday: fitting the bikes into that small Fiat Panda, the surprise in your eyes when I told you starting the car happened through pushing it and jumping in quickly (this was routine for me, as I did this for over a year that way), your exploding tire and consequent crash into that corn field, and so on. Then there is the foosball table. Thanks for always being there for us (although "there" is now upstairs unfortunately). Francesco, you're right, this is probably the most important piece of equipment that the department has.

Thanks also to other postdocs and staff. Gary, thanks for your contributions in the nanopore meetings. Good to see you found your place at Illumina back in the UK. Gautam and Xander, thanks for your novel ideas about nanopores and for all the hours you spent in the clean room making membranes. Tim, thanks for the enjoyable dinners we had together, all the best to you and Meghan. Adam, it was real fun working with you. Great to see you found your place in North Carolina. Iwijn, thanks for arranging that trip to the Ardennes, we had a great time there. Thanks also for all the professional and personal interactions I had with you, Jaan, Jan, Peter, Christine, Igor, Irene, Matthew, Peter, Freek, Aurelien, Matthew, David, Marijn, Magnus, Daniel (2x), Allard, and Hugo. Also, Elsemarieke, Emmylou, Dijana, Jennifer, Leonie, Dominique, and Liset, thanks for your lively presence and your patience in answering lots of questions about forms and other things. Thanks also for discussions and ideas to all the new Profs at BN. In particular, thanks to David for kindly allowing to use and modify your setup for my experiment. Christophe, it was fun to help you moving in. Of course there is a large number of people with whom I also had professional and personal interactions but that are not mentioned here. Thanks to you as well. To all the new people in the BN department, I'm sorry if I haven't had the time yet to properly meet you, that is a disadvantage of an expanding department.

Finally, I would like to thank you my friends outside of science and family. In particular my brothers, Jan and Michał, for our friendships throughout life, and for agreeing to be my 'paranimfen' without having a clue of what that means. Tata i Mama, dzięki za wszystko! Bez was nigdy bym nie osiągnął tego co osiągnąłem. Bedankt ook voor al jullie oppasdagen met Leora, (schoon-) pa en ma. Rebecca, ik kan het niet vaak genoeg zeggen: ik hou van je! Dank je voor je geduld met me in de afgelopen jaren en voor je onvoorwaardelijke liefde die mij draagt. Last but foremost, I want to thank God, who created us human beings and allows us to discover all the beauty He created. All praise be to Him.

Stefan Kowalczyk
Delft, September 2011

Contents

1	Introduction	11
1.1	The scale of things	12
1.2	Biology at the nanoscale	13
1.3	The 15-minute genome: from base pairs to bedside	15
1.4	DNA, RNA and proteins – essential constituents of cells	17
1.5	Nanopores in biology – compartments need channels	18
1.6	Scanning single molecules with solid-state nanopores	20
1.6.1.	Solid-state nanopores – a brief history	20
1.6.2.	Enter the graphene nanopore – it doesn’t get any thinner	23
1.7	The nuclear pore complex is a nanopore	24
1.8	Outline of this thesis	26
	References	28
2	Modeling the conductance and DNA blockade of solid-state nanopores	33
2.1	Introduction	34
2.2	Conductance of a cylindrical nanopore	34
2.3	Conductance of an hourglass-shaped nanopore	37
2.4	Modeling the DNA conductance blockade	39
2.5	Conclusions	41
2.6	Materials and Methods	42
	References	43
2.7	Supplementary Information	44

3	Translocation of RecA-coated double-stranded DNA through solid-state nanopores	57
3.1	Introduction	58
3.2	Solid-state nanopores	60
3.3	Nucleoprotein filament formation	61
3.4	Translocation of RecA-coated dsDNA	63
3.5	Rate of transversal of RecA-coated dsDNA	69
3.6	Discussion and conclusions	72
	References	73
4	Detection of local protein structures along DNA using solid-state nanopores	75
4.1	Introduction	76
4.2	Formation of local protein structures on DNA	76
4.3	Nanopore translocation data	78
4.4	Resolution	80
4.5	Methods	83
	References	84
4.6	Supplementary Figures	86
5	Charge reduction of DNA by transient binding of counterions	89
5.1	Introduction.	90
5.2	Nanopore experiments	90
5.3	MD simulations.	93
5.4	Effect of ion concentration and voltage	96
5.5	Discussion	97
5.6	Materials and Methods	98
	References	102
5.7	Supplementary Information	105

6	Unraveling single-stranded DNA in a solid-state nanopore . . .	111
6.1	Introduction	112
6.2	Creation of hybrid ssDNA-dsDNA molecules	114
6.3	Nanopore data on hybrid ssDNA-dsDNA molecules	116
6.4	Nanopore data on single-stranded DNA	120
6.5	Materials and Methods	122
	References	124
6.6	Supplementary Information	127
7	DNA translocation through graphene nanopores	131
7.1	Introduction	132
7.2	Free-standing graphene	132
7.3	Graphene nanopores	134
7.4	DNA translocation through graphene nanopores	136
7.5	Methods	139
	References	141
7.6	Supplementary Information	142
8	Biomimetic nanopores: learning from and about nature	145
8.1	Introduction	146
8.2	Biology-inspired engineering.	147
	8.2.1 Fabrication of artificial pores and channels	147
	8.2.2 Mimicking naturally occurring pores and channels	149
	8.2.3 Realizing selectivity and biosensing.	151
8.3	Mechanistic investigation of biological pores.	153
	8.3.1 Bulk investigations of a biomimetic NPC	154
	8.3.2 Single-molecule investigations of a biomimetic NPC . . .	154
8.4	Perspective	156
	References	158

9 Single-molecule transport across an individual biomimetic nuclear pore complex	163
9.1 Introduction	164
9.2 Biomimetic nuclear pore complex	164
9.3 Protein translocation through a biomimetic nuclear pore complex	168
9.4 Selectivity	170
9.5 Materials and Methods	173
References	177
9.6 Supplementary Information.	179
10 Outlook	197
10.1 Introduction	198
10.2 Alternative nanopore detection schemes	198
10.3 Nanopores for epigenetics	200
10.4 Biomimetic and hybrid strategies	203
References	206
Summary	209
Samenvatting	213
Curriculum Vitae	219
List of publications	221

Chapter 1

Introduction

This thesis deals with nanotechnology, DNA, proteins, nanopores, graphene, nuclear pore complexes, ions and much more. In this introductory chapter, we first zoom in on the nanoscale and describe the biological context for the experimental work described in this thesis. We introduce DNA, the molecule that carries our genetic information, and discuss its importance in health care. Part of this thesis is devoted to the studying aspects of bare DNA, for example, how the effective charge of DNA is affected by the presence of various ions, and how single-stranded DNA unravels when pulled through a tiny hole. Another part of this thesis is devoted to the development of a biosensor for scanning the location of proteins along a DNA molecule. This sensor, known as a solid-state nanopore, consists of a tiny hole that is drilled in a thin solid material with a focused electron beam. We also developed a novel – more sensitive – type of nanopores, which we drill in graphene, a carbon sheet that is only one atom thin. Interestingly, while all these nanopores are made in the lab, our cells are full of natural nanopores. One of them is the nuclear pore complex, also known as the gatekeeper of the cell nucleus. In the last part of this thesis, we show that this important natural pore can be mimicked by attaching nuclear pore proteins to a solid-state nanopore. We finish with a brief overview of the contents of each chapter of this thesis.

1.1 The scale of things

But first, let's start with more basic questions. How big is big? Or, how small is small? The classic movie "Powers of Ten" [1] takes us on a journey through the remarkable range of scales in the universe. In our daily lives, we typically encounter objects in the range between 10^2 m (a large airliner) down to 10^{-2} m (a coin). This is only a very tiny fraction of the dazzling 60 orders of magnitude that one can find in nature, with the size of the visible universe of about 10^{26} m – made up of building blocks such as atoms (10^{-10} m), electrons (10^{-15} m) and the like – down to the Planck scale at 10^{-35} m, where we encounter the fundamental uncertainty limits of quantum mechanics and the hypothetical strings of string theory.

In the past few centuries, scientists have engaged in a pursuit to make tools that would allow them to look at scales that are invisible to the unaided eye. In the early 17th century, the mastery of fabrication of lenses led to the developments of telescopes and microscopes to extend the range of observable scales. Developments have not stood still since then: while telescopes like the Hubble space telescope now make very sharp images of the early universe without interferences from the atmosphere, recent advances in optical microscopy allow to localize single molecules with a resolution of only tens of nanometers, far below the diffraction limit. Indeed, nowadays, we can look into the deep universe (Figure 1.1a), as well as study and even manipulate matter at the atomic scale (Figure 1.1f). Feynman was right with his prediction, formulated in his 1959 talk entitled "There's Plenty of Room at the Bottom" that soon we would be able to control matter at the nanoscale, atom by atom.

It is virtually impossible to conceptualize numbers like 10^{26} or 10^{-35} . Some examples of structures with a size in between 10^{-2} meter and 1 nanometer are shown in Figure 1.1b–f. For a moment, let's try to imagine how small a nanometer (10^{-9} m) is. One way of looking at it is that a nanometer compares to a meter as a marble compares to the size of the Earth. Alternatively, one can say that "a nanometer is roughly the amount an average man's beard grows in the time it takes him to raise the razor to his face" [2]. This short hair would have a thickness of some 80.000 nanometer, so you would have to slice it (using a *very* sharp knife) in both length and width in some billion equal-sized pieces to get hair cubes measuring 1 nm on each side. The volume of such a tiny cube would be similar to the volume inside a small graphene nanopore (see chapter 7 of this thesis).

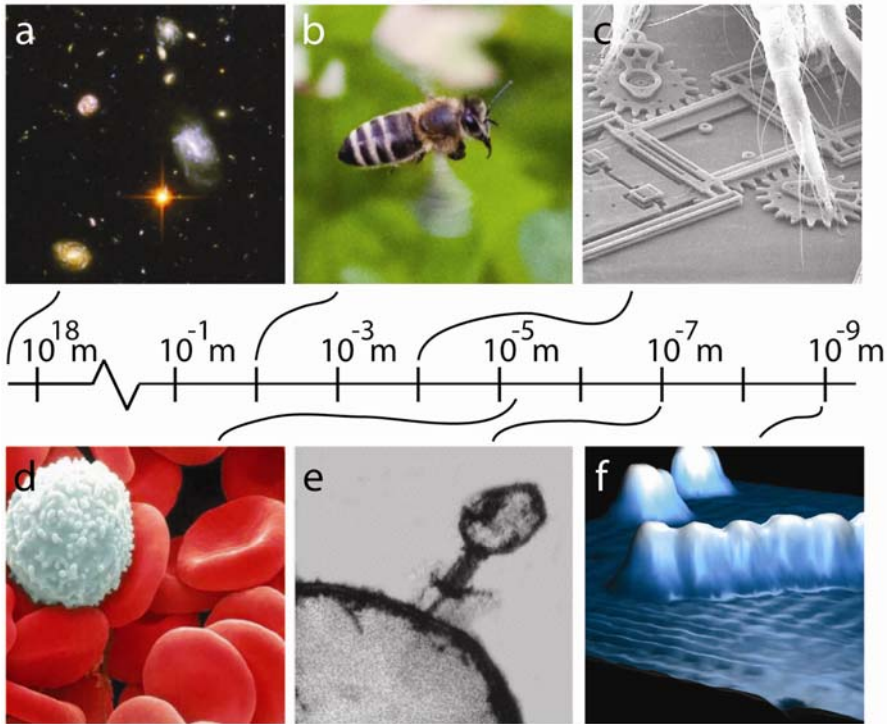


Figure 1.1 The scale of things. (a) Close-up on part of the Hubble Ultra Deep Field image. Credits: NASA/ESA. (b) A bee. Photo by Stefan Kowalczyk. (c) Spider mite on a MEMS chip. Credits: Sandia National Laboratories. (d) White and red blood cells. Credits: Science Photo Library. (e) Bacteriophage infecting an *E. Coli* cell. Credits: Elizabeth Kutter. (f) A row of C60 molecules on a silicon substrate formed by STM. Credits: Cees Dekker lab/TU Delft.

In short: we can now study the universe at the scale of many lightyears (the distance light travels in a year; $\sim 10^{16} \text{ m}$) all the way down to beardseconds (the distance a beard grows in a second; $\sim 10^{-9} \text{ m}$) and even smaller.

1.2 Biology at the nanoscale

Question: What do a bacterium, a spinach plant and a human being have in common?

Answer: All three are made out of cells. While a bacterium consists simply out of one cell, our human bodies are made out of some 10^{13} cells. Similar to photons as the quanta of light, cells are the quanta of all known living organisms. Organisms without

cells, or with ‘half cells’ do not exist, as far as we know. Cells are typically of the order of a several (tens of) micrometers and each is filled with billions of small biomolecules that cooperate on the nanoscale to form the cell into what it is (see Figure 1.2) [3].

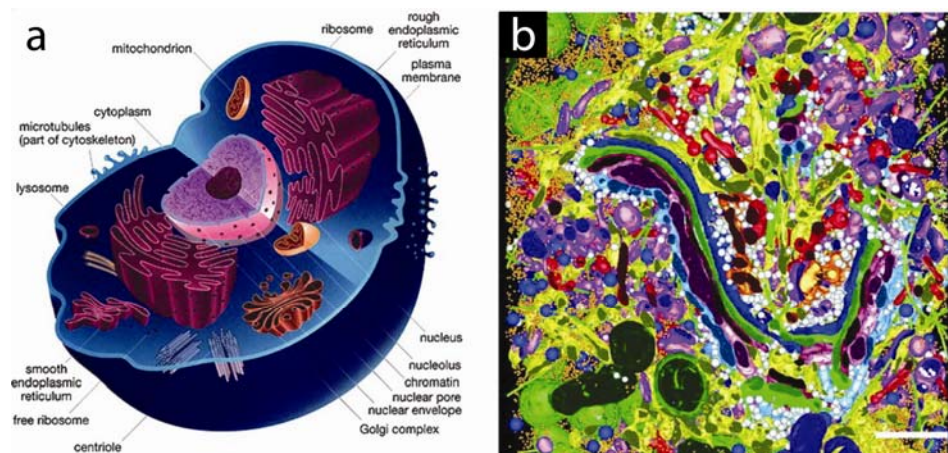


Figure 1.2 (a) Model of a eukaryotic cell (image taken from [4]). (b) Interpretation of an electron micrograph of 400-nm-thick section of a cell, highlighting the structural features in different colors [5]. Scale bar is 500 nm.

Many cellular functions are executed by protein complexes that act like molecular machines. Some examples include: ATP synthase (which uses two distinct rotary motors which are joined by a stator to produce adenosine triphosphate (ATP), the ‘fuel’ of the cell), kinesin (which transports cargo throughout cells by walking along ‘railways’ called microtubules), ribosome’s (complex molecular machines build out of some 300 proteins and RNA molecules which translate messenger RNA into proteins), hemoglobin (a small protein that executes the important task of carrying oxygen from the lungs to the rest of the body), and the bacterium flagellum (a rotary motor in bacteria that drives a propeller to spin, similar to a man-made outboard motor, enabling the bacterium to swim).

All these – and countless more – crucial tasks happen at the scale of 1–100 nanometer. While there is a wide variety of branches of biology, it is fair to say that, at the heart, biological systems operate at the nanoscale.

1.3 The 15-minute genome: from base pairs to bedside

A bacterium, a spinach and a human have much more in common than the fact that all three are made up of cells: All three carry DNA in their cells. DNA (deoxyribonucleic acid) is the universal language of all living things that we know [6]. It stores and transmits the hereditary information that describes how to make proteins, and when to make them. Its genetic alphabet consists out of four chemicals, called bases, abbreviated *A* (adenine), *C* (cytosine), *T* (thymine) and *G* (guanine). (Recently, more ‘letters’ have been discovered and synthesized, see chapter 10.) Two strands of DNA often wind around each other to form the famous double-helix structure discovered by Watson and Crick [7]. With only about 2 nm in diameter, DNA is very tiny, but understanding it can have a large impact on our lives.

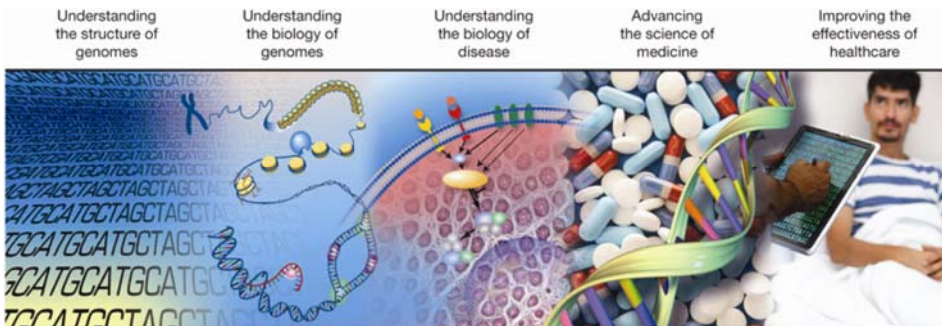


Figure 1.3 The progression from base pairs to bedside is depicted in five sequential, overlapping domains of genomics research (indicated along the top) [18].

It is only a decade ago, that we could read through the human ‘instruction book’ for the first time [8, 9]. This book can be found in two-fold in each of our trillions of cells, and each cell contains the information written in the 4-character language of life, DNA, roughly equivalent to 1000 PhD Theses. The completion of the first draft sequence of the human genome was a landmark achievement that raised high expectations and could “revolutionize the diagnosis, prevention, and treatment of most, if not all, human diseases”, as US President Bill Clinton said (Figure 1.3). Now, a decade later, the revolution in personalized medicine has yet to fully arrive [10]. But significant progress has been made: given the recent tremendous drop of costs in DNA sequencing [11], it will not be long before “the 15-minute genome” will become a reality [12] (Figure 1.4a). Driven by a vision for a \$1000 genome [13, 14], development of next-generation high-throughput DNA sequencing methods is booming

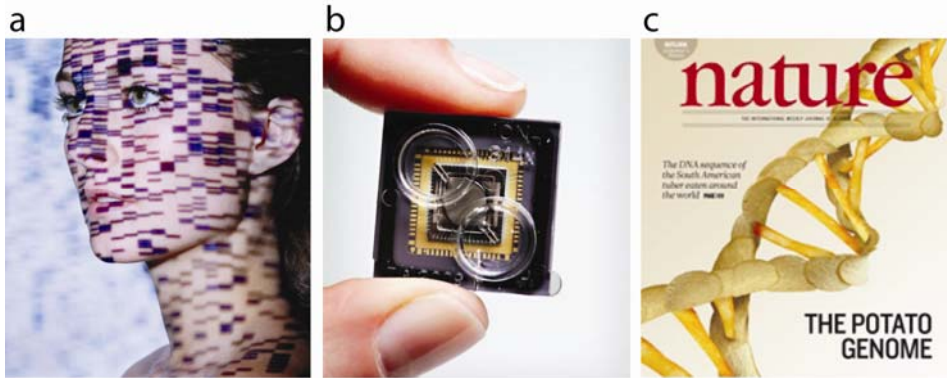


Figure 1.4 (a) Genomic information projected on a person [24]. (b) The 3rd generation DNA sequencing chip from Ion Torrent is of the size of thumbnail and exploits semiconductor technology [25]. It has 1.2 million DNA testing wells on each chip and allows to read a bacterial genome in as little as two hours on a machine of \$49,500. (c) DNA information is not only useful for personalized medicine. All living organisms, including plants like potatoes have DNA and understanding it can lead to more resistant crops [26].

business [15–17]; Figure 1.4b shows an example of one such recent device. Development of a cheap sequencing technology will also allow more labs to start sequencing with their own device instead of outsourcing.

The real question now is how to drink from the fire hose of DNA sequence data, i.e., how to apply these results in healthcare. Sequencing the genomes of many individuals allows to determine relations between DNA sequence and certain diseases. This is what genome-wide association studies (GWAS) aim to attain by probing (specific parts of) the DNA of many different individuals, in order to identify variations from person to person [19, 20]. Specific variations are then associated with different traits, including diseases. As of March 2011, 1319 human GWAS have examined 221 diseases and traits, and found about 4000 single-nucleotide polymorphisms (SNPs; single DNA mutations) [21].

Yet many unanswered questions remain about how to use the data obtained from such studies for screening, and predicting disease and improving the process of drug selection and dosing [22]. The long-anticipated field of personalized medicine – with the right drug at the right dose for a particular person – is now gaining momentum [6, 23]. For instance, targeted cancer drugs like Gleevec and Herceptin are already prescribed based on tests that determine individual differences in DNA [23].

The range of applications for genome sequencing extends beyond personalized medicine. For example, the recently completed sequencing of the potato genome [26] (Figure 1.4c) can lead to new crops that are more resistant to disease and to reduction of pesticides in agriculture. Sequencing multiple strains of *Vibrio cholerae*, the bacterium that causes Cholera, allowed to map its travel history over the past 40 years [27]. Similarly, ancient DNA of humans provided insights into how we migrated across the planet and how our genomes changed over time [28]. Finally, one can envision tracing the evolution of viral and bacterial resistance against medication and immune system in real time [29].

1.4 DNA, RNA and proteins – essential constituents of cells

There is even more to the similarity between a bacterium, a spinach and a human: all three also carry RNA (ribonucleic acid), a molecule that is similar to DNA, which uses a slightly different four-character alphabet (the *T* is replaced by a *U* (uracil)) and which is used for regulation and temporary information processing. And all three carry proteins. Like DNA and RNA, proteins are molecular chains. Proteins can be viewed as chains of 20 different types of marbles (amino acids) which are all different in size and chemical character, allowing them to form proteins in thousands of shapes and sizes, each folding in a different way, and performing innumerable functions in cells. Human cells have more than 20.000 different types of proteins, some of which consist of only tens of amino acids (for example, the hormone glucagon consists out of 29 amino acids), while others consist of tens of thousands of amino acids (for example, titin, which functions as a molecular spring in our muscles, and which consists out of some 34.000 amino acids). Considering all the possible proteins that could be formed from such a rich alphabet, it is remarkable that very similar proteins are present in, as you probably guessed by now, a bacterium, a spinach plant and a human (Figure 1.5).

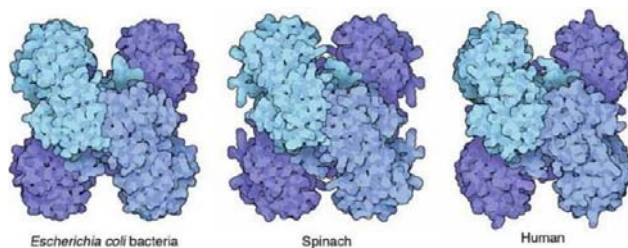


Figure 1.5 Similar looking proteins in *Escherichia Coli* bacteria, spinach and humans. Credits: David Goodsell [82].

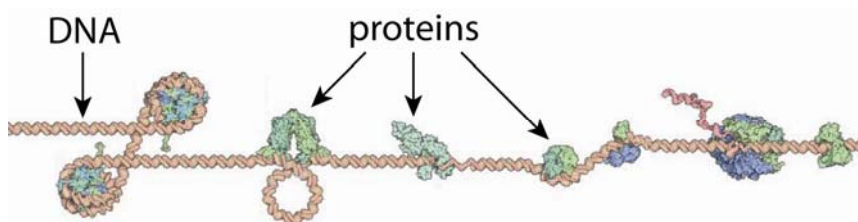


Figure 1.6 Proteins on DNA. Credits: David Goodsell/ RCSB Protein data bank.

DNA, RNA, and proteins should not be thought of as separate entities that do not interact. For example, in the biological cell, DNA is almost never ‘naked’, but it is continually acted upon by other agents. In a complex cascade of events, proteins constantly bind and process DNA in order to maintain, transcribe and replicate this carrier of genetic information (Figure 1.6). Examples include transcription factors that modulate the process of transcription, RNA polymerase which produces RNA, nucleases which cleave DNA, ligases that join DNA molecules, and histones which are involved in tight chromosome packaging in the cell nucleus. Another example, considered later in this thesis, is the RecA protein, which plays a central role in DNA repair in prokaryotes, where it catalyzes the pairing of broken DNA with complementary regions of undamaged DNA [30–32].

1.5 Nanopores in biology – compartments need channels

Cells not only have DNA, RNA, and proteins, but also nanometer-sized holes. The reason why most cell types have holes (nanopores) is straightforward. Unlike simpler bacterial cells (prokaryotic cells), each of our (eukaryotic) cells contains hundreds of compartments. The existence of such membrane-enclosed compartments has significant advantages in the life of a cell, as they allow many extra levels of control in basic processes. Perhaps the most important compartment of an eukaryotic cell is its nucleus, which harbors the genetic material. The division between nucleus and cytoplasm allows it to keep the genetic material and the protein factories separate from each other. This allows for processes like splicing (modification) of pre-mRNA, which in turn allows for many more different proteins to be synthesized out of a given piece of DNA than would be possible in a bacterial cell, which has no nucleus. Certain proteins (nucleosomes) package the long DNA into a smaller volume (chromatin) to fit inside the nucleus. However, the ‘packed’ DNA cannot be directly accessed for the production of proteins and hence there are regulators that temporarily

unpack the DNA to make it available. Compartmentalization allows for better control of the accessibility of transcriptional regulators to chromatin.

Use of compartments, however, also creates a problem: how can objects be moved across the barrier of the enclosing membrane? A perfectly sealed compartment is not very useful in most cases. Of course, cells present an answer to this problem with a variety of active and passive transport systems to traffic molecules across membranes.

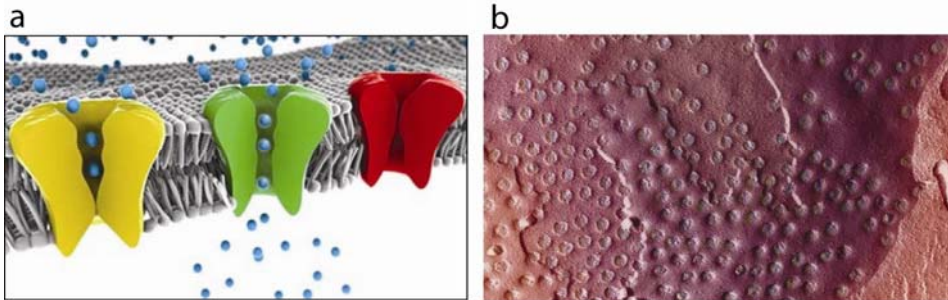


Figure 1.7 (a) Ion channels control the flow of electrically-charged ions across the cell membrane. The red and green structures show closed and open channels respectively. The yellow structure shows a mutation that inhibits ion flow. Credits: J.P. Cartailier, Symmation LLC. (b) Transmission electron micrograph of freeze-fractured nuclear pore complexes (small circles) in a nuclear envelope (purple) [33].

Indeed, the biological cell contains different types of nanopores that control trafficking of ions and molecules in and out of the cell and between subcellular structures (Figure 1.7). Most of these channels function to allow the passage of specific molecules. A good example is the potassium channel, which allows the passage of potassium ions but blocks passage of sodium and chloride ions. Examples of larger channels include bacterial porins, mitochondrial channels, some toxin channels (including the now widely studied α -hemolysin pore; see chapter 8 for more background on this remarkable pore), the nuclear pore complex (more about this pore later; see section 1.8 and chapters 8 and 9), and protein-conducting channels in the endoplasmic reticulum [34].

1.6 Scanning single molecules with solid-state nanopores

“What nature can do, we can do too!” is what the scientists who developed artificial nanopores perhaps thought. Studying biological nanopores does not only inform us concerning the inner workings of nature, but can also inspire us to employ (either biological or man-made) nanopores for technological purposes. While research conducted on protein nanopores has yielded fascinating results, advances in nanotechnology make it possible to develop artificial nanopores in solid-state materials. Such man-made nanopores have particular advantages over protein nanopores (while protein nanopores have specific advantages as well; for a review about biological, artificial, hybrid, and biomimetic nanopores, see chapter 8). In particular, the size of artificial pores can be chosen almost arbitrarily, which is not the case for biological pores whose size is fixed by nature. Also, solid-state membranes are more robust than biological membranes such as lipid bilayers.

1.6.1. Solid-state nanopores – a brief history

Let us take a step back into the 1940s when Wallace Coulter was attempting to standardize particle size in paints for the US Navy [35]. To this end, he developed a new measurement tool, based on a small aperture through which the particles would flow, restricting the flow of ions through the aperture as the particles passed. The story goes that one day he ran out of paint and instead tried a sample of his own blood. It was then that he realized that blood cells could be similarly detected. He patented his idea [36] (Figure 1.8), and later termed the ‘resistive-pulse technique’.

Nowadays, these Coulter counters are still widely used in hospitals for counting and sizing (red blood) cells. Coulter’s original idea has been refined over the years, and has been used to electronically detect bacteria [37], to electrophoretically drive and detect charged particles of approximately 60 nm in diameter through track-etched pores (1970; [38]) and a bit more recently, to detect single molecules of polyethylene glycol (PEG) passing through an alamethicin ion channels (1994; [39]). A breakthrough came in 1996, when both the structure of the α -hemolysin was determined at 0.19 nm resolution [40], and transversal of both (single-stranded) DNA and RNA through the α -hemolysin pore was demonstrated [41]. This work received much attention, not in the least because it provided the prospect of “direct, high-speed detection of the sequence of bases in single molecules of DNA or RNA”. In other words, the technique seemed to be well suited for the difficult task of the rapid sequencing (reading) of ‘the book of life’. Now, 15 years later, we are witnessing this

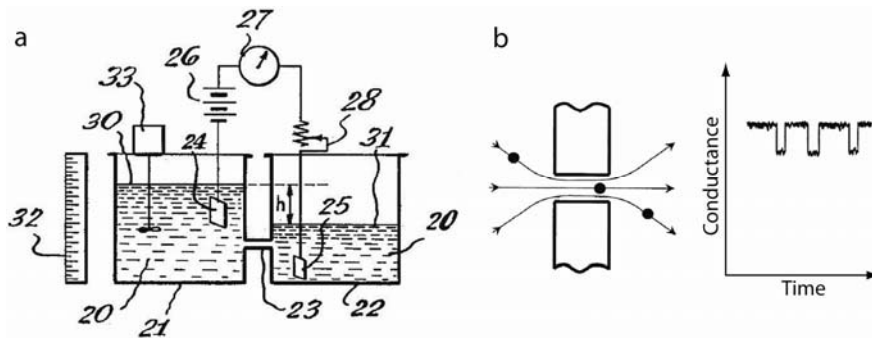


Figure 1.8 (a) Figure from the 1953 Coulter counter patent [36]. (b) Schematic of the detection principle used in conventional coulter counters. As particles flow through a narrow constriction, they are detected as temporal conductance blockades [34].

become a reality. For example, it has been shown that the α -hemolysin pore, when modified with a cyclodextrin adapter, can indeed distinguish the four bases of DNA as they translocate through the nanopore [42].

In the new millennium, a different route employing artificial counterparts of biological pores, called solid-state nanopores, is being explored by a growing number of research groups around the world (see chapter 10). As mentioned above, biological pores can be very useful for a range of applications, but they have the disadvantage of having fixed sizes and limited stability. Solid-state nanopores provide the options. Additionally, they have adjustable surface properties and can be more easily integrated into devices and arrays. Relatively large pores can be made by etching holes in glass slides [43]. Smaller nanopores (down to 2 nm in diameter) can be formed by etching preferentially along a defect-path that is first created by shooting high-energy heavy-metal ions through a polymer layer [44]. A more refined technique, termed ion beam sculpting, allows controlled fabrication of a single nanopore in a thin (typically 20 nm) silicon nitride (SiN) membrane [45]. A different approach [46] was developed in our group at Delft, where it was discovered that nanopores can be created and controlled with direct visual feedback by placing a thin SiN membrane in a commercial transmission electron microscope (TEM) and focusing the electron beam onto a tiny spot. In this way, nanopores down to 0.4 nm could be formed.

Like their biological counterparts, artificial nanopores have also been successfully employed as a new tool to rapidly detect single biopolymers, in particular DNA [47, 48]. The nanopore membrane can be placed in a microfluidic cell, between two

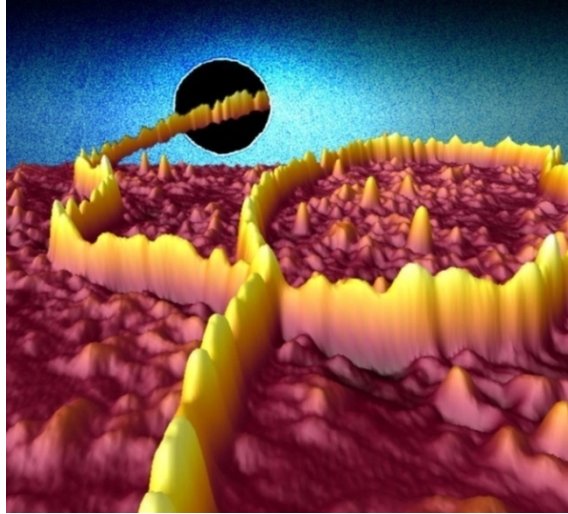


Figure 1.9 Artist impression, combining an atomic force microscopy image of a DNA molecule that is coated with RecA protein (AFM, bottom) and a transmission electron microscopy image of a solid-state nanopore (TEM, top). As the DNA–protein complex translocates through the nanopore, a change in ionic current is recorded. Protein-coated DNA can be easily discriminated from bare DNA, pointing toward future genetic screening applications with solid-state nanopores (see further chapter 3 and 4.) This image was featured on the cover of the September 2009 issue of *Nano Letters*.

compartments filled with a monovalent salt solution. Application of an electric field across the membrane results in a measurable ionic current through the pore, which is temporarily reduced upon passage of a molecule. Each molecule causes a characteristic temporary change in the trans-pore current which reflects its physical properties (see Figure 1.9). Recently, the field has rapidly expanded with now over 50 research labs [49] worldwide working on nanopores (chapter 10 and, for example, the reviews [50] and [51]). Also companies such as IBM, PacBio, Nabsys, Genia, and, most notably, Oxford Nanopore Technologies [52], which, focusing entirely on nanopores, raised over a 100 M\$ in funding, are investing heavily in nanopore research.

The quest for a practical sequencing apparatus is one thing, but nanopores can also be used to detect a wide range of other molecules, protein, or polymers. To date, nanopores have been successfully employed, for example, to distinguish DNA from RNA molecules [53], to measure the type and the concentration of small analytes [54–56], to detect proteins [57–59], to identify the stereoisomers of a common drug [60], to determine the mass spectrum of a polymer mixture [61], to exert forces on

biomolecules [62, 63], and to sort proteins [64, 65]. For a comprehensive overview of analytes that have been sensed and characterized using nanopores, see the list in Table 1 in [50], with over 60 entries.

1.6.2. Enter the graphene nanopore – it doesn't get any thinner

Notice that conventional solid-state nanopores are typically around 20 nm thick. In other words, the channel constituting the pore is long compared to the inter-base distance in DNA (~0.4 nm). This means that when a DNA molecule passes through the pore, the measured current reduction is intrinsically a smeared out average over many tens of bases. It would highly benefit the sensitivity to form nanopores in thinner membranes. One ideal candidate material is graphene, an atomically thin single layer of graphite (the material in the inner core of a pencil).

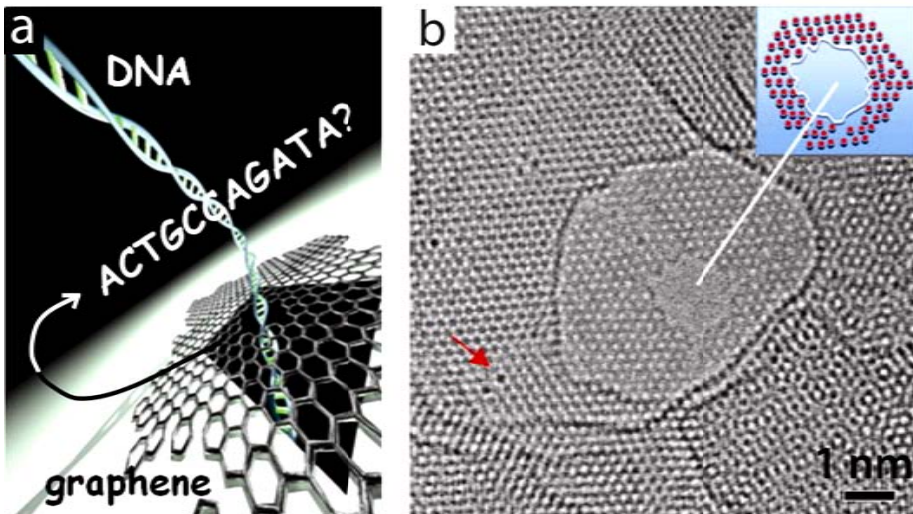


Figure 1.10 (a) Artist impression of DNA translocation through an atomically thin graphene nanopore. Credits: Cees Dekker lab / Tremani. (b) TEM image of a graphene nanopore [75].

Although theoreticians thought for a long time that such two-dimensional material would not be stable [66], the simple but beautiful experimental realization of graphene was an important discovery ([67-69]; 2010 Noble Prize in Physics). An additional advantage of graphene is that, while it is insulating for ions in the direction perpendicular to its plane, it is electrically conductive within the plane of the material.

Shortly after the theoretical prediction that a graphene gap might be ideal for fast DNA sequencing [72], three groups (our group at Delft being one of them) [71–73] independently fabricated nanopores in graphene and translocated DNA through them (Figure 1.10). As the Editor’s summary in *Nature* nicely remarked, “such a system has potential as the basis of devices that could significantly reduce the cost of DNA sequencing” [74].

Yet (graphene) nanopores have more potential applications than ‘just’ DNA sequencing [76] and ‘topographic reading’ of proteins along a DNA molecule. As mentioned above, our bodies are full of nanopores and artificial pores can improve our understanding of the inner workings of these natural pores.

1.7 The nuclear pore complex is a nanopore

One of the most intriguing natural pores is the nuclear pore complex (NPC), arguably the largest nanomachine in the cell [77] (Figure 1.11). Importantly, the NPC is the only known pathway connecting the genetic material and the protein-synthesizing ribosome factories. This means that nuclear proteins need to be imported from the cytoplasm, whereas, for example, messenger RNAs, and ribosomes are made in the nucleus and need to be exported to the cytoplasm. (The synthesis of ribosomes is an interesting case, as it involves multiple crossings of the NPC: ribosomal proteins are first imported to the nucleus, assembled in the nucleolus with ribosomal RNA, and finally exported to the cytoplasm as ribosomal subunits [78].)

All this nuclear import and export proceeds through NPCs, where in many cases a protein called Importin- β mediates the import. It does so by shuttling between the nucleus and cytoplasm and ferrying transport substrates along through the NPC that is otherwise impermeable for proteins (except for very tiny ones). This happens either by directly binding them or via adapter proteins. In this way, NPCs form the exclusive pathway’s across the nuclear envelope and they essentially act as gatekeepers of the cell nucleus [79]. They keep unwanted intruders away from the (genetic material in) the nucleus, and on the other hand make sure to only export particular molecules. For example, it keeps pre-mRNA in the nucleus until it is spliced and ready for export, which, if the RNA was released at a too early stage, could otherwise result in faulty proteins. The only known alternative way to get into or out of the nucleus is to sneak in during open mitosis, that is, once per cycle, when the cell divides and the nuclear envelope breaks down and nuclear and cytoplasmic compartments are mixed. For recent reviews of nucleocytoplasmic transport across NPCs, see [80, 81].

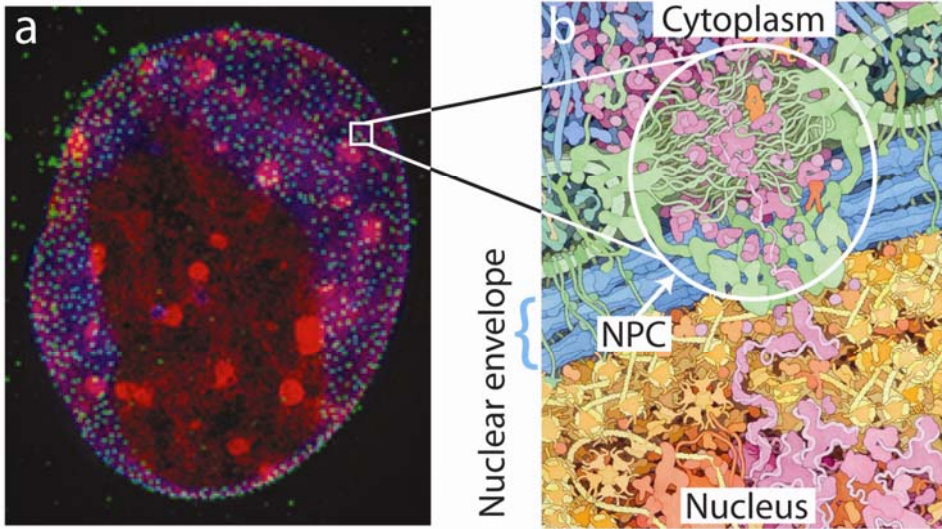


Figure 1.11 (a) The image shows a nucleus from a mouse myoblast cell; DNA is shown in red, the nuclear lamina in blue and nuclear pores in green. The upper surface of the nucleus has been clipped in this projection to reveal the DNA staining underneath the lamina. Image courtesy of P. M. Carlton, University of California, San Francisco, USA. (b) Artist impression of the NPC: Zoom-in on a nuclear pore complex in its natural crowded cellular environment [82].

More background information about the current understanding of NPC transport is presented in chapters 8 and 9, where we set out to build an artificial (or biomimetic) nuclear pore complex by tethering key nuclear pore proteins to a solid-state nanopore.

1.8 Outline of this thesis

This thesis describes mostly experimental work on solid-state nanopores.

In **chapter 2** we present measurements and theoretical modeling of the ionic conductance of solid-state nanopores up to 100 nm in diameter, with and without DNA inserted into the pore. We develop an exact solution for the ionic conductance of an hourglass-shaped pore. Furthermore, we discuss the conductance blockade due to the insertion of a dsDNA molecule into the pore, where we present new experimental data as a function of pore diameter and develop several theoretical models.

In **chapter 3** we report first translocation measurements of dsDNA molecules that are fully coated with DNA-repair protein RecA. We identify high-conductance-blockade events as translocation events of RecA-coated dsDNA. Additionally, we use an optical tweezer system to deliver bead-functionalized RecA-DNA molecules into the nanopore. We further distinguish two different regimes of translocation: a low-voltage regime (< 150 mV) in which the event rate increases exponentially with voltage, and a high-voltage regime in which it remains constant.

Building on this work, we examine in **chapter 4** the translocation of dsDNA with discrete patches of the RecA attached along its length. Using the fact that RecA-coated DNA and bare DNA yield very different current-blockade signatures, we demonstrate that it is possible to map the locations of the proteins along the length of a single molecule using a solid-state nanopore, which is promising for future high-speed, direct-read genetic screening. We currently obtain a spatial resolution of about 8 nm, or 5 RecA proteins binding to 15 base pairs of DNA.

In **chapter 5** we study the partial reduction of the DNA charge due to counterion binding by means of nanopore translocation experiments and all-atom molecular dynamics (MD) simulations. Surprisingly, we find that DNA in a lithium chloride (LiCl) solution has a much lower effective charge than in the traditionally used ionic solutions like potassium chloride (KCl). These insights also provide a practical method for achieving at least a ten-fold enhanced temporal resolution in nanopore applications, simply by exchanging measurement buffer.

Where as so far most studies focused on double-stranded DNA (dsDNA) molecules, in **chapter 6** we explore the translocation of long random-sequence single-stranded DNA (ssDNA), which is of great interest as well. From atomic force microscopy measurements, we observe the ssDNA to hybridize into large entangled structures, which have to unravel when they arrive at the pore entrance. We observe

translocation times that are exponentially dependent on voltage, $\tau \sim e^{-V/V_0}$, which is markedly different than for dsDNA, for which $\tau \sim 1/V$.

In **chapter 7** we present exciting first measurements of DNA translocation through graphene nanopores. The fact that graphene is so thin presents substantial advantages over much thicker conventional nanopores, where the pore channel is relatively long and the signal from a passing DNA molecule is averaged out over tens of bases. (The work presented in this chapter, was mentioned by the Nobel committee as one of the possible exciting future applications of graphene [83].)

In **chapter 8** we explore biomimetic nanopores and nanochannels. Biomimetics – the development of synthetic systems that imitate biological structures and processes – is now feasible at the nanoscale. Biological nanoscale channels and pores have inspired researchers to devise artificial pores that demonstrate molecular selectivity or other functional advantages. Moreover, with a biomimetic approach we can also study biological pores, through bottom-up engineering approaches whereby constituent components can be investigated outside the complex cellular environment.

A showcase of a biomimetic nanopore is presented in **chapter 9**. Here, we built a *de novo* designed ‘minimalist NPC’ that faithfully reproduces the essential feature of selectivity of the NPC. We show selective transport of proteins across this biomimetic NPC at the single molecule level. The biomimetic NPC is constructed by covalently tethering the natively unfolded phenylalanine-glycine rich (FG) domains of human nucleoporins (Nups), the key component of NPCs, to a solid-state nanopore. Individual translocation events are monitored using ionic current measurements. Our biomimetic NPC provides a quantitative platform for studying nucleocytoplasmic transport phenomena at the single-molecule level *in vitro*.

Chapter 10 provides an outlook of where developments in the nanopore field may be going in the near future.

References

- 1 Powers of Ten, <http://www.powersof10.com/> Directed by Charles and Ray Eames (1968).
 - 2 Kahn, J., Nano's big future. *National Geographic* **209**(6): 98–119 (2006).
 - 3 Alberts, B. *et al.*, Molecular biology of the cell (5th ed.), New York: Garland Science (2008).
 - 4 <http://www2.estrellamountain.edu/faculty/farabee/biobk/biobooktoc.html>
 - 5 Marsh, B. J. *et al.*, Organellar relationships in the Golgi region of the pancreatic beta cell line, HIT-T15, visualized by high resolution electron tomography, *Proc. Natl. Acad. Sci. USA*, **98**: 2399-2406 (2001).
 - 6 Collins, F., The language of life: DNA and the revolution in personalized medicine, New York: HarperCollins (2010).
 - 7 Watson, J. D. and Crick, F. H. C., A structure for deoxyribose nucleic acid. *Nature* **171**: 737–738 (1953).
 - 8 Lander, E. S. *et al.*, Initial sequencing and analysis of the human genome, *Nature* **409**: 860–921 (2001).
 - 9 Venter, J. C. *et al.*, The sequence of the human genome, *Science* **291**: 1304–51 (2001).
 - 10 Lander, E. S., Initial impact of the sequencing of the human genome, *Nature* **470**: 187–197 (2011).
 - 11 <http://www.genome.gov/sequencingcosts/>
 - 12 Nanopore sequencing: Towards the 15-minute genome, *The Economist*, March 10th 2011.
 - 13 Schloss, J. A., How to get genomes at one ten-thousandth the cost. *Nat. Biotechnol.* **26**: 1113–5 (2008).
 - 14 Davies, K., The \$1,000 Genome: The revolution in DNA sequencing and the new era of personalized medicine, Free Press (2010).
 - 15 Shendure, J. and Ji, H., Next-generation DNA sequencing, *Nat. Biotechnol.* **26**: 1135–45 (2008).
 - 16 Metzker, M. L., Sequencing technologies - the next generation, *Nat. Rev. Genet.* **11**: 31–46 (2010).
 - 17 Niedringhaus, T. P. *et al.*, Landscape of next-generation sequencing technologies, *Anal. Chem.* **83**: 4327–41 (2011).
 - 18 Green, E. D. and Guyer, M. S., Charting a course for genomic medicine from base pairs to bedside, *Nature* **470**: 204–213 (2011)
 - 19 Manolio, T. A., Genomewide association studies and assessment of the risk of disease, *N. Engl. J. Med.* **363**(2):166–76 (2010).
-

- 20 International HapMap Consortium, The International HapMap Project, *Nature* **426**: 789–96 (2003).
 - 21 <http://www.genome.gov/GWASudies/>
 - 22 Feero, W. G. *et al.*, Genomic medicine – an updated primer, *N. Engl. J. Med.* **362**(21): 2001–11 (2010).
 - 23 Allison, M., Is personalized medicine finally arriving? *Nat. Biotechnol.* **26**: 509–17 (2008).
 - 24 Khoury, M. J. *et al.*, A reality check for personalized medicine, *Nature* **464**: 680 (2010).
 - 25 Rothberg, J. M. *et al.*, An integrated semiconductor device enabling non-optical genome sequencing. *Nature* **475**: 348–352 (2011).
 - 26 The Potato Genome Sequencing Consortium, Genome sequence and analysis of the tuber crop potato, *Nature* **475**: 189–195 (2011).
 - 27 Mutreja A, *et al.*, Evidence for several waves of global transmission in the seventh cholera pandemic, *Nature*, 2011 Aug 24. doi: 10.1038/nature10392. [Epub ahead of print].
 - 28 Callaway, E., Ancient DNA reveals secrets of human history, *Nature* **476**: 136–137 (2011).
 - 29 Kahvejian, A. *et al.*, What would you do if you could sequence everything? *Nat. Biotechnol.* **26**: 1125–33 (2008).
 - 30 Roca, A. I. and Cox, M. M., RecA protein: Structure, function, and role in recombinational DNA repair, in *Progress in Nucleic Acid Research and Molecular Biology* **56**, Academic Press Inc, San Diego (1997).
 - 31 Cox, M. M., The bacterial RecA protein: structure, function, and regulation in *Topics in Current Genetics* **1** (eds Aguilera, A. and Rothstein, R.), Springer-Verlag GmbH, Heidelberg (2007).
 - 32 van der Heijden, T. *et al.*, Homologous recombination in real time: DNA strand exchange by RecA, *Molecular Cell* **30**: 530–538 (2008).
 - 33 Fawcett, D.W. / Science photo library. <http://sciencephoto.com/media/99428/view>
 - 34 Bezrukov, S. M., Ion channels as molecular Coulter counters to probe metabolite transport, *J. Membr. Biol.* **174**: 1–13 (2000).
 - 35 http://www.whcf.org/WHCF_WallaceHCoulter.htm
 - 36 Coulter W. H., Means for counting particles suspended in a fluid, US Patent 2656508 (1953).
 - 37 Kubitschek, H. E., Electronic counting and sizing of bacteria. *Nature* **182**: 234–235 (1958).
 - 38 Deblois, R.W. and Bean, C. P., Counting and sizing of submicron particles by resistive pulse technique, *Rev. Sci. Instr.* **41**: 909 (1970).
-

-
- 39 Bezrukov, S. W. *et al.*, Counting polymers moving through a single-ion channel, *Nature* **370**: 279–281 (1994).
- 40 Song, L. Z. *et al.*, Structure of staphylococcal alpha-hemolysin, a heptameric transmembrane pore, *Science* **274**: 1859–1866 (1996).
- 41 Kasianowicz, J. J. *et al.*, Characterization of individual polynucleotide molecules using a membrane channel, *Proc. Natl. Acad. Sci. USA* **93**:13770–13773 (1996).
- 42 Clarke, J. *et al.*, Continuous base identification for single-molecule nanopore DNA sequencing, *Nat. Nanotech.* **4**: 265–270 (2009).
- 43 Schmidt, C. *et al.*, A Chip-Based Biosensor for the Functional Analysis of Single Ion Channels, *Angew. Chem. Int. Ed. Engl.* **39**: 3137–3140 (2000).
- 44 Siwy, Z. and Fuliński, A., Fabrication of a synthetic nanopore ion pump, *Phys. Rev. Lett.* **89**: 198103 (2002).
- 45 Li, J. *et al.*, Ion-beam sculpting at nanometre length scales, *Nature*. **412**: 166–169 (2001).
- 46 Storm, A. J. *et al.*, Fabrication of solid-state nanopores with single-nanometre precision, *Nat. Mater.* **2**: 537–540 (2003).
- 47 Li, J. L. *et al.*, DNA molecules and configurations in a solid-state nanopore microscope. *Nat. Mater.* **2**: 611–615 (2003).
- 48 Storm, A. J. *et al.*, Fast DNA Translocation through a solid-state nanopore. *Nano Lett.* **5**: 1193–1197 (2005).
- 49 <http://www.thenanoporesite.com/>
- 50 Howorka, S. and Siwy, Z., Nanopore analytics: sensing of single molecules. *Chem. Soc. Rev.* **38**: 2360–2384 (2009).
- 51 Dekker, C., Solid-state nanopores. *Nat. Nanotech.* **2**: 209–215 (2007).
- 52 <http://www.nanoporetech.com/>
- 53 Skinner, G. M. *et al.*, Distinguishing single- and double-stranded nucleic acid molecules using solid-state nanopores. *Nano Lett.* **9**: 2953–2960 (2009).
- 54 Gu, L. Q. *et al.*, Stochastic sensing of organic analytes by a pore-forming protein containing a molecular adapter. *Nature* **398**: 686–690 (1999).
- 55 Braha, O. *et al.*, Simultaneous stochastic sensing of divalent metal ions, *Nat. Biotechnol.* **9**:1005–7 (2000).
- 56 Bezrukov, S. M., Ion channels as molecular Coulter counters to probe metabolite transport. *J. Membr. Biol.*, **174**: 1–13 (2000).
- 57 Movileanu, L. *et al.*, Detecting protein analytes that modulate transmembrane movement of a polymer chain within a single protein pore, *Nat. Biotechnol.* **10**:1091–5 (2000).
- 58 Kasianowicz, J. J. *et al.*, Simultaneous multianalyte detection with a nanometer-scale pore. *Anal. Chem.* **10**: 2268–72 (2001).
-

-
- 59 Benner, S. *et al.*, Sequence-specific detection of individual DNA polymerase complexes in real time using a nanopore, *Nat. Nanotechnol.* **11**: 718–24 (2007).
- 60 Kang, X. F. *et al.*, Stochastic detection of enantiomers, *J. Am. Chem. Soc.* **128**(33): 10684–5 (2006).
- 61 Robertson, J. W. *et al.*, Single-molecule mass spectrometry in solution using a solitary nanopore, *Proc. Natl. Acad. Sci. USA* **104**(20): 8207–11 (2007).
- 62 Keyser, U. F. *et al.*, Direct force measurements on DNA in a solid-state nanopore. *Nature Physics* **2**: 473–477 (2006).
- 63 van Dorp, S. *et al.*, Origin of the electrophoretic force on DNA in solid-state nanopores, *Nature Physics* **5**: 347–351 (2009).
- 64 Striemer, C. C. *et al.*, Charge- and size-based separation of macromolecules using ultrathin silicon membranes, *Nature* **445**: 749–53 (2007).
- 65 Wolfe, A. J. *et al.*, Catalyzing the translocation of polypeptides through attractive interactions, *J. Am. Chem. Soc.* **129**(45):14034–41 (2007).
- 66 Landau, L. D. and Lifshitz, E. M., *Statistical Mechanics, Part I*, Pergamon, Oxford, 1980.
- 67 Novoselov, K. S. *et al.*, Electric field effect in atomically thin carbon films, *Science* **306**: 666–669 (2004).
- 68 Geim, A. K. and Novoselov, K. S., The rise of graphene, *Nat. Mater.* **6**(3): 183–191 (2007).
- 69 Geim, A. K., Graphene: status and prospects, *Science*, **324**:1530–1534 (2009).
- 70 Postma, H. W. C., *Nano Lett.* **10**: 420–425 (2010).
- 71 Schneider, G. F. *et al.*, DNA translocation through graphene nanopores. *Nano Lett.* **10**: 3163–3167 (2010).
- 72 Merchant, C. A. *et al.*, DNA translocation through graphene nanopores. *Nano Lett.* **10**: 2915–2921 (2010).
- 73 Garaj, S. *et al.* Graphene as a subnanometre trans-electrode membrane. *Nature* **467**: 190–193 (2010).
- 74 Editor’s summary, DNA sequencing: enter the graphene nanopore, *Nature* **467** (2010).
- 75 Song, B. *et al.*, Atomic-Scale Electron-Beam Sculpting of Near-Defect-Free Graphene Nanostructures, *Nano Letters* **11**: 2247–2250 (2011).
- 76 Branton, D. *et al.*, The potential and challenges of nanopore sequencing. *Nat. Biotechnol.* **26**: 1146–1153 (2008).
- 77 Alber, F. *et al.*, The molecular architecture of the nuclear pore complex, *Nature* **450**: 695–701 (2007).
- 78 Görlich, D. and Kutay, U., Transport between the cell nucleus and the cytoplasm, *Annu. Rev. Cell. Dev. Biol.* **15**: 607–660 (1999).
-

- 79 Wentze, S.R., Gatekeepers of the nucleus, *Science* **288**: 1374–1377 (2000).
- 80 Grünwald, D. *et al.*, Nuclear export dynamics of RNA-protein complexes, *Nature* **475**: 333–41 (2011).
- 81 Wentze, S. R. and Rout, M. P., The nuclear pore complex and nuclear transport, *Cold Spring Harb. Perspect. Biol.* **10**: a000562 (2010).
- 82 Goodsell, D. S., *The Machinery of Life*, New York: Springer (2009).
- 83 www.nobelprize.org/nobel_prizes/physics/laureates/2010/announcement.html/
-

Chapter 2

Modeling the conductance and DNA blockade of solid-state nanopores

We present measurements and theoretical modeling of the ionic conductance G of solid-state nanopores with 5–100 nm diameters, with and without DNA inserted into the pore. First, we show that it is essential to include access resistance to describe the conductance, in particular, for larger pore diameters. We then present an exact solution for G of an hourglass-shaped pore, which agrees very well with our measurements without any adjustable parameters, and which is an improvement over the cylindrical approximation. Subsequently we discuss the conductance blockade ΔG due to the insertion of a DNA molecule into the pore, which we study experimentally as a function of pore diameter. We find that ΔG decreases with pore diameter, contrary to the predictions of earlier models that forecasted a constant ΔG . We compare three models for ΔG , all of which provide good agreement with our experimental data.

This chapter has been published as S.W. Kowalczyk, A.Y. Grosberg, Y. Rabin, and C. Dekker, *Nanotechnology* **22**, 315101 (2011).

2.1 Introduction

Solid-state nanopores, nanometer-size holes in a thin synthetic membrane, are a versatile tool for the detection and manipulation of charged biomolecules [1, 2]. An external electric field drives a biomolecule through the nanopore, producing a characteristic transient change in the trans-pore ionic current. This approach can be used for sensitive single-molecule biosensing platforms, and much current research is directed towards nanopore sequencing of DNA.

Understanding the conductance of a nanopore is the basis for any nanopore experiment. In most previous studies of DNA translocation through nanopores, with a few exceptions [3–5], it was assumed that (a) the potential drop occurs predominantly across the pore and (b) that the pore has a cylindrical shape. However, in many cases, particularly when the pore is relatively wide and not very long, the resistance of the medium outside the pore, called the access resistance, and the corresponding potential drop are significant [6–9]. Furthermore, it has been experimentally measured that solid-state nanopores are hourglass-shaped rather than cylindrical [10–14]. Models that do not include these factors predict incorrect open pore conductance values G (especially for wide pores with pore diameters larger than the membrane thickness), as well as constant conductance blockade values ΔG independent of pore diameter, in contradiction with experimental data.

We therefore develop a more realistic parameter-free model for the ionic conductance of a hourglass-shaped (hyperboloid) nanopore that captures both the pore-dominated and access-dominated regimes of resistance. Comparison of theoretical predictions and experimental data shows an excellent match between the two. Furthermore, we address the question: how does the ionic conductance change upon insertion of a DNA molecule into the pore? To answer this, we measure how ΔG depends on pore size, and compare the results to geometrical models of either a cylindrical or hourglass-shaped pore.

2.2 Conductance of a cylindrical nanopore

We measure the conductance versus pore diameter of pores drilled into a 20 nm thin silicon nitride (SiN) membrane. Detailed information about the experiments is presented in the materials and methods section. Briefly, a membrane with a nanopore is mounted in a microfluidic flow cell and sealed to liquid compartments on both sides of the sample. Measurements are performed in 1 M KCl salt solution containing

10 mM Tris-HCl and 1 mM EDTA at pH 8.0 at room temperature. Voltages between -0.2 V and +0.2 V are applied across the pore and ionic currents are recorded. Fully linear current-voltage curves are obtained in this range of voltages. We measured the conductance for a large number of nanopores with diameters in the range of 5 – 100 nm, see Figure 2.1. We observe a slightly nonlinearly rising conductance with increasing pore diameter.

We first address the question: how can the conductance ($G = I/V$, the reciprocal of the resistance) of these pores be modeled? Note that we limit ourselves to geometry-based models for the conductance because we consider the high-salt limit where one can neglect the effect of surface charges on the membrane, as well as conduction along the DNA molecule (see also [22]). We first consider the expression for a cylindrical pore that is frequently used in the nanopore literature:

$$G = \sigma \frac{\pi d^2}{4l} \quad (1).$$

Here the bulk conductivity σ (10.5 S/m at 23°C [15]), is the reciprocal of the bulk resistivity ρ , d is the diameter of the circular pore, and l is the thickness of the membrane. Note that the only role of the membrane is the obstruction of space available for the current; no other physical effects are considered. A fit of this equation to the data (grey line in Figure 2.1a) shows that while in the narrow pore regime ($d \leq 15$ nm) the data is well described by the above equation, the model fits the data very poorly for larger pore diameters. The reason for the discrepancy is that the access resistance, which is only implicitly (i.e., one can introduce a larger thickness of the membrane to account for access resistance in this model, as was shown in [3]) present in Eq. (1), becomes the dominant contribution at larger pore diameters.

The concept of access resistance stems from the following fact known in general physics (see, for example, reference [16]): if we consider the electrical resistance of a medium between two spherical electrodes submerged in that medium, then this resistance – quite surprisingly at first glance – does not depend on the distance between electrodes, but only on their sizes. This happens because the resistance is dominated by the narrow region where the electric current approaches the electrode. More specifically, the resistance between two spherical electrodes in an infinite media equals $4\rho/\pi d$, where d is the diameter of the electrode. Based on this idea, Hille [6, 7] argued that the access resistance of a pore should also depend only on the pore dimension, and not on any macroscopic dimensions. Specifically, he estimated the access resistance by considering a semi-spherical cupola above the pore entrance as an effective electrode, leading to $R_{\text{access}} = \rho/\pi d$. The coefficient is explained by the fact

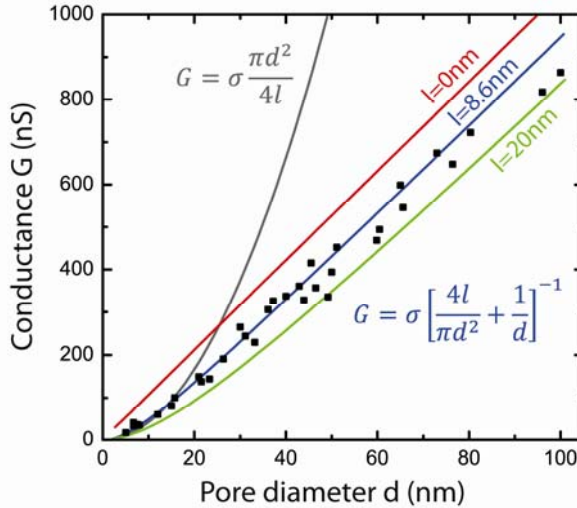


Figure 2.1 Experimental data of conductance versus pore diameter of pores drilled into a 20 nm thin silicon nitride (SiN) membrane. The solid lines are fits to Eq. 1 (grey line; $l = 20$ nm) and Eq. 2 (red, $l = 0$; blue, $l = 8.6$ nm; green, $l = 20$ nm).

that, first, we have only one electrode of size d , while the other one is macroscopic and its access resistance is negligible; and, second, we have only half a sphere on one side of the pore. Later on, Hall [8] realized that a semi-spherical cupola is not a reasonable representation of the actual electrode. He considered instead a planar disc at the pore entrance, and obtained $R_{\text{access}} = \rho/2d$. In this paper we will adopt this equation for the access resistance.

As was noted before [9], one can subsequently write the total resistance of a nanopore as

$$R = R_{\text{channel}} + 2R_{\text{access}} \quad (2).$$

Hence, using the equation from Hall, we obtain the following equation for the conduction:

$$G = \sigma \left[\frac{4l}{\pi d^2} + \frac{1}{d} \right]^{-1} \quad (3).$$

A least-square fit shows that this equation gives an excellent fit to the data ($\chi^2_{\text{red}} = 1.44$) for a membrane thickness of $l = 8.6$ nm (blue line in Figure 2.1). The fact that this value of l is lower than the given 20 nm membrane thickness, is a consequence of the non-cylindrical, hourglass shape of the pore that is due to the e-beam drilling process [10–14]. As a result, the pore diameter is larger at the entrance and exit than

at the middle of the membrane, and the effective pore length is lower than the membrane thickness.

2.3 Conductance of an hourglass-shaped nanopore

The actual shape of a nanopore, as obtained from electron microscopy tomographs [10–14], is typically much closer to an hourglass shape than to a cylindrical shape. We therefore now consider hourglass-shaped pores. Unlike for a cylindrical pore, an hourglass-shaped pore is characterized by three lengths: in addition to l (membrane thickness) and d (narrowest diameter), there is also the widest diameter (at the membrane surface), D (see Figure 2.2a). We can approximate such a pore surface by the hyperboloid

$$x^2 + y^2 = z^2 \frac{D^2 - d^2}{l^2} + \frac{d^2}{4} \quad (4),$$

in which $x^2 + y^2 = (d/2)^2$ at $z = 0$ and $x^2 + y^2 = (D/2)^2$ at $z = \pm l/2$. For this hourglass-shaped pore, we can find an exact solution for the resistance R_{hyp} between the two blue equipotential pieces of a spheroid depicted in Figure 2.2a. To do so, we solve analytically, by standard methods, the Laplace equation with proper boundary conditions, as given by the pore shape (see SI for details). This yields the following expression:

$$R_{\text{hyp}} = \frac{2\rho}{\pi d} \cdot \frac{\sin \alpha}{1 - \cos \alpha} \arctan\left(\frac{\sqrt{D^2 - d^2}}{d}\right) \quad (5),$$

where α is the asymptotic opening angle of the hyperboloid (see Figure 2.2a) given by

$$\sin^2 \alpha = \frac{D^2 - d^2}{l^2 + D^2 - d^2} \quad (6).$$

Now, we have to include the access resistance from the pore to infinity. Unfortunately, it appears difficult to properly match the contributions from the access resistance and from the pore itself. However, we know the resistance from infinity to the purple hemisphere in the inset of Figure 2.2b (given by $\rho/\pi D$ as determined by Hille [6, 7]), and the resistance from infinity to the orange disk (given by $\rho/2D$ from the calculation by Hall [8]). Since the blue cupola is always in between the purple and orange lines, we can state the following upper (1) and lower (2) limits on the total resistance:

$$R_{\text{hyp}} + \frac{2\rho}{\pi D} < R < R_{\text{hyp}} + \frac{\rho}{D} \quad (7),$$

where R is the full measured resistance between remote electrodes.

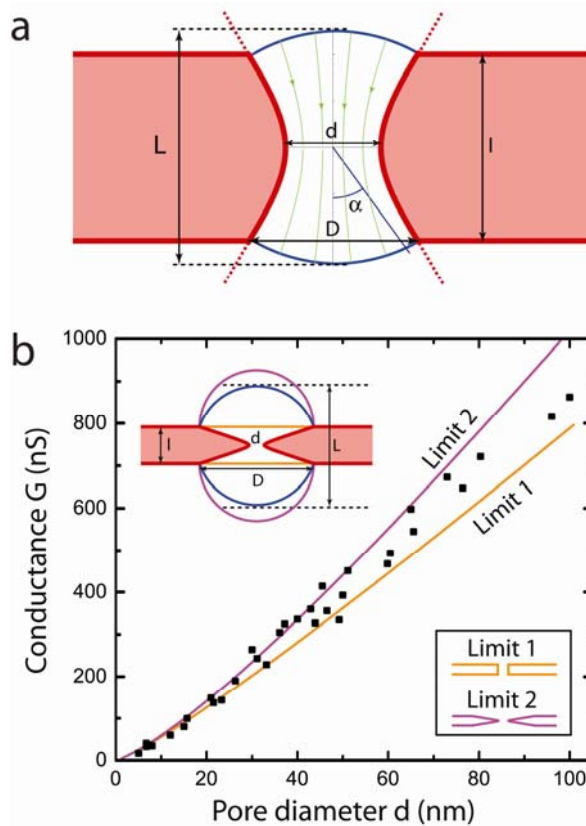


Figure 2.2 (a) Cross section of an hourglass-shaped nanopore for which the solution in the closed form is obtained. Thick red lines show the surfaces of the SiN dielectric membrane. Thick blue lines indicate equipotentials. Thin green lines are current lines. Angle α , lengths L , l , and diameters d , D are shown. In this image, $d = 1$, $L = 5$, $\alpha = \pi/5$. (b) Experimental data of Figure 2.1 with solid lines that are the predictions from the exact model (Eq. 7) with an upper and lower limit for the access resistance. Note that the model fits the data quite well with no free parameters. As expected the experimental values lay within the two limits. The inset at the bottom right shows pore shapes with $D = d$ (orange) and with $D \gg d$ (purple); the later pore is predicted to have a conductance very close to limit 2, while the former will have a conductance closer (although not exactly equal) to limit 1.

From experimental studies of the pore shape [10–14], we deduce that $D \approx d + 20$ nm for typical beam conditions (note that the exact pore shape depends on the TEM beam conditions and hence might not be the same even for pores of equal diameter).

It should be noted that taking slightly different $D(d)$, does not influence the result much, in the sense that the data points still are in between the two bounds in Figure 2.2b (fits not shown). Figure 2.2b shows the experimental data for $G(d)$ and compares it to the hyperboloid model calculations for the two limits of Eq. 7. Note that, upon adopting the experimental result for $D(d)$, the hourglass model has no adjustable parameters. The model predictions for the two bounds (two lines in Figure 2.2b) bracket the data remarkably well. Note that the cylindrical model can only be forced to fit the data on the expense of adjusting the “effective” membrane thickness to an incorrect value (in our case the best fit was for 8.6 nm, i.e., less than half the actual membrane thickness of 20 nm).

2.4 Modeling the DNA conductance blockade

Having obtained an adequate description of the ionic conductance of solid-state nanopores we now ask: how does the conductance change upon insertion of a DNA molecule into the pore? Naively, one might expect the change in conductance upon insertion of a DNA molecule into the pore, ΔG , to be constant, independent of pore diameter, since the molecular volume that is blocking part of the pore is the same in all cases. However, we measured ΔG for B-form double stranded DNA (λ -DNA) for a number of pore sizes, and we find that ΔG clearly decreases with pore diameter. Typical events of DNA translocation through pores of diameters of 5 nm, 15 nm, and 65 nm are shown in Figure 2.3a. Experimental values for ΔG versus pore diameter are presented in Figure 2.3b.

Assuming l does not change with d (which might not be true in case l is understood to be the ‘effective’ thickness of the membrane, in the sense that the access resistance is accounted for by a larger l than what is the physical membrane thickness, see [3]), the model of Eq. 1 fails to describe $\Delta G(d)$, as it would predict a constant ΔG . Instead, let us first consider the model of a cylindrical pore including the access resistance (Eq. 3) and examine its prediction for the reduction in the conductance when DNA translocates through the pore. Although the DNA molecule is present both inside and outside the pore, its presence has a larger effect on the pore resistance than on the access resistance, because its volume fraction inside the pore (the volume of the DNA divided by the volume inside the pore) is much larger than that outside the pore. For large pores, where the access resistance dominates the total resistance, the presence of DNA in the pore thus has a relatively smaller effect and

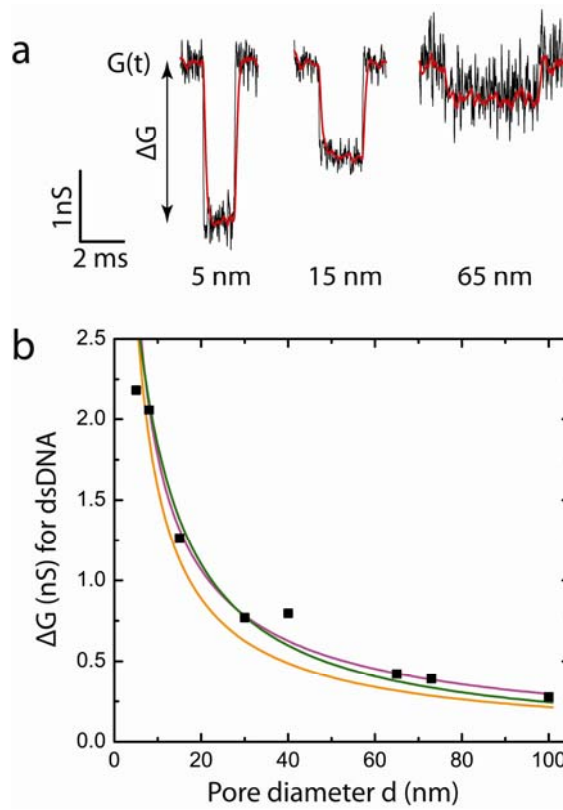


Figure 2.3 (a) Typical ionic conductance $G(t)$ traces when a DNA molecule translocates a nanopore of 5 nm (left), 15 nm (middle) or 65 nm (right) in diameter. The open pore conductance was 18 nS, 81 nS, and 599 nS, resp. The data is low-pass filtered at 10 kHz (black) and 2 kHz (red). (b) Experimental data for the change in pore conductance ΔG upon insertion of a dsDNA molecule, as a function of pore diameter. Solid lines are for a geometric model with cylindrical DNA in a cylindrical pore (green), and in a hyperboloid-shaped pore in two limits (purple and orange; same color coding as in Figure 2.2b).

ΔG decreases compared to its value for narrow pores. Based on geometrical considerations, we can calculate ΔG simply as:

$$\Delta G = G_{\text{open pore}} - G_{\text{with DNA}} = G(d) - G(d_{\text{with DNA}}) \quad (8),$$

where G is given by Eq. 3 and $d_{\text{with DNA}}$ is the effective diameter of the pore with DNA in the pore, given by

$$d_{\text{withDNA}} = \sqrt{d^2 - d_{\text{DNA}}^2} \quad (9).$$

Taking $d_{\text{DNA}} = 2.2$ nm, for B-form double stranded DNA, this model fits the data for ΔG for dsDNA versus pore diameter d remarkably well without any free fit parameters (blue line in Figure 2.3b; $\chi^2_{\text{red}} = 1.97$). Here we adopted the effective membrane thickness $l = 8.6$ nm, as found from fitting the data in Figure 2.1. A least-squares fit with l as a free parameter gives a similar value $l = 11.0$ nm, with almost the same χ^2_{red} value of 1.92.

Note that the case of single stranded DNA is more complex, and will not be considered in this paper, because single stranded DNA is very flexible, and therefore will coil up in a complex way in the access resistance region, contributing in an unpredictable way to ΔG . Furthermore, it was experimentally found that ΔG for ssDNA depends on the DNA sequence: while ssDNA homopolymers produce relatively small conductance blockade amplitudes [17], heteropolymeric ssDNA produces very large amplitudes [18]. Including these factors goes beyond our current modeling, which is only valid for polymers with a persistence length (~ 1 nm for ssDNA; ~ 50 nm for dsDNA) that is longer than the pore length (20 nm in our case).

Alternatively, one may use the same approach (i.e., Eqs. 8 and 9) to calculate ΔG when the (cylindrical) DNA is put in an hourglass-shape pore with $l = 20$ nm (i.e., with G as given by Eq. 7). This yields similar results, with $\chi^2_{\text{red}} = 1.63$ for limit 1 and $\chi^2_{\text{red}} = 6.3$ for limit 2 (see Figure 3b). A different model was used by Wanunu *et al* [19]; however, they extracted the open pore conductance from measurements (rather than from a model), and only considered a limited size range of very narrow pores (2.7 – 4.7 nm in diameter). Finally, in SI section 4, we present a model for ΔG with dsDNA in the pore for which the solution in the closed form is obtained, where the DNA molecule is treated as a hyperboloid inserted along the symmetry axis of the hourglass-shaped pore. Note that, while DNA is obviously better modeled as a cylinder, the assumption that both DNA and pore have the same hyperbolic geometry simplifies the boundary conditions and allows an analytical solution of the Laplace equation for the electrostatic potential in the pore. We find that this model fits the experimental data reasonably well (Figure S2.8). While having academic value, this model is less practical in usage since DNA obviously is not a hyperboloid.

2.5 Conclusions

In conclusion, we have presented new experimental data on nanopore conductance and DNA blockade for a large range of pore sizes. We have developed several theoretical models to describe both, and obtained excellent agreement between theory

and experiments. We have found that, in general, it is essential to include both the access and the pore resistance. An exact solution for the open pore conductance G of an hourglass-shaped pore agrees, without any adjustable parameters, with measurements of G . Additionally, we measured the conductance blockade ΔG due to the insertion of a dsDNA molecule for a number of pore sizes, and we found that ΔG strongly decreases with pore diameter, contrary to the predictions of earlier models that forecasted a constant ΔG . We developed several models for ΔG that provide excellent agreement with our experimental data. The models for G and ΔG presented in this paper can provide the foundation for understanding a multitude of conductance-based experiments on nanopores.

2.6 Materials and Methods

Solid-state nanopores

Fabrication of solid-state nanopores starts with the fabrication of 20 nm thin free-standing SiN membranes through the use of electron-beam lithography and wet etching [20]. For the electrical measurements, a membrane with a single nanopore is mounted in a polyether ether ketone (PEEK) microfluidic flow cell and sealed to liquid compartments on either side of the sample. Measurements are performed in 1 M KCl salt solution containing 10 mM Tris-HCl and 1 mM EDTA at pH 8.0 at room temperature. Ag/AgCl electrodes are used to detect ionic currents and to apply electric fields. Current traces are measured at 10 kHz bandwidth using a resistive feedback amplifier (Axopatch 200B, Axon Instruments) and digitized at 100 kHz. For the dsDNA unmethylated λ -DNA (10 ng/ μ L, Promega, Madison, WI) was used. The event-fitting algorithm used to analyze and label the translocation events was the same as the one described before [21].

Fitting

The lowest reduced χ^2_{red} value was calculated using

$$\chi^2_{\text{red}} = \frac{1}{N-n-1} \sum_{i=1}^N \left(\frac{x_i - \mu_i}{\sigma_i} \right)^2,$$

with N the number of data points and n the number of fitting parameters. The error of the experimental data points is estimated at $\sigma_i = 0.1 * G$, a relative error of 10%. Fitting was done using a custom written code in *Matlab*.

Acknowledgements. We acknowledge discussions with G. F. Schneider. This work is supported by the NanoSci-E+ program, the European Union's Seventh Framework Programme (FP7/2007-2013) under grant agreement n° 201418 (READNA), and ERC-2009-AdG Grant 247072 NANOFORBIO. YR and AYG would like to acknowledge the support of the US-Israel Binational Science Foundation. YR would like to thank the Israel Science Foundation for financial support.

References

- 1 Dekker, C., Solid-state nanopores. *Nature Nanotech.* **2**, 209–215 (2007).
 - 2 Branton, D., *et al.*, The potential and challenges of nanopore sequencing. *Nature Biotech.* **26**, 1146–1153 (2008).
 - 3 Smeets, R. M. M., *et al.*, Salt Dependence of Ion Transport and DNA Translocation through Solid-State Nanopores. *Nano Lett.* **6**, 89–95 (2006).
 - 4 Wanunu, M., Morrison W., Rabin Y., Grosberg, A. Y., and Meller, A., Electrostatic Focusing of Unlabeled DNA into Nanoscale Pores using a Salt Gradient. *Nature Nanotech.* **5**, 160–165 (2009).
 - 5 Grosberg, A. Y. and Rabin, Y., DNA capture into a nanopore: Interplay of diffusion and electrohydrodynamics. *J. Chem. Phys.* **133**, 165102 (2010).
 - 6 Hille, B., Pharmacological modifications of the sodium channel of frog nerve. *J. Gen. Physiol.* **51**, 199–219 (1968).
 - 7 Hille, B., Ionic channels in nerve membranes. *In: Progress in Biophysics and Molecular Biology.* J. A. V. Butler, editor. Pergamon Press, N. Y. 21:1 (1970).
 - 8 Hall, J. E., Access resistance of a small circular pore. *J. Gen. Physiol.* **66**, 531–532 (1975).
 - 9 Vodyanoy, I. and Bezrukov, S. M., Sizing of ion pore by access resistance measurements. *Biophys. J.* **62**, 10–11 (1992).
 - 10 Liebes, Y., *et al.*, Reconstructing solid state nanopore shape from electrical measurements. *Applied Physics Letters* **97**, 223105 (2010).
 - 11 Kim, M. J., McNally, B., Murata, K., and Meller, A., Characteristics of solid-state nanometre pores fabricated using a transmission electron microscope. *Nanotech.* **18**, 205302 (2007).
 - 12 van den Hout, M., *et al.*, Controlling nanopore size, shape and stability. *Nanotech.* **21**, 115304 (2010).
 - 13 Kim, M.J., Wanunu, M., Bell, D. C., and Meller, A., Rapid Fabrication of Uniformly Sized Nanopores and Nanopore Arrays for Parallel DNA Analysis. *Adv. Mater.* **18**, 3149–3153 (2006).
-

- 14 Wu, M-Y., *et al.*, Control of Shape and Material Composition of Solid-State Nanopores. *Nano Lett.* **9**, 479–484 (2009).
- 15 Haynes, W. M. (Editor), CRC Handbook of Chemistry and Physics, 91st Edition. CRC Press (2010).
- 16 Purcell, E. M., Electricity and Magnetism (Berkeley Physics Course, Vol. 2), Chapter 4, Problem 4.10. McGraw-Hill (1984).
- 17 Skinner, G. M., *et al.*, Distinguishing Single- and Double-Stranded Nucleic Acid Molecules Using Solid-State Nanopores. *Nano Lett.* **9**, 2953–2960 (2009).
- 18 Kowalczyk, S. W., *et al.*, Unraveling Single-Stranded DNA in a Solid-State Nanopore. *Nano Lett.* **10**, 1414–1420 (2010).
- 19 Wanunu, M., Sutin, J., McNally, B., Chow, A., and Meller, A., DNA Translocation Governed by Interactions with Solid-State Nanopores. *Biophys. J.* **95**, 4716–4725 (2008).
- 20 Kowalczyk, S. W., Hall, A. R., and Dekker, C., Detection of Local Protein Structures along DNA Using Solid-State Nanopores. *Nano Lett.* **10**, 324–328 (2010).
- 21 Storm, A. J., *et al.*, Fast DNA Translocation through a Solid-State Nanopore. *Nano Lett.* **5**, 1193–1197 (2005).
- 22 Aguilera-Arzo, M., Aguilera, V. M., Eisenberg, R. S., Computing numerically the access resistance of a pore. *European Biophysical Journal* **34**, 314–322 (2005).

2.7 Supplementary Information

TEM image and I-V curves

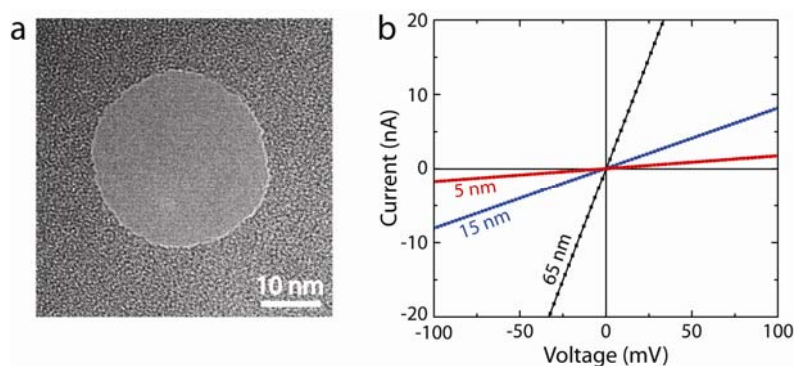


Figure S2.1 (a) Transmission electron microscope (TEM) image of a nanopore of 30 nm in diameter. (b) Current-Voltage (I-V) curves for nanopores of 5 nm (red), 15 nm (blue), and 65 nm (black) in diameter, where the solid lines are linear fits to the data.

Exactly solvable model for an hourglass-shaped pore

Consider the hourglass shaped pore in the form of a single sheet hyperboloid of revolution, given by the equation

$$x^2 + y^2 = z^2 \tan^2 \alpha + \frac{d^2}{4} \quad (\text{S1}).$$

The narrowest part of the pore is at $z = 0$. This disc with diameter d is our pore. The wide parts of hyperboloid are asymptotically approaching a cone with opening angle α . The surface of the pore is depicted in Figure S2.2: inside this surface we have conducting liquid, outside – insulator. Depending on the specific value of the angle α , we can obtain a variety of pore shapes, as shown in Figure S2.3.

The equations governing the problem are simple. Assuming the conductivity $\sigma = 1/\rho$ is constant everywhere in the conducting part, charge conservation and Ohm's law $\mathbf{j} = \sigma \nabla V$ lead to the Laplace equation $\nabla^2 V = 0$ with the boundary condition that normal component of the current vanishes on the dielectric side surface, while the tangential component vanishes on the electrode surface. For the suggested shape of the pore, we address the problem in oblate spheroidal coordinates (see section 6). The surface of the pore in this case is simply

$$\eta = \eta_0 + \cos \alpha \quad (\text{S2}).$$

The pore diameter is

$$d = 2a\sqrt{1 - \eta_0^2} = 2a \sin \alpha \quad (\text{S3});$$

in other words, the coordinate parameter a is readily expressed in terms of pore diameter and opening angle: $a = d/2 \sin \alpha$. Note that the internal cavity of hyperboloid corresponds to η in the interval $\eta_0 < \eta < 1$ (upper part) and $-1 < \eta < -\eta_0$ (lower part).

We imagine that the electrodes are the parts of spheroid surface which close the hyperboloid, as shown in Figure S2.4. These surfaces correspond to the ellipsoid of revolution (also called spheroid) $\xi = \xi_0$, or in cartesian coordinates:

$$\frac{x^2 + y^2}{a^2(1 + \xi_0^2)} + \frac{z^2}{a^2 \xi_0^2} = 1 \quad (\text{S4}).$$

Thus, half-axes of this ellipsoid are $a\xi_0$ and $a\sqrt{1 + \xi_0^2}$, which reveals the meaning of parameter ξ_0 . Specifically, if the overall vertical distance between top and bottom electrodes is $L = 2a\xi_0$, therefore,

$$\xi_0 = \frac{L}{a} \sin \alpha \quad (\text{S5}).$$

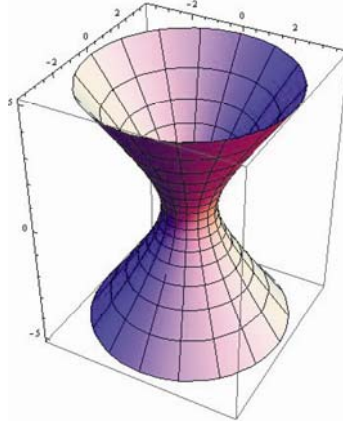


Figure S2.2 Surface of an exactly solvable hourglass shaped pore.

The convenient property of a hyperboloid shape is that the potential V in this case depends on ξ only. The ellipsoids $\xi = \text{const}$ are equipotential surfaces. They are normal to the side hyperboloid and, therefore, the boundary condition on the side surface is automatically satisfied. Thus, the solution reads $V(\xi)$, and it must satisfy

$$\frac{1}{a^2(\xi^2 + \eta^2)} \left\{ \frac{\partial}{\partial \xi} \left[(1 + \xi^2) \frac{\partial V}{\partial \xi} \right] \right\} = 0 \quad (\text{S6}).$$

(see equation (S35)), or

$$\frac{\partial V}{\partial \xi} = \frac{A}{1 + \xi^2} \Rightarrow V(\xi) = A \arctan \xi + B \quad (\text{S7}).$$

This must be true for $0 \leq \xi \leq \xi_0$. Since $\zeta = 0$ corresponds to the horizontal plane in the middle of the pore, we can assume $V(0) = 0$ there, meaning $B = 0$. If the overall applied voltage is U , we must have $V(\xi_0) = U/2$, which means $U/2 = A \arctan \xi_0$. Thus, the potential finally reads

$$V(\xi) = \frac{U}{2} \frac{\arctan \xi}{\arctan \xi_0} \quad (\text{S8}).$$

This is valid in the upper cavity of the hyperboloid, at positive η . The nature of spheroid coordinates is, in principle, such that the lower cavity is described by positive ζ as well as the upper part – because they correspond to the same ellipsoidal surfaces $\xi = \text{const}$; they are actually distinguished by the sign of η (the lower part corresponds to negative η). Thus, in the lower part, where η is negative, we have a similar looking expression for $V(\zeta)$, except with the opposite sign.

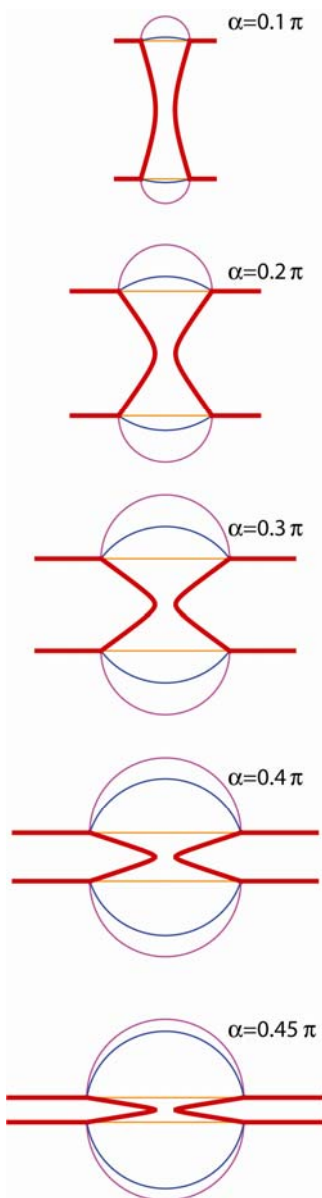


Figure S2.3 Variation of pore shape and the auxiliary geometric constructions of Figure S2.5 with a changing angle α , while d remains constant. Note how the blue cupola shifts from being nearly on top of the flat orange disc to being very close to the purple hemisphere.

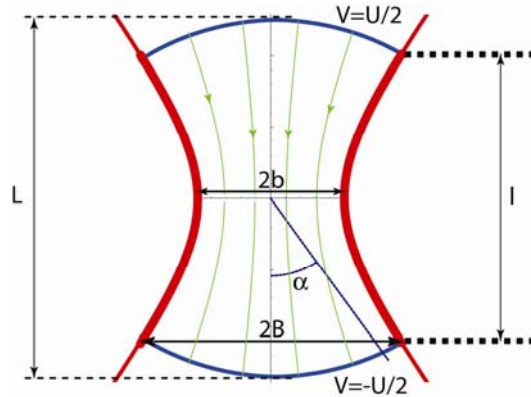


Figure S2.4 Cross section of an exactly solvable hourglass shaped pore. Thick red lines show the dielectric walls. Thick blue lines are electrodes; one of them is supported at the potential $V = U/2$, another at $V = -U/2$. Several thin green lines are current lines. Thin blue line is an ellipse, this line shows how electrodes are actually two parts of the surface of a spheroid (note: a spheroid is an ellipsoid of revolution). Angle α as well as lengths L , l , d , and D are shown. In this picture, $d = 2$, $L = 5$, $\alpha = \pi/5$.

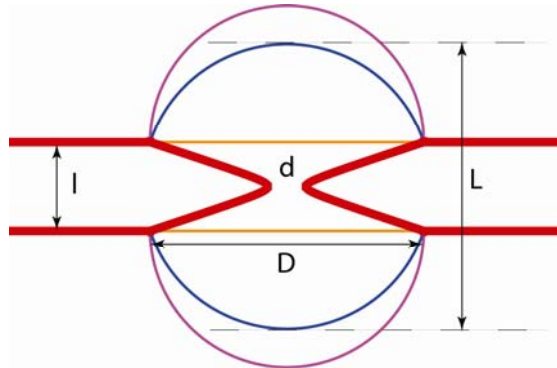


Figure S2.5 Cross section of an hourglass shaped pore in a membrane. Thick red lines show the walls of a dielectric: flat membrane of thickness l with a pore of outside diameter D and inside diameter d . Thin lines in blue, purple, and orange represent auxiliary constructions: purple represents a hemisphere of radius $D/2$; orange represents a flat disc of diameter D ; blue represents a segment of spheroid conjugate to the hyperboloid pore sides. In this picture $\alpha = 0.4\pi$.

The only thing that remains is to compute the current. The current density is $\mathbf{j} = \sigma \nabla V$ and the current itself is the surface integral of this density:

$$\mathbf{J} = \int \mathbf{j} \cdot \mathbf{ds} \quad (\text{S9}),$$

where the integration runs along any surface crossing the pore, and the vector \mathbf{ds} is normal to the surface. The simplest choice of this surface is any $\xi = \text{const}$ surface. The normal to this surface is $\hat{\xi}$ – one of the vectors of the coordinate system, and the normal component of the gradient is simply $\frac{1}{h_\xi} \frac{\partial V}{\partial \xi}$, where h_ξ is the corresponding metric (Lame) coefficient (see below, section 6). Of course, $\partial V / \partial \xi$ does not depend on η and φ , but h_ξ , arising from the nature of curvilinear coordinates, does depend on η . This indicates that the current density does depend on η . It does not depend on φ , because the current density does possess an obvious symmetry, but the current density does depend on the proximity to the axis (or proximity to the wall), which is η . The surface element in the integration can be written as $ds = h_\eta d\eta h_\varphi d\varphi$. Therefore, the current finally reads

$$\begin{aligned} J &= \sigma \frac{\partial V}{\partial \xi} \int_{\eta_0}^1 d\eta \int_0^{2\pi} d\varphi \left(\frac{h_\eta h_\varphi}{h_\xi} \right) \\ &= \sigma \left(\frac{A}{1+\xi^2} \right) \int_{\eta_0}^1 d\eta \int_0^{2\pi} d\varphi a(1+\xi^2) \\ &= \frac{\pi U d (1 - \cos \alpha)}{2\rho \sin \alpha \arctan \xi_0} \end{aligned} \quad (\text{S10}).$$

As it must be, the result does not depend on ξ . Finally, this gives for the resistance of hyperboloid pore

$$R_{\text{hyp}} = \frac{2\rho}{\pi d} \frac{\sin \alpha}{1 - \cos \alpha} \arctan \left(\frac{L}{d} \sin \alpha \right) \quad (\text{S11}).$$

It is instructive to check various limits.

When the opening angle is very small, $\alpha \rightarrow 0$, we must return to the familiar result for a cylinder; indeed, this is what happens, we get $R_{\text{hyp}} \simeq 4\rho L / \pi d^2$. The first correction term reads

$$R_{\text{hyp}}|_{\alpha \ll 1} \simeq \frac{4\rho L}{\pi d^2} \left[1 - \alpha^2 \left(\frac{1}{4} + \frac{L^2}{3d^2} \right) \right] \quad (\text{S12}).$$

The correction is always negative, the resistance gets smaller if at least part of the pore becomes wider; this makes sense. However, $\alpha \ll 1$ is not a sufficient condition for this approximation, the stricter condition $\alpha L / d \ll 1$ is necessary.

In the limit $L \gg d$ and not very small α , i.e., when $L \gg d \sin \alpha$, we get

$$R_{\text{hyp}}|_{L \gg d \sin \alpha} \simeq \frac{\rho}{d} \frac{\sin \alpha}{1 - \cos \alpha} \quad (\text{S13}).$$

In particular, when $\alpha \rightarrow \pi/2$, still assuming $L \gg d$, we are back to another familiar result, that of Hall [S1] for the access resistance for a hole in an infinitely thin membrane, $R_{\text{hyp}} \simeq \rho/d$. The first correction term reads

$$R_{\text{hyp}}|_{L \gg d \text{ and } \alpha \rightarrow \pi/2} \simeq \frac{\rho}{d} \left[1 + \left(\frac{\pi}{2} - \alpha \right) \right] \quad (\text{S14}).$$

This also makes sense, the resistance gets larger as the opening angle becomes smaller.

In the limit when $\alpha \ll 1$, but $L\alpha/d \gg 1$ we have $\arctan \frac{L\alpha}{d} \simeq \frac{\pi}{2}$ and then $R_{\text{hyp}} \simeq \frac{2\rho}{d\alpha}$. This is conveniently re-written in terms of diameter D of the widest part of the pore and the distance l between the two widest places (see Figure S2.4); since in the limit at hand $D \gg d$, we have $\alpha \simeq D/l$, and then we arrive at

$$R_{\text{hyp}} \simeq \frac{2\rho L}{Dd} \quad (\text{S15}).$$

This formula can be independently derived by considering two cones connected tip-to-tip.

Approximation and interpolation including access resistance

Consider now a membrane of thickness l with an hourglass shaped pore of internal diameter d and entrance diameter D . The cross-section is shown in Figure S2.5. This is probably as close as we can get to the reality. The pore itself can be reasonably approximated as a hyperboloid pore with properly chosen parameters. We assume that the membrane thickness l along with the inner and outer diameters of the pore, d and D , are all known (i.e, they can be measured independently). Then determination of parameters L and α is a matter of straightforward geometry, they are given by the explicit formulae

$$\sin^2 \alpha = \frac{D^2 - d^2}{l^2 + D^2 - d^2} \quad (\text{S16a}).$$

$$L^2 = l^2 + D^2 - d^2 \quad (\text{S16b}).$$

as derived below in section 5; we can think of L and α as known quantities.

The resistance of such pore cannot be computed in an exact explicit analytical form. But we can consider Figure S2.5 and make the following educated guess. We know the following resistances: the resistance from infinity to the purple hemisphere is $\rho/\pi D$; the resistance from infinity to the orange disc is $\rho/2D$ [1]; the resistance from the upper blue cupola to the lower is computed above and is given by formula (11), in which the parameters L and α are determined via equations (S16a, S16b).

Importantly, the blue cupola in Figure S2.5 is always positioned between the purple hemisphere and the orange disc. This can be seen both geometrically (because the blue curve is normal to the hyperboloid pore side, while the orange disc is horizontal and the purple hemisphere has a vertical tangent at the point where it touches the membrane, i.e., at the point where they all meet), and from the equations. Re-naming the resistance (11) R_{hyp} , we can make the following statement about the total resistance R from one infinity to the other:

$$R_{\text{hyp}} + \frac{2\rho}{\pi D} < R < R_{\text{hyp}} + \frac{\rho}{D} \quad (\text{S17}).$$

Here, the resistance at the left side of the formula is smaller than R because it does not take into account the part between the purple hemisphere and the blue spheroid; the resistance on the right hand side of the equation is too large, because it double counts the interval between the blue spheroid and the orange disc. In reality, depending on the parameters, the blue curve may be very close to the orange one (if α is small, or D is close to d), or it may be very close to the purple one (if $D \gg d$). These possibilities are clearly seen in the Figure S2.3. Trying to go beyond establishing upper and lower bounds of the resistance (S17), one option would be to make a linear interpolation of access resistance between $2\rho/\pi D$ and ρ/D , like:

$$R \approx R_{\text{hyp}} + \frac{\rho}{D} \left[1 - \frac{L-l}{D} \left(1 - \frac{2}{\pi} \right) \right] \quad (\text{S18}).$$

Of course, we can equally well use a linear interpolation for the conductivity, in which case we would get

$$R \approx R_{\text{hyp}} + \frac{\rho}{D} \left[1 + \frac{L-l}{D} \left(\frac{2}{\pi} - 1 \right) \right] \quad (\text{S19}).$$

And sure enough we can invent many expressions like this. Further work will be necessary to find the physically justified and convenient interpolation.

Exactly solvable model for ΔG with DNA in the pore

Consider now a pore in which part of the aperture is occluded with DNA, as shown in Figure S2.6. We do not consider here any electrolytic properties of DNA, assuming the Debye screening length is very small. All DNA does in this model is to occupy some space in the middle of the pore.

Such a problem can be solved exactly for a pore in which in the middle of the conducting hyperboloid with opening angle α there is an insulating hyperboloid with opening angle $\beta < \alpha$, as illustrated in Figures S2.6 and S2.7. The resistance of such object reads

$$R_{\text{hyp}} = \frac{\rho}{\pi b} \frac{\sin \alpha}{\cos \beta - \cos \alpha} \arctan \left(\frac{L}{2b} \sin \alpha \right) \quad (\text{S20}),$$

because the only difference in the above derivation is that integration over η in formula (S10) now runs from η_0 to $\eta_1 = \cos \beta$ instead of running to 1. This is an exact answer!

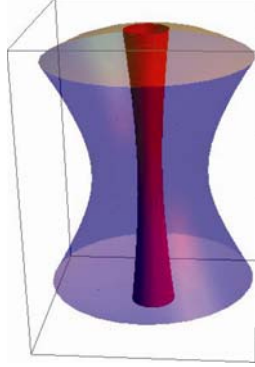


Figure S2.6 Hyperboloid pore with “hyperboloid DNA” in the middle. The hyperboloid in the middle, concentric with the main hyperboloid, does not conduct; all it does in this model is to occlude part of the pore. In this Figure, $L = 2.5d$, $\alpha = 0.2\pi$, and $\beta = 0.2\alpha$.

Can this answer be applied to the real DNA case? There are several issues related to this. First, DNA is not a hyperboloid, but – if anything simple – a cylinder. Unfortunately, as the analysis shows, we cannot choose parameters such that the internal hyperboloid is a cylinder and get analytical results. Indeed, the geometric parameters of such an insulating core are all determined by β . Namely, the thinnest diameter of this new hyperboloid, d_{DNA} , its widest diameter, D_{DNA} , and its height from top to bottom, λ , are determined by the following three equations:

$$d_{\text{DNA}} = d \frac{\sin \beta}{\sin \alpha} \quad (\text{S21a}),$$

$$D_{\text{DNA}}^2 = \lambda^2 \tan^2 \beta + d_{\text{DNA}}^2 \quad (\text{S21b}),$$

$$\frac{D_{\text{DNA}}^2}{(d/\sin \alpha)^2 + L^2} + \frac{\lambda^2}{L^2} = 1 \quad (\text{S21c}).$$

Several lines of straightforward (but cumbersome) algebra produce the following solution to the above equations:

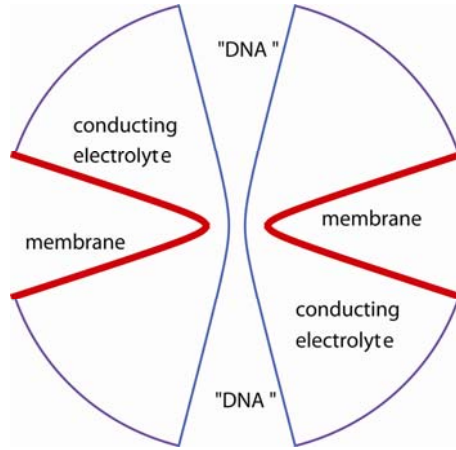


Figure S2.7 Cross-section of the hyperboloid pore with “hyperboloid DNA” in the middle. The hyperboloid in the middle, concentric with the main hyperboloid, does not conduct; all it does in this model is to occlude part of the cross-section.

$$d_{\text{DNA}} = d \frac{\sin \beta}{\sin \alpha} < d \quad (\text{S22a})$$

$$D_{\text{DNA}}^2 = d_{\text{DNA}}^2 \left[1 + \left(\frac{L}{a} \sin \alpha \right)^2 \right] \quad (\text{S22b}).$$

Thus, at least for a pore with $\frac{L}{a} \sin \alpha \ll 1$, which necessarily means $\alpha \ll 1$, we can approach the limit of a hyperboloid pore with an excluded cylinder. In this limit, formula (S20) is simplified to

$$R_{\text{hyp}} \simeq \frac{4\rho L}{\pi d^2} \frac{\alpha^2}{\alpha^2 - \beta^2} = \frac{4\rho L}{\pi[d^2 - d_{\text{DNA}}^2]} \quad (\text{S23}),$$

which is exactly the expected answer for two coaxial cylinders, where the inner cylinder occludes part of the crosssection. This regime is, of course, not particularly interesting, because it can be analyzed by simpler methods, while in the other limit we get $D_{\text{DNA}}/d_{\text{DNA}} \gg 1$, which means the internal hyperboloid widens significantly and cannot be considered a cylinder.

Thus, strictly speaking, we cannot consider the cylindrical DNA in this model. Nevertheless, Figure S2.6 shows that it does not look that bad. Another problem is that DNA is charged and its counterions, including the Onsager-Manning condensed ones, are going to contribute to both conductivity and electroosmosis (such effects are expected to be small at high concentrations – of order 1M – normally used in DNA translocation experiments). And, of course, even the straight DNA does not

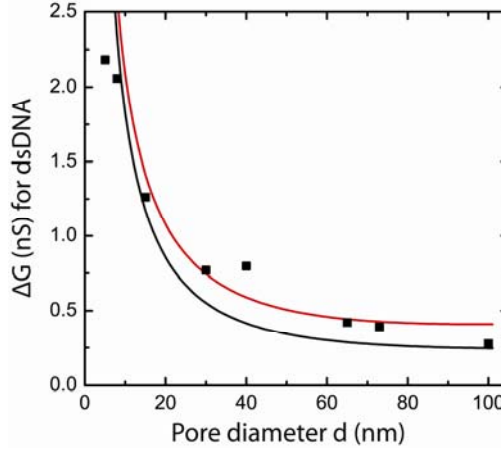


Figure S2.8 Experimental data for the change in pore conductance ΔG upon insertion of a dsDNA molecule, as a function of pore diameter. Solid lines are for an exact solution for a parameter-free model of a hyperboloid-shaped DNA in a hyperboloid-shaped nanopore (black, limit 1; red, limit 2).

have to pass through the pore center and be coaxial with the pore. Despite all that, formula (S20) seems to deserve some attention, because at least it is exact for the well formulated model.

Finally, we plot the experimental data for the change in pore conductance ΔG upon insertion of a dsDNA molecule, as a function of pore diameter and compare with the parameter-free model of a hyperboloid-shaped DNA in a hyperboloid-shaped nanopore in two limits (Figure S2.8). The model fits the data reasonably well, with $\chi_{\text{red}}^2 = 21.7$ for limit 1 and $\chi_{\text{red}}^2 = 9.8$ for limit 2.

Geometrical relations

In our expressions for resistance, we have five geometrical variables: D , d , l , L , α . They are explained in Figures S2.4 and S2.5. In fact, α and L can be determined from the equations (which arise essentially from (S1) and (S4)) through the conditions that the rim connecting spheroidal cap with the hyperboloid has diameter D and sits at height $z = \pm l/2$:

$$\tan \alpha = \frac{\sqrt{D^2 - d^2}}{l} \quad (\text{S24a}),$$

$$\frac{D^2}{(d/\sin \alpha)^2 + L^2} + \frac{l^2}{L^2} = 1 \quad (\text{S24b}).$$

Since $1/\sin^2 \alpha = 1 + 1/\tan^2 \alpha$, we find from Eq. (S24a)

$$\sin^2 \alpha = \frac{D^2 - d^2}{l^2 + D^2 - d^2} \quad (\text{S25}),$$

which we can use to eliminate $\sin \alpha$ from Eq. (S24b), transforming it to become:

$$\frac{D^2(D^2 - d^2)}{d^2(l^2 + D^2 - d^2) + L^2(D^2 - d^2)} + \frac{l^2}{L^2} = 1 \quad (\text{S26}).$$

This is quadratic equation with respect to L^2 :

$$\begin{aligned} L^4(D^2 - d^2) + L^2[d^2(l^2 + D^2 - d^2) - (D^2 + l^2)(D^2 - d^2)] \\ = l^2 d^2 (l^2 + D^2 - d^2) \end{aligned} \quad (\text{S27}).$$

To simplify writing, we introduce a temporary notation $u^2 = l^2 + D^2 - d^2$; then we exclude D in favor of u :

$$L^4(u^2 - l^2) + L^2[u^2 d^2 - (u^2 + d^2)(u^2 - l^2)] - l^2 d^2 u^2 = 0 \quad (\text{S28}).$$

This now invites re-grouping of terms:

$$L^2 u^2 - L^2 u^4 - L^4 l^2 + L^2 u^2 l^2 + L^2 l^2 d^2 - u^2 l^2 d^2 = 0 \quad (\text{S29}).$$

yielding

$$(L^2 - u^2)[L^2(u^2 - l^2) + l^2 d^2] = 0 \quad (\text{S30}).$$

The solution $L^2 = -\frac{l^2 d^2}{u^2 - l^2} = -\frac{l^2 d^2}{D^2 - d^2} < 0$ is negative and meaningless, so the relevant solution is $L^2 = u^2$ or

$$L^2 = u^2 + D^2 - d^2 \quad (\text{S31}).$$

Equation (S22b) is derived in a similar way; note that it returns (S31) when $d_{\text{DNA}} = d$ or $\beta = \alpha$.

Oblate spheroidal coordinates

We use oblate spheroidal coordinates $\{\xi, \eta, \varphi\}$. There are several ways to define these coordinates. We use a combination of versions from [S2–S4]. Here is, for the record, the exact formulation of what specifically we used. The surfaces of constant ξ are oblate spheroids, the surfaces of constant η are the single-sheet hyperboloids of revolution, and surfaces of constant φ are semi-planes. The coordinate ξ varies in the interval $0 \leq \xi < \infty$, while η varies in the interval $-1 \leq \eta \leq 1$, and angle φ as usual $0 \leq \varphi < 2\pi$.

The relationship to Cartesian coordinates is not very important for us here, but here it is for completeness:

$$x = a\sqrt{(1 + \xi^2)(1 - \eta^2)} \cos \varphi \quad (\text{S32a}).$$

$$y = a\sqrt{(1 + \xi^2)(1 - \eta^2)} \sin \varphi \quad (\text{S32a}).$$

$$z = a\xi\eta \quad (\text{S32c}).$$

The so-called metric (or Lamé) coefficients (also called scale factors), $\{h_\xi, h_\eta, h_\varphi\}$, play a key role. The meaning of Lamé coefficients is revealed by the fact that the length element is expressed in curvilinear coordinates as follows:

$$dl^2 = (h_\xi d\xi)^2 + (h_\eta d\eta)^2 + (h_\varphi d\varphi)^2 \quad (\text{S33}).$$

The Lamé coefficients for the oblate spheroidal coordinates read:

$$h_\xi = a \sqrt{\frac{\xi^2 + \eta^2}{1 + \xi^2}} \quad (\text{S34a}).$$

$$h_\eta = a \sqrt{\frac{\xi^2 + \eta^2}{1 - \eta^2}} \quad (\text{S34b}).$$

$$h_\varphi = a\sqrt{(1 + \xi^2)(1 - \eta^2)} \quad (\text{S34c}).$$

The Laplacian then equals

$$\begin{aligned} \nabla^2 V &= \frac{1}{h_1 h_2 h_3} \sum_{i=1}^3 \frac{\partial}{\partial u_i} \left(\frac{h_{i+1} h_{i+2}}{h_i} \frac{\partial V}{\partial u_i} \right) \\ &= \frac{1}{a^2(\xi^2 + \eta^2)} \left\{ \frac{\partial}{\partial \xi} \left[(1 + \xi^2) \frac{\partial V}{\partial \xi} \right] \right\} + \frac{1}{a^2(\xi^2 + \eta^2)} \left\{ \frac{\partial}{\partial \eta} \left[(1 - \eta^2) \frac{\partial V}{\partial \eta} \right] \right\} \\ &\quad + \frac{1}{a^2(1 + \xi^2)(1 - \eta^2)} \frac{\partial^2 V}{\partial \varphi^2} \end{aligned} \quad (\text{S35}).$$

And the gradient reads

$$\nabla V = \frac{1}{h_\xi} \frac{\partial V}{\partial \xi} \hat{\xi} + \frac{1}{h_\eta} \frac{\partial V}{\partial \eta} \hat{\eta} + \frac{1}{h_\varphi} \frac{\partial V}{\partial \varphi} \hat{\varphi} \quad (\text{S36}).$$

SI References

- S1. J. E. Hall, *Journal of General Physiology* **66**, 531 (1975).
- S2. L. D. Landau, E. M. Lifshitz, and L. P. Pitaevskii, *Electrodynamics of Continuous Media (Course of Theoretical Physics, Volume 8)* (Butterworth Heinemann; 2 edition, 1984).
- S3. P. M. Morse and H. Feshbach, *Methods of Theoretical Physics* (McGraw Hill Book Company, 1953).
- S4. I.S.Gradshstein and I.M.Ryzhik, *Table of Integrals, Series, and Products* (edited by A.Jeffrey) (Academic Press, 1994).

Chapter 3

Translocation of RecA-coated double-stranded DNA through solid-state nanopores

We report translocation of dsDNA molecules that are coated with RecA protein through solid-state nanopores. Translocation measurements show current-blockade events with a wide variety in time duration (10^{-4} – 10^{-1} s) and conductance blockade values (3 – 14 nS). Large blockades (11.4 ± 0.7 nS) are identified as being caused by translocations of RecA-dsDNA filaments. We confirm these results through a variety of methods, including changing molecular length and using an optical tweezer system to deliver bead-functionalized molecules to the nanopore. We further distinguish two different regimes of translocation: a low-voltage regime (< 150 mV) in which the event rate increases exponentially with voltage, and a high-voltage regime in which it remains constant. Our results open possibilities for a variety of future experiments with (partly) protein-coated DNA molecules, which is interesting for both fundamental science and genomic screening applications.

This chapter has been published as R.M.M. Smeets*, S.W. Kowalczyk*, A.R. Hall, N.H. Dekker, and C. Dekker, *Nano Letters* **9**(9), 3089–3095 (2009). *equal contribution.

3.1 Introduction

Nanopores can be used as single-molecule sensors to detect the passage of DNA, RNA, or proteins. Such charged biomolecules are driven through a nanometer-sized constriction by an applied electric field. Translocation through the nanopore results in a transient current blockade, a consequence of the volume displaced by the passing molecule (see Figure 3.1). Both biological pores, in particular α -hemolysin, and fabricated nanopores have been used to obtain dynamic and structural information on polynucleotides [1]. Proteins were studied by translocation through nanopores [2, 3], or by sensing DNA-protein rupture where the nanopore acts as a local force actuator to pull the two molecules apart [4–7]. Here, we use the recombination protein A (RecA), which is known to form stable nucleoprotein filaments on dsDNA in the presence of magnesium and ATP γ S [8] to investigate translocation of protein coated DNA. RecA protein plays a central role in homologous recombination and DNA repair in prokaryotes where it catalyzes the pairing of single strand DNA with complementary regions of double strand DNA. Using nanopores, the identification of RecA-coated regions along DNA strands may provide for a scheme of *in situ* homologous sequence detection of target DNA, analogous to previous atomic force microscopy studies [9]. More generally, the sequential detection of proteins along DNA may have applications in, for example, screening for transcription factors along a genome.

In this study, we present translocation measurements of RecA-coated double-strand (ds)DNA molecules. We first demonstrate the formation of complete RecA-dsDNA structures by atomic force microscopy (AFM), and subsequently show that translocation measurements result in pronounced current depressions compared to bare dsDNA molecules. We analyze the recorded events by their time duration and conductance blockade. The events can be well classified into two groups, based on the value of their conductance blockade. By carrying out translocation measurements on RecA protein alone and on RecA-coated dsDNA of different lengths, we show that the events with high conductance-blockade values correspond to the translocation of the nucleoprotein filaments, whereas events with low conductance-blockade values correspond to the translocation of free RecA proteins. We compare the high conductance-blockade events to measurements on bare dsDNA and deduce a nucleoprotein filament diameter of 7.5 ± 0.5 nm, in agreement with available structural data.

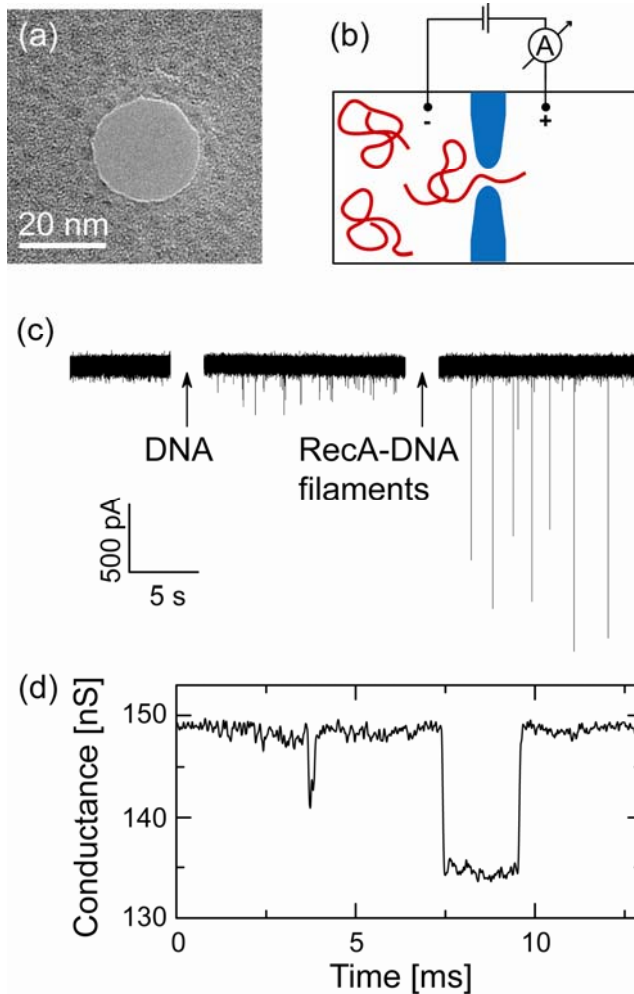


Figure 3.1 (a) Transmission electron microscopy image of a 23.3 nm diameter nanopore. (b) Schematic of the experiment, showing a nanopore in between two liquid compartments. We apply an electric field across the nanopore and measure the resulting current. Molecules are added to a single liquid compartment and translocate through the nanopore towards the positive biased electrode (c) Current recording of a 31.3 nm diameter nanopore at 120 mV before and after the addition of bare λ -DNA or 5 kbp dsDNA/RecA filaments to the negatively biased electrode. Time and current scales as well as the molecules addition are indicated. Clear current spikes from the baseline appear upon addition of the molecules, with much larger current blockades for the RecA-dsDNA filaments as compared to the bare dsDNA. (d) Example of two typical translocation events after addition of RecA-coated DNA.

Additionally, we use the nanopore system in conjunction with an integrated optical tweezer, which allows us to insert the RecA-DNA complex into the nanopore. Finally, we present measurements on the event rate of RecA-dsDNA filament translocations as a function of voltage and identify two different regimes that cross over at a voltage of 150 mV.

Our data provide the first reported measurements on translocation of protein-coated DNA structures. They not only provide a framework to identify sequences on a target DNA strand, but also form a starting point to address local DNA-protein structures using solid-state nanopores.

3.2 Solid-state nanopores

Solid-state nanopore fabrication starts with the use of standard microfabrication technology to create free-standing membranes. The manufactured 20 nm thin low-stress silicon nitride (SiN) membranes are mostly covered by a layer of 20 nm sputtered silicon oxide (SiO₂), on both sides. In each membrane we fabricate a single nanometer-sized pore through the use of a highly focused electron beam in a transmission electron microscope (TEM). Subsequently, the diameter of the fabricated nanopore can be enlarged with the highly focused beam or made smaller by exposure to a de-focused electron beam with lower intensity. Details of the fabrication process are described elsewhere (10). Figure 3.1a shows a TEM image of a fabricated solid-state nanopore of 23.3 nm diameter. In this study, we use nanopores with diameters from approximately 20 to 35 nm with good low-frequency noise properties [11]. All nanopores are treated in an oxygen plasma for about 30 s on both sides prior to use. Subsequently, the nanopores are mounted in a polyetheretherketone (PEEK) microfluidic flow cell, and sealed to liquid compartments on either side of the sample. Both compartments provide easy access for the placement of electrodes and exchange of solutions. Ag/AgCl electrodes are used to detect ionic currents and apply electrical fields. The currents are detected using a resistive feedback amplifier (Axopatch 200B, Axon Instruments) and low-pass filtered at 10 kHz before digitization at 100 kHz. The experiments are performed in a 1 M KCl salt solution containing 50 mM Tris-HCl at pH= 7.9, 1 mM EDTA and 3.1 volume % glycerol. The glycerol is added to ensure equal conditions in both compartments upon addition of the nucleoprotein filament to a single compartment. A schematic of the experimental lay-out is shown in Figure 3.1b.

3.3 Nucleoprotein filament formation

Figure 3.2a shows a tapping-mode atomic force microscopy (AFM) image (Nanoscope IIIa, Digital Instruments, Santa Barbara, CA, USA) of 20 kbp dsDNA. AFM images are made in air after depositing DNA from an imaging buffer containing 10 mM MgCl_2 and 5 mM Tris-HCl at pH=7.9 on freshly cleaved mica. The DNA molecules have an apparent height of $Z \approx 0.5$ nm, as is evident from the line scan shown in Figure 3.2a. Note that the Z is lower than the expected value from the DNA crystal structure, as is commonly observed in AFM imaging of DNA.

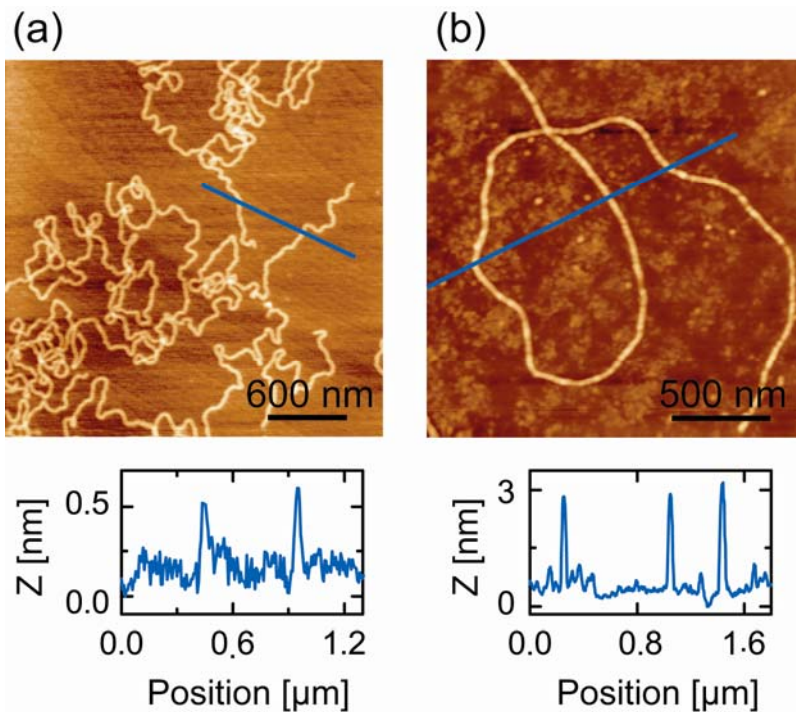


Figure 3.2 Atomic force microscopy (AFM) images of (a) 20 kbp dsDNA and (b) RecA-coated λ -DNA on mica. Note the presence of free RecA proteins visible as small blobs in (b). The bottom of both images contains a recorded height profile along the line indicated in blue.

We coat λ -DNA molecules (or DNA molecules of shorter length) with the RecA protein by subsequently adding λ -DNA (Promega, WI, USA), RecA (New England Biolabs, MA, USA), and ATP γ S (Roche, Switzerland) with final concentrations of

approximately 1.2 nM, 6.5 μ M, and 1.5 mM, respectively. The ATP γ S, a poorly hydrolyzable ATP analog, is required to prevent ATP-hydrolyzation induced disassembly from the DNA. Filaments formed in the presence of the ATP γ S are known to be very stable [12]. The final solution contains 100 mM NaCl, 10 mM MgCl₂, and 5 mM Tris-HCl, pH= 7.9 and is incubated for 1 h at 37 °C. The ratio of RecA protein versus DNA basepairs was varied to obtain fully coated DNA molecules with a low background of free proteins.

Figure 3.2b shows an AFM image of the resulting nucleoprotein filaments. From the line scan along the direction indicated by the blue line in Figure 3.2b, we find an apparent height of $Z \approx 2.5$ nm for the DNA-protein complexes. This is clearly much larger than the value measured for the bare dsDNA molecules, shown in Figure 3.2a. We observe the increased height along the total length of the DNA, indicating full coverage. Comparison of the molecular flexibility in the images of Figure 3.2a and Figure 3.2b also shows that the RecA-dsDNA filaments are much stiffer than dsDNA, as expected. The nucleoprotein filaments are stable for hours even in a 1 M KCl salt solution, as confirmed by subsequent AFM imaging (data not shown). The results obtained compare well with previously performed AFM studies on RecA-dsDNA complexes, which show comparable filaments with a height ranging from 2.5 to 4.4 nm [13–16]. Note that in Figure 3.2b also some free RecA proteins are visible as small blobs.

Much is known about the structure of the RecA protein [17], and recently also the crystal structure of the RecA-dsDNA complex was resolved [18,19]. This study shows that the nucleoprotein filament is a right-handed helix composed of 6.2 RecA units per turn over a pitch of 9.2 – 9.5 nm. The dsDNA is bound within this filament with approximately one RecA monomer bound per three duplex base pairs, resulting in a 1.5 fold increase in the DNA extension. This means that λ -DNA molecule will be extended to about 25 μ m upon full coating with RecA. The values of the persistence length and the diameter of the filaments are much larger than those of naked dsDNA. The persistence length is increased upon RecA coating to a value of approximately 950 nm [20]. From the obtained crystal structure of the RecA-dsDNA complex [18] we estimate a 7.0 ± 0.5 nm filament diameter of the local cross section of the filament. This value equals the diameter of the smallest cylinder enveloping the helical RecA-dsDNA nucleoprotein filament within the 10.0 nm diameter outer envelope of the structure.

3.4 Translocation of RecA-coated dsDNA

Figure 3.1c shows current recordings of a 31.3 nm diameter nanopore at 120 mV before and after the addition of bare dsDNA and RecA-coated dsDNA molecules. The open pore conductance of this pore was 244 nS. When no molecules are present in solution, the ionic current recording displays a stable baseline with no significant deviations to lower or higher current values. Upon addition of λ -DNA molecules to the negatively biased compartment, short temporal current blockades appear. These blockades can be seen to reduce the ionic current through the nanopore to approximately 100 – 300 pA lower values. After flushing out these λ -DNA molecules, we add 5 kbp RecA-coated dsDNA filaments to the same compartment, which also results in temporal current blockades. However, these current decreases differ substantially in magnitude from the blockades measured for the bare dsDNA, reducing the current by as large as 1000 – 1500 pA. The much larger current blockades measured for the RecA-coated dsDNA compared to the bare dsDNA, are expected because of the larger diameter of the nucleoprotein filament. Its translocation from the negatively to the positively biased electrode indicates an overall negative charge, in agreement with the isoelectric point (≈ 5.6) of purified RecA protein [8].

We now analyze the translocation events of RecA-coated dsDNA molecules according to their conductance blockade and time duration. All events with conductance blockades that exceed the nanopore current noise are taken into account. The value of the conductance blockade is determined with respect to the open-nanopore conductance and represents the average blockade over the time duration of the event. The open-pore conductance is simply the average conductance (averaged over 2.5 ms before and after each translocation event) and we define that events begin and end when the conductance deviates one standard deviation from this average.

Figure 3.3a shows the conductance blockade versus time duration of RecA-coated λ -DNA translocation events in a semi-logarithmic scatter plot. The measurements are performed using a 23.3 nm diameter nanopore (shown in Figure 3.1a) and at a bias voltage of 180 mV. The open pore conductance of this pore was 144 nS. The events show a large variation in both the conductance blockade and the event duration, ranging from approximately 2 to 14 nS, and from 10^{-4} to 10^{-1} s. We classify the events in two distinct groups, indicated by the dotted areas in Figure 3.3a. Most events either show a relatively low (≈ 4 nS, black) or large (≈ 12 nS, blue) conductance blockade, as is also evident from the histograms shown in Figure 3.3b.

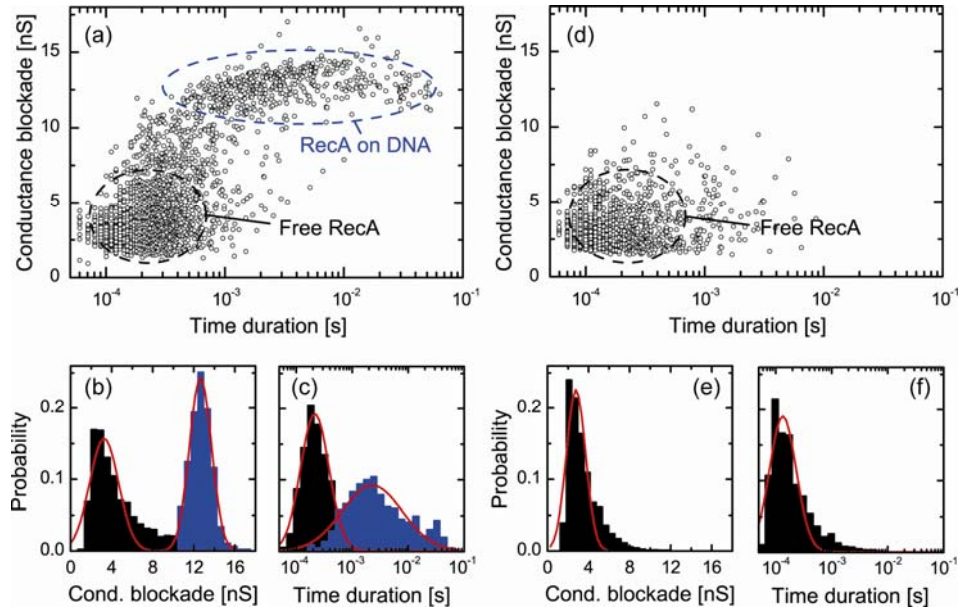


Figure 3.3 (a) Event scatter plot of time duration vs. conduction blockade of RecA-coated dsDNA translocation events and their respective histograms (b, c). The dotted circles indicate two distinct groups of events. We analyze the events as having either a low (< 10.3 nS, black) or high (> 10.3 nS, blue) conduction blockade, and we made separate histograms for each group as shown by the color coding in (b, c). (d) Event scatter plot of time duration vs. conduction blockade of free RecA protein translocation events and their respective histograms (e, f). The dotted circle indicates that there is only one group of events, similar in size and duration to the low conduction blockade events of (a).

The duration of events with relatively small blockade values ranges from 10^{-4} to 10^{-3} s. In contrast, the events with large conduction blockades show a larger spread in event duration with values ranging from 5×10^{-4} to 5×10^{-2} s. Figure 3.1d shows two typical events, one from each group. We characterize the events of the two groups by their most probable conduction blockade and time duration. These values are obtained by fitting a Gaussian and log-normal distribution to the conduction blockade and event duration histograms as shown in Figure 3.3b and 3.3c, respectively. We find $\Delta G = 3.3 \pm 1.4$ nS and $t = 216$ (-100, +150) μ s for the events with low conduction blockades, and $\Delta G = 12.6 \pm 1.1$ nS and $t = 2.3$ (-1.6, +5.6) ms for the events showing large conduction blockades. The error bars denote the standard deviations of the distributions.

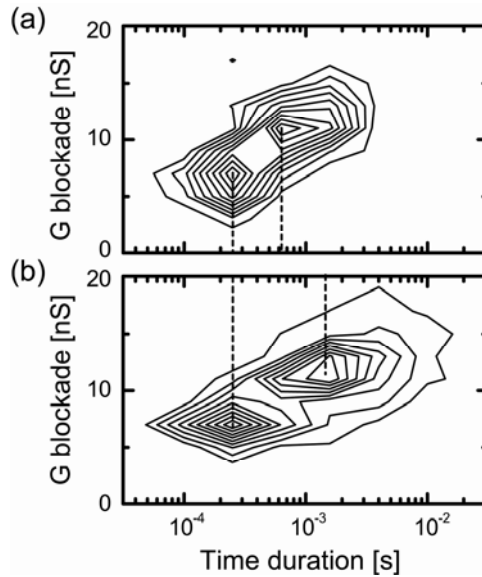


Figure 3.4 Event duration versus conductance blockade of RecA-coated (a) 5 kbp and (b) 48.5 kbp dsDNA, presented as contour plots. The data is recorded at 120 mV, using nanopores of 31.1 and 24.2 nm diameter, respectively. Both contour plots show two distinct groups of blockade events. Only the event time duration of the higher-conductance-blockade events clearly depends on the length of the nucleoprotein filament, which indicates that these events result from RecA-DNA nucleoprotein filament translocation.

We now identify the high- and low-conductance-blockade events with the translocation of RecA-dsDNA filaments and the translocation of free RecA, respectively. Evidence for this is twofold. First, we measure the translocation of free RecA proteins without any DNA present, resulting in the scatter plot shown in Figure 3.3d. The translocation only results in the events with a low conductance blockade and short time duration. From a comparison of the scatter plots shown in Figure 3.3a and d it is clear that these events are similar to the low conductance blockade events measured during the RecA-coated dsDNA translocation experiments. We also characterize the RecA translocation events by their most probable conductance blockade and time duration. These values are obtained by fitting a Gaussian and log-normal distribution to the conductance blockade and event time duration histograms shown in Figure 3.3e and 3.3f, respectively. We find $\Delta G = 2.8 \pm 0.9$ nS and $t = 141(-60, +103)$ μ s, where the error bars again denote the standard deviation of the

distributions. The values found agree with the values reported for the low conductance blockade events of Figure 3.3a, identifying these events with the translocation of free RecA protein.

Secondly, Figure 3.4a and 3.4b shows contour plots of the event duration versus conductance blockade of 5 kbp and 48.5 kbp RecA-coated dsDNA respectively. We can again clearly identify the two distinct groups of events, which can be separated by their conductance blockade value. We can again characterize the events of each group by their most probable conductance blockade and time duration. We obtain values of $t = 224(-68, +97) \mu\text{s}$, $\Delta G = 6.9 \pm 1.4 \text{ nS}$ and $t = 865(-428, +847) \mu\text{s}$, $\Delta G = 11.2 \pm 2.1 \text{ nS}$ for the two groups of the 5 kbp long construct presented in Figure 3.4a. For the 48.5 kbp long construct shown in Figure 3.4b we find $t = 276 (-129, +373) \mu\text{s}$, $\Delta G = 7.4 \pm 1.0 \text{ nS}$, and $t = 1.9 (-1.2, +3.5) \text{ ms}$, $\Delta G = 11.6 \pm 1.9 \text{ nS}$. When comparing the data obtained on different nucleoprotein filament lengths, we notice that the time duration of the high-conductance blockades depends on the lengths of the filaments (shorter filaments translocate faster), whereas the time duration of the low-conductance blockade-events is clearly independent of the length. As the time duration of translocation events is expected to depend on the length of the construct [21], we again conclude that the high-conductance blockade events represent translocation events of RecA-coated dsDNA, whereas the low-conductance blockade events represent translocation events of free RecA protein.

We can analyze the measured RecA-coated λ -DNA translocation events and compare them to the well-studied translocation of bare λ -DNA. Unfolded, head-to-tail translocation events of bare λ -DNA show most probable translocation times and conductance blockades of approximately $1.1 \pm 0.3 \text{ ms}$ (at 120 mV) and $0.8 \pm 0.1 \text{ nS}$, respectively [22]. The average values of the RecA-coated λ -DNA translocation events are larger (see i.e. Figure 3.4b), with translocation times of approximately 1.9 (-1.3, +3.6) ms (at 120 mV) and conductance blockades of $11.4 \pm 0.7 \text{ nS}$ (combined data from three different nanopores at various voltages). Furthermore, the spread in the translocation times is also very different. Whereas for the bare dsDNA the translocation time can be fitted to a Gaussian on a linear scale, the event time duration of the RecA-coated dsDNA is fitted to a log-normal distribution (i.e., a Gaussian on a logarithmic scale) over two decades.

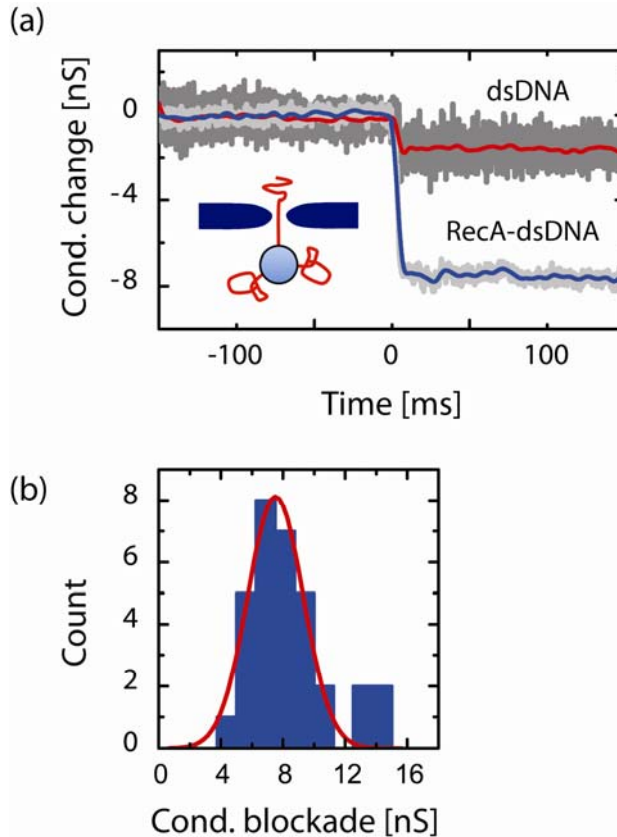


Figure 3.5 (a) A typical optical tweezer capture event for RecA-coated dsDNA (blue) compared to that of bare dsDNA (red). The capture events are set to start at 0 ms. Inset: schematic of the integrated optical tweezer measurement. (b) Conductance blockade histogram for RecA-dsDNA captures with the optical tweezer system.

Longer translocation times for the nucleoprotein filament as compared to the bare dsDNA (1.9 ms versus 1.1 ms) are expected as RecA binding along the total DNA length results in a 1.5 fold extension of the molecule. The measured translocation times reasonably agree with the predicted 1.5 fold increase. However, this agreement might be fortuitous: The nucleoprotein filament has an increased persistence length and likely a different effective charge as compared to the naked DNA. As a result, both the driving and the dominant counteracting forces may be different [21]. Disentanglement of these effects is necessary for a detailed understanding of the differences in translocation times.

Moreover, the value of the translocation time of the RecA-coated dsDNA may also differ due to intrinsic reasons. The large spread in the measured translocation time values of the RecA-coated dsDNA is similar to that found in experiments performed on protein-DNA rupture through an α -hemolysin protein nanopore [4]. In these experiments, the nanopore acts as a local force actuator pulling the protein-DNA complex apart after which only the latter can proceed to translocate through the nanopore. The resulting time duration of these events shows a very broad distribution over almost two decades, similar to duration distributions shown in Figure 3.3a. We confirmed translocation of the full RecA-coated dsDNA through the nanopore in recapture experiments (data not shown), a method published recently [23], which indicates that the structure of the filaments remains unaffected in the translocation process. We speculate that the long translocation times measured for the nucleoprotein filament reflect intra-filament or filament-nanopore interactions during translocation, which oppose the electrophoretic velocity of the coated DNA molecule.

The most probable conductance blockade of the nucleoprotein filament is 14 ± 2 times larger than the blockade measured for the bare dsDNA (11.4 nS versus 0.8 nS). The value of the conductance blockade results from a combination of the volume of the translocating molecule and its effective charge [22]. We can crudely estimate the diameter of the nucleoprotein filament by neglecting the effect of the charge of the molecule (high-salt approximation), which gives $\Delta G_{RecA} / \Delta G_{DNA} = (d_{RecA} / d_{DNA})^2$, with ΔG_{RecA} and ΔG_{DNA} the conductance blockade, and d_{RecA} and $d_{DNA} = 2.0$ nm the diameter of the nucleoprotein filament and the bare dsDNA molecule [24], respectively. The 14 times larger blockade yields a value of 7.5 ± 0.5 nm for the diameter d_{RecA} which represents the average cross-section of the helical nucleoprotein filament. The obtained value compares well to the cross-section of 7.0 ± 0.5 nm determined from the crystal structure of the RecA-dsDNA filament [18] estimated above.

As a final check of the larger conductance blockade by RecA-coated DNA filaments, we use an optical tweezer in conjunction with the solid-state nanopore to statically capture single complexes. The details of the technique have been described previously [25]. Briefly, a polystyrene bead (diameter 2 μ m) with tethered RecA-coated dsDNA molecules is trapped and brought within a few micrometers of a nanopore using the optical tweezer. Once there, a bias is applied which pulls a molecule through the pore (see inset of Figure 3.5). Consequently, when a filament is captured, the measured conductance across the pore drops and does not return to its open-pore value since the optically trapped bead prevents total translocation. For the

present measurements, the nucleoprotein filament is formed on DNA that is conjugated to the beads using a biotin-streptavidin bond at one end.

Figure 3.5a shows an example of typical nucleoprotein capture events. Clearly the RecA-coated DNA filament shows a much larger current blockade (~ 8 nS) than that of a bare dsDNA molecule (~ 1 nS). The distribution of measured conductance blockades (Figure 3.5b) yields a value of 7.5 ± 1.8 nS. This large value qualitatively confirms a much thicker molecule than bare dsDNA. Whether there is a systematic difference between ΔG measured in dynamic translocation and static capturing is an open question that currently is under study. We can also directly measure the event duration with the optical tweezer method [25]. This yields a value of 8.6 (+13.7, -5.3) ms which falls well within the distribution obtained by translocation. Summing up, these capture events of RecA-DNA filaments support our conclusion that high conductance blockades are indicative of molecules which are much thicker than bare dsDNA.

3.5 Rate of transversal of RecA-coated dsDNA

We now report and analyze the number of events in a given time interval, the event rate, for the RecA-coated dsDNA filaments as a function of the applied voltage. Figure 3.6a shows 10 seconds long current-time traces of RecA-coated dsDNA translocation measurements at five different voltages. The number of current blockade events clearly depends on the voltage, varying from 0.5 ± 0.2 events per second at 80 mV to 11.6 ± 0.4 events per second at 160 mV. We can describe the occurrence of blockade events by a Poisson process [26], where the probability of observing *no* RecA-coated dsDNA blockade events, P_0 , during a time interval t is given by

$$P_0(t) = e^{-Rt}$$

where R denotes the event rate. We can now determine P_0 versus t by analyzing the time between successive translocation events δt . We use a constant nucleoprotein filament concentration and only analyze events which reach a conductance blockade > 5 nS. The use of higher cutoff values yields similar results. Plotting the δt values in a histogram immediately gives the probability distribution to observe an event after a specific elapsed time t . From this we simply obtain the probability P_e to observe an event after a time t , by addition. The resulting P_0 versus t now follows from $P_0 = 1 - P_e$. Figure 3.6b shows the obtained probability density distribution P_0 of RecA-coated-dsDNA events versus time for five different voltages. All distributions show a

clear exponential behavior, with values ranging from $R = 2.3 \pm 0.2 \text{ s}^{-1}$ to $R = 13.9 \pm 0.4 \text{ s}^{-1}$ for 120 to 200 mV. The error in the event rate R is calculated using R/\sqrt{N} , where N is the number of observed blockade events. We plot the extracted event rate values as a function of voltage in Figure 3.6c. As the voltage is increased, the event rate initially increases exponentially, but at voltages larger than 150 mV it attains a constant value. We fit an exponential function to the data for voltages $< 150 \text{ mV}$, as shown by the red line in Figure 3.6c, and find an exponent of $0.048 \pm 0.002 \text{ mV}^{-1}$.

The exponential rate dependence can be described with a model where molecules cross a potential barrier U' under influence of the electrical potential $\Delta U = nze\Delta V$. For the expected rate we can write $R \propto \exp((U' - \Delta U)/k_B T)$, with n the number of charged monomers units of effective charge ze within the potential drop ΔV (27). Using these equations we find $nz \approx 1.2$. This value is a lower bound to the real value because the actual potential drop involved in crossing the barrier is smaller than the applied potential V . An exponential dependence in event rate as a function of voltage was previously measured for DNA translocation through the protein pore α -hemolysin [26–28], and recently for protein (BSA) translocation through a synthetic nanopore [29]. The event rate of DNA translocation through fabricated nanopores was measured to be linear over voltages from 200 to 1000 mV [30, 31].

At voltages $> 150 \text{ mV}$, the event rate for our RecA-dsDNA molecules does not further increase but attains a constant value of $13.4 \pm 0.6 \text{ s}^{-1}$, as shown by the red line in Figure 3.6c. A cross-over from an exponential to a roughly linear regime, was previously reported for α -hemolysin [26, 28]. Our results compare well to theoretical predictions where the exponential dependence results from an entropic entry barrier and the plateau is due to diffusion-limited transport [32, 33].

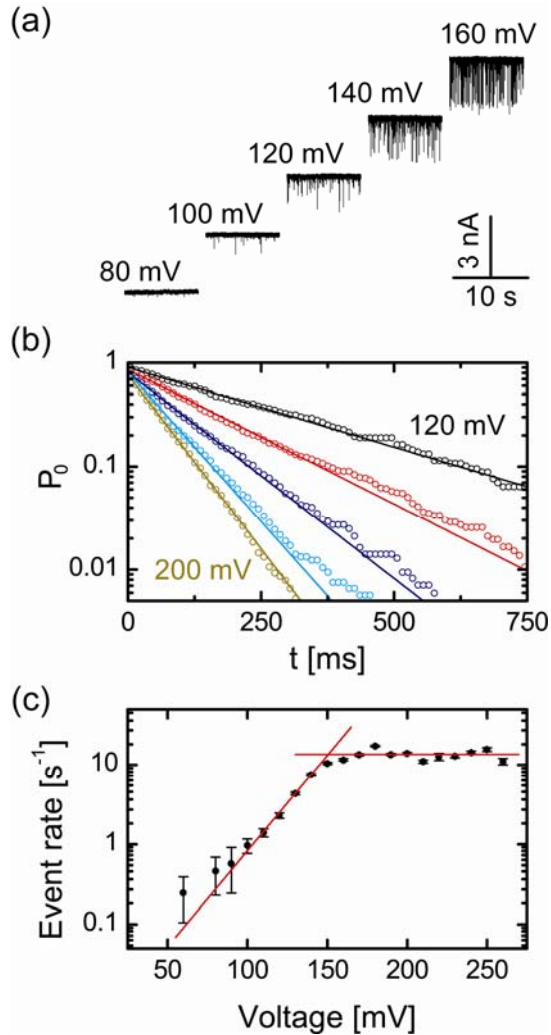


Figure 3.6 (a) Current time traces of RecA-coated dsDNA blockade events at different voltages. The event rate becomes larger as the voltage is increased. (b) Probability distribution to observe no RecA-coated dsDNA blockade events, P_0 , for an elapsed time, t , at 120, 130, 140, 160, and 200 mV. The solid lines are exponential fits to the data at each voltage value, showing good agreement. (c) The event rate of RecA-coated dsDNA conductance blockades as a function of voltage. Each value is extracted from an exponential fit such as the ones shown in (b). The event rate exponentially increases at low voltages < 150 mV, and attains a constant value at high voltages > 150 mV. The two regimes are fitted by an exponential and a constant, respectively, as show by the two red lines.

3.6 Discussion and conclusions

We have reported the translocation of fully RecA-coated dsDNA through solid-state nanopores. The translocation events of the nucleoprotein filaments show a large spread in event time duration as well as in the conductance blockade. We separate the events in two distinct groups, based on their conductance-blockade value. We identify the high-conductance-blockade events as translocation events of RecA-coated dsDNA. The value range of the high-conductance blockade group of events compares quite well to the expected filament diameter as determined from crystallography and electron microscopy [19, 34, 35].

We demonstrate that upon changing the length of RecA-DNA filament, the event duration changes accordingly. Further, we perform captures of single nucleoprotein filaments with an optical tweezer-nanopore system and again find much larger blockades than previously measured for bare dsDNA. The event duration of RecA-coated λ -DNA molecule translocation shows no strong voltage dependence (as is for example evident from a comparison of the data at 120 mV in Figure 3.4b and at 180 mV in Figure 3.3b). This may indicate filament filament interaction within the molecule or an interaction of the protein with the membrane which hinders free translocation. For the latter, chemical coating of nanopores [36] might result in a reduced spread in the event duration and hence yield a better identification of the translocation events.

We find that the event rate of RecA-coated dsDNA molecules can be well described by a Poisson process. We measure the event rate as a function of the applied voltage and identify two different regimes. In the low-voltage regime, the event rate is found to increase exponentially with voltage, whereas in the high-voltage regime it attains a constant value. The reported translocation experiments are the first translocations of DNA-protein structures. The detection of RecA-dsDNA filaments is a first step towards sequentially identifying local structures on a target DNA strand using nanopores.

Acknowledgements. We thank M.Y. Wu for contributions to the experimental work and T. van der Heijden for discussions. This work is part of the research programme of the ‘Stichting voor Fundamenteel Onderzoek der Materie (FOM)’, the ‘Nederlandse Organisatie voor Wetenschappelijk Onderzoek (NWO)’, and the EC project READNA. NHD acknowledges funding from the European Science Foundation through a EURYI Award.

References

- 1 Dekker, C. *Nature Nanotechnol.* **2**, 209–215 (2007).
- 2 Sutherland, T. C.; Long, Y. T.; Stefureac, R. I.; Bediako-Amoa, I.; Kraatz, H. B.; Lee, J. S. *Nano Lett.* **4**, 1273–1277 (2004).
- 3 Fologea, D.; Ledden, B.; McNabb, D. S.; Li, J. L. *Appl. Phys. Lett.* **91**, 053901 (2007)
- 4 Hornblower, B.; Coombs, A.; Whitaker, R. D.; Kolomeisky, A.; Picone, S. J.; Meller, A.; Akeson, M. *Nature Meth.* **4**, 315–317 (2007).
- 5 Zhao, Q.; Sigalov, G.; Dimitrov, V.; Dorvel, B.; Mirsaidov, U.; Sligar, S.; Aksimentiev, A.; Timp, G. *Nano Lett.* **7**, 1680–1685 (2007).
- 6 Benner, S.; Chen, R. J. A.; Wilson, N. A.; Abu-Shumays, R.; Hurt, N.; Lieberman, K. R.; Deamer, D. W.; Dunbar, W. B.; Akeson, M. *Nature Nanotechnol.* **2**, 718–724 (2007).
- 7 Cockroft, S. L.; Chu, J.; Amorin, M.; Ghadiri, M. R. *J. Am. Chem. Soc.* **130**, 818–820 (2008).
- 8 Roca, A. I.; Cox, M. M. *Prog. Nucleic Acid Res. Mol. Biol.* **56**, 129–223 (1997).
- 9 Seong, G. H.; Niimi, T.; Yanagida, Y.; Kobatake, E.; Aizawa, M. *Anal. Chem.* **72**, 1288–1293 (2000).
- 10 Krapf, D.; Wu, M. Y.; Smeets, R. M. M.; Zandbergen, H. W.; Dekker, C.; Lemay, S. G. *Nano Lett.* **6**, 105–109 (2006).
- 11 Smeets, R. M. M.; Keyser, U. F.; Wu, M. Y.; Dekker, N. H.; Dekker, C. *Phys. Rev. Lett.* **97**, 088101 (2006).
- 12 Cox, M. M. in *Topics in Current Genetics*; eds Aguilera A. and Rothstein R., Springer-Verlag, Berlin Heidelberg, pp 53–77 (2007).
- 13 Seitz, E. M.; Brockman, J. P.; Sandler, S. J.; Clark, A. J.; Kowalczykowski, S. C. *Genes Dev.* **12**, 1248–1253 (1998).
- 14 Umemura, K.; Komatsu, J.; Uchihashi, T.; Choi, N.; Ikawa, S.; Nishinaka, T.; Shibata, T.; Nakayama, Y.; Katsura, S.; Mizuno, A.; Tokumoto, H.; Ishikawa, M.; Kuroda, R. *Biochem. Biophys. Res. Commun.* **281**, 390–395 (2001).
- 15 Sattin, B. D.; Goh, M. C. *Biophys. J.* **87**, 3430–3436 (2004).
- 16 Shi, W. X.; Larson, R. G. *Nano Lett.* **5**, 2476–2481 (2005).
- 17 Bell, C. E. *Mol. Microbiol.* **58**, 358–366 (2005).
- 18 Chen, Z. C.; Yang, H. J.; Pavletich, N. P. *Nature* **453**, 489–496 (2008).

-
- 19 Kowalczykowski, S. C. *Nature* **453**, 463–466 (2008).
 - 20 Hegner, M.; Smith, S. B.; Bustamante, C. *Proc. Natl. Acad. Sci. USA* **96**, 10109–10114 (1999).
 - 21 Storm, A. J.; Storm, C.; Chen, J. H.; Zandbergen, H.; Joanny, J. F.; Dekker, C. *Nano Letters* **5**, 1193–1197 (2005).
 - 22 Smeets, R. M. M.; Keyser, U. F.; Krapf, D.; Wu, M. Y.; Dekker, N. H.; Dekker, C. *Nano Lett.* **6**, 89–95 (2006).
 - 23 Gershow, M.; Golovchenko, J. A. *Nature Nanotechnol.* **2**, 775–779 (2007).
 - 24 Nelson, D. L.; Cox, M. M. *Principles of Biochemistry*, 3rd ed.; Freeman Publishers, New York, 2000.
 - 25 Keyser, U. F.; Koeleman, B. N.; Van Dorp, S.; Krapf, D.; Smeets, R. M. M.; Lemay, S. G.; Dekker, N. H.; Dekker, C. *Nature Physics* **2**, 473–477 (2006).
 - 26 Meller, A.; Branton, D. *Electrophoresis* **23**, 2583–2591 (2002).
 - 27 Henrickson, S. E.; Misakian, M.; Robertson, B.; Kasianowicz, J. J. *Phys. Rev. Lett.* **85**, 3057–3060 (2000).
 - 28 Nakane, J.; Akeson, M.; Marziali, A. *Electrophoresis* **23**, 2592–2601 (2002).
 - 29 Sexton, L. T.; Horne, L. P.; Sherrill, S. A.; Bishop, G. W.; Baker, L. A.; Martin, C. R. *J. Am. Chem. Soc.* **129**, 13144–13152 (2007).
 - 30 Chen, P.; Gu, J. J.; Brandin, E.; Kim, Y. R.; Wang, Q.; Branton, D. *Nano Lett.* **4**, 2293–2298 (2004).
 - 31 Harrell, C. C.; Choi, Y.; Horne, L. P.; Baker, L. A.; Siwy, Z. S.; Martin, C. R. *Langmuir* **22**, 10837–10843 (2006).
 - 32 Ambjornsson, T.; Apell, S. P.; Konkoli, Z.; Di Marzio, E. A.; Kasianowicz, J. J. *J. Chem. Phys.* **117**, 4063–4073 (2002).
 - 33 Meller, A. *J. Phys. Condens. Matter* **15**, R581–R607 (2003).
 - 34 Story, R. M.; Weber, I. T.; Steitz, T. A. *Nature* **355**, 318–325 (1992).
 - 35 Egelman, E. H.; Stasiak, A. *Micron* **24**, 309–324 (1993).
 - 36 Wanunu, M.; Meller, A. *Nano Letters* **7**, 1580–1585 (2007).
-

Chapter 4

Detection of local protein structures along DNA using solid-state nanopores

Nanopores have been successfully employed as a new tool to rapidly detect single biopolymers, in particular DNA. When a molecule is driven through a nanopore by an externally applied electric field, it causes a characteristic temporary change in the trans-pore current. Here, we examine the translocation of DNA with discrete patches of the DNA-repair protein RecA attached along its length. Using the fact that RecA-coated DNA and bare DNA yield very different current-blockade signatures, we demonstrate that it is possible to map the locations of the proteins along the length of a single molecule using a solid-state nanopore. This is achieved at high speed and without any staining. We currently obtain a spatial resolution of about 8 nm, or 5 RecA proteins binding to 15 base pairs of DNA, and we discuss possible extensions to single protein resolution. The results are a crucial first step towards genomic screening, as they demonstrate the feasibility of reading off information along DNA at high resolution with a solid-state nanopore.

This chapter has been published as S.W. Kowalczyk, A.R. Hall, and C. Dekker, *Nano Letters* **10**(1), 324–328 (2010).

4.1 Introduction

In a complex cascade of events, proteins constantly bind and process DNA in order to maintain, transcribe and replicate this carrier of genetic information. RecA protein, for example, plays a central role in DNA repair in prokaryotes, where it catalyzes the pairing of broken DNA with complementary regions of undamaged DNA [1–3]. Other examples of DNA-binding proteins include transcription factors which modulate the process of transcription, nucleases which cleave DNA, and histones which are involved in tight chromosome packaging in the cell nucleus. The need for the sensitive detection of proteins bound to DNA is manifest. Solid-state nanopores are a good candidate for such a DNA-protein sensor. Both biological pores [4–8] and artificial solid-state nanopores [9–15] have proven their ability to detect single biopolymers. Solid-state nanopores can be fabricated with great control of pore size [10], allowing molecules of large and variable diameter, such as DNA-protein complexes, to translocate. Here, we demonstrate for the first time that it is possible to obtain length-wise “topographic reading” of proteins along a single, unstained DNA molecule at high speed and high resolution using a solid-state nanopore.

Figure 4.1a shows the experimental layout, depicting a DNA molecule that is locally coated with proteins at a number of sites along its length. Upon threading the molecule through a nanopore, one can monitor the changes in the ionic current and thus potentially distinguish protein-coated patches along the DNA. The experimental setup has been described in detail previously [16]. Briefly, a single nanopore is fabricated in a 20 nm thick, low-stress silicon nitride (SiN) membrane using the focused electron beam of a transmission electron microscope (TEM). The inset of Figure 4.1a depicts an example of such a nanopore. The membrane is then placed between two compartments filled with a monovalent salt solution (1M KCl). Application of an electric field across the membrane results in a measurable ionic current through the pore, which is temporarily reduced upon passage of a molecule.

4.2 Formation of local protein structures on DNA

In order to investigate the ability of the solid-state nanopore system to detect local molecular structure, we use the RecA protein as a model DNA-binding protein to create discrete protein patches on DNA. Related to its *in vivo* role, this protein is able to polymerize long filaments on both double-stranded DNA (dsDNA) molecules and single-stranded DNA (ssDNA) molecules, as well as form sequence-defined filament

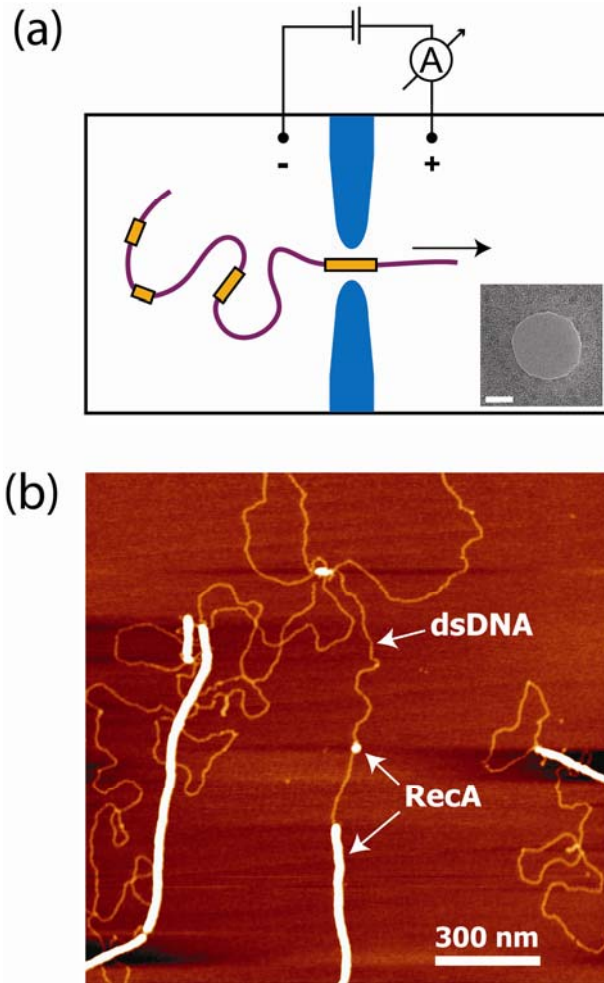


Figure 4.1 Schematic layout and AFM image of partly RecA-coated DNA molecules. (a) Schematic layout of the experiment, showing a nanopore between two liquid compartments. DNA molecules (purple) that are locally coated with RecA proteins (orange) are added to the left liquid compartment and are then pulled through the nanopore electrophoretically. The inset shows a transmission electron micrograph (TEM) of a 30 nm diameter nanopore. The scale bar is 10 nm. (b) Atomic force microscopy (AFM) image of partly RecA-coated dsDNA molecules on mica. Thick regions are RecA-coated dsDNA; thinner, more flexible lines are bare dsDNA.

stretches involved with triple-strand DNA constructs [17, 18]. RecA binding to dsDNA is highly cooperative and RecA-dsDNA complexes formed in the presence of ATP γ S (a poorly hydrolyzable ATP analogue) are known to be very stable [2]. The DNA is bound within this filament at a ratio of one RecA monomer per three base pairs and the resultant filament is a factor of 1.5 longer than bare DNA [17, 19]. From the crystal structure [17], we estimate a 7.0 ± 0.5 nm diameter of the local cross section [20] of the RecA-dsDNA complex.

In the current work, we form discrete RecA patches on dsDNA of 48.5 kilobase pair length by using low protein concentrations and a mechanical filtering method (details in Methods section). Figure 4.1b shows an atomic force microscopy (AFM) image of the resultant molecules (see Figure S4.1 for a height profile along the length of this molecule). Discrete RecA patches (thick, white regions in Figure 4.1b) of variable length – ranging from a few monomers to filaments several microns long – can be observed on the dsDNA (thinner, more flexible regions). We obtain a solution with a mixture of DNA molecules with a partial coverage of RecA, ranging from bare DNA to fully RecA-coated DNA. The fraction of RecA-coated DNA is found to be around 20% (see Figure S4.2). This is in good agreement with the stoichiometric ratio of 1:15 (RecA monomers: bp of DNA) that was used for the formation of the molecules, considering that one RecA protein binds to 3 DNA base pairs.

4.3 Nanopore translocation data

Upon addition of these molecules to the negatively biased reservoir, we observe short temporal current blockades (see Figure 4.2a). Each downward spike ΔI in the current represents the translocation of an individual molecule through the pore. We distinguish a number of discrete current levels in this trace. The origin of these levels becomes manifest in examining a histogram of conductance blockades ($\Delta G = \Delta I/V$) of the recorded events ($N = 2799$; Figure 4.2b). The first peak (0 nS, corresponding to a current of 15.9 nA at 60 mV) is the open pore conductance, which is recorded before and after each event. The peaks at 0.8 nS and 1.6 nS indicate the presence of one and two strands of bare dsDNA in the nanopore, respectively [11, 21]. Finally, the broad peak at 10-16 nS represents the passage of RecA-coated DNA. The peak value agrees well with the earlier measurements of 11.4 ± 0.7 nS for fully RecA-coated DNA [22].

The distribution of RecA blockade levels found is slightly broader than reported by Smeets *et al* [22]. This is because the molecules in the current work are only *locally* coated with RecA proteins, in contrast to this previous work. In addition to the

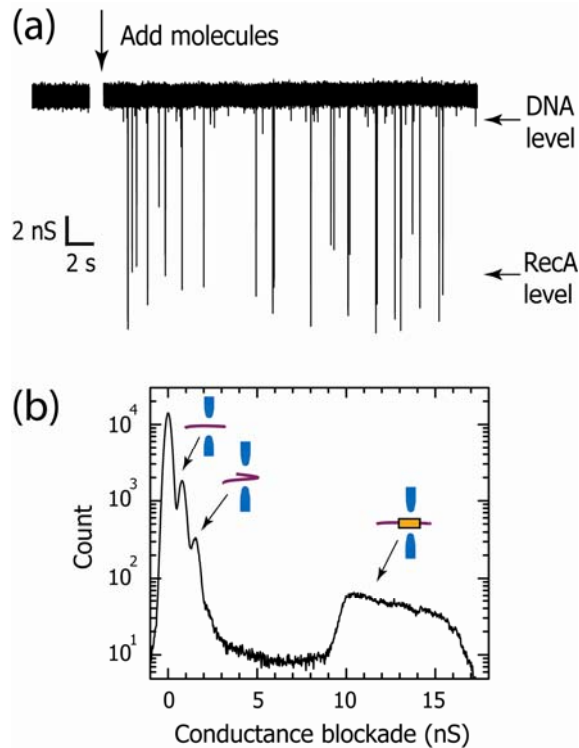


Figure 4.2 Nanopore data. (a) Example current trace before and after addition of the molecules. (b) Conductance histogram of all events recorded at 60 mV (10 μ s current samples obtained from 2799 events, including 4 ms of baseline before and after each event). The peaks corresponding to unfolded bare DNA, folded bare DNA and RecA-coated DNA are indicated in the insets.

RecA-coated DNA, also bare DNA is thus present. This bare DNA is relatively flexible and can sometimes enter the pore simultaneously with the RecA-coated part, something which is not possible for fully coated molecules. This can result in somewhat larger conductance blockades, and thus contributes to a broader distribution in the RecA blockade level.

Interestingly, we observe that individual events can demonstrate over their entire time duration a low-blockade level (< 2 nS, 65 % of the recorded data) (Figure 4.3a), a high-blockade level (> 10 nS, 6 %) (Figure 4.3b) or can interchange between the two (Figure 4.3c). We identify this behavior with the passage through the pore of bare dsDNA, fully coated RecA-dsDNA, and partially coated RecA-dsDNA, respectively.

Of the partially coated events, we occasionally detect events in which the current level changes frequently between the DNA and RecA levels (Figure 4.3d, e), in agreement with the random patchiness of the protein coating observed in AFM imaging. For example, Figure 4.3d shows an event with two sharp spikes: at the left, a downward spike, presumably due to a tiny spot of RecA on a bare section of dsDNA, and at the right, an upward spike, presumably due to a small piece of bare dsDNA between two filaments of protein-covered DNA. These example traces show that for each single-molecule translocation event, we can identify the absence or presence and position of proteins along a DNA molecule.

We observe that partially RecA-coated dsDNA molecules show a preference to enter the nanopore with the more flexible bare DNA part first (for example, at 60 mV, bare DNA enters the pore first in 89 % of the cases). Presumably, this is due to the lower persistence length of bare DNA (50 nm for bare dsDNA compared to 800 nm for RecA-coated dsDNA [17, 18]). We also note that the translocation times are quite similar (see also the scatter plot, Figure S4.3) for both bare and fully RecA-coated DNA molecules (with log-normal average values of 1.44 ± 0.07 ms and 1.45 ± 0.18 ms at 60 mV for example), consistent with previous observations [22]. Since the speed at which bare DNA and coated DNA translocates is approximately the same, the time trace is a direct representation of the spatial distribution of RecA protein along the linear DNA molecule, if we assume a uniform translocation speed.

4.4 Resolution

Having established the ability to discriminate local structures along a single molecule, we comment on the resolution capabilities of the technique. The ultimate goal would be to measure a single RecA protein on bare DNA. The (spatial) resolution Δl for the shortest distance that can be resolved along a DNA molecule of length L is defined as $\Delta l = L * (\Delta t / \tau)$, where Δt is the minimum resolvable time set by the measurement bandwidth, and τ is the total translocation time of the molecule. A slower translocation speed (with consequent increase in event duration) thus yields a higher resolution, provided that the transitory spikes caused by locally bound proteins can be discriminated above the noise. In Figure 4a, we plot the average translocation time for a range of voltages from 5 to 300 mV. We find that the average translocation time τ increases markedly at lower voltages. A clear $\tau \sim 1/V$ dependence is observed. This dependence is expected intuitively: lower voltage yields a lower electrophoretic force on the molecule, which leads to proportionally lower velocity and thus a longer

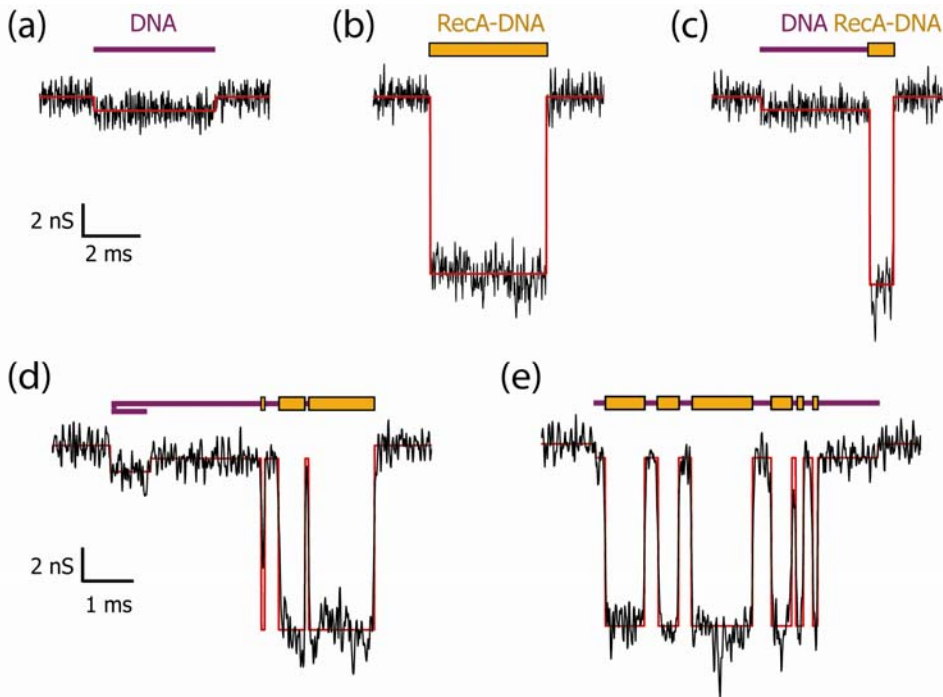


Figure 4.3 Typical nanopore translocation events recorded at 60 mV. Example of current recording of translocations of (a) bare DNA, (b) fully RecA-coated DNA and (c) partially RecA-coated DNA. (d, e) Current recordings of more complex events, in which the current level changes frequently between the DNA and RecA level. The cartoon molecules above the traces indicate the type of molecule that went through the nanopore, where purple stands for DNA and orange for RecA protein.

translocation, a lower driving voltage must be applied, which in turn decreases the signal-to-noise ratio.

In order to allow for discrimination of sharp spikes above the noise, we impose the condition that the signal conductance peak depth ΔG , is appreciably larger than the noise level. That is, $\Delta G > p^* (\delta G)_{RMS}$, where $(\delta G)_{RMS}$ indicates the RMS conductance fluctuations around the average conductance. We adopt a conservative estimate of $p = 3$ (i.e., the signal exceeds 3 times the RMS noise level). Thus, we plot the obtained resolution Δl for detection of a RecA protein patch on the DNA versus applied voltage in Figure 3.4b. In the lowest voltage range ($V < 12$ mV), additional low-pass filtering is required to meet the criterion of $p = 3$, increasing the value of Δt and thus of Δl . The best resolution is observed in the 10 – 15 mV range, where we obtain a

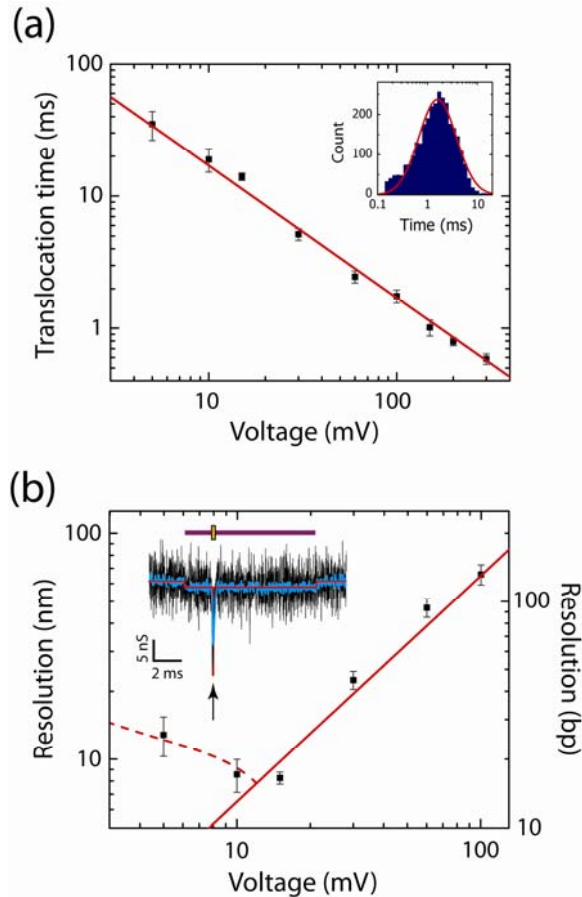


Figure 4.4 Voltage-dependence of translocation time and resolution. (a) Average translocation time versus voltage. The red line is a fit to $\tau \sim 1/V$. The error bars denote the errors from the fit on the positions of the peaks. Only unfolded events are considered. The inset shows a log-normal-distribution fit to a histogram of translocation times at 60 mV. (b) Resolution versus voltage. We find a minimum resolvable distance of about 8 nm (5 RecA proteins binding to 15 base pairs of DNA) at voltages around 10 – 15 mV. The solid red line is the interpolated resolution at full bandwidth (70 kHz), assuming $\tau \sim 1/V$, as fitted in (a). At low voltages, additional low-pass filtering is required for sufficient signal-to-noise (see text), resulting in a deviation described by the dashed red line. The inset shows the current recording for a DNA molecule with a tiny spot of RecA protein, recorded at 15 mV.

spatial resolution of about 8 nm. This corresponds to a protein patch of about 5 RecA proteins, binding to 15 base pairs of DNA.

It may be possible to improve the resolution even further. Folega *et al* [23] reported that DNA translocation can be slowed down by increasing the viscosity of the fluid through the addition of glycerol, and additionally by lowering the temperature. This projects a potential resolution approaching single RecA monomers, close to a few base pairs. Alternatively, an integrated optical tweezer approach [24, 25], which allows for the controllable insertion of a DNA molecule into the nanopore, could provide arbitrary control over molecular position relative to the nanopore.

In conclusion, we have demonstrated the detection of proteins locally along DNA using solid-state nanopores for the first time. We show a voltage-dependent resolution of these structures, reaching dimensions as small as 8 nm, or 5 RecA monomers binding to 15 base pairs of DNA. This new capability of measuring local structures along DNA at high resolution is promising for future high-speed, direct-read genetic screening.

4.5 Methods

Solid-state nanopores

Solid-state nanopore fabrication starts with the production of 20 nm thin, free-standing SiN membranes through the use of electron-beam lithography and wet etching. In each such membrane, we drill a nanopore of the desired size through the use of a highly focused electron beam in a transmission electron microscope (TEM). Details of the fabrication process are described elsewhere [16]. In this study, we used nanopores of 30 nm diameter. Nanopores are treated in an oxygen plasma for 30 s on both sides prior to use. Subsequently, the nanopores are mounted in a polyether ether ketone (PEEK) microfluidic flow cell and sealed to liquid compartments on either side of the sample. Measurements are generally performed in 1 M KCl salt solution containing 100 mM Tris-HCl at pH 8.0 at room temperature. The measurements presented in Figure 4.4 were performed at 1.5 M KCl, 10 mM Tris-HCl. Ag/AgCl electrodes are used to detect ionic currents and to apply electric fields. Current traces are measured at 100 kHz using a resistive feedback amplifier (Axopatch 200B, Axon Instruments). When necessary, further low-pass filtering is performed before digitization at 500 kHz. Only pores with minimal low-frequency current noise (<20 pA RMS) are used [26].

Formation of DNA molecules with random RecA coating

A mixture of 2.4 nM Lambda-DNA (Promega, WI), 7.6 μ M RecA (New England Biolabs, Ipswich, MA), 8.6 mM ATP γ S (Roche, Switzerland) in 570 mM KCl and 8 mM MgCl₂ was incubated for 1 h at 37 °C. ATP γ S, a poorly hydrolysable ATP analogue, was used to prevent ATP hydrolyzation-induced disassembly of RecA from the DNA [1, 2]. Subsequent centrifuge filtration (100kDa filter) serves to both remove unbound protein from the solution and detach loosely bound protein from the DNA itself. The resultant material is left with randomly sized patches of protein-coated DNA. Filtering conditions were 10,000 rpm for 5 minutes in formation buffer, then rinsing with deionized H₂O under the same spin conditions. Finally, the filtered material was resuspended in 30 μ l of measurement buffer (described above). Tapping-mode atomic force microscopy (AFM) images (Nanoscope IIIa, Digital Instruments, Santa Barbara, CA) were made in air after depositing the DNA molecules from measurement buffer containing an additional 20 mM MgCl₂ on freshly cleaved mica.

Acknowledgements. We thank N. H. Dekker, M. van den Hout, G. M. Skinner, M. Y. Wu, H. W. Zandbergen, and U. Ziese for contributions and discussions. This work is supported by the EC project READNA and the NanoSci-E+ programme.

References

- 1 Roca, A. I. & Cox, M. M. RecA protein: Structure, function, and role in recombinational DNA repair in *Progress in Nucleic Acid Research and Molecular Biology*, Vol. 56 (Academic Press Inc, San Diego, 1997).
 - 2 Cox, M. M. The bacterial RecA protein: structure, function, and regulation in *Topics in Current Genetics*, Vol. 1 (eds Aguilera, A. & Rothstein, R.) (Springer-Verlag GmbH, Heidelberg, 2007).
 - 3 van der Heijden, T. *et al.* Homologous recombination in real time: DNA strand exchange by RecA. *Molecular Cell* **30**, 530–538 (2008).
 - 4 Kasianowicz, J. J., Brandin, E., Branton, D. & Deamer, D. W. Characterization of individual polynucleotide molecules using a membrane channel. *Proc. Natl Acad. Sci. USA* **93**, 13770–13773 (1996).
 - 5 Akesson, M., Branton, D., Kasianowicz, J. J., Brandin, E. & Deamer, D. W. Microsecond time-scale discrimination among polycytidylic acid, polyadenylic
-

- acid, and polyuridylic acid as homopolymers or as segments within single RNA molecules. *Biophys. J.* **77**, 3227–3233 (1999).
- 6 Meller, A., Nivon, L., Brandin, E., Golovchenko, J. & Branton, D. Rapid nanopore discrimination between single polynucleotide molecules. *Proc. Natl Acad. Sci. USA* **97**, 1079–1084 (2000).
 - 7 Clarke, J., Wu, H.-C., Jayasinghe, L., Patel, A., Reid, S. and Bayley, H., Continuous base identification for single-molecule nanopore DNA sequencing. *Nat. Nanotech.* **4**, 265–270 (2009).
 - 8 Butler, T. Z., Pavlenok, M., Derrington, I. M., Niederweis, M. & Gundlach, J. H. Single-molecule DNA detection with an engineered MspA protein nanopore. *Proc. Natl Acad. Sci. USA* **105**, 20647–20652 (2008).
 - 9 Li, J. *et al.* Ion-beam sculpting at nanometre length scales. *Nature* **412**, 166–169 (2001).
 - 10 Storm, A. J., Chen, J. H., Ling, X. S., Zandbergen, H. W. & Dekker, C. Fabrication of solid-state nanopores with single-nanometre precision. *Nature Mater.* **2**, 537–540 (2003).
 - 11 Li, J. L., Gershow, M., Stein, D., Brandin, E. & Golovchenko, J. A. DNA molecules and configurations in a solid-state nanopore microscope. *Nature Mater.* **2**, 611–615 (2003).
 - 12 Fologea, D. *et al.* Detecting single stranded DNA with a solid state nanopore. *Nano Lett.* **5**, 1905–1909 (2005).
 - 13 Storm, A. J. *et al.* Fast DNA translocation through a solid-state nanopore. *Nano Lett.* **5**, 1193–1197 (2005).
 - 14 Dekker, C. Solid-state nanopores. *Nature Nanotech.* **2**, 209–215 (2007).
 - 15 Branton, D. *et al.* The potential and challenges of nanopore sequencing. *Nature Biotech.* **26**, 1146–1153 (2008).
 - 16 Krapf, D. *et al.* Fabrication and characterization of nanopore-based electrodes with radii down to 2 nm. *Nano Lett.* **6**, 105–109 (2006).
 - 17 Chen, Z. C., Yang, H. J. & Pavletich, N. P. Mechanism of homologous recombination from the RecA-ssDNA/dsDNA structures. *Nature* **453**, 489–496 (2008).
 - 18 Kowalczykowski, S. C. Structural biology - Snapshots of DNA repair. *Nature* **453**, 463–466 (2008).
 - 19 Stasiak, A., Di Capua, E. & Koller, Th., Elongation of duplex DNA by RecA protein. *J. Mol. Biol.* **151**, 557–564 (1981).
-

- 20 This is the local cross section within a helical filament with an outer diameter of 10.0 nm.
- 21 Storm, A. J., Chen, J. H., Zandbergen, H. W. & Dekker, C. Translocation of double-strand DNA through a silicon oxide nanopore. *Phys. Rev. E* **71**, 051903 (2005).
- 22 Smeets, R. M. M., Kowalczyk, S. W., Hall, A. R., Dekker, N. H. & Dekker, C. Translocation of RecA-coated double-stranded DNA through solid-state nanopores, *Nano Lett.* **9**, 3089–3095 (2009).
- 23 Fologea, D., Uplinger, J., Thomas, B., McNabb, D. S. & Li, J. L. Slowing DNA translocation in a solid-state nanopore. *Nano Lett.* **5**, 1734–1737 (2005).
- 24 Keyser, U. F., van der Does, J., Dekker, C. & Dekker, N. H. Optical tweezers for force measurements on DNA in nanopores. *Rev. Sci. Instr.* **77**, 105105 (2006).
- 25 Keyser, U. F. *et al.* Direct force measurements on DNA in a solid-state nanopore. *Nature Physics* **2**, 473–477 (2006).
- 26 Smeets, R. M. M., Keyser, U. F., Wu, M. Y., Dekker, N. H. & Dekker, C. Nanobubbles in solid-state nanopores. *Phys. Rev. Lett.* **97**, 088101 (2006).

4.6 Supplementary Figures

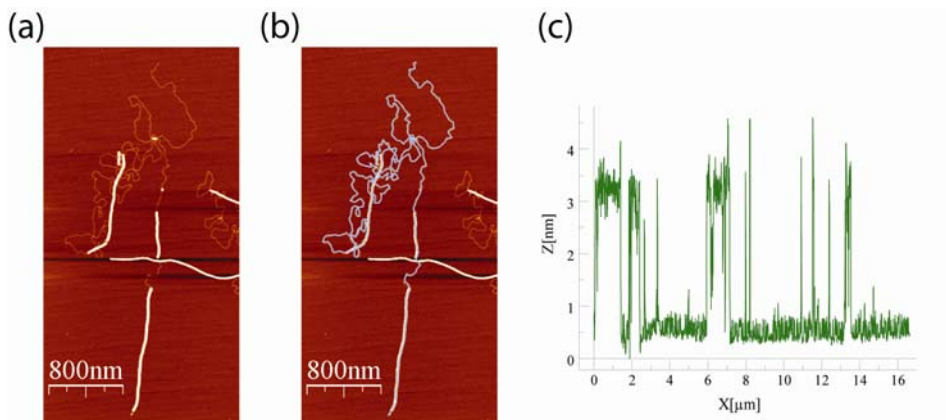


Figure S4.1 Atomic force microscope (AFM) image and molecule profile. (a) Large-scale view of the molecule shown in Figure 4.1b. (b) The same molecule traced along its entire length (blue line) using AFM data processing software WSxM (Nanotec Electronica). (c) Resultant height profile along the length of the molecule.

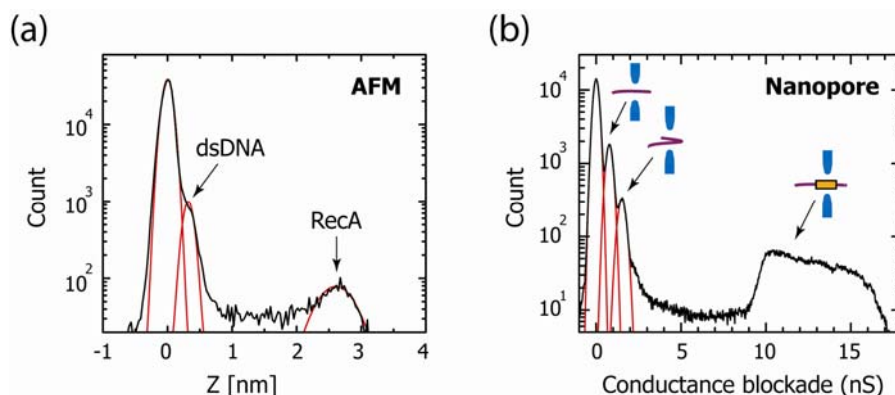


Figure S4.2 Comparison of the fraction of RecA-coated DNA to that of bare DNA, as measured by atomic force microscopy (AFM) and solid-state nanopore. (a) Height histogram from AFM data of partially RecA-coated molecules, indicating 22.3% RecA-coated DNA versus 77.7% bare DNA. (b) Conductance histogram of all nanopore translocation events recorded at 60 mV, indicating 20.9% RecA-coated DNA versus 79.1% bare DNA, in good agreement with the AFM result. These numbers were obtained by integrating the Gaussian fits (shown in red) of the respective peaks, except for the nanopore RecA peak, for which the raw data was integrated from 9-17 nS. The fraction of RecA-coated DNA found by both methods agrees well with the stoichiometric ratio of 1:15 (RecA monomers: bp of DNA) that was used for the formation of the molecules, considering that one RecA protein binds to 3 DNA base pairs, giving an expected coverage of around 20%.

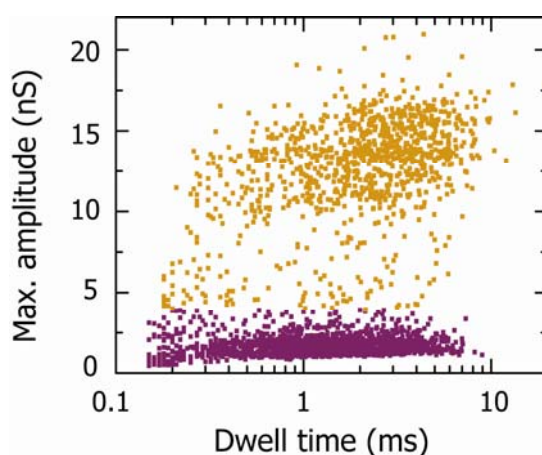


Figure S4.3 Conductance-blockade versus translocation time scatter plot. For each event, one can identify the average and maximum amplitudes by which the current

is reduced as well as the total duration of the blockage. Here, we plot the maximum conductance blockade versus time duration for all translocation events recorded at 60 mV on a semi logarithmic scale (each point represents a single-molecule translocation event). Bare DNA and (partially) protein-coated DNA molecules can be readily distinguished by their low (~ 2 nS, purple) and high (~ 14 nS, orange) maximum conductance blockade levels, respectively.

Chapter 5

Charge reduction of DNA by transient binding of counterions

The charge of a DNA molecule is a crucial parameter in many DNA detection and manipulation schemes such as gel electrophoresis and lab-on-a-chip applications. Here, we study the partial reduction of the DNA charge due to counterion binding by means of nanopore translocation experiments and all-atom molecular dynamics (MD) simulations. Surprisingly, we find that the translocation time of a DNA molecule through a solid-state nanopore strongly increases as the counterions decrease in size from K^+ to Na^+ to Li^+ , both for double-stranded DNA (dsDNA) and single-stranded DNA (ssDNA). MD simulations elucidate the origin of this effect: Li^+ can approach the charged phosphate groups on the DNA more closely than Na^+ and K^+ and transiently bind up to a thousand-fold longer. Hence, DNA in a LiCl solution has a low effective charge, and thus experiences a low electrophoretic force and slow translocation. These fundamental insights into the charge of DNA also provide a practical method for achieving at least ten-fold enhanced resolution in nanopore applications.

This chapter is in preparation for publication as S.W. Kowalczyk*, D.B. Wells *, A. Aksimentiev, and C. Dekker. *equal contribution.

5.1 Introduction

It is well known that, because DNA is highly charged, interactions between DNA and counterions can profoundly affect its physical properties [1–2]. Although valuable as first-order approximations, traditional models for polyelectrolyte-counterion interactions, i.e., Manning [1] and Poisson-Boltzmann [3] theory, ignore relevant details like the discrete nature of charges on DNA, the type of cation, and ion-ion interactions. Here, we combine nanopore translocation experiments with MD simulations to quantitatively reveal the effect of different counterions (K^+ , Na^+ , Li^+) on the charge of a DNA molecule. Surprisingly, we find that the various monovalent ions can have very different effects.

Nanopores have emerged as a versatile tool for the detection and manipulation of charged biomolecules [4–9]. In a typical setup, an external electric field drives a biomolecule through a nanometer-size pore in a thin synthetic membrane, producing a characteristic temporary change in the trans-pore ionic current. This can be used for sensitive single-molecule biosensing platforms, including DNA sequencing. A major difficulty in experiments to date, however, has been the average speed of DNA translocation, which has been too high to measure the ionic current with accuracy sufficient for sequence determination. The average speed is set by the electrophoretic drive which in turn is determined by the charge on the DNA. A lower charge would result in lower translocation speed and therefore higher read-out accuracy in these types of experiments. In this paper, we use the nanopore as a tool to determine the DNA charge.

5.2 Nanopore experiments

Figure 5.1a shows the experimental layout, depicting a double stranded (ds) DNA molecule in an ionic solution containing KCl, NaCl, or LiCl. Briefly, a single nanopore is fabricated using the focused electron beam of a transmission electron microscope (TEM) in a thin, low-stress silicon nitride (SiN) membrane (see inset of Figure 5.1b). The membrane is placed between two compartments filled with a monovalent salt solution. Subsequent application of an electric voltage (~ 0.1 V) across the membrane results in an ionic current (~ 10 nA) through the pore, which is temporarily reduced upon passage of a molecule. For this study, we used nanopores of 15–20 nm in diameter, with linear I-V relations, and good noise characteristics [10]. The open-pore conductance is approximately proportional to the cation mobility

(I-V curves shown in Figure 5.1b), as reported previously for slightly different (conical) pore geometries [11]. All experiments were reproduced multiple times, with essentially the same results.

Figure 5.1c shows an example current trace. Spikes appear in the current upon addition of dsDNA. Each spike represents a single dsDNA molecule translocating through the pore. Figure 5.1d shows current traces for some typical events of 48.5 kbp dsDNA translocations in 1M KCl, NaCl, and LiCl salt solution (from left to right). Interestingly, while the event amplitudes are similar ($\sim 1\text{--}1.5$ nS; for scatter diagrams see Figure S5.1), the translocation times increase greatly upon changing the solute from KCl to NaCl to LiCl. Figure 5.1g shows histograms of the translocation times (τ) for a large number of events. We find that for 1M solutions, the ratios for the experimental translocation times of dsDNA are KCl:NaCl:LiCl = 1:1.7:4.8. This is a surprising observation since, a priori, one would expect that the monovalent K^+ , Na^+ , and Li^+ ions would behave very similarly. Note that we limit our studies to monovalent ions. Experiments performed in the presence of divalent ions (MgCl_2) resulted in clear sticking of DNA to the membrane, which does not come as a surprise as divalent ions like Mg^{2+} are regularly used to adhere DNA to inorganic surfaces such as mica or SiO_2 .

Higher salt concentrations of LiCl result in even longer translocation times, with for 1M:2M:4M a ratio of 1:1.5:2 (see Figure 5.1e for typical events and Figure 5.1h for translocation time histograms). Also, larger current blockades are observed at higher salt concentrations. Note that changing the measurement buffer from the one typically used in nanopore experiments (1M KCl) to 4M LiCl thus slows down the dsDNA in the nanopore by a factor of 10, which is very beneficial for read-out resolution. The number of events per second is found to scale inversely with the measured translocation times (see Figure S5.2). This can be understood based on the reduced capture probability of a lower charged object at fixed voltage [12]. These results are qualitatively consistent with bulk measurements on the electrophoretic mobility of DNA [13]. However, the ion-type dependence appears to be much stronger in the case of a nanopore. The reason likely is that these bulk measurements were done at very low ionic strength (30 mM), whereas much higher ionic strengths can be applied in nanopore experiments, leading to stronger screening.

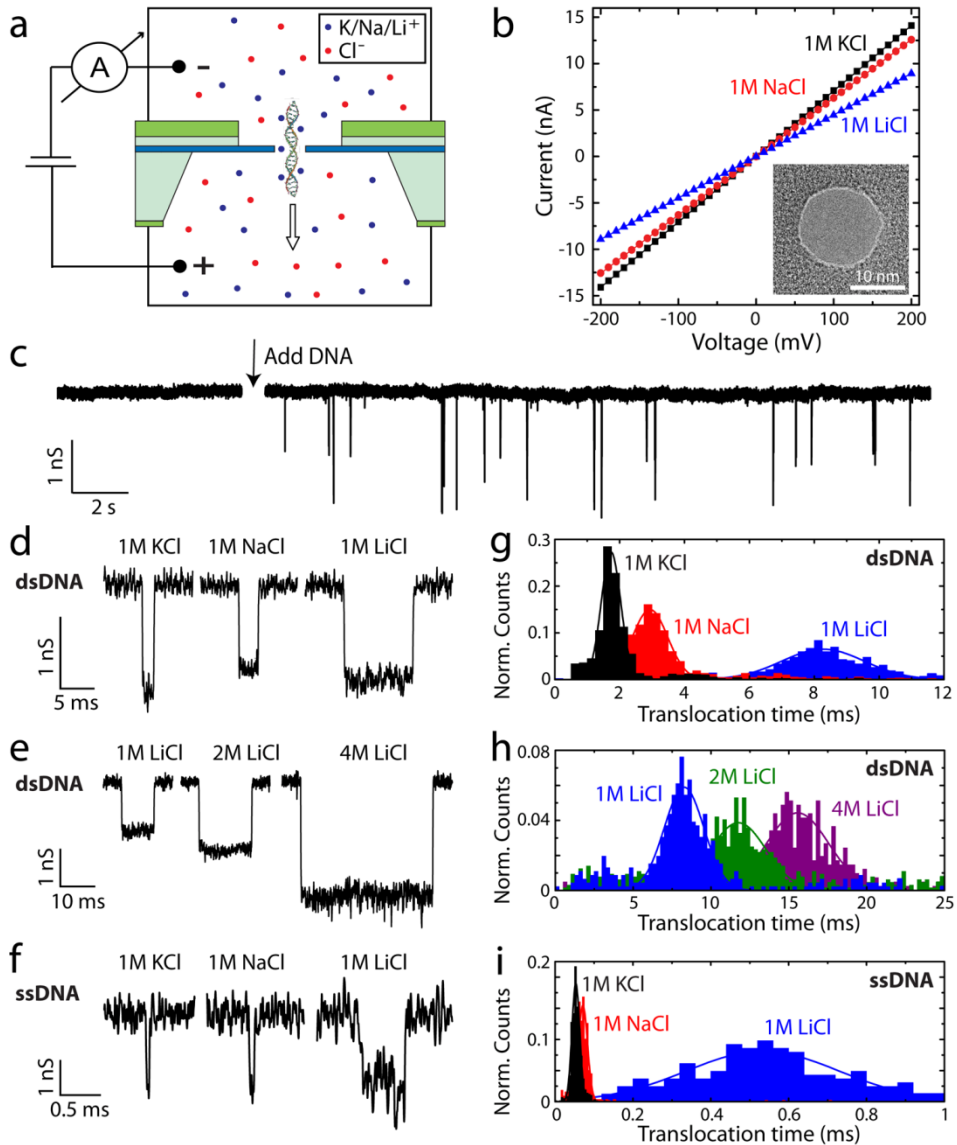


Figure 5.1 Experimental data. (a) Side-view schematic of our device, consisting of a 20 nm thin free-standing silicon nitride window (blue layer) embedded in a silicon wafer. Upon application of an electric field across the nanopore, DNA translocates through the pore. (b) Current-voltage curves for the same nanopore in 1M KCl (black squares), 1M NaCl (red circles) and 1M LiCl (blue triangles). The inset shows a TEM image of a 15 nm diameter nanopore. (c) Raw data trace. Spikes in the current can be seen to appear upon addition of DNA. Each spike represents a single DNA molecule

passing through the pore. Data taken in 1M KCl at 120 mV, and filtered at 1kHz for display. (d) Example current recordings for 48.5 kbp λ -dsDNA filtered at 5 kHz in 1M KCl (left), 1M NaCl (middle) and 1M LiCl (right). (e) Same for 1M LiCl, 2M LiCl and 4M LiCl. (f) Same for heat-shocked M13mp18 ssDNA in an additional 8M Urea, filtered at 30 kHz. (g-i) Translocation time histograms corresponding to (d-f). For the dsDNA we find translocation times of $\tau = 1.72 \pm 0.29$ ms, 2.94 ± 0.55 ms, 8.23 ± 1.43 ms, 12.1 ± 1.9 ms, and 16.5 ± 2.2 ms in 1M KCl, 1M NaCl, 1M LiCl, 2M LiCl, and 4M LiCl respectively. For the ssDNA we find translocation times of $\tau = 52 \pm 10$ μ s, 71 ± 13 μ s, and 530 ± 190 μ s in 1M KCl, NaCl, and LiCl respectively.

For ssDNA, we also find that the event amplitudes are similar between the different solutions (for scatter diagrams, see Figure S5.1). To ensure the 7.2 kb long circular M13mp18 ssDNA is in a denatured state (no secondary structures), the ssDNA is heat-shock treated prior to experiments and measurements are done in 8 M Urea (see Materials and Methods). Event amplitudes of ~ 1.5 – 2 nS are measured (example events shown in Figure 5.1f). Note that the ssDNA used is circular, resulting in the presence of two single strands of DNA at each point in time during translocation through the pore. The measured amplitude of about 1 nS per strand indicates that the ssDNA is indeed denatured [9], because non-denatured ssDNA under similar conditions gives much higher (~ 10 nS) event amplitudes due to the formation of large ssDNA blobs that stall at the pore entrance [14]. Similar to dsDNA, but quantitatively even more pronounced, the ssDNA exhibits a slowing down upon changing the solute from KCl to NaCl to LiCl with translocation times of ssDNA for KCl:NaCl:LiCl = 1:1.4:10.2 (see Figure 5.1i for translocation time histograms). Investigation at much higher salt concentrations is not possible for ssDNA because the 8M Urea solution saturates at about 1.5 M salt concentration.

5.3 MD simulations

How can we understand this unexpected but pronounced slowing down of DNA translocation upon merely changing the buffer from KCl to LiCl? All-atom molecular dynamics (MD) simulations elucidate the molecular origin of this phenomenon. Figure 5.2a shows the MD simulation result for the average velocity v (note that v simply scales as $\sim 1/\tau$ with the translocation time τ) of dsDNA molecules in 1 M KCl, NaCl, and LiCl that translocate through an 8 nm wide nanopore. Similar to what was observed in the experiments above, the change from KCl to NaCl to LiCl salt solution dramatically decreases the average translocation speed. In fact, in the case of 1 M LiCl, MD simulations show an average velocity close to zero (even a slight reversal of

translocation direction in this simulation, which we attribute to imperfections in the force field). Simulations were also performed with a system containing a 4.4 nm wide nanopore, with similar results (see Figure S5.3).

While the observed trends are the same, the simulations and experiments show a large quantitative difference in dwell times (approximately six orders of magnitude). This can however be reconciled to a difference of a mere factor of 4 once the voltage difference, water viscosity [15], and power-law dependence of dwell time on DNA length [16] are taken into account (see Supplemental Information).

Figure 5.2b shows the result of similar simulations carried out on ssDNA homopolymers, which display the same trend as dsDNA. The average translocation velocity is seen to depend strongly on the type of the nucleobases, with pyrimidines translocating faster than purines, consistent with the smaller size of the former. While the MD simulations capture the qualitative effect of counterions, the absolute velocities seen in the simulations are much higher (up to a factor of 70) than in experiments. This difference can be primarily attributed to the different length of the DNA. In the MD simulations, short pieces of DNA (20 bp) were considered. In the experiments, however, the dsDNA length was 48,502 bp. For such a length, the untranslocated DNA forms a hydrodynamic “blob”, which leads to a drag force opposite to the driving force and thus significantly slower translocation kinetics, see also SI [16].

The MD simulations also reveal the microscopic mechanism for the slow translocation for DNA in LiCl versus KCl. We find that this is due to counterion binding to the charged DNA backbone. Lithium is seen to bind strongly to the phosphate oxygens, shown in Figure 5.2c (counterion binding locations are detailed in Figure S5.4). Figure 5.2d plots the number of ions bound per base as a function of minimum bond duration for the three types of counterions, viz., it plots the number of bonds lasting at least a certain amount of time, $b(t) = \int_t^\infty p(\tau) d\tau$, where $p(\tau)$ is the probability density per base of having an ion bound for duration τ . The number of bound ions per base is directly related to the electrical neutralization of DNA; a value of unity indicated complete neutralization. For lithium, a very high value $b(0) = 0.84$ is found, whereas much lower values are found for sodium and potassium. The decay times of these curves indicate the lifetimes of the counterion-DNA bonds. Lithium bond lifetimes are seen to be on the order of 10 ns (9.22 ns), orders of magnitude longer than those of sodium (0.13 ns) or potassium (0.023 ns). Similar values for sodium and potassium have been reported before (17). In addition, lithium ions were observed to be partially dehydrated while bound to DNA, reducing the average number of water molecules bound to the lithium from 3.4 to 2.7.

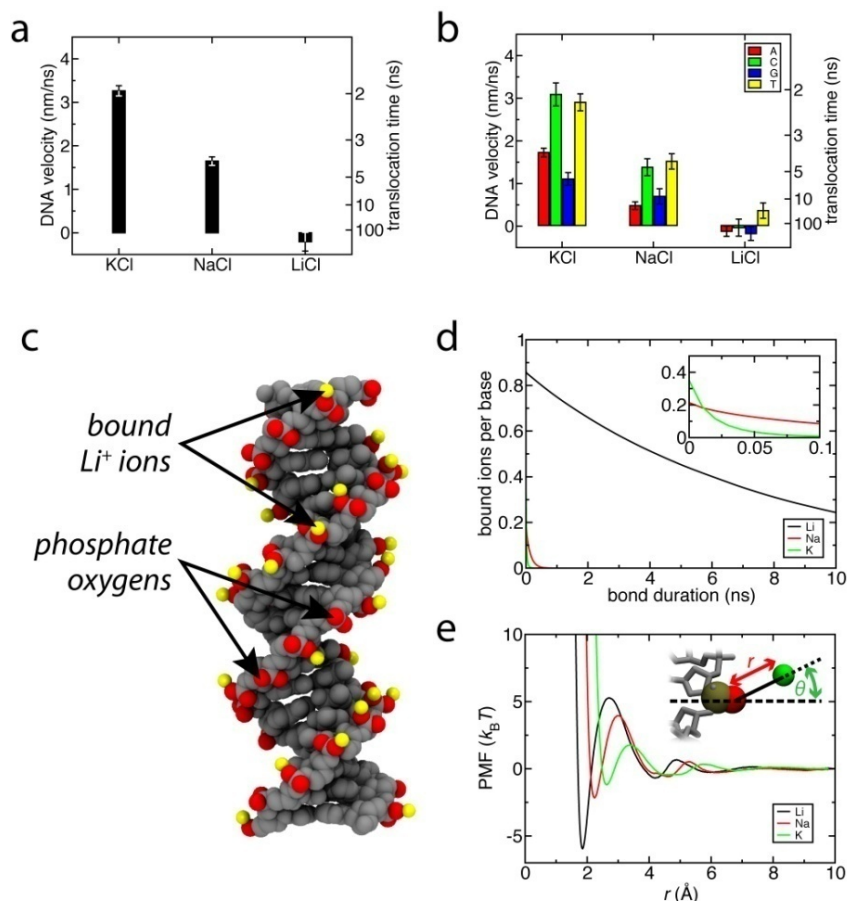


Figure 5.2 Molecular dynamics simulations. (a) Average center-of-mass velocity of dsDNA as a function of ion species. Translocation time (right axis) is given as the time for a 20-bp DNA fragment to transit the 6.4 nm thick nanopore. (b) Average center-of-mass velocity of ssDNA homopolymers of different bases as a function of ion species. Bars are shown for poly(dA) (red), poly(dC) (green), poly(dG) (blue), and poly(dT) (yellow). Translocation time is calculated as in (a). (c) Binding of lithium ions (yellow) to DNA phosphate oxygens (red). Nanopore, water, coions, and counterions not bound to DNA are not shown. (d) Number of bound ions per base as a function of bond duration for dsDNA. An ion is considered bound if it resides within 3.4 Å of the same DNA atom. Inset shows an enlargement of the Na and K curves. (e) Potential of mean force calculated for interactions of each counterion with the phosphate oxygens of DNA. Inset shows the distance between the centers of the ion and O2P oxygen atom r (solid line), and the angle between the ion and an axis passing through the center of the O2P oxygen atom and center of the DNA θ (dashed line). Ion concentration is 1 M in all cases.

In order to quantify the strength of ion binding to the DNA backbone, we calculated the potential of mean force (PMF) between a counterion and a phosphate oxygen as a function of distance. Results of this analysis are shown in Figure 5.2e. The PMF reveals a deep potential well of $6.0 k_B T$ for lithium, and shallower wells of 2.2 and $1.2 k_B T$ for sodium and potassium, respectively. Error in the PMF was estimated to be $0.5 k_B T$ for lithium, $0.3 k_B T$ for sodium, and $0.5 k_B T$ for potassium [16]. The deeper well for lithium is a result of the ion's smaller van der Waals radius (0.71 \AA , compared to 0.97 and 1.41 \AA for sodium and potassium, respectively [19]), which allows its positive electric charge to more closely approach the negative charge of the phosphate oxygen atoms. The deeper potential well results in the much longer residence time, and thus a more significant electrical neutralization of the DNA.

5.4 Effect of ion concentration and voltage

Figure 5.3a shows the average DNA velocity from MD simulations as a function of ion concentration. For all three ion types studied, we find that increasing the ion concentration leads to decreasing the DNA velocity, presumably due to a more complete electrical neutralization of the DNA. Figure 5.3b shows the average number of bound counterions per base, $b(20 \text{ ps})$, seen in the simulations, depicted as symbols. The simulation data confirm that, as expected, an increasing ion concentration results in greater counterion binding to DNA. To validate the PMFs shown in Figure 5.2e, an independent prediction of the number of counterions bound to phosphate oxygens of the DNA for each ion species (see Methods) can be made using the PMFs. Results of these calculations are plotted in Figure 5.3b. The agreement between the two analysis methods is reasonably good, given the very sensitive dependence of the predicted number of bound counterions per base on the PMF and the presence of binding sites other than phosphate oxygen at the DNA surface (see Figure S5.4).

Figure 5.3c shows the experimental dsDNA translocation times as a function of ion concentration. As in the MD simulations, for all three ion types studied, we find that increasing the ion concentration leads to an increase of the translocation time, i.e., a decrease in the average DNA velocity. Finally, Figure 5.3d shows the experimental voltage dependence of translocation times. We find that for all solutes, translocation times are inversely proportional to the applied voltage, as was previously found for KCl [20]. MD simulations show very similar results (see Figure S5.5).

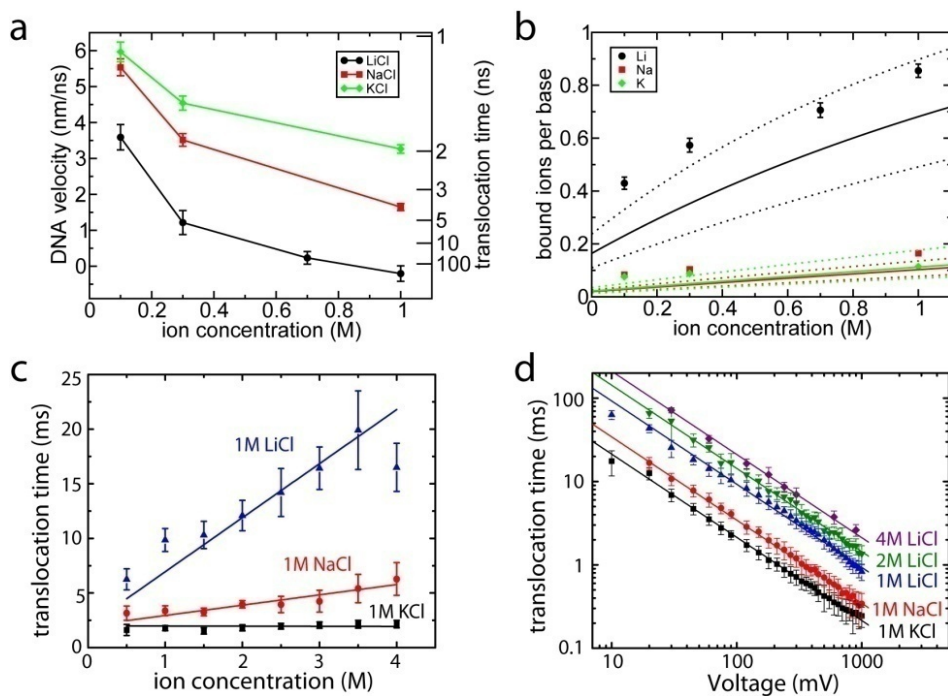


Figure 5.3 Effect of ion concentration and applied voltage on DNA velocity. (a) MD simulation result for the simulated average velocity of dsDNA as a function of ion concentration. Curves are shown for LiCl (black), NaCl (red) and KCl (green). Translocation time is calculated as in Figure 5.2. (b) MD result for the average number of counterions bound per dsDNA base versus ion concentration. An ion is considered bound when it is within 3.4 \AA of the same DNA heavy atom for at least 20 ps. Solid curves represent the predicted binding fraction based on the calculated K_{eq} , where the dashed lines around each curve represents the error from the PMF calculation. (c) Experimental translocation times for dsDNA as a function of ion species and concentration. Solid lines are linear fits to the data. (d) Experimental translocation times for dsDNA as a function of applied voltage for 1M KCl, 1M NaCl, 1M LiCl, 2M LiCl, 4M LiCl. Solid lines are fits to $\tau = 1/V$.

5.5 Discussion

Through a combination of MD simulations and nanopore translocation experiments, we have thus characterized the charge of a DNA molecule in monovalent electrolytes. While it has been known that the charge of a DNA molecule sensitively depends on the valence of counterions [21, 22], here we demonstrate that the size of counterions

can dramatically influence the DNA charge, and hence the average translocation speed through a nanopore.

One may ask whether interactions between DNA and the nanopore surface play a role in the reducing the average translocation speed. In very small pores (well under 5 nm in diameter) DNA-pore wall interactions were reported that also slowed down DNA translocation [23, 24] as well as led to a considerable spread in event characteristics [25]. In our case however, we used wide pores of ~ 20 nm in diameter where such effects have not been reported and there are no obvious reasons to assume adsorption because of the negative charge of both the membrane surface and DNA. Indeed, we obtained similar results for graphene nanopores, both in experiments [26] and simulations (Figure S5.7), confirming that the slowing down is intrinsic to the Li-DNA interactions rather than due to extrinsic reasons such as sticking to the SiN surface.

At the molecular level, we found a partial neutralization of the DNA charge that originates from transient binding of counterions to specific sites at the DNA surface. In particular, we found that lithium ions are transiently bound over hundred to thousand-fold longer than sodium or potassium ions, yielding a very low net charge for DNA in a 1 M LiCl solution, viz., a reduction by 86% compared to the bare DNA charge, whereas the DNA charge in a similar KCl solution would be reduced by merely 21%. Our results present a considerable departure from the classical theory of ion condensation [1] that predicts a 75% neutralization of the DNA charge in monovalent electrolytes and an independence on ion type. Recently, theoretical extensions to the Poisson-Boltzmann theory have been developed by adding an ion-size-dependent term into the energy, predicting preferential binding of Li^+ in qualitative agreement with our results [27]. From a practical perspective, our findings indicate that LiCl offers significant advantages compared to the traditionally used ionic solutions for nanopore applications.

5.6 Materials and Methods

MD Methods

All simulations were performed using the software package NAMD [28], 2–2–6-fs multiple timestepping, CHARMM27 parameters [29] with CMAP corrections [30], a 7–8 Å cutoff for van der Waals and short-range electrostatic forces, and the Particle Mesh Ewald (PME) method for long-range electrostatics computed over a 2.0 Å-spaced grid. The temperature was maintained at 295 K using the Lowe-Andersen

thermostat. For NPT simulations, the Langevin piston method was used, with a period of 200 fs and a decay of 100 fs. Ions were simulated with Young-Cheatham [31] Lennard-Jones parameters, which have recently been successfully tested using the biological pore α -hemolysin [32]. Trajectory frames were saved every 10 ps. Visualization and analysis were performed using VMD [33].

The simulation systems consisted of a block of annealed SiO₂ [34] of $9.956 \times 9.956 \times 6.4$ nm³ containing an 8 nm diameter circular pore along the short axis of the block, DNA, and ionic solution of 0.1, 0.3, 0.7, or 1 M of LiCl, NaCl, or KCl (0.7 M only done for LiCl). Simulations with larger systems in which the pore connected to a solution bath verified that the ion concentrations quoted correspond to bulk concentrations. Systems of dsDNA contained poly[d(A·T)]₂₀ (two turns). Systems of ssDNA contained poly(dN)₂₀. To avoid interaction of DNA with the silica surface, the center of mass of DNA phosphate atoms was radially restrained to the center of the pore, with a spring constant of $93.72 \text{ kcal mol}^{-1} \text{ \AA}^{-2}$. Periodic boundary conditions were used, with DNA covalently bonded over the periodic boundaries, effectively making the simulation system an infinite nanopore containing infinite DNA. An electric field was applied parallel to the nanopore/DNA axis. Electric potential differences reported refer to the difference over a single 6.4 nm periodic image.

Potential of mean force (PMF) calculations were carried out using umbrella sampling [35] with 0.1 Å windows and a spring constant of $28.8 \text{ kcal mol}^{-1} \text{ \AA}^{-2}$. Starting conformations were taken after approximately 20 ns of simulation in a 500 mV electric bias with the DNA center of mass harmonically restrained in the axial direction with a $0.1 \text{ kcal mol}^{-1} \text{ \AA}^{-2}$ spring constant. A single ion (lithium, sodium, or potassium) was restrained to a prescribed center-to-center radial distance from a specific O2P oxygen atom ranging from 1.1 to 10 Å for lithium, 1.6 to 10 Å for sodium, and 2.1 to 10 Å for potassium. Independent simulations were run for 1.44 ns for each window, recording the ion-DNA distance every 20 fs. To prevent the ion from interacting with other DNA binding sites more strongly than the specified site, an additional angular harmonic restraint of $20 \text{ kcal mol}^{-1} \text{ rad}^{-2}$ kept the ion along the axis normal to the DNA axis and passing through the oxygen atom and the DNA center (represented by the dashed line in the inset of Figure 5.2e.) Additionally, DNA phosphate atoms were harmonically restrained using a $1 \text{ kcal mol}^{-1} \text{ \AA}^{-2}$ spring constant. No electric field was applied during PMF calculations. PMFs were calculated using the weighted histogram analysis method [36], discarding the first 0.1 ns of each trajectory.

The equilibrium binding constant K_{eq} was calculated following the method of Woo and Roux [18], which takes into account the effect of the restraining angular potential on the free energy of binding. Briefly, the method involves calculating the free energy cost of: (i) turning on the angular restraining potential (G_{on}); (ii) binding of the ion to DNA (G_{PMF}); and (iii) turning off the angular restraining potential (G_{off}). The first term is calculated analytically as

$$G_{on} = -k_B T \ln \frac{\int_0^\pi \sin \theta e^{-k\theta^2/k_B T} d\theta}{\int_0^\pi \sin \theta d\theta} \quad (1)$$

where k is the angular force constant. The second term is calculated from the PMF as

$$G_{PMF} = -k_B T \ln [c_0 \int_S 4 \pi r^{*2} e^{-[W(r)-W(r^*)]/k_B T} dr] \quad (2)$$

where c_0 is a concentration (which cancels out when converting to K_{eq} below), r^* is a distance far from the binding site (10 Å in our case), and the integration is carried out over the portion of the PMF corresponding to the binding site (0 to 2.25 Å for lithium, 0 to 2.6 Å for sodium, and 0 to 3 Å for potassium). The third term is calculated using free energy perturbation (FEP). For FEP calculations, simulations with the ion bound to DNA were carried out with the angular force constant k ranging from 0 to the value used for the PMF calculations in 0.5 kcal mol⁻¹ rad⁻² increments. For each ion, FEP simulations were started from the end of the PMF simulation with the window nearest the PMF minimum for that ion. During FEP calculations, the ion was not radially restrained as during the PMF simulations, but kept bound to the DNA by applying a force of 1.39 nN on the ion toward the DNA oxygen if the ion was more than 2.05, 2.5, or 2.9 Å from the oxygen for lithium, sodium, and potassium, respectively. Data from simulation steps with this extra force were not used to calculate G_{off} . Otherwise, simulation parameters during FEP calculations were identical to those used during PMF calculations. K_{eq} is then given by

$$K_{eq} = e^{-(G_{on}+G_{PMF}+G_{off})/k_B T} / c_0 \quad (3)$$

Results of the individual binding components, in units of $k_B T$ with $T = 295$ K, were as follows for lithium (sodium, potassium): $G_{on} = +4.92$ (+4.92, +4.92), $G_{PMF} = -0.36$ (+2.63, +2.88) – $\ln c_0$, and $G_{off} = -3.83$ (-4.45, -4.80). For G_{PMF} , c_0 is the ion concentration given in M. N_{bound} is then found from the definition of K_{eq} :

$$K_{eq} = \frac{[AB]}{[A][B]} = \frac{N_{bound}/V}{(N_{sites}-N_{bound})(N_{total}-N_{bound})/V^2} \quad (4)$$

where N_{bound} is the number of bound counterions, $N_{sites} = 80$ (the number of phosphate

oxygens in the simulation system) is the number of binding sites on DNA, N_{total} is the total number of counterions, and V is the volume of the system.

Solid-state nanopores

Solid-state nanopore fabrication starts with the fabrication of 20 nm thin free-standing SiN membranes through the use of electron-beam lithography and wet etching. In each such membrane, we drill a nanopore of the desired size through the use of a highly focused electron beam in a transmission electron microscope (TEM). Details of the fabrication process are described elsewhere [37]. The reported data on dsDNA was taken on a 15.3 nm pore, the data on ssDNA on a 19.8 nm pore. Nanopores are treated in an oxygen plasma for 30 s on both sides prior to use. Subsequently, the nanopores are mounted in a polyether ether ketone (PEEK) microfluidic flow cell and sealed to liquid compartments on either side of the sample. Measurements are performed in KCl/NaCl/LiCl salt solution of the stated molarity containing 10 mM Tris-HCl and 1mM EDTA at pH 8.0 at room temperature. The viscosities of these solutions ($\eta = 0.99, 1.10, 1.15 \times 10^{-3}$ Pa·s respectively) do not differ much. Experiments with divalent ions were performed in 1M MgCl₂ containing 10 mM Tris-HCl and 1mM EDTA at pH 8.0. Ag/AgCl electrodes are used to detect ionic currents and to apply electric fields. Current traces are measured at 100 kHz using a resistive feedback amplifier (Axopatch 200B, Axon Instruments) and digitized at 500 kHz. When necessary, further low-pass filtering is performed. Only pores with minimal low-frequency current noise (<20 pA RMS) are used [10].

The experimental data were collected in salt concentrations ranging from 0.5 M to 4 M, while the simulations were performed in the range of 0.1 M up to 1 M. While there is considerable overlap in the salt concentrations used, the overlap is not complete. There are two reasons for this. First, in the simulations, for higher salt concentration, we start to see crystallization effects which originate from imperfections of the force field. Second, in the experiments, there is a crossover from current enhancement to current reduction at around 0.3 M [38], with the result that DNA translocations experimentally cannot be detected around this salt concentration due to a limited signal-to-noise ratio. These two circumstances limit the possible ranges that can be investigated in both simulations and experiments. However, the trends that are observed in experiments and simulations clearly are the same.

Preparation of single-stranded DNA

To ensure that no secondary structure is present in the ssDNA, the M13mp18 circular ssDNA is heat-shock treated for 10 minutes at 90°C which removes all secondary structure. The final DNA concentration used in the nanopore experiment was 2 ng/μl. Measurements are done in 1M salt solutions with an additional 8M Urea to prevent refolding of the ssDNA [39]. This results in a reduction of ~40% of the open-pore pore conductance (see Figure S5.6) as reported before [40], because of the increased viscosity (1.7×10^{-3} Pa·s for 8M Urea) and the fact that the ionic electrophoretic mobility (and hence the total current) is proportional to the inverse of the viscosity [41].

Acknowledgements. We thank Jan Lipfert, Christopher Maffeo, Gregory Schneider, and Gautam Soni for discussions. This work is supported by the NanoSci-E+ program, the European Union's Seventh Framework Programme (FP7/2007-2013) under grant agreement n° 201418 (READNA), and ERC-2009-AdG Grant 247072 NANOFORBIO. D.W. and A.A. acknowledge support from the National Institutes of Health (R01-HG003713), the National Science Foundation (PHY-0822613 and DMR-0955959) and Teragrid (MCA05S028).

References

- 1 Manning GS, Molecular theory of polyelectrolyte solutions with applications to electrostatic properties of polynucleotides. *Q Rev Biophys* **11**, 179–246 (1978).
- 2 Keyser UF, *et al.* Direct force measurements on DNA in a solid-state nanopore. *Nat Phys* **2**, 473–477 (2006).
- 3 Wilson RW, Rau DC, Bloomfield VA, Comparison of poly-electrolyte theories of the binding of cations to DNA. *Biophys J* **30**, 317–325 (1980).
- 4 Dekker C, Solid-state nanopores. *Nat Nanotechnol* **2**, 209–215 (2007).
- 5 Howorka S, Siwy Z, Nanopore analytics: sensing of single molecules. *Chem Soc Rev* **38**, 2360–2384 (2009).
- 6 Branton D, *et al.* The potential and challenges of nanopore sequencing. *Nat Biotechnol* **26**, 1146–1153 (2008).
- 7 Aksimentiev A, Deciphering ionic current signatures of DNA transport through a nanopore. *Nanoscale* **2**, 68–483 (2010).

- 8 Li JL, Gershow M, Stein D, Brandin E, Golovchenko JA, DNA molecules and configurations in a solid-state nanopore microscope. *Nat Mater* **2**, 611–615 (2003).
 - 9 Skinner GM, van den Hout M, Broekmans O, Dekker C, Dekker NH, Distinguishing Single- and Double-Stranded Nucleic Acid Molecules Using Solid-State Nanopores. *Nano Lett* **9**, 2953–2960 (2009).
 - 10 Smeets RMM, Keyser UF, Wu MY, Dekker NH, Dekker C, Nanobubbles in solid-state nanopores. *Phys Rev Lett* **97**, 088101 (2006).
 - 11 Gillespie D, Boda D, He Y, Apel P, Siwy ZS, Synthetic Nanopores as a Test Case for Ion Channel Theories: The Anomalous Mole Fraction Effect. *Biophys J* **95**, 609–619 (2008).
 - 12 Wanunu M, Morrison W, Rabin Y, Grosberg AY, Meller A, Electrostatic Focusing of Unlabeled DNA into Nanoscale Pores using a Salt Gradient. *Nat Nanotechnol* **5**, 160–165 (2009).
 - 13 Stellwagen E, Dong Q, Stellwagen NC, Monovalent Cations Affect the Free Solution Mobility of DNA by Perturbing the Hydrogen-Bonded Structure of Water. *Biopol* **78**, 62 (2005).
 - 14 Kowalczyk SW, Tuijtel MW, Donkers SP, Dekker C, Unraveling Single-Stranded DNA in a Solid-State Nanopore. *Nano Lett* **10**, 1414–1420 (2010).
 - 15 Yeh IC, Hummer G, Diffusion and electrophoretic mobility of single-stranded RNA from molecular dynamics simulations. *Biophys J* **86**, 681–689 (2004).
 - 16 Storm AJ, *et al.*, Fast DNA translocation through a solid-state nanopore. *Nano Lett* **5**, 1193–1197 (2005).
 - 17 Várnai P, Zakrzewska K, DNA and its counterions: a molecular dynamics study. *Nucl. Acids Res* **32**, 4269–4280 (2004).
 - 18 Woo H-J, Roux B, Calculation of absolute protein-ligand binding free energy from computer simulations. *Proc Natl Acad Sci USA* **102**, 6825–6830 (2005).
 - 19 Marcus Y, Ionic radii in aqueous solutions. *Chem Rev* **88**, 1475–1498 (1988).
 - 20 Kowalczyk SW, Hall AR, Dekker C, Detection of Local Protein Structures along DNA Using Solid-State Nanopores. *Nano Lett* **10**, 324–328 (2010).
 - 21 Besteman K, Van Eijk K, Lemay SG, Charge inversion accompanies DNA condensation by multivalent ions. *Nat Phys* **3**, 641–644 (2007).
 - 22 Luan B, Aksimentiev A, Electric and electrophoretic inversion of the DNA charge in multivalent electrolytes. *Soft Matter* **6**, 243–246 (2010).
 - 23 Wanunu M, Sutin J, McNally B, Chow A, Meller A, DNA Translocation Governed by Interactions with Solid-State Nanopores. *Biophys J* **95**, 4716–4725 (2008).
 - 24 Yeh IC, Hummer G, Nucleic acid transport through carbon nanotube membranes. *Proc Natl Acad Sci USA* **101**, 12177–12182 (2004).
-

- 25 Van den Hout M, Krudde V, Janssen XJA, Dekker NH, Distinguishable Populations Report on the Interactions of Single DNA Molecules with Solid-State Nanopores. *Biophys J* **99**, 3840–3848 (2010).
 - 26 Schneider GF, *et al.* to be published.
 - 27 Chu VB, Bai Y, Lipfert J, Herschlag D, Doniach S, Evaluation of Ion Binding to DNA Duplexes Using a Size-Modified Poisson-Boltzmann Theory. *Biophys J* **93**, 3202–3209 (2007).
 - 28 Phillips JC, *et al.* Scalable molecular dynamics with NAMD. *J Comp Chem* **26**, 1781–1802 (2005).
 - 29 MacKerell AD Jr, *et al.* All-atom empirical potential for molecular modeling and dynamics studies of proteins. *J Phys Chem B* **102**, 3586–3616 (1998).
 - 30 MacKerell AD Jr, Empirical force fields for biological macromolecules: Overview and issues. *J Comp Chem* **25**, 1584–1604 (2004).
 - 31 Joung IS, Cheatham TE, Determination of alkali and halide monovalent ion parameters for use in explicitly solvated biomolecular simulations. *J Phys Chem B* **112**, 9020–9041 (2008).
 - 32 Bhattacharya S, *et al.* Rectification of the current in alpha-hemolysin pore depends on the cation type: the alkali series probed by Molecular Dynamics simulations and experiments. *J Phys Chem C* **115**, 4255–4264 (2011).
 - 33 Humphrey W, Dalke A, Schulten K, VMD – Visual Molecular Dynamics. *J Mol Graphics* **14**, 33–38 (1996).
 - 34 Cruz-Chu ER, Aksimentiev A, Schulten K, Water-Silica Force Field for Simulating Nanodevices. *J Phys Chem B* **110**, 21497–21508 (2006).
 - 35 Torrie GM, Valleau JP, Nonphysical sampling distributions in Monte Carlo free-energy estimation: umbrella sampling. *J Comp Phys* **23**, 187–199 (1977).
 - 36 Kumar S, Rosenberg JM, Bouzida D, Swendsen RH, Kollman PA, The weighted histogram analysis method for free-energy calculations on biomolecules. I. The method. *J Comp Chem* **13**, 1011–1021 (1992).
 - 37 Krapf D, *et al.* Fabrication and characterization of nanopore-based electrodes with radii down to 2 nm. *Nano Lett* **6**, 105–109 (2006).
 - 38 Smeets RMM, *et al.* Salt Dependence of Ion Transport and DNA Translocation through Solid-State Nanopores. *Nano Lett* **6**, 89–95 (2006).
 - 39 Tinland B, Pluen A, Sturm J, Weill G, Persistence Length of Single-Stranded DNA. *Macromolecules* **30**, 5763–5765 (1997).
 - 40 Singer A, Kuhn H, Frank-Kamenetskii M, Meller A, Solid-State Nanopore based Detection of Urea-Induced Internal Denaturation of dsDNA. *J Phys: Condens Matter* **22**, 454111 (2010).
-

41 Fologea D, Uplinger J, Thomas B, McNabb DS, Li JL, Slowing DNA translocation in a solid-state nanopore. *Nano Lett.* **5**, 1734–1737 (2005).

5.7 Supplementary Information

We observe a strong quantitative difference if we compare the DNA translocation time in the experiments versus the simulations, where the DNA appears to move much faster in the simulations. How can we account for this?

Following earlier work from our group [S1], which showed a power-law scaling of dwell time versus DNA length with an exponent of 1.27, we estimate an experimental versus simulation dwell time ratio of $(48500/20)^{1.27} \approx 2 \times 10^4$, given the fact that we compare experiments on 48500 bp long DNA and perform calculations on 20 bp long DNA. After furthermore correcting for the different voltages used in simulation and experiment (a factor of $500 \text{ mV}/120 \text{ mV} = 4.2$), and the low viscosity of the TIP3 water (factor of 3) used in the simulations [S2], we expect the experimental dwell times to be at least 3×10^5 times those seen in simulation. If we compare experiment versus simulation for KCl at 1.0 M, we find a ratio of $2 \text{ ms}/2 \text{ ns} = 1 \times 10^6$, i.e., a factor of 3-4 higher than this estimate.

In view of the many approximate steps to arrive at these numbers, we consider this factor 3-4 difference a good agreement. Note also that the power-law scaling [S1] has not been experimentally verified for DNA pieces shorter than 6500 bp (which is still more than 300-fold longer than the DNA used in the MD simulations) and it is certainly not obvious that it will remain valid for very short DNA pieces. For alpha-hemolysin, for example, it was found that translocation speeds rapidly increase for very short DNA pieces [S3]. Taking such effects into account might bring the experimental and simulation results even closer together than a factor 4.

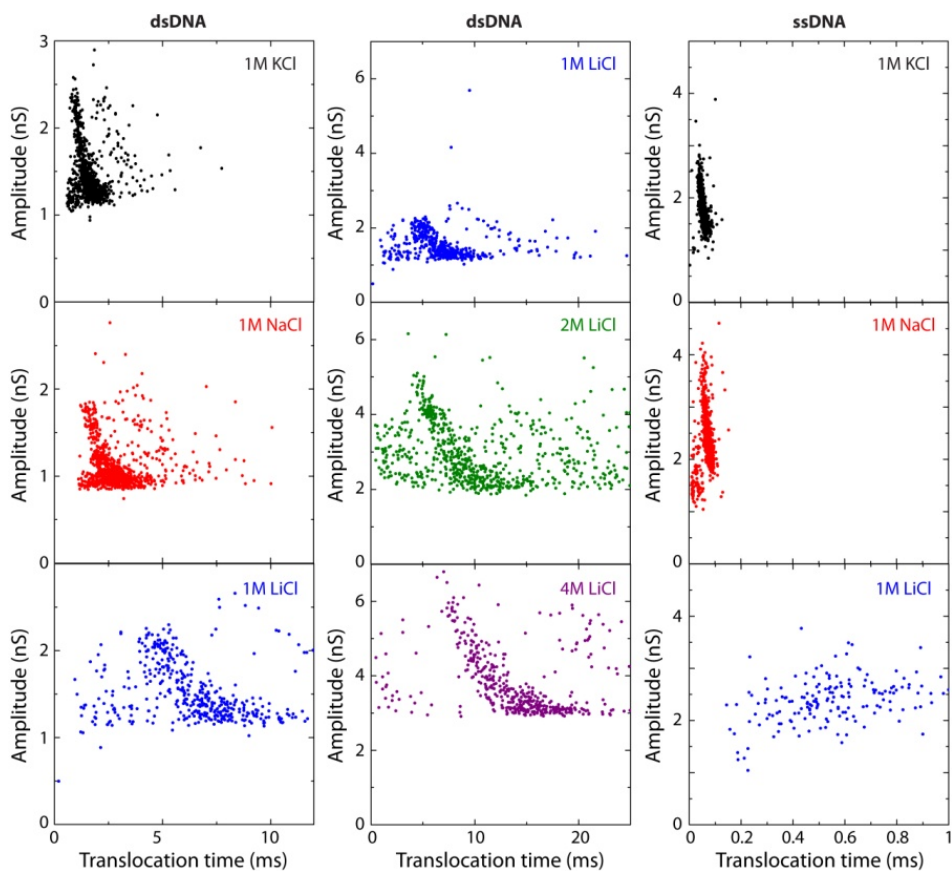


Figure S5.1 Scatter diagrams of current-blockade amplitude versus translocation time for dsDNA and ssDNA at several salt concentrations of KCl, NaCl, LiCl. All data was recorded at 120 mV.

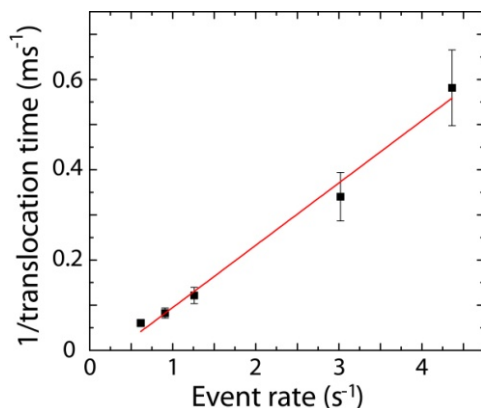


Figure S5.2 Measured inverse translocation time versus number of events per second (event rate). The number of events per second is found to scale inversely with the translocation times. λ -DNA concentration used was 10 ng/ μ l. The data was taken at 120 mV in (in order from low to high event rate) 4M LiCl, 2M LiCl, 1M LiCl, 1M NaCl, 1M KCl.

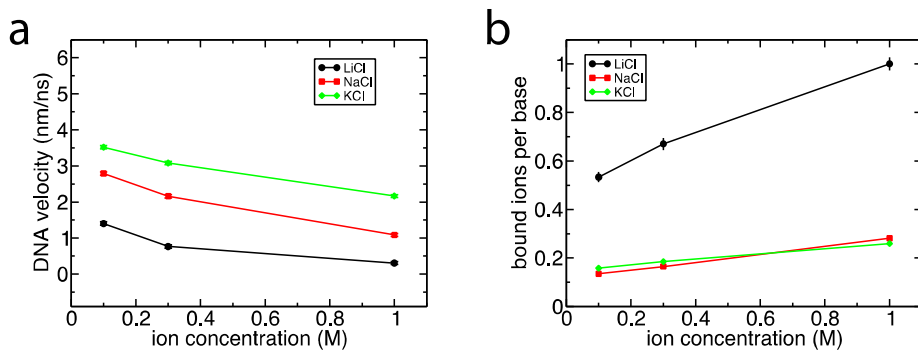


Figure S5.3 MD results for a 4.4 nm wide nanopore, for LiCl (black circles), NaCl (red squares), and KCl (green diamonds). Plots show the DNA velocity (a) and the average number of bound ions per base (b) for different salt concentrations.

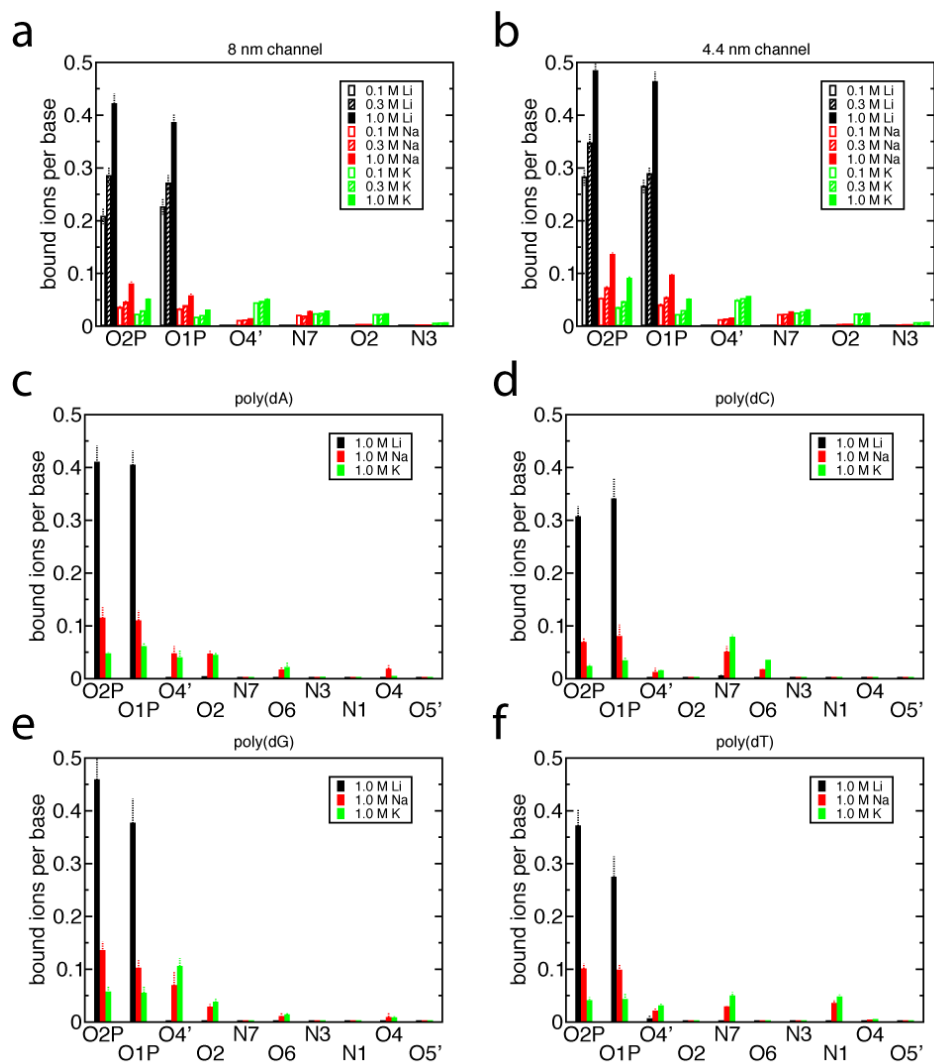


Figure S5.4 Ion binding locations on DNA. Plots show the average number of ions per base bound to a specific DNA atom. DNA atom names are given on the x-axes, and are from the CHARMM force field [S4]. The most prevalent binding locations are seen to be O1P and O2P, the phosphate oxygens, especially in the case of lithium. Binding data is given for the 8 nm (a) and 4.4 nm (b) nanopores containing dsDNA, and for the 8 nm nanopore containing ssDNA (c–f).

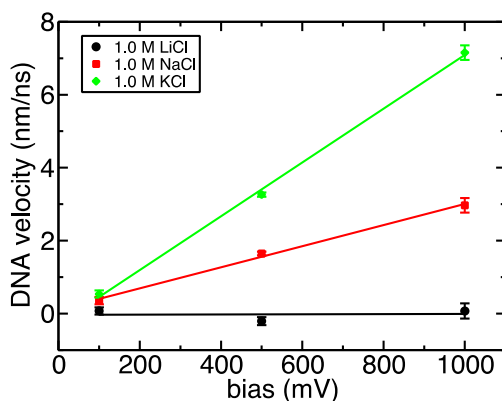


Figure S5.5 Voltage dependence of DNA velocity in MD simulations. The velocity is seen to scale linearly with applied voltage as seen in experiment, see Figure 5.3d in the main text. Systems containing an 8 nm nanopore were used for these simulations.

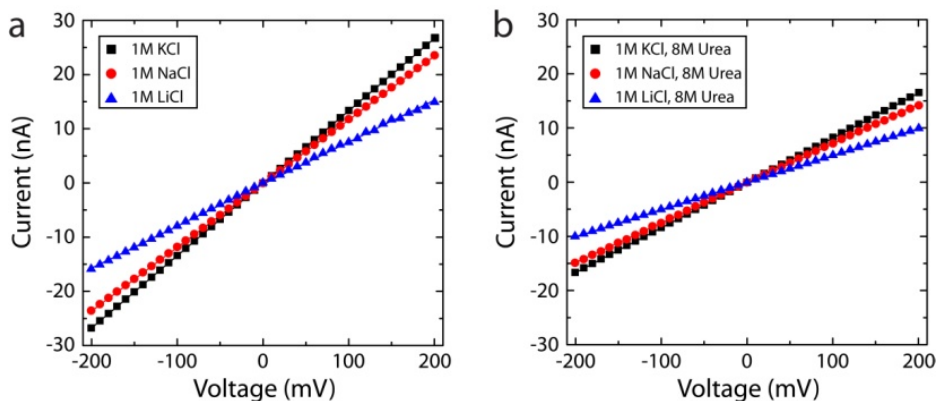


Figure S5.6 (a) Measured current-voltage curves for 1M KCl, 1M NaCl, and 1M LiCl. (b) The same with additional 8M Urea, resulting in a reduction of ~40% of the open-pore current.

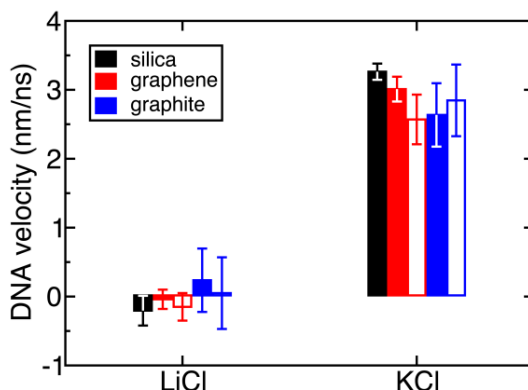


Figure S5.7 MD simulation result for the DNA velocity through a 8-nm-diameter silica nanopores (black bars) at 1.0 M LiCl and 1.0 M KCl compared to DNA velocity through 8-nm-diameter monolayer graphene (red bars) and multilayer graphene (blue bars) nanopores. Open bars indicate results of the simulations where DNA was not restrained to the pore center. Graphite systems were produced by replacing the silica of the original system with nine layers of graphite. Hexagonal periodic boundary conditions were used in the xy plane to accommodate the bonding of the graphite sheets. Monolayer graphene systems were produced by removing all but one carbon layer of the graphite system, and adding more solvent to achieve the correct water density.

SI References

- S1. Storm AJ, *et al.* Fast DNA translocation through a solid-state nanopore. *Nano Lett* **5**, 1193-1197 (2005).
- S2. Gonzalez MA and Abascal JLF The shear viscosity of rigid watermodels. *J Chem Phys* **132**, 096101 (2010).
- S3. Meller A, Nivon L, Branton D Voltage-driven DNA translocations through a nanopore. *Phys Rev Lett* **86**, 3435-3438 (2001).
- S4. MacKerell AD Jr, *et al.* All-atom empirical potential for molecular modeling and dynamics studies of proteins. *J Phys Chem B* **102**, 3586-3616 (1998).

Chapter 6

Unraveling single-stranded DNA in a solid-state nanopore

Solid-state nanopores are an emerging class of single-molecule sensors. Whereas most studies so far focused on double-stranded DNA (dsDNA) molecules, exploration of single-stranded DNA (ssDNA) is of great interest as well, for example to employ such a nanopore device to read out the sequence. Here, we study the translocation of long random-sequence ssDNA through nanopores. Using atomic force microscopy, we observe the ssDNA to hybridize into a random coil, forming blobs of around 100 nm in diameter for 7 kb ssDNA. These large entangled structures have to unravel, when they arrive at the pore entrance. Indeed, we observe strong blockade events with a translocation time that is exponentially dependent on voltage, $\tau \sim e^{-V/V_0}$. Interestingly, this is very different than for dsDNA, for which $\tau \sim 1/V$. We report translocations of ssDNA but also of ssDNA-dsDNA constructs where we compare the conductance-blockade levels for ssDNA versus dsDNA as a function of voltage.

This chapter has been published as S.W. Kowalczyk, M.W. Tuijtel, S.P. Donkers, and C. Dekker, *Nano Letters* **10** (4), 1414–1420 (2010).

6.1 Introduction

Solid-state nanopores [1, 2] have proven to be an interesting new class of devices to characterize biopolymers such as DNA [3, 4], RNA [5], as well as DNA/protein [6, 7] and DNA/ligand [8] complexes at the single-molecule level. The basic principle is simple: when a molecule is driven through a nanopore by an externally applied electric field, it causes a characteristic temporary change in the trans-pore current, allowing one to scan the molecule along its length. Both biological and solid-state nanopores have been proposed as candidates for sequencing applications [9–11]. While many beautiful single-molecule results have been reported for α -hemolysin [12–16], the instability issues of the lipid bilayers in which these α -hemolysin pores are inserted, remain a challenge. Solid-state nanopores do not suffer from such instabilities and allow flexibility in pore size and shape. Here, we demonstrate, for the first time, the translocation of long random-sequence single-stranded DNA through solid-state nanopores at neutral pH. These ssDNA molecules hybridize in a complicated three-dimensional entangled structure through local hybridization at many hundreds of spots, or so-called nuclei, see for example [17]. This yields a highly connected structure that needs to unravel to fit through the nanopore.

While many experiments on double-stranded molecules have been performed in solid-state nanopores, the single-stranded arena is much less explored. Double-stranded DNA that was denatured at very high pH (~ 12) could be studied [18], and recently single-stranded homopolymers poly(A), poly(U), and poly(C) were translocated through solid-state nanopores [5]. Refs. 19 and 20 studied translocation of short ssDNA with a single hairpin. We take two approaches to address long heterosequence single-stranded DNA at neutral pH. First, we construct long single-stranded tails of different lengths on double-stranded DNA, using an Exonuclease III enzyme [21, 22]. This enables us to study the pore entrance dynamics of single-stranded versus double-stranded DNA. We find that the double-stranded DNA enters the pore much more easily than the single-stranded DNA. Secondly, we study the translocation of the single-stranded viral DNA M13mp18 that was isolated from a phage vector, and we compare the results to those obtained with our hybrid ds/ss-molecules. Both types of molecules are also studied by atomic force microscopy (AFM). This provides the typical length scales of the single-stranded DNA, which has a complex secondary structure due to hybridization. The ssDNA blobs give rise to large current blockades. We find a marked increase in the amplitude of the blockage current during translocation with increasing driving voltages. This suggests that the

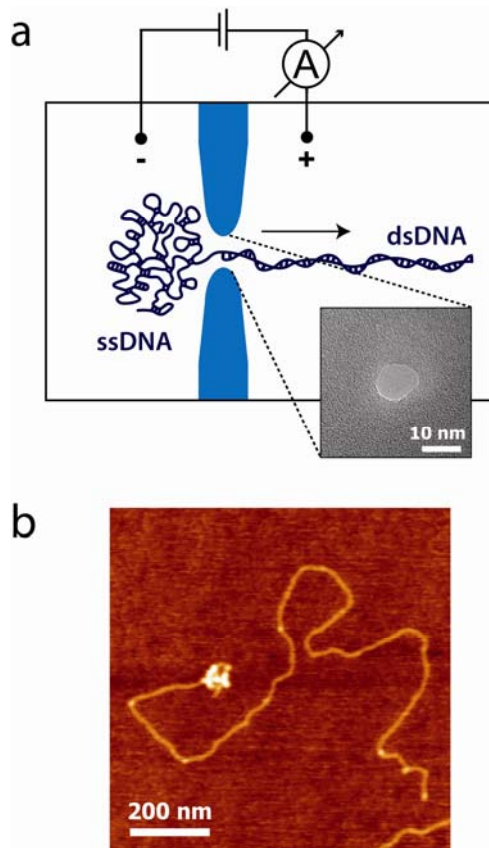


Figure 6.1 (a) Cartoon showing a partly double-stranded and partly single-stranded DNA molecule which is translocated through a nanopore. Intramolecular hybridization causes the single-stranded DNA to have a complex secondary structure which partly has to unravel in order to fit through the pore. Inset: TEM image of a solid-state nanopore. (b) Atomic force microscope (AFM) image showing a partly double-stranded (the main part) and partly single-stranded (the white blob on the left end of the molecule) DNA molecule that was constructed from double-stranded DNA using ExonucleaseIII.

single-stranded DNA is pushed closer to the nanopore at higher voltages, thereby increasingly blocking the ion transport through the pore. A higher applied voltage thus results in a larger access resistance. Furthermore, we demonstrate that the translocation time for single-stranded DNA scales exponentially with voltage, $\tau \sim e^{-V/V_0}$. This can be modeled by a barrier-lowering process, very different than for double-stranded DNA, for which $\tau \sim 1/V$ (cf. Ref. 7 for example).

Figure 6.1a sketches the idea of the experiment, depicting a double-stranded DNA molecule with a single-stranded DNA tail. The long dsDNA is captured into the pore and moves to the right, thus applying a force to the hybridized ssDNA blob which subsequently unravels and translocates as well. The experimental setup has been described in detail previously [23]. Briefly, a single nanopore is fabricated in a 20 nm thick, low-stress silicon nitride (SiN) membrane using the focused electron beam of a transmission electron microscope (TEM). The inset of Figure 6.1 shows a TEM image of a pore that is 9.6 nm in diameter. In this work, we used nanopores of 6.7 – 9.6 nm in diameter. The membrane is placed between two compartments filled with a monovalent salt solution (1 M KCl) and buffer (10mM Tris-HCL, pH = 8.0 and 1mM EDTA). Application of an electric field across the membrane results in an ionic current through the pore, which is temporarily reduced if a molecule passes.

6.2 Creation of hybrid ssDNA-dsDNA molecules

To investigate the translocation and nanopore entrance dynamics of single-stranded versus double-stranded DNA, we constructed long single-stranded tails on double-stranded DNA. Using an Exonuclease III enzyme [21], we created single-stranded overhangs of three different lengths (3.7 kb, 1.9 kb, and 0.7 kb). Figure 6.2a shows a schematic of the protocol. First, circular 10.7 kb double-stranded DNA is cut with endonuclease *Acc65I* to create linear dsDNA (*step 1* in Figure 6.2a). This results in 5'-protruding ends on both sides of the DNA molecule, which are unprotected against *ExoIII*. In *step 2*, the ends are filled in with dNTP α S-nucleotides using Klenow, creating protective blunt ends. Subsequently, a nick is made in the backbone of the DNA-construct using the *Nb.BbvCI* enzyme (*step 3*). Finally, the *ExoIII* enzyme stepwise removes the nucleotides from the nicking site in 3' to the 5' direction (*step 4*). After this step, some purification and precipitation steps are carried out to purify the construct (*step 5*). A detailed description of the protocol is found in the methods section.

We study the structure of the molecules using both atomic force microscopy (AFM) and gel electrophoresis. Figure 6.1b shows an AFM image that displays a molecule with both a single-stranded (flexible) and double-stranded DNA (stiff) part. The single-stranded DNA is highly curled because it has only one backbone with a persistence length of ~ 1 nm, significantly smaller than the 50 nm value for dsDNA. Furthermore, the random coil of ssDNA will hybridize to itself. From the AFM data, we found the yield of the desired intact ssDNA-dsDNA construct to be around 84%

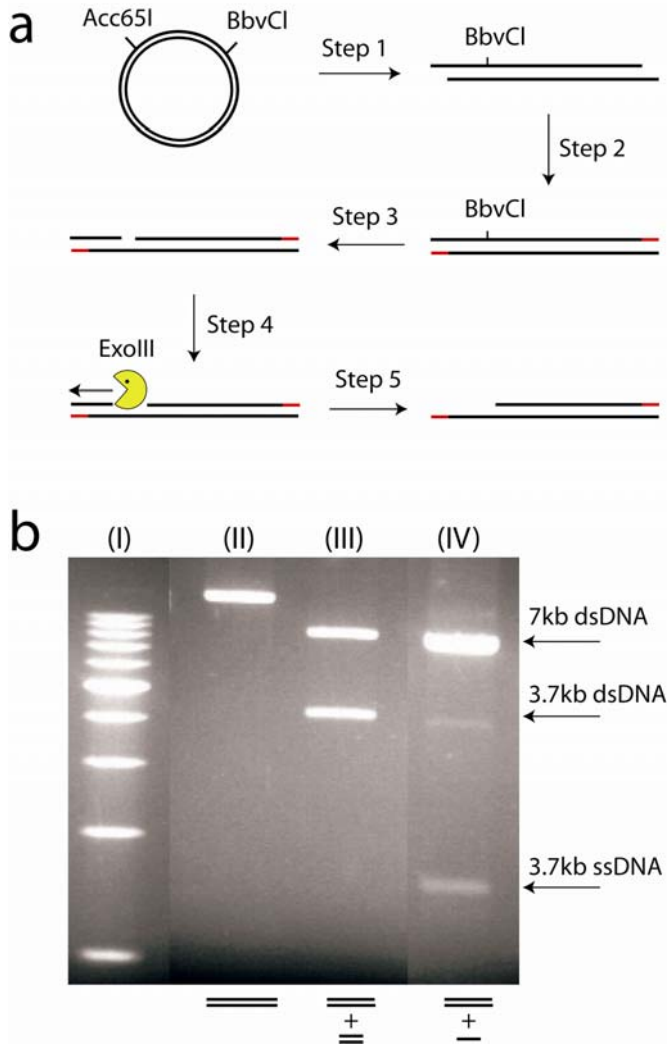


Figure 6.2 (a) Protocol to create double-stranded DNA with a single-stranded tail (details in methods section). (b) Agarose gel, showing: (I) 1-10 kb dsDNA step ladder, (II) linearized 10.7 kb dsDNA, (III) linearized 10.7 kb dsDNA cut with *EcoRI*, giving bands at 3.7 kb and at 7 kb, (IV) linearized 10.7 kb dsDNA cut with *EcoRI* after creation of the hybrid DNA. The band at 3.7 kb dsDNA has disappeared, while another band appears near the 1.8 kb dsDNA position. Since ssDNA migrates roughly twice faster than dsDNA, this band is indicative of a ssDNA fragment with a length of about 3.7 kb.

($n = 50$). The remaining part seems to have been broken right at or near the junction, which may be due to the deposition of the molecules onto the mica or the purification. For the intact molecules, we measured the lengths of the dsDNA parts of the molecules from the AFM images. We find an average length of 6.6 ± 0.7 kb for the dsDNA, in good agreement with the expected length of $10.7 - 3.7$ kb = 7.0 kb (see Figure S6.2). From the worm-like-chain (WLC) model, generally used for dsDNA (24-27), we find a radius of gyration of $R_g = 840$ nm for this 7 kb dsDNA (see Supporting Information). From AFM image analysis, we estimate the size of the ssDNA coil as well. Taking the average of the major and minor axes of an ellipse fit to the image of the ssDNA, we find an approximate size of 63 ± 4 nm for 3.7 kb ssDNA ($n = 8$). Following Ref. 28, which studied the relation between DNA coil size in solution connected to that as imaged by AFM on mica and other substrates (see also Supporting Information), this give an estimated blob diameter in solution of 45 ± 3 nm. Based on the freely jointed chain (FJC) model, which is generally used for ssDNA [24-27], we estimate a diameter of 80 nm for this length ssDNA (see Supporting Information), i.e., a fairly similar size. Note that this model is not taking into account intramolecular hybridization. The effect of hybridization on coil size is a priori not clear because there are two competing effects. Hybridization will make local connections that will compact the blob. However, locally hybridized structures have a much higher stiffness due to the 50-fold increased persistence length of the hybridized ssDNA (dsDNA) over ssDNA, which will tend to increase the blob size.

Additionally, we performed a gel analysis of these ds-ssDNA constructs, as presented in Figure 6.2c. Lane I is a 1-10 kb dsDNA step ladder. Lane II shows the linearized 10.7 kb dsDNA. This DNA is cut right at the junction using EcoRI both before (lane III) and after (lane IV) creation of the hybrid construct. As expected, lane III shows two double-stranded DNA pieces, one at around 7 kbp and one at around 3.7 kbp. When the DNA is cut after creation of the hybrid ds-ssDNA (lane IV), we see that the band at 3.7 kb has disappeared, while another band appears near the 1.8 kb dsDNA position, indicative of a ssDNA fragment with a length of 3.7 kb.

6.3 Nanopore data on hybrid ssDNA-dsDNA molecules

Next we turn to the nanopore data. We successfully translocated the hybrid ss/ds-DNA constructs through solid-state nanopores with a diameter of about 8 nm. Figure 6.3a shows an example of a time trace of the ionic current through the pore without DNA in the flow cell. A stable baseline is observed, with no spikes in the current.

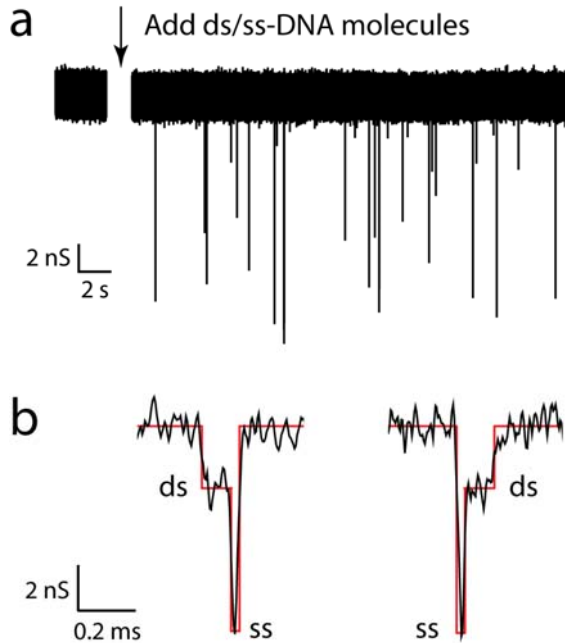


Figure 6.3 (a) Ionic current versus time at an applied voltage of 240 mV. Upon addition of ds/ss-DNA molecules downward spikes appear in the current. The data is recorded at 100 kHz bandwidth and is not filtered additionally. (b) Example traces for translocating ds/ss-DNA molecules. Each translocation event shows two levels, one associated with the dsDNA part, and one with the ssDNA part. We find that in about 80% of the events, the dsDNA enters the pore first, i.e., events show the behavior of the trace on the left. The two example traces shown were recorded at 240 mV and filtered at 5 kHz for clarity.

After addition of the ss/ds-DNA construct (indicated by the arrow), spikes are observed in the current trace. We zoom in on two example events in Figure 6.3b. Two blockade levels can be distinguished. We attribute the lower blockade level to dsDNA and the higher blockade level to ssDNA, based on the following. From a large number of such ‘events’ (defined as such a current spike including the current signal 2 ms before and after the event), we can make a conductance histogram as displayed in Figure 6.4a. A scatter plot of dwell time versus amplitude is presented in the Supporting Information. Next to the base current peak at zero conductance blockade, two peaks are observed near 2 nS and 8 nS. Comparison with extensively reported previous data for dsDNA translocation experiments (e.g., Ref. 4) where blockade

values of $\sim 1 - 2$ nS were found, argues that the lower blockade level at around 2 nS is caused by the dsDNA part of the ss/ds-DNA molecules. We subsequently identify the other peak near 8 nS with the ssDNA part of the molecules.

We thus find that the single-stranded DNA induced a very large blockade. This might be surprising in the light of Ref. 5, where a *smaller* blockade level of ~ 1 nS was found for single-stranded RNA. However, those data were obtained for ssRNA *homopolymers* such as poly(A), which cannot hybridize since there are no complementary bases available within the molecule. In the current work, however, the ssDNA is a heteropolymer with a random sequence with all nucleotides present, which results in intramolecular hybridization at hundreds of spots, see [17] and Refs. 1-5 therein. This yields a highly connected structure that needs to unravel into much smaller local structures that can each fit through the 8 nm pore in order to translocate the whole construct in a linear fashion. Our nanopores have the shape of an hourglass, and the ssDNA blob will be forced partly into the pore – to the extent allowed by the topology of the interconnected DNA blob – as well as be pressed closely unto the pore entrance due to the electrostatic forces on all DNA segments. This leads to a highly increased conductance blockade. It is interesting to observe that the partial unraveling of the hybridized ssDNA blob indeed occurs under the experimental conditions used, viz. with an applied voltage of ~ 100 mV which corresponds to forces of tens of pN [29]. Threshold values to mechanically separate two complementary strands of dsDNA have both experimentally [30, 31] and theoretically [32] been found to be in the range of approximately 9 - 20 pN, in accordance with the data presented here.

The voltage dependence of the conductance blockade provides an interesting handle to further distinguish dsDNA and ssDNA. As can be seen from Figure 6.4b, we find a constant value for the blockade level for dsDNA (2.0 nS) versus voltage, but a highly voltage-dependent value for the blockade level (~ 6 nS – 15 nS) for ssDNA. Interestingly, this result appears to be independent of the length of the ssDNA as the data obtained for different lengths (0.7 – 3.7 kb) overlap. At higher voltages, dsDNA and ssDNA can be very clearly discriminated. The voltage dependence of the ssDNA blockade level can be understood by considering the access resistance [33]: at higher voltages the ssDNA blob (which does not fit through the pore without unraveling) is pushed closer to the pore due to the larger electrophoretic forces, thereby increasing the access resistance. We empirically find a dependence $\Delta G = aV^b$, with $a = 2.0 \pm 0.3$ nS and $b = 0.37 \pm 0.03$, where V is the applied voltage in mV, independent on the length of the ssDNA within the range probed (0.7 – 3.7 kb).

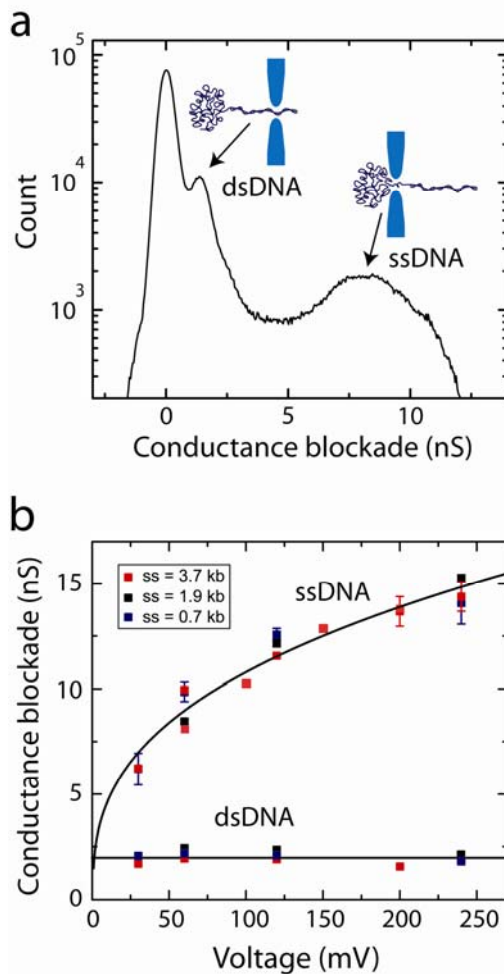


Figure 6.4 (a) Conductance blockade histogram for hybrid 7 kb-dsDNA/ 3.7 kb-ssDNA at 60 mV. Two peaks are visible. We attribute the lower peak to the dsDNA part, and the higher peak to the ssDNA part. (b) Conductance blockade versus applied voltage, for both the double-stranded DNA and single-stranded DNA pieced of hybrid ds/ss DNA molecules for three different lengths of ssDNA (0.7, 1.9, and 3.7 kb). The data show an approximately constant blockade level for dsDNA (2.0 ± 0.3 nS), and a large, voltage-dependent blockade level (~ 6 nS – 15 nS) for ssDNA. The solid lines are fits to the data. For ssDNA we find $\Delta G = aV^b$, with $a = 2.0 \pm 0.3$ nS and $b = 0.37 \pm 0.03$, with V the voltage in mV. The ssDNA conductance blockade value is, within experimental error, not dependent on the length of the single-stranded part.

For each translocation event of the ssDNA-dsDNA construct, we determined whether the ssDNA or the dsDNA part entered the pore first. We find that the dsDNA entered the pore first in 80% of the events ($N = 11,166$), only then followed by the ssDNA part. In 20% of the events the ssDNA entered first. As an additional experiment, we cut the ssDNA-dsDNA construct right at the junction, using the EcoRI restriction enzyme. We then translocated this mixture of both ssDNA and dsDNA (not attached to each other; see Figure S6.3 for an AFM image), and compared the number of events of dsDNA translocation and ssDNA translocation. This gives similar numbers: 79% of the events are dsDNA translocations; 21% are ssDNA translocations ($N = 487$). The dsDNA is thus more effective in getting to the pore entrance than ssDNA. While a detailed and quantitative model is lacking at this point, we suggest that the difference in captures rates can be explained simply by the fact that dsDNA has a larger hydrodynamic radius than the ssDNA and thus a larger probability of approaching and entering the pore first.

6.4 Nanopore data on single-stranded DNA

Additionally, we studied translocation of single-stranded viral DNA isolated from M13mp18 (New England Biolabs). The ssDNA of this M13 lac phage vector is circular and 7.2 kb in length, and has no dsDNA attached to it. AFM imaging of this ssDNA again reveals blob-like structures (see Figure 6.5a) and taking the average of the minor and major axes of an ellipse fit to the the ssDNA images gives a typical diameter of 147 ± 6 nm ($n = 7$). Following [28], this gives an estimated typical diameter in solution of 104 ± 4 nm (see also Supporting Information). Based on the FJC model (thus neglecting intramolecular hybridization) and taking into account that theoretically [34] the relation between circular and linear DNA blob size is given by $\langle R_g^2 \rangle_{\text{circular}} = \langle R_g^2 \rangle_{\text{linear}}/2$, we estimate a diameter of gyration of 78 nm for this ssDNA, i.e., similar to the size as obtained from the AFM data.

Upon translocating the M13mp18 ssDNA through a solid-state nanopore of 7.0 nm in diameter, we observe large peaks with well-defined amplitudes (Figure 6.5b). Again, the peaks are much larger (about ten-fold) than expected from volume exclusion of one strand of ssDNA. The conductance histogram in Figure 6.5c shows only one peak, at around 11 nS, next to the base current peak at zero conductance blockade. Compared to the ssDNA-dsDNA (Figure 6.4a), the peak at around 2 nS is absent. This confirms our claim that the latter peak is caused by dsDNA and that the high-conductance peak is due to ssDNA. The inset of Figure 6.5d shows the voltage

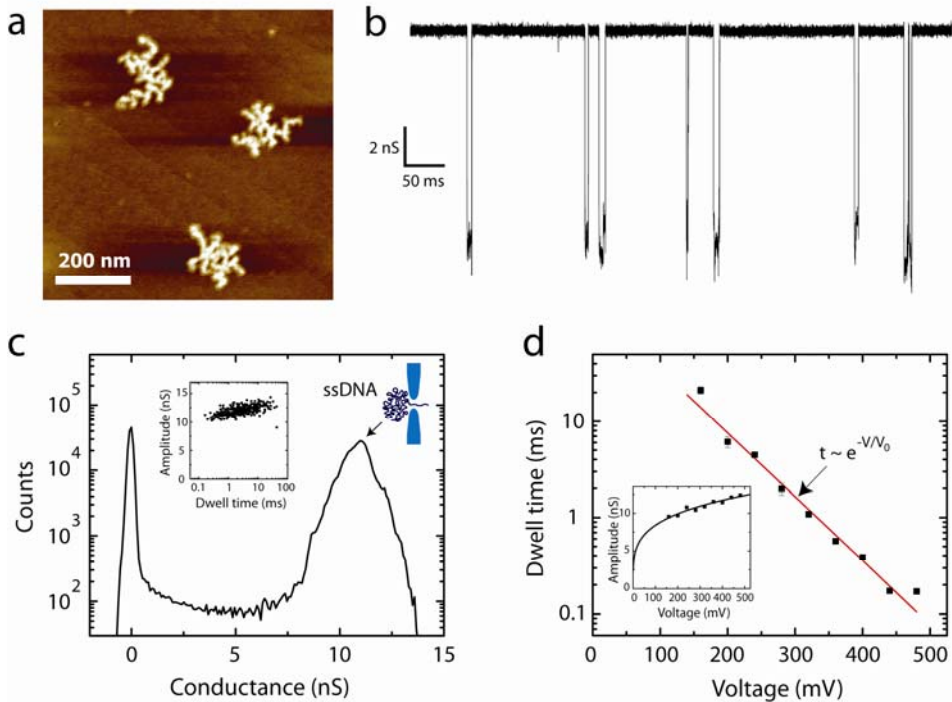


Figure 6.5 (a) AFM image of 7.2 kb M13mp18 ssDNA. Structures of around 150 nm in diameter can be seen to form due to hybridization. (b) Ionic current versus time after addition of this ssDNA at an applied voltage of 240 mV. (c) Conductance histogram, taken at 240 mV. The ssDNA gives a large peak at around 11 nS. Notice that a dsDNA peak is absent. The inset shows a scatter plot at 240 mV. The typical dwell time can be fitted with a log-normal distribution. (d) Dwell time versus voltage for the same ssDNA. We find an exponential voltage dependence. The line is an exponential fit to the data: $\tau = Ae^{-V/V_0}$, where $A = 160 \pm 13$ ms, and $V_0 = 66 \pm 1$ mV. The inset shows ΔG as a function of voltage. The solid line is a fit to the data, with $\Delta G = aV^b$, where $a = 2.8 \pm 0.4$ nS and $b = 0.24 \pm 0.03$, with V the applied voltage in mV.

dependence of the ssDNA peak for M13mp18 ssDNA. Again, we find that increased voltage leads to higher blockade values.

It is interesting to see how the dwell times for M13mp18 ssDNA, which can be viewed as the unraveling times, depend on voltage. At each applied voltage, we fit a log-normal distribution to the translocation times (cf. inset to Figure 6.5c), which yield a typical translocation time at that voltage. The voltage dependence of this dwell

time is displayed in Figure 6.5d. Notably, we find that the ssDNA dwell time depends exponentially on applied voltage, $\tau \sim e^{-V/V_0}$. This is in contrast with what was found for dsDNA, namely $\tau \sim 1/V$ (cf. Ref 7). Clearly the physics in both cases is different: in the case of dsDNA, the DNA is simply threaded through the pore, and a larger voltage results in a larger force on the molecule and therefore to a proportionally shorter translocation time. In the case of ssDNA, however, the polymer does not fit through the pore and has to unravel. Presumably in this case, many hydrogen bonds formed during hybridization need to be broken, leading to a large barrier for the molecules to pass through the pore. Apparently the complex unraveling process can be modelled as a barrier-lowering process, $\tau \sim e^{-V/V_0}$, if driven by a force due to an externally applied voltage.

Summing up, with these translocation measurements of both viral single-stranded DNA as well as ssDNA-dsDNA constructs, we have explored the distinct behavior of random sequence single-stranded DNA molecules in solid-state nanopores. Surprisingly, we find larger current blockades for ssDNA than for dsDNA, which we account for by an increased resistance due to a large random-coiled blob of hybridized ssDNA at the pore entrance. This blob has to unzip in order to pass through the pore. We find characteristic ssDNA unzipping times at a range of voltages (forces), as well as an exponential dependence on voltage, which is a much stronger dependence than for dsDNA. These findings may be beneficial for nanopore sequencing of ssDNA.

6.5 Materials and Methods

Method for making ss/dsDNA molecules

For the construction of single-stranded tails on double-stranded DNA, we developed an enzymatic assay using the 3' to 5' exonuclease activity of *ExoIII* [21]. This enzyme can initiate on nicks within the DNA, on 3' recessed ends, blunt ends, and some 3' protruding ends [22]. In this work, a unique nicking site in the DNA is used for *ExoIII* initiation. The DNA ends are protected with special nucleotides that block the initiation of the exonuclease to establish a controlled process with fixed size of the single-stranded tail. The example discussed here, is to make a 7 kb double-stranded fragment with a 3' protruding single strand tail of 3.7 kb. For this and other fragments made, a 10.7 kb vector is used as starting molecule. This vector has a unique *BbvCI* nicking site for *ExoIII* initiation. First, the vector is linearized with *Acc65I* to create 5' protruding ends. We then heat inactivated the *Acc65I*, keeping it for 20 minutes at 65°C. The ends are then filled-in with modified alpha-thio deoxynucleotides (Jena

Bioscience) using exo- Klenow (New England Biolabs) at 37°C for 25 minutes. These nucleotides protect the ends for exonuclease initiation by ExoIII [22]. The restriction and Klenow reactions are performed in NEB3 buffer (New England Biolabs). We then purify using silica membrane columns NucleoSpin Extract II (Macherey Nagel) to change buffers. Subsequently, we nick one strand of the double-stranded molecule with *Nb.BbvCI* in NEB2 and purify again using silica membrane columns to exchange buffers to NEB1 for the ExoIII reaction. We then determine the concentration of the DNA and use 10 units *ExoIII*/μg DNA in NEB1 buffer and incubate for 1 hour at 37°C. Longer incubation times can result in non-specific exonuclease activity. The DNA is now purified using ethanol precipitation (silica membrane columns could break the single-stranded tails). We found that the processing time is crucial for a successful assay. The various steps are preferably done one right after the other and performed on freshly isolated vector DNA or DNA that is stored in ethanol. Any damage (nicks) on the DNA will result in initiation start sites for *ExoIII* on non-specific locations on the DNA. Variations in length of the single-stranded tail and the size of the double-stranded DNA are controlled by the choice of endonucleases used to linearize the vector. Besides the described 3.7 kb ssDNA fragment, two other fragments were made: using endonuclease *XhoI*, we created a single-stranded tail of 1944 bp and a double-stranded part of 8.7 kb; using endonuclease *AscI*, we made a 720 bp single-stranded tail and a double-stranded part of 9.9 kb. Interestingly, variations like dsDNA-ssDNA-dsDNA, or ssDNA-dsDNA-ssDNA are also possible by choosing different nicking and/or cleavage sites (see Supporting Information).

Solid-state nanopores and AFM imaging

Solid-state nanopore fabrication starts with the production of 20 nm thin, free-standing SiN membranes through the use of electron-beam lithography and wet etching. In each such membrane, we drill a nanopore of the desired size through the use of a highly focused electron beam in a transmission electron microscope (TEM). Details of the fabrication process are described elsewhere [23]. In this study, we used nanopores of 6.7 – 9.6 nm in diameter. Directly after drilling, the pores are stored in a solution containing 50% ethanol and 50% ddH₂O. Prior to use, the nanopores are treated in an oxygen plasma for 30 s on both sides. Subsequently, the nanopores are mounted in a polyether ether ketone (PEEK) microfluidic flow cell and sealed to liquid compartments on either side of the sample. Measurements are performed in 1 M KCl salt solution containing 10 mM Tris-HCl and 1mM EDTA at pH 8.0 at room

temperature. The high salt is chosen for increased signal-to-noise in the nanopore current signals. Ag/AgCl electrodes are used to detect ionic currents and to apply electric fields. Current traces are measured at 100 kHz bandwidth using a resistive feedback amplifier (Axopatch 200B, Axon Instruments), and digitalized at 500 kHz. When necessary, low-pass filtering is applied. Only pores with minimal low-frequency current noise (<20 pA RMS) are used [35]. Tapping-mode atomic force microscopy (AFM) images (Nanoscope IIIa, Digital Instruments, Santa Barbara, CA) were made in air after depositing the DNA molecules in a 20mM Tris-HCl pH 8.0 and 10mM MgCl₂ buffer on freshly cleaved mica. DNA molecules were tracked using the tracking function in the WSxM software for AFM data analysis.

Acknowledgements. We thank N. H. Dekker, A. R. Hall, M. van den Hout, G. M. Skinner, G. Schneider, M. Y. Wu, and V. Svechnikov for contributions and discussions. This work is supported by the NanoSci-E+ programme and a NWO Spinoza award.

References

- 1 Dekker, C., Solid-state nanopores. *Nat Nanotech* **2**, 209–215 (2007).
 - 2 Howorka, S. and Siwy, Z., Nanopore analytics: sensing of single molecules. *Chemical Society Reviews* **38**, 2360–2384 (2009).
 - 3 Li, J. L., Gershow, M., Stein, D., Brandin, E. and Golovchenko, J. A., DNA molecules and configurations in a solid-state nanopore microscope. *Nat Mater* **2**, 611–615 (2003).
 - 4 Storm, A. J., *et al.*, Fast DNA translocation through a solid-state nanopore. *Nano Letters* **5**, 1193–1197 (2005).
 - 5 Skinner, G. M., van den Hout, M., Broekmans, O., Dekker C. and Dekker, N.H., Distinguishing single- and double-stranded nucleic acid molecules using solid-state nanopores. *Nano Letters* **9**, 2953–2960 (2009).
 - 6 Smeets, R. M. M., Kowalczyk, S. W., Hall, A. R., Dekker, N. H. and Dekker, C., Translocation of RecA-coated double-stranded DNA through solid-state nanopores. *Nano Letters*, **9**, 3089–3095 (2009).
 - 7 Kowalczyk, S. W., Hall, A. R. and Dekker, C., Detection of local protein structures along DNA using solid-state nanopores. *Nano Letters* **10**, 324–328 (2010).
-

- 8 Wanunu, M., Sutin, J. and Meller, A., DNA profiling using solid-state nanopores: detection of DNA-binding molecules. *Nano Letters* **9**, 3498–3502 (2009).
 - 9 Soni, G.V., and Meller, A., Progress toward ultrafast DNA sequencing using solid-state nanopores. *Clinical Chemistry* **53**, 1996–2001 (2007).
 - 10 Branton, D., *et al.*, The potential and challenges of nanopore sequencing. *Nat Biotech* **26**, 1146–1153 (2008).
 - 11 Clarke, J., Wu, H.-C., Jayasinghe, L., Patel, A., Reid, S. and Bayley, H., Continuous base identification for single-molecule nanopore DNA sequencing. *Nat Nanotech* **4**, 265–270 (2009).
 - 12 Kasianowicz, J. J., Brandin, E., Branton, D. and Deamer, D. W., Characterization of individual polynucleotide molecules using a membrane channel. *Proc. Natl Acad. Sci. USA* **93**, 13770–13773 (1996).
 - 13 Akeson, M., Branton, D., Kasianowicz, J. J., Brandin, E. and Deamer, D. W., Microsecond time-scale discrimination among polycytidylic acid, polyadenylic acid, and polyuridylic acid as homopolymers or as segments within single RNA molecules. *Biophys. J.* **77**, 3227–3233 (1999).
 - 14 Meller, A., Nivon, L., Brandin, E., Golovchenko, J. and Branton, D., Rapid nanopore discrimination between single polynucleotide molecules. *Proc. Natl. Acad. Sci. USA* **97**, 1079–1084 (2000).
 - 15 Meller, A., Nivon, L. and Branton, D., Voltage-driven DNA translocations through a nanopore. *Phys. Rev. Lett.* **86**, 3435–3438 (2001).
 - 16 Stoddart, D., Heron, A. J., Mikhailova, E., Maglia, G. and Bayley, H., Single nucleotide discrimination in immobilized DNA oligonucleotides with a biological nanopore. *Proc. Natl Acad. Sci. USA*. **106**, 7702–7707 (2009).
 - 17 Chen, C. L., Wang, W. J., Wang, Z., Wei, F. and Zhao, X. S., Influence of secondary structure on kinetics and reaction mechanism of DNA hybridization. *Nucleic Acids Research* **35**, 2875–2884 (2007).
 - 18 Fologea, D., *et al.*, Detecting single stranded DNA with a solid state nanopore. *Nano Letters* **5**, 1905–1909 (2005).
 - 19 Zhao, Q., Comer, J., Dimitrov, V., Yemenicioglu, S., Aksimentiev, A. and Timp, G., Stretching and unzipping nucleic acid hairpins using a synthetic nanopore. *Nucleic Acids Research* **36**, 1532–1541 (2008).
 - 20 McNally, B., Wanunu, M. and Meller, A., Electromechanical unzipping of individual DNA molecules using synthetic sub-2 nm pores. *Nano Letter* **8**, 3418–3422 (2008).
-

- 21 Hoheisel, J. D., On the activities of Escherichia-Coli Exonuclease-III. *Analytical Biochemistry* **209**, 238–246 (1993). All enzymes used are from New England Biolabs.
 - 22 Sambrook, J., *et al*, Molecular Cloning: A Laboratory Manual. Chapter 13.72: mutagenesis, 1989.
 - 23 Krapf, D., *et al.*, Fabrication and characterization of nanopore-based electrodes with radii down to 2 nm. *Nano Letters* **6**, 105–109 (2006).
 - 24 Bustamante, C., Smith, S. B., Liphardt, J., Smith, D., Single-molecule studies of DNA mechanics. *Current Opinion in Structural Biology* **10**, 279–285 (2000).
 - 25 Seol, Y., Skinner, G. M., Visscher, K., Elastic properties of a single-stranded charged homopolymeric ribonucleotide. *Phys. Rev. Lett.* **93**, 118102 (2004).
 - 26 Tanaka, F., Introduction to Physical Polymer Science. Shokabo: Tokyo, 1994.
 - 27 Rawat, N., Biswas, P., Size, shape, and flexibility of proteins and DNA. *J. Chem. Phys.* **131**, 165104 (2009).
 - 28 Rivetti, C., Guthold, M. and Bustamante, C., Scanning force microscopy of DNA deposited onto mica: Equilibration versus kinetic trapping studied by statistical polymer chain analysis. *J. Mol. Biol.* **264**, 919–932 (1996).
 - 29 Keyser, U. F., *et al.*, Direct force measurements on DNA in a solid-state nanopore. *Nature Physics*. **2**, 473–477 (2006).
 - 30 Essevaz-Roulet, B., Bockelmann, U., Heslot, F., Mechanical separation of the complementary strands of DNA. *Proc. Natl. Acad. Sci.* **94**, 11935–11940 (1997).
 - 31 Rief, M., Clausen-Schaumann, H., Gaub, H. E., Sequence-dependent mechanics of single DNA molecules. *Nature Structural Biology* **6**, 346–349 (1999).
 - 32 Cocco, S., Monasson, R., Marko, J. F., Force and kinetic barriers to unzipping of the DNA double helix. *Proc. Natl. Acad. Sci.* **98**, 8608–8613 (2001).
 - 33 Aguilera-Arzo, M., Aguilera, V. M., Eisenberg, R. S., Computing numerically the access resistance of a pore. *European Biophysical Journal* **34**, 314–322 (2005).
 - 34 Grosberg, A. and Khokhlov, A., Statistical Physics of Macromolecules. American Institute of Physics, New York, NY, 1994.
 - 35 Smeets, R. M. M., Keyser, U. F., Dekker, N. H., Dekker, C., Noise in solid-state nanopores. *Proc. Natl. Acad. Sci. USA* **105**, 417–421 (2008).
 - 36 Araki, S., Nakai, T., Hizume, K., Takeyasu, K. and Yoshikawa, K., Hydrodynamic radius of circular DNA is larger than that of linear DNA. *Chem. Phys. Lett.* **418**, 255–259 (2006).
-

6.6 Supplementary Information

Estimates of radii of gyration for ssDNA and dsDNA from FJC and WLC models

We estimate the sizes of both ssDNA and dsDNA molecules using the freely joined chain (FJC) model for ssDNA, and the worm like chain (WLC) model for dsDNA [24–27]. For the 3.7 kb ssDNA piece of the hybrid ds-ssDNA molecules, we estimate a diameter of $2R_g = 2b \sqrt{N/6} = 80$ nm using the FJC model, where b the Kuhn length (1.6 nm for ssDNA), and N the number of segments (3678 for our ssDNA). For the 7 kb dsDNA piece of the hybrid molecules, we use the WLC model and estimate a diameter of $2R_g = 2\sqrt{bN} = 1.68$ μm , with b the Kuhn length (100 nm for dsDNA), and N the number of segments (7017 for our dsDNA). For an estimate of the size of the M13mp18 ssDNA we again use the FJC model, where we now take into account that this ssDNA is circular. The radius of gyration for a circular molecule as compared to a linear molecule can be deduced theoretically [34] to be: $\langle R_g^2 \rangle_{\text{circular}} = \langle R_g^2 \rangle_{\text{linear}}/2$. This gives an additional factor of $1/\sqrt{2}$ smaller radius of gyration than for a linear molecule. We thus find a diameter of $2R_g = 2(1/\sqrt{2}) b \sqrt{N/6} = 78$ nm, with b the Kuhn length (1.6 nm for ssDNA), and N the number of segments (7249 for M13mp18 ssDNA). Experimentally, Ref. 36 compared the hydrodynamic radius of circular and linear DNA and found the hydrodynamic radius of linear DNA to be markedly (~25%) smaller than of circular DNA. This experimental result would instead predict a diameter of gyration of 134 nm for the M13mp18 ssDNA, i.e., also close to our AFM result of 104 nm.

Relation between DNA radius of gyration in solution and DNA deposited onto mica

Rivetti *et al.* [28], discuss the process of deposition of DNA molecules onto a mica surface: DNA molecules deposited onto freshly cleaved mica are able to equilibrate on the surface as in an ideal two-dimensional solution. They find the relation between the mean-square end-to-end distances in 2D and 3D to be $\langle R^2 \rangle_{2D} = 2\langle R^2 \rangle_{3D}$. We thus need to correct with a factor of $\sqrt{2}$ when comparing the size of a molecule obtained from an AFM image to that in solution.

Diameters of nanopores used

The effective pore diameters were obtained by tracing the area of the pore TEM image using the data analysis program *ImageJ*. The pores used were 6.7 nm, 7.0 nm,

7.4 nm, 9.3 nm and 9.6 nm in diameter. The ds-ssDNA construct with 3.7 kb ssDNA tail was measured on the 9.6 nm pore; the construct with the 1.9 kb ssDNA tail on the 7.4 nm pore; the construct with the 0.7 kb ssDNA tail on the 9.3 nm pore. The ds-ssDNA construct that was cut with EcoRI was measured on the 6.7 nm pore. The data on the M13mp18 ssDNA was all taken on a 7.0 nm in diameter nanopore.

Supplementary Figures

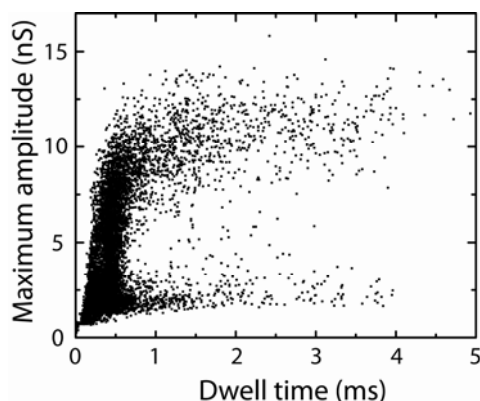


Figure S6.1 Maximum amplitude versus dwell time scatter plot for ssDNA-dsDNA, recorded at 60 mV ($N = 11,166$).

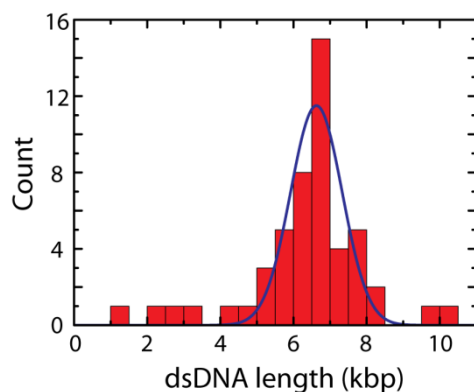


Figure S6.2 For the ssDNA-dsDNA molecules, we measured the lengths of the dsDNA parts using the tracking function in the WSxM software for AFM data analysis. We find an average length of 6.6 ± 0.7 kb for the dsDNA, in good agreement with the expected length of 7.0 kb.

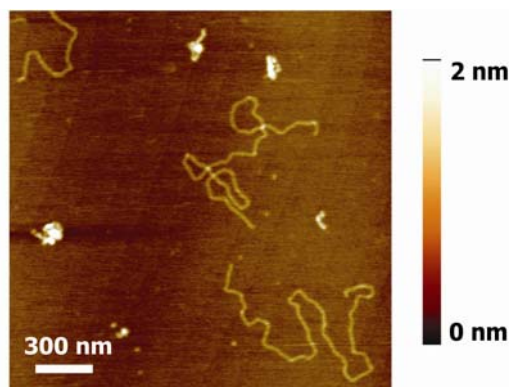


Figure S6.3 AFM image of ssDNA-dsDNA cut with EcoRI. This results in separate fragments of ssDNA (3.7 kb) and dsDNA (7 kb). Height scale ranges from 0 – 2 nm. The height scale in all AFM images in the paper ranges from 0 – 2 nm.

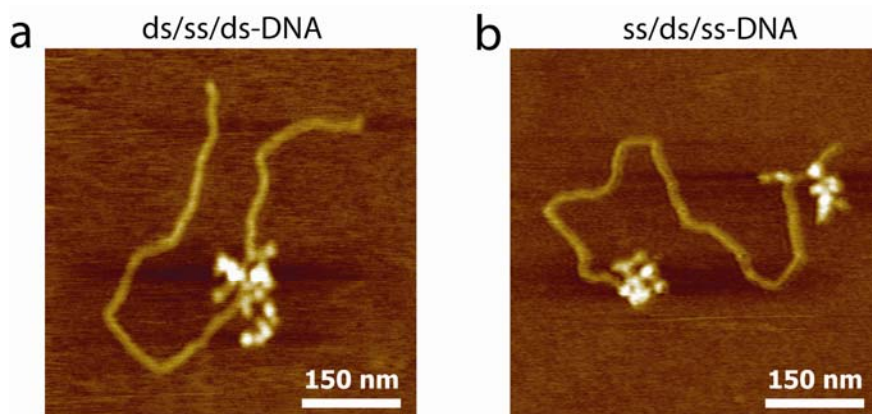


Figure S6.4 AFM images of (a) ds/ss/ds DNA and (b) ss/ds/ss DNA molecules, created with the ExoIII enzyme. By choosing a different nicking enzyme and/or cutting the circular dsDNA open at a different location, a variety of molecules can be constructed.

Chapter 7

DNA translocation through graphene nanopores

Nanopores – nanosized holes that can transport ions and molecules – are very promising devices for genomic screening, in particular DNA sequencing. Solid-state nanopores currently suffer from the drawback, however, that the channel constituting the pore is long, ~100 times the distance between two bases in a DNA molecule (0.5 nm for single-stranded DNA). This paper provides proof of concept that it is possible to realize and use ultrathin nanopores fabricated in graphene monolayers for single-molecule DNA translocation. The pores are obtained by placing a graphene flake over a microsize hole in a silicon nitride membrane and drilling a nanosize hole in the graphene using an electron beam. As individual DNA molecules translocate through the pore, characteristic temporary conductance changes are observed in the ionic current through the nanopore, setting the stage for future single-molecule genomic screening devices.

This chapter has been published as G.F. Schneider, S.W. Kowalczyk, V.E. Calado, G. Pandraud, H.W. Zandbergen, L.M.K. Vandersypen, and C. Dekker, *Nano Letters* **10**(8), 3163–3167 (2010).

7.1 Introduction

In the past few years, nanopores have emerged as a new powerful tool to interrogate single molecules [1-3]. They have been successfully used to rapidly characterize biopolymers like DNA [4, 5], RNA [6], as well as DNA-ligand complexes [7] and local protein structures along DNA [8] at the single-molecule level. A key driving force for nanopore research in the past decade has been the prospect of DNA sequencing. However, a major roadblock for approaching high-resolution DNA sequencing with pores is the finite length of the channel constituting the pore (Figure 7.1a). In a typical solid-state nanopore in a say 30 nm thick membrane, the current blockade resulting from DNA translocation is due to a large number of bases (~100) present in the pore. Here, we demonstrate that this limitation can be overcome by realizing an ultimately thin nanopore device, that is, two aqueous flow chambers separated by a nanopore in a graphene monolayer. Furthermore, we show the translocation of individual DNA molecules through such graphene nanopores. Fabrication of nanopores in graphene layers was reported previously in the vacuum of a transition electron microscope (TEM) [9, 10], but graphene nanopore devices that ionically probe the translocation of single molecules were so far not realized.

7.2 Free-standing graphene

Graphene is a two-dimensional layer of carbon atoms packed into a honeycomb lattice with a thickness of only one atomic layer (~0.3 nm) [11]. Despite its minimal thickness, graphene is robust as a free standing membrane [12, 13]. In addition, graphene is a very good electrical conductor [14]. Graphene therefore opens up new opportunities for nanopores such as new analytical platforms to detect, for example, local protein structures on biopolymers or sequencing with single-base resolution. Indeed, theoretical calculations of DNA translocation through a nanopore in graphene have already indicated the possibility for single-base resolution by probing the translocating molecule electrically in the transverse direction by use of the intrinsic conductive properties of graphene [15].

We obtain single-layer graphene (Figure 7.1b) by mechanical exfoliation from graphite on SiO₂ [16]. We preferred graphene obtained by mechanical exfoliation over synthetic graphene [17] because it contains fewer defects and it allows to select graphene sheets with a range of thicknesses (i.e. number of layers). Monolayer graphene is identified by its particular optical contrast [18] in the optical microscope

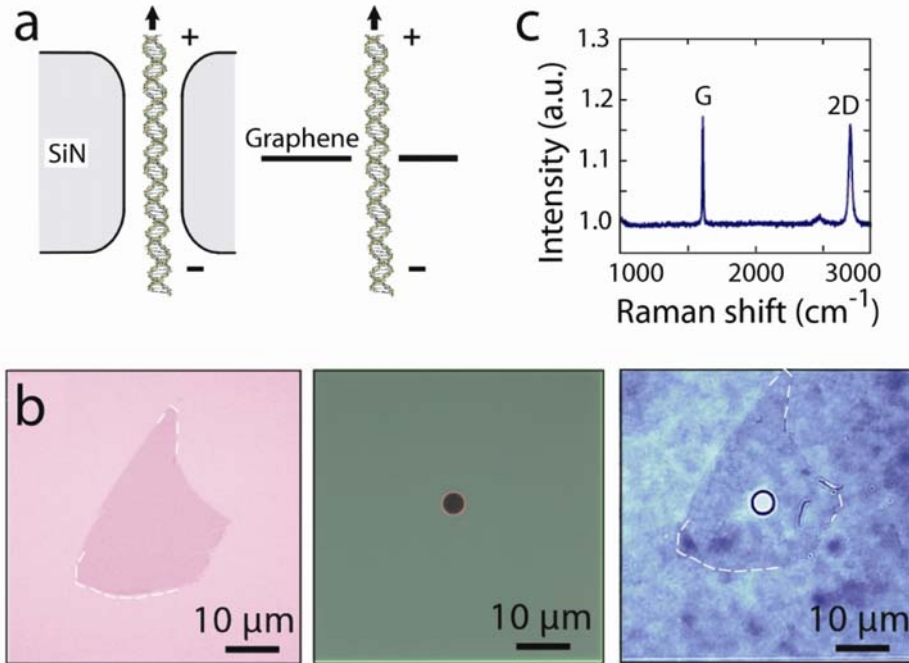


Figure 7.1 Graphene Nanopores for DNA translocation (a) To-scale side-view illustration comparing DNA translocation through a SiN solid-state nanopore with that through a freestanding one-atom-thick graphene nanopore. (b) Optical micrographs depicting the transfer of graphene from Si/SiO₂ (left) onto a micro-fabricated silicon nitride chip containing a 5 μm hole (right). After the transfer by wedging, the flake entirely covers the hole (bottom image). (c) Raman spectrum of the flake on Si/SiO₂ before the transfer.

and by Raman measurements (Figure 7.1c). At $\sim 1590\text{ cm}^{-1}$, we measure the so-called G resonance peak and at $\sim 2690\text{ cm}^{-1}$ the 2D resonance peak. In the case of multilayer graphene, the 2D resonance peak splits off in multiple peaks in contrast to monolayer graphene which has a very sharp single resonance peak. In this way, we are well able to distinguish single-layer graphene from multilayer graphene [19].

We select a monolayer of graphene and transfer it onto a SiN support membrane with a 5 micron sized hole [20] by use of our recently developed ‘wedging transfer’ technique [21]. This transfer procedure is straightforward: flakes can be overlaid to support membranes in less than an hour. Briefly, a hydrophobic polymer is spun onto a hydrophilic substrate (here plasma-oxidized SiO₂) with graphene flakes, and

wedged off the substrate by sliding it at an angle in water. Graphene flakes are peeled off the SiO₂ along with the polymer. The polymer is then floating on the water surface, located near a target SiN substrate, the water level is lowered, and the flakes are positioned onto the SiN membrane with micrometer lateral precision. In the final step the polymer is dissolved.

7.3 Graphene nanopores

We then drill a nanopore into the graphene monolayer using the highly focused electron beam of a transmission electron microscope (TEM). The acceleration voltage is 300 kV, well above the 80-140 kV knock-out voltage for carbon atoms in graphene [22] (see Methods). Drilling the holes by TEM is a robust well-reproducible procedure (we drilled 39 holes with diameters ranging from 2 to 40 nm, in monolayer as well as in multilayer graphene; some examples of pores are shown in Figure 7.2). Because of the high acceleration voltage of the electron beam, drilling could potentially induce damage to the graphene around the pore. However, electron beam diffraction measurements across the hole (Figure 7.2b and c) confirm the crystallinity of the monolayer surrounding the hole, as evidenced by the well-defined hexagonal diffraction patterns (Figure 7.2c).

Subsequently, we mount a pore into a microfluidic flow cell, add a 1M saline solution (1M KCl, TE, pH 8.0) on both sides of the graphene membrane, and measure current-voltage (IV) curves from ion transport through the graphene nanopores (inset of Figure 7.3). The resistance value (5.1 M Ω in the example of the inset of Figure 7.3) and the linearity of the IV curve indicate that the current is consistent with ion flow through the pore and does not arise from electrochemical processes at the conductive graphene surface [23]. Furthermore, samples with a graphene layer but without a nanopore exhibit a very high ionic resistance (>10 G Ω), which indicates that the graphene flake adheres well to the SiN surface and forms an insulating seal.

We measured IV curves for a number of pores ranging from 5 to 25 nm in diameter, in six monolayer graphene devices and seven multilayer graphene devices. Sample thickness is determined based on transmitted light intensity (2.3% reduction per layer) [24]. Figure 7.3 shows the obtained resistances versus pore diameter, for both monolayers and multilayers up to 8 layers (with a total layer thickness between 0.3 and 2.7 nm). We do not observe a strong dependence on the number of layers constituting the nanopore membrane. Note that these data are all taken in the regime where the pore diameter is much larger than the thickness of the graphene membrane.

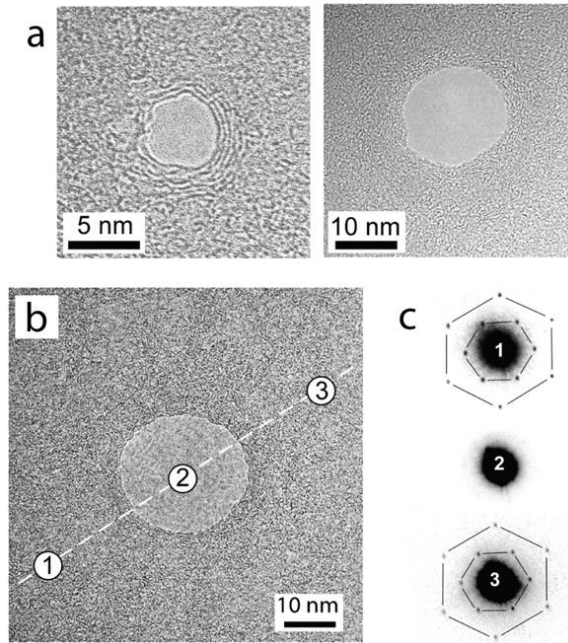


Figure 7.2 Drilling of graphene nanopores. (a) Transmission electron microscopy (TEM) of some nanopores drilled into multilayer graphene (b) TEM image (top) and diffraction patterns (bottom) across a 25 nm diameter pore in a monolayer of graphene. Numbers of the diffraction images indicate the spots where the patterns were recorded. (c) Diffraction patterns measured across the monolayer nanopore of panel B. The diffraction pattern was measured at three spots – indicated in panel b – with a 3 nm electron beam. The hexagonal lattice of diffraction spots is highlighted by the solid lines for clarity.

We determined how the pore resistance R scales with the pore diameter d , by fitting the diameter dependence of the resistance and conductance with a variety of functional dependences (see supplementary information for an extensive discussion of these fits). Surprisingly, we find that the dependence of pore resistance R on diameter d is better described by $R \sim 1/d^2$, which is the expected behavior for a cylindrical pore, than by a $R \sim 1/d$ dependence, which is expected if the access resistance dominates [25]. Since the membrane thickness is smaller than the pore diameter, we would have expected the access resistance of the pore to dominate the total resistance. A crossover between a $1/d$ and $1/d^2$ dependence or other functional dependencies cannot be excluded with the current data (see Supplementary Information).

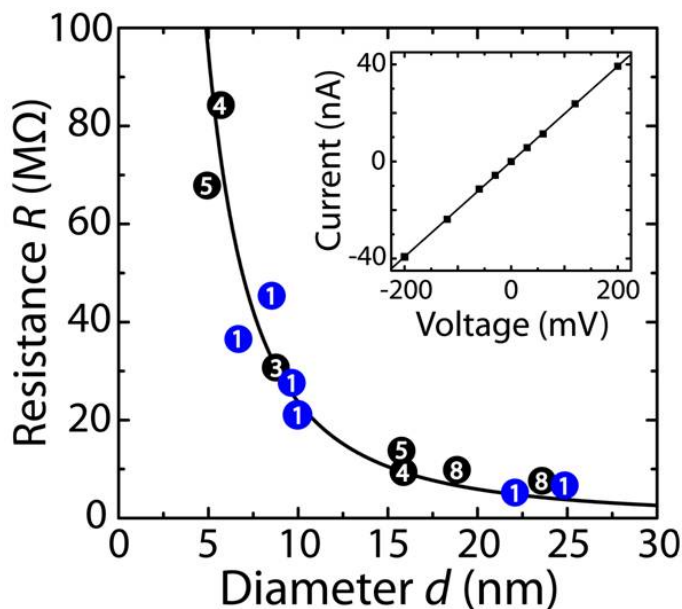


Figure 7.3 Nanopore resistances. Measured values of pore resistance versus diameter for 13 graphene nanopores. For each pore, the number of graphene layers is indicated by the number within the circle: “1” denotes graphene monolayers (blue); “ x ” denotes x layers of graphene (black). The solid line denotes a $1/d^2$ dependence. The inset shows an IV curve of a 22 nm nanopore in a graphene monolayer recorded in 1M KCl. A linear resistance of 5.1 M Ω is observed.

7.4 DNA translocation through graphene nanopores

Double-stranded DNA (dsDNA) can be driven electrophoretically through the nanopore and detected by monitoring the ion current. Upon addition of the 48.5 kbp λ -DNA (16 micron long) on one side of the pore and applying a voltage of 200 mV across the graphene membrane, a series of spikes is observed in the conductance traces (Figure 7.4a). Each temporary drop in the measured conductance, ΔG , arises from a single DNA molecule that translocates through the pore. As for conventional SiN nanopores [26], three characteristic signals are observed, corresponding to three types of translocation events: nonfolded (where the molecule translocates in a linear head-to-tail fashion), partially folded (where the molecule is randomly grabbed from the side of the DNA coil, and first translocates in a singly folded fashion) or fully

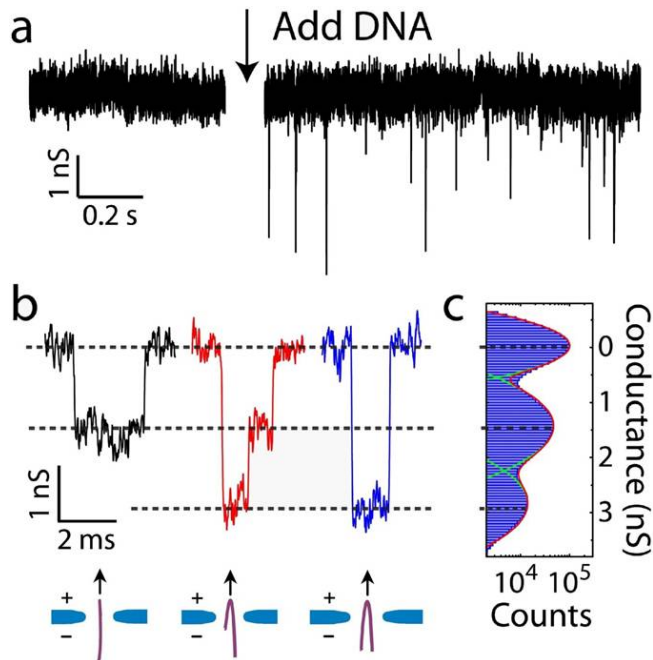


Figure 7.4 DNA translocation through a nanopore in a graphene monolayer. (a) Translocation of 48 kbp double-stranded λ -DNA across a 22 nm nanopore within a graphene monolayer, showing the baseline conductance (left) and blockade events upon addition of DNA (right). (b) Examples of translocation events of nonfolded (black), partially folded (red) and fully folded (blue) DNA molecules recorded at 200 mV in the 22 nm pore represented in Figure 7.3. (c) Conductance histogram collected from 1222 translocation events, including 1 ms of open-pore conductance before and after the event.

folded molecules (where the DNA happens to be grabbed in the middle of the molecule) [5]. Example events are shown in Figure 7.4b. The events are color coded in black (nonfolded), red (partially folded) and blue (fully folded). From a large number ($n = 1222$) of such events, we obtain a histogram of conductance blockade levels ΔG , as presented in Figure 7.4c. Three peaks are visible, the first being the open-pore current at 0 nS (i.e., the baseline); the peak at ~ 1.5 nS which corresponds to one strand of DNA in the pore; and the peak at ~ 3 nS due to two strands of the same DNA molecule in the pore. We measured DNA translocations on seven graphene

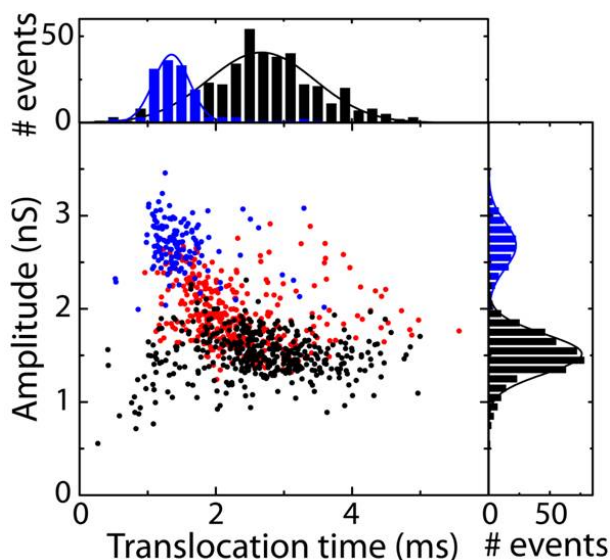


Figure 7.5 Scatter diagram of the amplitude of the conductance blockade versus translocation time for DNA translocation through a 22 nm diameter nanopore in a graphene monolayer. The accompanying histograms for the nonfolded and fully folded data are included at the top and the right. Color coding as in Figure 7.4b. Each point in this scatter diagram corresponds to a single translocation event. Applied voltage is 200 mV.

nanopores (monolayer and multilayer graphene membranes with pore diameters ranging from 10 to 25 nm), and collected good statistics on three devices (two monolayers and an eight-layer multilayer with pore diameters of 22, 25, and 24 nm respectively).

A scatter plot of ΔG versus the time duration of the events is shown in Figure 7.5, with the same color coding as used in Figure 7.4b. Each dot in this diagram represents a single DNA translocation event. The blockade amplitude $\Delta G = 1.5 \pm 0.4$ nS for nonfolded DNA in these graphene pores is quite similar in magnitude to that measured for pores of similar sizes in a 20 nm thick SiN membrane (1.4 ± 0.3 nS) for the same conditions [27]. This is unexpected as we would expect the ionic current blocked by a DNA molecule to scale as the inverse of the thickness of the nanopore membrane [22], leading to higher blockade amplitudes for DNA in graphene pores.

In addition to the event amplitude, we studied the translocation times of the events. The average translocation time is 2.7 ± 0.8 ms for the nonfolded DNA (Figure

7.5), a value that is similar, albeit slightly larger than for solid-state nanopores in a 20 nm SiN membrane for which the translocation time is 1.2 ± 0.3 ms under the same applied voltage of 200 mV and for a similar pore diameter [27]. A slightly larger translocation time compared to SiN pores was also observed for our other monolayer device for which we also got good statistics. We note that the translocation time is expected to be independent of the membrane thickness because the driving electrostatic force is the same: in a thinner membrane, the electric field over the graphene pore is higher (same voltage applied over a shorter distance) which however is exactly compensated by the smaller number of charges present on the piece of the DNA molecule that resides in the pore [28]. This is only a crude scaling argument however, and there can be various reasons why the translocation time is somewhat different for ultrathin nanopores. At a practical level, a slower translocation will be helpful for analytical applications where maximizing spatial resolution is needed.

The establishment of double-stranded DNA translocation through single-layer graphene nanopores represents an important first step towards pushing the spatial-resolution limits of single-molecule nanopore analytics to subnanometer accuracy. Future research will be aimed at exploring single-strand DNA translocation, single-base detection, and ultimately sequencing.

7.5 Methods

Preparation of graphene samples for wedging transfer

We prepared graphene sheets on clean and freshly plasma-oxidized (O_2 , Diener) Si/SiO₂ substrates by mechanical exfoliation of natural graphite (NGS Naturgraphit GmbH) with blue NITTO tape (SPV 224P). The plasma serves to make the substrate hydrophilic, which is needed for the wedging transfer. To render graphene monolayers visible, we used Si/SiO₂ wafers with a 90 nm thermally grown SiO₂ layer (IDB Technologies). We located the single and few layer graphene sheets under an optical microscope and identified the number of layers by their optical contrast as well as by Raman spectroscopy. Graphene flakes were transferred onto microfabricated Si/SiO₂/SiN chips described before [20]. We used cellulose acetate butyrate (Sigma-Aldrich) dissolved in ethyl acetate (30 mg/mL) as the transfer polymer [18]. Contrary to the design described by Krapf *et al*, prior the transfer of graphene, we etched the 20 nm thin SiN membrane using hot phosphoric acid (200 °C) for 45 minutes.

Transmission electron microscopy and fabrication of nanopores in graphene

Nanopores were fabricated and imaged using a Cs-corrected Titan Cubed Supertwin/STEM FP5600/40 microscope operated at an accelerating voltage of 300 kV. An electron beam with a diameter of 15 nm at full width at half-maximum height and a beam density of 10^6 electrons/(s·nm²) was used for drilling. Gatan 2k x 2k CCD with binning 1 was used for image recording. Diffraction patterns were acquired with a beam size of 3 nm and a beam density of 10^5 electrons/(s·nm²). To remove contamination, samples were heated at 200 °C for at least 20 minutes prior to their insertion in the vacuum chamber of the microscope. After drilling, samples were stored in ethanol.

Nanopore experiments

For the electrical measurements, a membrane with a single graphene nanopore is mounted in a polyether ether ketone (PEEK) microfluidic flow cell and sealed to liquid compartments on either side of the sample. Measurements are performed in 1 M KCl salt solution containing 10 mM Tris-HCl and 1 mM EDTA at pH 8.0 at room temperature. Ag/AgCl electrodes are used to detect ionic currents and to apply electric fields. Current traces are measured at 100 kHz bandwidth using a resistive feedback amplifier (Axopatch 200B, Axon Instruments), and digitized at 500 kHz. Before injecting dsDNA, the graphene-SiN-microchip was flushed with a 1 mg/mL solution of 16-mercaptohexadecanoic acid in 8:2 toluene/ethanol and additionally rinsed in respectively clean 8:2 toluene/ethanol and ethanol. This is expected to form a flat self-assembled monolayer on the graphene surface which demotes DNA adhesion (this treatment is not mandatory to observe DNA translocations) [29]. dsDNA was unmethylated λ -DNA (20 ng/uL, Ref. No. D152A, lot no. 27420803, Promega, Madison, USA). The event-fitting algorithm used to analyze and label the translocation events was the same as the one described before [5]. Only events exceeding six times the standard deviation of the open-pore root-mean-square noise are considered. Due to possible baseline fluctuations, we only considered events whose current before and after the event does not change more than 10% of the event amplitude. We additionally filtered the data at 10 kHz for better signal-to-noise ratio, and we discarded events shorter than 200 μ s.

Acknowledgements. We thank M.-Y. Wu and Q. Xu for their assistance in TEM, H. Postma for discussions, V. Karas and K. van Schie for technical assistance, and the Netherlands Organisation for Scientific Research (NWO), the NanoSci-E+ Program, the Foundation for Fundamental Research on Matter (FOM), and the EC project READNA for funding.

References

- 1 Branton, D. *et al. Nat. Biotechnol* **26**, 1146-1153 (2008).
- 2 Dekker, C. *Nat. Nanotechnol.* **2**, 209-215 (2007).
- 3 Ma, L.; Cockroft, S. L. *Chembiochem.* **11**, 25-34 (2010).
- 4 Li, J. L.; Gershow, M.; Stein, D.; Brandin, E.; Golovchenko, J. A. *Nat. Mater.* **2**, 611-615 (2003).
- 5 Storm, A. J.; Storm, C.; Chen, J. H.; Zandbergen, H.; Joanny, J. F.; Dekker, C. *Nano Lett.* **5**, 1193-1197 (2005).
- 6 Skinner, G. M.; van den Hout, M.; Broekmans, O.; Dekker, C.; Dekker, N. H. *Nano Lett.* **9**, 2953-2960 (2009).
- 7 Wanunu, M.; Sutin, J.; Meller, A. *Nano Lett.* **9**, 3498-3502 (2009).
- 8 Kowalczyk, S. W.; Hall, A. R.; Dekker, C. *Nano Lett.* **10**, 324-328 (2010).
- 9 Fischbein, M. D.; Drndic, M. *Appl. Phys. Lett.* **93**, 113107 (2008).
- 10 Girit, C. O.; Meyer, J. C.; Erni, R.; Rossell, M. D.; Kisielowski, C.; Yang, L.; Park, C. H.; Crommie, M. F.; Cohen, M. L.; Louie, S. G.; Zettl, A. *Science* **323**, 1705-1708 (2009).
- 11 Novoselov, K. S.; Geim, A. K.; Morozov, S. V.; Jiang, D.; Zhang, Y.; Dubonos, S. V.; Grigorieva, I. V.; Firsov, A. A. *Science* **306**, 666-669 (2004).
- 12 Tsoukleri, G.; Parthenios, J.; Papagelis, K.; Jalil, R.; Ferrari, A. C.; Geim, A. K.; Novoselov, K. S.; Galiotis, C. *Small* **5**, 2397-2402 (2009).
- 13 Meyer, J. C.; Geim, A. K.; Katsnelson, M. I.; Novoselov, K. S.; Booth, T. J.; Roth, S. *Nature* **446**, 60-63 (2007).
- 14 Castro Neto, A. H.; Guinea, F.; Peres, N. M. R.; Novoselov, K. S.; Geim, A. K. *Rev. Mod. Phys.* **81**, 109-162 (2009).
- 15 Postma, H. W. C. *Nano Lett.* **10**, 420-425 (2010).
- 16 Novoselov, K. S.; Jiang, D.; Schedin, F.; Booth, T. J.; Khotkevich, V. V.; Morozov, S. V.; Geim, A. K. *Proc. Natl. Acad. Sci. U. S. A.* **102**, 10451-10453 (2005).
- 17 Park, S.; Ruoff, R. S. *Nat. Nanotechnol.* **4**, 217-224 (2009).

- 18 Blake, P.; Hill, E. W.; Neto, A. H. C.; Novoselov, K. S.; Jiang, D.; Yang, R.; Booth, T. J.; Geim, A. K. *Appl. Phys. Lett.* **91**, 063124 (2007).
- 19 Ferrari, A. C.; Meyer, J. C.; Scardaci, V.; Casiraghi, C.; Lazzeri, M.; Mauri, F.; Piscanec, S.; Jiang, D.; Novoselov, K. S.; Roth, S.; Geim, A. K. *Phys. Rev. Lett.* **97**, 187401 (2006).
- 20 Krapf, D.; Wu, M. Y.; Smeets, R. M. M.; Zandbergen, H. W.; Dekker, C.; Lemay, S. G. *Nano Lett.* **6**, 105-109 (2006).
- 21 Schneider, G. F.; Calado, V. E.; Zandbergen, H. W.; Vandersypen, L. M. K.; C., D. *Nano Lett.* **10**, 1912-1916 (2010).
- 22 Hashimoto, A.; Suenaga, K.; Gloter, A.; Urita, K.; Iijima, S. *Nature* **430**, 870-873 (2004).
- 23 Heller, I.; Chatoor, S.; Mannik, J.; Zevenbergen, M. A. G.; Oostinga, J. B.; Morpurgo, A. F.; Dekker, C.; Lemay, S. G. *Nano Lett.* **10**, 1563-1567 (2010).
- 24 Nair, R. R.; Blake, P.; Grigorenko, A. N.; Novoselov, K. S.; Booth, T. J.; Stauber, T.; Peres, N. M. R.; Geim, A. K. *Science* **320**, 1308-1308 (2008).
- 25 Hall, J. E. *Journal of General Physiology* **66**, 531-532 (1975).
- 26 Wu, M. Y.; Smeets, R. M. M.; Zandbergen, M.; Ziese, U.; Krapf, D.; Batson, P. E.; Dekker, N. H.; Dekker, C.; Zandbergen, H. W. *Nano Lett.* **9**, 479-484 (2009).
- 27 Kowalczyk, S. W., *et al*, unpublished.
- 28 Keyser, U. F.; Koeleman, B. N.; Van Dorp, S.; Krapf, D.; Smeets, R. M. M.; Lemay, S. G.; Dekker, N. H.; Dekker, C. *Nat. Phys.* **2**, 473-477 (2006).
- 29 Xu, S. L.; Yin, S. X.; Liang, H. P.; Wang, C.; Wan, L. J.; Bai, C. L. *J. Phys. Chem. B* **108**, 620-624 (2004).

7.6 Supplementary Information

As mentioned in the manuscript, we have measured the ionic resistance R of pores with various diameters d , in monolayer and multilayer graphene. Here, we discuss various ways to fit the data.

We have plotted and fitted the data both as $R(d)$ and as $G(d) = 1/R(d)$, which will have the effect of emphasizing the weight of data points at small and large diameters, respectively. We fitted a variety of fitting functions to these data. Table S7.1 displays the resulting fitting parameters as well as the χ^2 value, the reduced sum of the squared residuals. From a comparison of these fits, we can note a number of things:

- The trends for comparing different fitting functions are similar when we compare fits to $R(d)$ with fits to $G(d)$.
 - Most prominently, we observe that the fits to a square dependence on diameter, e.g., $R \sim 1/d^2$, are better than fits to a linear dependence, $R \sim 1/d$.
-

- When we allow for an offset, the fits improve (χ^2 values are lower), which is not surprising since a second fit parameter β is introduced. However, we do not have a good rationale to physically explain such an offset, since we firmly expect $G(0)=0$.
- A loglog plot of $G(d)$ shows a straight line, revealing that a power law $G \sim d^{1.6}$ also fits the conductance data quite well. It is, however, unclear to us what type of microscopic model would lead to such power law dependence.
- Finally, a combination of a linear and square dependence, $G(d) = 1/(\alpha/d + \beta/d^2)$, also fit the data quite well. We cannot exclude such a crossover dependence which could represent contributions of both the access resistance (α/d) and the resistance of a cylindrical pore (β/d^2).

The final conclusion from the data presented here is that a square dependence fits the data better than a linear dependence on diameter, but we cannot rigorously exclude more sophisticated models.

Formula	Fitting Parameters	χ^2
$R(d) = \frac{\alpha}{d}$	$\alpha = 255 \pm 15 \text{ M}\Omega \cdot \text{nm}$	$\chi^2 = 3.7$
$R(d) = \frac{\alpha}{d^2}$	$\alpha = 2140 \pm 120 \text{ M}\Omega \cdot \text{nm}^2$	$\chi^2 = 2.3$
$G(d) = \alpha \cdot d$	$\alpha = 4.8 \pm 0.2 \text{ nS/nm}$	$\chi^2 = 8.3$
$G(d) = \alpha \cdot d^2$	$\alpha = 0.32 \pm 0.02 \text{ nS/nm}^2$	$\chi^2 = 2.0$
$G(d) = \alpha \cdot d + \beta$	$\alpha = 7.1 \pm 0.3 \text{ nS/nm}$ $\beta = -27.1 \pm 0.5 \text{ nS}$	$\chi^2 = 3.2$
$G(d) = \alpha \cdot d^2 + \beta$	$\alpha = 0.3 \pm 0.02 \text{ nS/nm}^2$ $\beta = 5.6 \pm 2.8 \text{ nS}$	$\chi^2 = 1.4$
$G(d) = d^\alpha$	$\alpha = 1.58 \pm 0.01 \text{ ns/nm}^\alpha$	$\chi^2 = 2.6$
$G(d) = \frac{1}{\frac{\alpha}{d} + \frac{\beta}{d^2}}$	$\alpha = 0.09 \pm 0.02 \text{ nm/nS}$ $\beta = 1.6 \pm 0.3 \text{ nm}^2/\text{nS}$	$\chi^2 = 2.7$

Table S7.1 Fit functions and corresponding fit parameters and χ^2 values obtained for fits to the data for $R(d)$ and $G(d)$.

Chapter 8

Biomimetic nanopores: learning from and about nature

Through recent advances in nanotechnology and molecular engineering, biomimetics – the development of synthetic systems that imitate biological structures and processes – is now emerging at the nanoscale. In this review, we explore biomimetic nanopores and nanochannels. Biological systems are full of nano-scale channels and pores that inspire us to devise artificial pores that demonstrate molecular selectivity or other functional advantages. Moreover, with a biomimetic approach we can also study biological pores, through bottom-up engineering approaches whereby constituent components can be investigated outside the complex cellular environment.

This chapter will appear as S.W. Kowalczyk, T.R. Blosser, and C. Dekker, *Trends in Biotechnology*, December issue (2011).

8.1 Introduction

The biological cell is filled with many different types of pores and channels that control the exchange of ions and molecules between subcellular compartments. These passageways are of vital importance to cellular function [1]. Examples include: ion channels at the cell surface that regulate the flow of ions; pores inserted into cell membranes upon viral infection that serve as conduits for genome transfer; the nuclear pore complex (NPC) that controls the transport of messenger RNA and proteins across the nuclear envelope of eukaryotic cells; and pores that are used for protein secretion into cell organelles.

Advances in nanotechnology now make it possible to study and shape matter at the nanometer scale, opening the way to imitate biological structures at the molecular level to both study and harness their ingenuity [2–6]. Indeed, since their first fabrication about a decade ago, nanometer-sized pores and channels in solid-state materials have served as a scaffold for a variety of biology-inspired applications [7–9]. A major direction of these efforts has been to devise molecular separation methods that exhibit selectivity based on specific biochemical properties. In other work, wild-type and genetically modified biological pores have been employed as sensitive biosensors to detect molecules in solution. In a third application, a biomimetic approach has enabled the investigation of underlying principles of molecular biology: by employing a bottom-up engineering strategy, using both biological and synthetic components, a complex biological system can be simplified for *in vitro* studies that are not otherwise possible. A related approach – similar but different to biomimetics – is the emerging field of synthetic biology, which aims to use and develop biology as an engineering-like science to achieve new biological structures and functions [10]. Typically, however, synthetic biology does not involve artificial (non-biological) materials, as does biomimetics.

In this work, we review the field of biomimetic pores and channels, focusing specifically on two different approaches (Figure 8.1) and their applications. In the first case, we highlight engineering efforts inspired by the ingenuity and physical characteristics of natural biological systems. This entails both purely synthetic systems that seek to mimic a biological counterpart and systems that incorporate biomolecules or complexes to harness their specificity or function. Secondly, we discuss the how biomimetic pores have been employed to study the mechanistic properties of their biological counterparts.

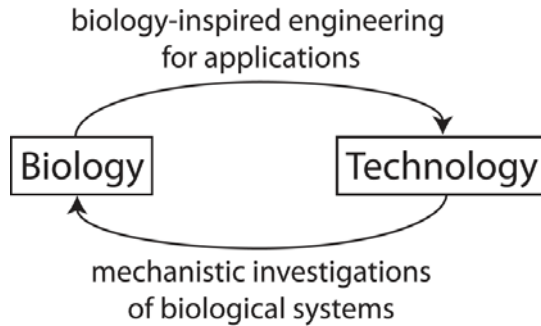


Figure 8.1 Engineering efforts can be inspired by the ingenuity and physical characteristics of natural biological systems. On the other hand, biomimetic devices can be employed to study the mechanistic properties of their biological counterparts.

8.2 Biology-inspired engineering

8.2.1 Fabrication of artificial pores and channels

Central to the construction of a biomimetic pore or channel is the fabrication of an artificial pore or channel which can serve as a scaffold for further modification. Note that the naming of pores/channels merely reflects the aspect ratio of the passageway: where a pore has a diameter larger than its depth, a channel has a depth much larger than its diameter. Using various fabrication technologies (reviewed in, for example, Ref. 7 and 11–14), nanopores or channels can be obtained in a variety of different shapes and structures. For example, nanochannels can be made by straightforward planar lithography but also by ion-track etching. In the latter case, a single high-energy heavy-metal ion from a cyclotron is shot through a thick polymeric film, followed by chemical wet etching, which removes damaged material faster than undamaged material, resulting in a conical nanochannel with a diameter down to 2 nm [15] (Figure 8.2a,b). Similarly made membranes, with multiple channels ranging in size from 10 nm to 10 μm and density from 10^5 to 10^9 pores/ cm^2 , are commercially available [16].

Nanopores can be made using two different approaches. First, ion beam sculpting [8] has been used to create single nanopores in thin free-standing silicon nitride (SiN) membranes. Here, an ion beam is focused at the membrane to open up a tiny hole with a diameter down to a few nanometers. Feedback from ion detectors below the membrane signals when to turn off the beam. Alternatively, an electron beam from a transmission electron microscope can be used to drill and shape pores down to sub-

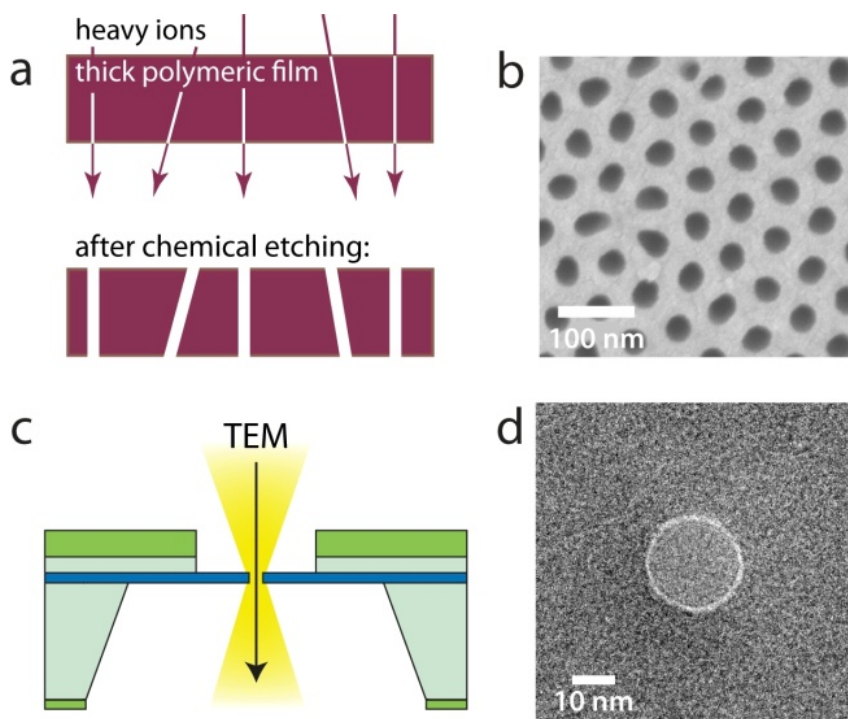


Figure 8.2 Fabrication of artificial nanochannels/nanopores. (a) Schematic showing heavy ions that penetrate a thick polymer membrane. The resulting damaged zones are then selectively etched with a chemical etchant and transformed into hollow nanochannels. (b) Scanning electron micrograph of the surface of an alumina membrane with a thickness of 40 μm with channels of 35 nm in diameter. Adapted from [38]. (c) Side-view schematic showing a device consisting of a 20 nm thin free-standing silicon nitride window (blue layer) embedded in a silicon wafer (light green). A single nanopore is drilled using a highly focused electron beam (yellow). (d) Transmission electron micrograph of a nanopore with a diameter of 20 nm.

nanometer diameters [9] (Figure 8.2c, d). The latter method allows direct visual feedback as well as modes to enlarge (with a locally focused beam) or shrink (with wide-field illumination) the nanopore in a controlled manner.

Even without any additional modifications, these pores have proven to be useful as single-molecule biosensors, for example for the detection of DNA [17–20], RNA [21], proteins [22, 23], carbon nanotubes [24], or local protein structures along DNA [25, 26]. However, engineering efforts inspired by biological systems can enhance the functionality of bare nanopores. Typically this starts with chemical modification and

coating of bare nanopores that enables their chemical properties to be tuned [27]. A chemical scheme that is often used in the case of polymeric membranes consists of coating the membrane with a gold layer through electroless deposition, followed by functionalization via thiol chemistry [28]. While this approach is also applicable to silica or alumina membranes, these membranes may also be directly reacted with functionalized silanes [29], thereby reducing the number of chemical treatments needed. We first discuss a few examples of biomimetic pores that have demonstrated selectivity for specific molecular species, as inspired by naturally occurring pores and channels.

8.2.2 Mimicking naturally occurring pores and channels

Yusko *et al.* [30] recently coated a single solid-state nanopore with a fluid lipid bilayer (Figure 8.3a). They reported that this approach was inspired by the olfactory systems of insects, which have lipid-coated nanochannels in their external skeleton. The lipid coatings bind and pre-concentrate odorant molecules before transporting them to the olfactory neurons in the antennae. The biomimetic lipid-coated nanopores showed several advantages over bare nanopores, such as the possibility of fine tuning the translocation speed of proteins by regulating the lipid-bilayer viscosity, the prevention of non-specific adsorption of proteins to the membrane, and the possibility to selectively bind streptavidin-functionalized molecules to a lipid bilayer that contains biotin groups.

Caspi *et al.* [31] realized an artificial system that mimicked all major components of the receptor-mediated transport of the nuclear pore complex (Figure 8.3b). They found that nanoporous membrane filters functionalized with polyisopropylacrylamide (pNIPAM) allowed faster translocation of ssDNA-pNIPAM compared to single-stranded DNA (ssDNA) alone, in spite of the larger size of the complex. This is similar to mediated transport through the NPC, in which a transporter (pNIPAM in this case) ferries a cargo (ssDNA) through the pore. Ion channels [32] have also inspired a number of mimics. These membrane protein complexes facilitate the transport of ions across membranes, often gated by allosteric binding or transmembrane voltage. Many types of ion channels exist and they are well documented. Atomic-resolution structures have been determined for ion channels that are selective for the four most abundant ions in biology: sodium, potassium, calcium, and chloride [1].

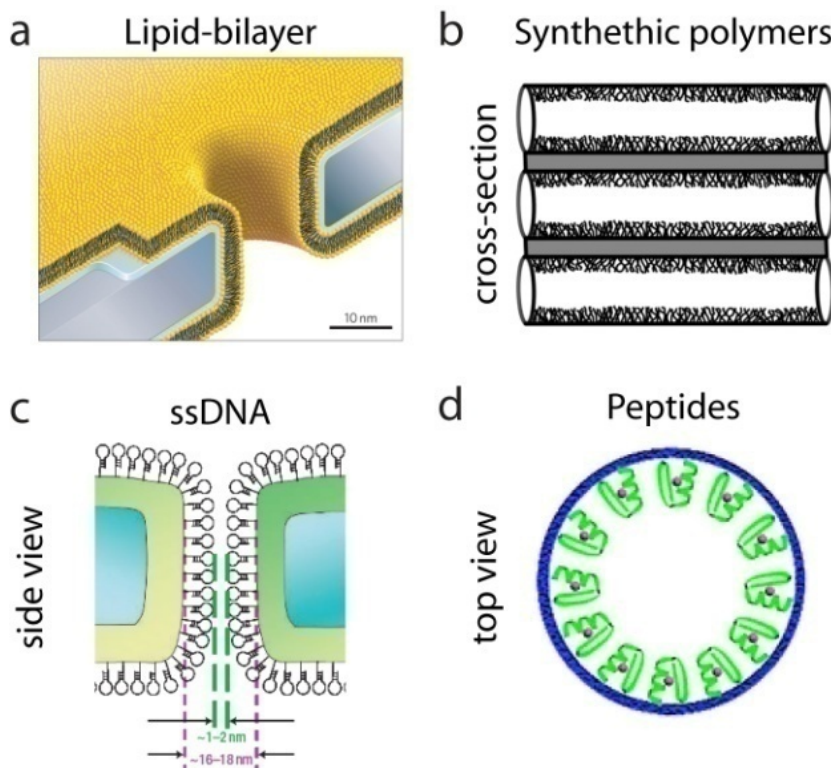


Figure 8.3 Biology-inspired nanopore functionalization. (a) A lipid-coated (yellow) synthetic nanopore in a silicon nitride substrate (grey). Adapted from [30]. (b) Cross-section of a membrane with an array of nanopores grafted with pNIPAM. Adapted from [31]. (c) Side-view of a solid-state nanopore functionalized with hairpin-DNA molecules (not drawn to scale). Adapted from [41]. (d) Top view of zinc fingers (green) immobilized into a nanochannel: after Zn^{2+} binding (pink), the zinc fingers fold to finger-like conformations, yielding an increase of the effective channel diameter. Adapted from [34].

Recently, a biomimetic potassium-responsive nanochannel was demonstrated [33]. Here, a nanochannel was lined with bound G-quadruplex DNA, which, upon addition of potassium, undergoes a conformational change that alters the effective channel size. Similarly, a biomimetic zinc-activated ion channel was demonstrated by incorporating zinc finger peptides into a polymeric nanochannel [34] (Figure 8.3d). Artificial proton-reactive channels with transport properties that are dependent on their surrounding proton concentration were also shown [35], mimicking biological

proton-gated ion channels that switch between an “off” to an “on” state in response to a pH change. This was achieved by binding pH-responsive poly(4-vinyl pyridine) brushes onto solid-state nanopores. Yet another example are conical nanopores in polymeric membranes, where the asymmetric shape of the pore together with the negative carboxylate groups that are left over from the chemical etching lead to ion current rectification, mimicking an effect found in voltage-gated ion-channels [36]. A recent idea, inspired by the light-driven cross-membrane proton pump rhodopsin, was to fabricate a nanopore-based photoelectric conversion system by grafting photosensitive molecules to a nanopore [37].

8.2.3 Realizing selectivity and biosensing

We next discuss approaches that are not directly aimed at mimicking biological pores, but that use biomolecules to confer selectivity. An early study [38] showed that through attaching antibodies to the inner walls of silica nanochannels, enatiomeric selectivity was achievable. Similarly, by immobilizing apoenzymes (enzymes that require a cofactor but do not have one bound) to a membrane with pores, selective transport of the substrate molecule was shown [39]. The same approach works for complementary DNA pieces: by attaching short ssDNA hairpin ‘probes’ to either a membrane with nanochannels [40] or a single nanopore [41], complementary ssDNA molecules will transiently bind and unzip and thereby work its way through the pore, while mismatched DNA exhibits a lower translocation probability, attributed to electrostatic and mechanical friction (Figure 8.3c). This is a remarkably sensitive technique: translocation events for short (15 bases) DNA oligomers with a single base mismatch occurred 30 times less frequently than that for perfectly complementary DNA [41]. Other examples of bio-inspired artificial pores have successfully demonstrated the separation of proteins [42–44], fluorophores [43, 44], and other small molecules [25, 45, 46]. In a differing approach, functional polymers can be used as the bases for separation filters. For example, poly(acrylic acid) was bound to tin (Sn^{2+}) binding sites in nanochannels of commercial polycarbonate membranes that were pre-treated with a solution of Sn^{2+} ions [44]. It was shown that this approach allows separation of multiple polymers, dyes, and proteins based on size, charge, and hydrophobicity.

One may also employ biological pores as sensitive biosensors, which is an extension of the above approach where one uses biomolecules to functionalize a pore or channel. We first discuss applications using biological pores in their natural environments, and then continue to discuss how it can be advantageous to put them in a synthetic environment, combining the best of both worlds.

The archetypical protein nanopore for biosensing is alpha-hemolysin [47–49], a toxin protein released by the bacterium *Staphylococcus aureus* that spontaneously inserts itself into lipid bilayers. It contains a heptameric transmembrane channel with a width of about 1.4 nm at its narrowest constriction, making it just large enough to allow the passage of ssDNA, but not that of double-stranded DNA (dsDNA). Indeed, transport of ssDNA and ssRNA through alpha-hemolysin has been extensively studied [48, 50]. While these biological pores have the disadvantage of being inserted into relatively fragile free-standing lipid-bilayers (no solid-state support), a big advantage of such biological pores is that they can be engineered with molecular biology techniques, such as mutagenesis [51–54], to make very specific local changes in their structure that can influence transport properties. For example, the internal charge can be manipulated [53] in such a way that the speed of DNA translocation can be strongly reduced [54]. The alpha-hemolysin pore has been used to detect proteins [55], organic molecules [56], and (enantiomers of) drug molecules [57] (for an extensive overview see [58]). Other examples of biological pores that have been employed as biosensors include anthrax pores, which have a structure very similar to alpha-hemolysin [59], and the OmpF porin, which interacts with antibiotics [60]. Recently a mutant of the MspA porin, with an inner diameter of ~1.2 nm, was used to detect single-molecule translocation events of ssDNA [61] and even to distinguish all four DNA nucleotides [62]. One of the main advantages of the MspA porin over alpha-hemolysin is that the inner constriction of MspA is very short in its longitudinal direction, whereas alpha-hemolysin has a narrow barrel that is relatively long (Figure 8.4a,b). As a result, MspA has a higher specificity for individual bases, and is therefore potentially more suitable for DNA sequencing, similar to the advantage of using atomically thin graphene nanopores [63–65] versus thicker SiN nanopores. Another biological pore that was employed for bioengineering, is the mechanosensitive MscL channel of *Escherichia coli* that was chemically modified into a light-activated nano-valve and utilized for triggered delivery in synthetic liposomal vesicles [66, 67]. For a comprehensive review of applications of biological pores in nanomedicine, sensing, and nanoelectronics, see Ref. 68.

Recently, hybrid biological/artificial pores have been demonstrated. Balme *et al.* [69] reported confinement of the biological ion channel Gramacidin-A into a nanopore channel. Hall *et al.* [70] established the controlled and oriented insertion of an individual alpha-hemolysin protein into a narrow solid-state nanopore, combining the two most experimentally studied nanopores. Hybrid approaches have the great advantage of combining a biological, atomically precise, structure that can be genetically engineered with the robustness, sustainability and potential for parallelization and device-integration of solid-state nanopores (Figure 8.4c,d). Given the

promising sequencing characteristics of both MspA [62], and alpha-hemolysin [71], a hybrid approach may turn out to be useful for genomic sequencing devices.

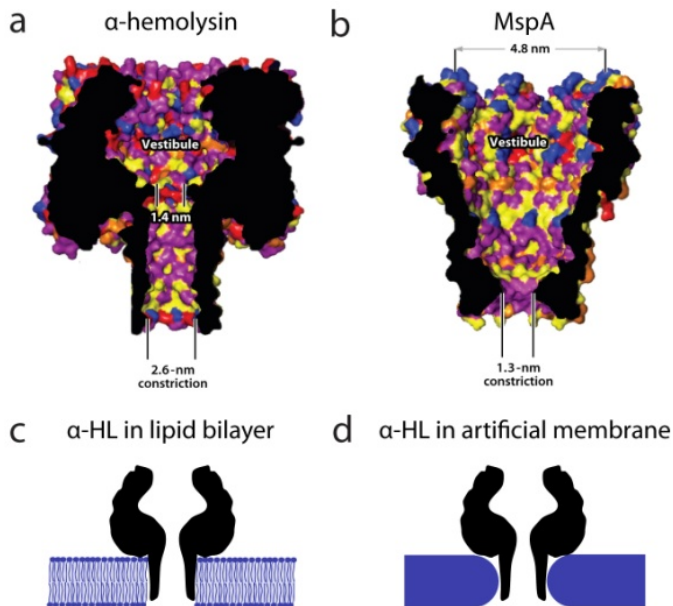


Figure 8.4 Biological nanopores. (a, b) Structural comparison of alpha-hemolysin and MspA nanopores [82]. (c) Alpha-hemolysin inserted into a lipid bilayer, its natural setting. (d) Hybrid nanopore: alpha-hemolysin inserted into a solid-state nanopore.

8.3 Mechanistic investigation of biological pores

Complementary to bio-inspired engineering, one can take advantage of the recent technological advances in nanoengineering to construct biomimetic pores for the purpose of studying the biological principles of their natural counterparts. Nature is highly organized in a hierarchical manner from the molecular to the macroscopic scale, starting with nano-architectures that together form a multitude of different macromolecular assemblies and interactions. Bottom-up engineering approaches, whereby complex biological systems are simplified to their constituent components, can be used to dissect essential biological functioning at the fundamental level. We will discuss both a bulk [72] and a single-molecule [73] investigation of the nuclear pore complex to illustrate this point.

8.3.1 Bulk investigations of a biomimetic NPC

Nuclear pore complexes (Figure 8.5a) are the sole connection between the nucleus and the cytosol of eukaryotic cells, thus playing a key role in connecting the genetic material and the protein-synthesizing apparatus [74]. This remarkable cellular machine forms a pore with a ~ 40 nm inner diameter and controls all transport of proteins and RNA across the nuclear envelope. The NPC acts as a selective sieve: while permeable to ions and small solutes (up to ~ 40 kDa), transport through this gate is otherwise reserved for transport receptors (karyopherins) that ferry cargo across the complex. Vertebrate NPCs have a total mass of ~ 120 MDa and are composed of about 30 distinct types of proteins (nucleoporins) [75]. About one-third of these nucleoporins contain natively unfolded domains rich in phenylalanine-glycine repeat motifs (FG-domains) [76], which are believed to be critical for the process by which transport receptor-cargo complexes gain selective access to the NPC channel [77].

By tethering FG-nucleoporins to commercial polycarbonate filters, Jovanovic-Talisman *et al.* [72] reconstituted NPC-like transport selectivity in an artificial system (Figure 8.5b). Using track-etched polycarbonate membranes with cylindrical nanopores of 30 nm in diameter and 6 μm in length, they first sputtered a thin layer of gold on one side of the membrane. Next, thiol-modified yeast nucleoporins, Nsp1, were attached to the gold layer. The functionalized membranes were then mounted between two fluid chambers and the flux of fluorescently labeled karyopherin proteins through the pores was measured using confocal microscopy. Importantly, they observed that transport receptor-bound cargo molecules translocate much faster than molecules of similar size that do not bind FG domains. The degree of selectivity was found to depend on the pore diameter and on the binding strength between nucleoporins and transport receptors. Interestingly, a single nuclear pore protein (Nup) was sufficient for selectivity: when comparing the flux of BSA (an inert protein) and NTF2 (a transport receptor) through the functionalized membrane, the authors found that the transport receptors would translocate (at best) 5 times more efficiently than the inert protein. This study thus reproduced the remarkable selectivity of the NPC and has the potential to be employed for application in separation and bioanalytical devices. However, a limitation to this approach is that measurement of single translocation events is not possible.

8.3.2 Single-molecule investigations of a biomimetic NPC

Recently, we have taken this approach one step further and used solid-state nanopores to carry out single-molecule transport studies on an individual biomimetic NPC [73]

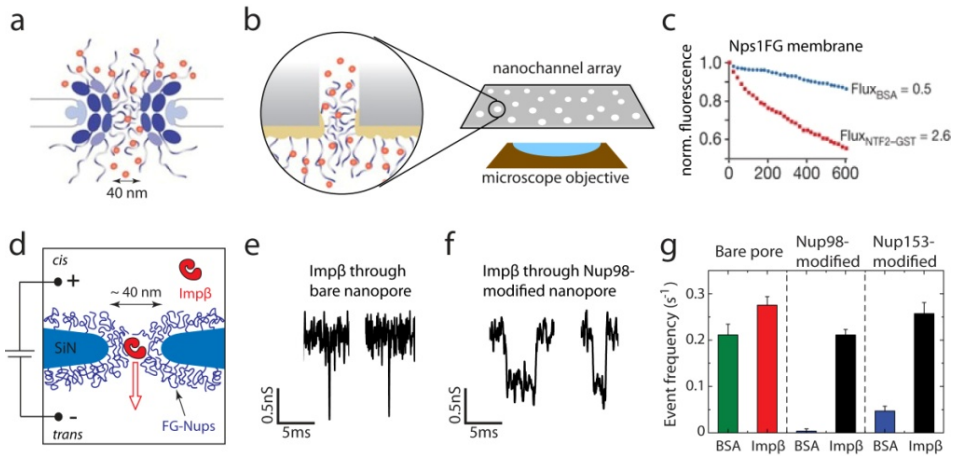


Figure 8.5 Biomimetic nuclear pore complex (NPC). (a) Schematic representation of the cellular NPC [83]. (b) Schematic of an artificial pore [83] in a functionalized membrane with many channels in parallel. The membrane was coated on one face with a ~ 15 -nm-thick gold layer to which FG-nucleoporins were attached by a single carboxy-terminal cysteine. (c) Two-channel fluorescence measurements of simultaneous diffusion of fluorescently labelled BSA (blue) and NTF2–GST (red) through an Nps1FG-coated membrane [72]. (d) A sketch showing the concept of the single-molecule biomimetic NPC study, which is engineered by attaching FG-Nups to a solid-state nanopore and transport of Imp β is measured by monitoring the trans-pore current [73]. (e, f) Single-molecule translocation events. Ion current after addition of Imp β in a bare pore (e) and a Nup98-modified (f) pore. Each spike is a single-molecule event. Event amplitudes are similar while the dwell times differ by more than an order of magnitude [73]. (g) Event frequencies through bare and Nup-modified pores, showing NPC-like selectivity [73].

(Figure 8.5c). First, we drilled a nanopore into a 20 nm thin membrane with a focused TEM beam and covalently tethered human nucleoporins (Nup98 or Nup153) to it using maleimide chemistry. The membrane was then placed in a microfluidic flow cell where the nanopore forms the only connection between two fluidic compartments. Individual translocation events were monitored using sensitive ionic current measurements with sub-millisecond temporal resolution. We found that the nucleoporins form a very dense, low-conductivity network with pores up to ~ 25 nm in diameter while larger pores form a more open structure. Transport receptors (Imp β) proceeded with a dwell time of a few ms, whereas the passage of non-specific proteins (BSA) was strongly inhibited (with selectivity factors of up to 60) with differing degrees of selectivity depending on the nucleoporin type. Also here, it was

found that one type of FG-nucleoporin was sufficient to form a selective permeability barrier. By reproducing key features of the NPC, this biomimetic approach provides a quantitative platform to study nucleocytoplasmic transport phenomena at the single-molecule level *in vitro*.

The transport through the NPC poses many interesting questions: How does the pore generate a diffusion barrier? How is this influenced by the composition of the nucleoporins, the sequence of their FG-repeats, and the number of repeats? Do the nucleoporin chains interact with one another? Do they interpenetrate to form a gel? Do they form a molecular brush? How exactly do receptors move through the pore? Do they change the local structure of the nucleoporin network? Do they 'slide' along individual nups or 'jump' from one to the next? Some of these questions may well be addressed using the biomimetic approach, which offers a new type of testing platform for mechanistic studies. Similar measurements on biomimetic NPCs may not only shed light on the fundamental workings of this important protein machine, but also provide new opportunities for, for example, studying gene and drug delivery into the nucleus.

8.4 Perspective

This last example illustrates the emerging biomimetic techniques can give insights into key molecular processes occurring in biology. Although there are multiple challenges that face biomimetics of pores, it has already proven a fruitful approach. The main challenge is that biological systems are often so complex that it seems out of reach to assemble them completely *in vitro*. Furthermore, for many systems, a lack of structural data limits our knowledge of the biological system and hence makes it challenging to accurately mimic. Finally, even though technology has rapidly advanced, there are still obvious fabrication as well as surface chemistry limitations.

Despite these challenges, the emergence of techniques to investigate transport through pores and channels in new ways can open up new avenues for research. For example, Soni *et al.* [78] recently described the construction of an instrument that demonstrated synchronous optical and electrical detection of biomolecules traversing solid-state nanopores. This instrument combined total internal reflection fluorescence (TIRF) microscopy with ionic current measurements. A similar instrument could be used for biomimetic nanopores, for example, for imaging the diffusion of transport factors in nucleoporin-coated nanochannels. Alternatively, an integrated nanopore-optical tweezer setup [79] would allow measurement of the force on transport factors

during the translocation process. These type of experiments may yield new information about the forces governing the translocation process, and accordingly shed new light on the mechanism of translocation.

An important question in the field of nucleocytoplasmic transport is which route the transporters take through the NPC. While Ma and Yang [80] recently made a step toward monitoring interactions between nucleoporins and transporters using subdiffraction microscopy, they could not yet solve the complete puzzle due to limited resolution in their setup. A comprehensive analysis of the biophysical properties of yeast FG-Nups by Yamada *et al.* [81] found that Nups organize as extended random coils and molten globules described as ‘trees’ and ‘shrubs’ depending upon whether the Nups are strongly charged or relatively uncharged. One can envision that by tethering FG-Nups to nano-patterned slits, one could study through which pathway (i.e., tree or shrub) the transporter molecules diffuse through this ‘forest’. Such measurements would require nanometer-accuracy tracking, which appears to be possible to achieve using state-of-the-art single-molecule fluorescence methods.

To conclude, new technological abilities to study and shape matter at the nanoscale have enabled the development and exploration of various types of biomimetic nanopores. Such pores can be used in an array of applications in biotechnology, notably as biosensors and separation filters. By constructing artificial systems that resemble biological pores from the bottom up, the biomimetic approach has also yielded new knowledge about biological pores, in particular, the nuclear pore complex. Overall, biomimetic nanopores form an exciting emerging research field with ample opportunities for new applications and discoveries.

Acknowledgements. We thank the EC program NanoSci E+, the EC project READNA, and the ERC project NANOforBIO for funding. TRB was supported by a Marie Curie International Incoming Fellowship within the 7th European Community Framework Programme.

References

- 1 Gouaux, E. and MacKinnon, R. Principles of Selective Ion Transport in Channels and Pumps. *Science* **310**, 1461-1465 (2005).
 - 2 Bhushan, B. Biomimetics: lessons from nature-an overview. *Phil. Trans. R. Soc. A* **367**, 1445-1486 (2009).
 - 3 Bar-Cohen, Y. Biomimetics: Biologically Inspired Technologies (1st ed.). CRC Press (2005).
 - 4 Ball, P. Life's lessons in design. *Nature* **409**, 413-416 (2001).
 - 5 Sarikaya, M. *et al.* Molecular biomimetics: nanotechnology through biology. *Nature Materials* **2**, 557-585 (2003).
 - 6 Bayley, H. and Cremer, P. S. Stochastic sensors inspired by biology. *Nature* **413**, 226-230 (2001).
 - 7 Dekker, C. Solid-state nanopores. *Nature Nanotechnology* **2**, 209-215 (2007).
 - 8 Li, J. *et al.* Ion-beam sculpting at nanometer length scales. *Nature* **412**, 166-169 (2001).
 - 9 Storm, A. J. *et al.* Fabrication of solid-state nanopores with single-nanometre precision. *Nature Materials* **2**, 537-540 (2003).
 - 10 Zhang, Y. *et al.* Artificial cells: building bioinspired systems using small-scale biology. *Trends in Biotechnology* **26**, 14-20 (2008).
 - 11 Rhee, M. and Burn, M. A. Nanopore sequencing technology: nanopore preparations. *Trends in Biotechnology* **25**, 174-181 (2007).
 - 12 Gyurcsáni, R. E. Chemically-modified nanopores for sensing. *Trends Anal. Chem.* **28**, 627-639 (2008).
 - 13 Baker, L.A. *et al.* Biomaterials and Biotechnologies Based on Nanotube Membranes. *Crit. Rev. Solid State and Mater. Sci.* **30**, 183-205 (2005).
 - 14 Huo, X. *et al.* Biomimetic smart nanopores and nanochannels. *Chem. Soc. Rev.* Advance Article, DOI: 10.1039/C0CS00053A (2011).
 - 15 Siwy, Z. and Fuliński, A. Fabrication of a Synthetic Nanopore Ion Pump. *Phys. Rev. Lett.* **89**, 198103 (2002).
 - 16 Poretics, <http://www.sterlitech.com>.
 - 17 Li, J. *et al.* DNA molecules and configurations in a solid-state nanopore microscope. *Nature Materials* **2**, 611-615 (2003).
 - 18 Fologea, D. *et al.* Detecting Single Stranded DNA with a Solid State Nanopore. *Nano Letters* **5**, 1905-1909 (2005).
 - 19 Kowalczyk, S. W. *et al.* Unraveling single-stranded DNA in a solid-state nanopore. *Nano Letters* **10**, 1414-1420 (2010).
-

- 20 Storm, A. J. *et al.* Fast DNA Translocation through a Solid-State Nanopore. *Nano Letters* **5**, 1193-1197 (2005).
 - 21 Skinner, G. M. *et al.* Distinguishing Single- and Double-stranded Nucleic Acids using Solid-State Nanopores. *Nano Letters* **9**, 2953-2960 (2009).
 - 22 Han, A. *et al.* Sensing protein molecules using nanofabricated pores. *Appl. Phys. Lett.* **88**, 093901 (2006).
 - 23 Talaga, J. S. and Li, J. Single-molecule protein unfolding in solid state nanopores. *J. Am. Chem. Soc.* **131**, 9287-9297 (2009).
 - 24 Hall, A. R. *et al.* Translocation of Single-Wall Carbon Nanotubes Through Solid-State Nanopores. *Nano Letters*, DOI: 10.1021/nl200873w (2011).
 - 25 Kowalczyk, S. W. *et al.* Detection of local protein structures along DNA using solid-state nanopores. *Nano Letters* **10**, 324-328 (2010).
 - 26 Wanunu, M. *et al.* DNA Profiling Using Solid-State Nanopores: Detection of DNA-Binding Molecules. *Nano Letters* **9**, 3498-3502 (2009).
 - 27 Wanunu, M. and Meller, A. Chemically Modified Solid-State Nanopores. *Nano Lett.* **7**, 1580-1585 (2007).
 - 28 Jirage, K. B. *et al.* Effect of thiol chemisorption on the transport properties of gold nanotubule membranes. *Anal. Chem.* **71**, 4913-4918 (1999).
 - 29 Martin, C. R. Nanomaterials: A Membrane-Based Synthetic Approach. *Science* **266**, 1961-1966 (1994).
 - 30 Yusko, E. C. *et al.* Controlling protein translocation through nanopores with bio-inspired fluid walls. *Nature Nanotechnology* **6**, 253-260 (2011).
 - 31 Caspi, Y. *et al.* Synthetic Mimic of Selective Transport Through the Nuclear Pore Complex. *Nano Letters* **8**, 3728-3724 (2008).
 - 32 Hille, B. *Ion Channels of Excitable Membranes* (3rd ed.). Sinauer Associates (2001).
 - 33 Hou, X. *et al.* A Biomimetic Potassium Responsive Nanochannel: G-Quadruplex DNA Conformational Switching in a Synthetic Nanopore. *J. Am. Chem. Soc.* **131**, 7800-7805 (2009).
 - 34 Tian, Y. *et al.* A biomimetic zinc activated ion channel. *Chem. Commun.* **46**, 1682-1684 (2010).
 - 35 Yameen, B. B. *et al.* Synthetic Proton-Gated Ion Channels via Single Solid-State Nanochannels Modified with Responsive Polymer. *Nano Letters* **9**, 2788-2793 (2009).
 - 36 Siwy, Z. Ion Current Rectification in Nanopores and Nanotubes with Broken Symmetry – Revisited. *Advances Functional Materials* **16**, 735-746 (2006).
 - 37 Wen L. *et al.* Bioinspired Smart Gating of Nanochannels Toward Photoelectric-Conversion Systems. *Advanced Materials* **22**, 1021-1024 (2010).
-

- 38 Lee, S. B. *et al.* Antibody-Based Bio-Nanotube Membranes for Enantiomeric Drug Separations. *Science* **296**, 2198-2200 (2002).
 - 39 Lakshmi, B. and Martin, C. R. Enantioseparation Using Apoenzymes Immobilized in a Porous Polymeric Membrane. *Nature* **388**, 758-760 (1997).
 - 40 Kohli, P. *et al.* DNA-Functionalized Nanotube Membranes with Single-Base Mismatch Selectivity. *Science* **305**, 984-986 (2004).
 - 41 Iqbal, S. M. *et al.* Solid-state nanopore channels with DNA selectivity. *Nature Nanotechnology* **2**, 243-248 (2007).
 - 42 Yu, S. F. *et al.* Size-Based Protein Separations in Poly(ethylene glycol)-Derivatized Gold Nanotubule Membranes. *Nano Letters* **1**, 495-498 (2001).
 - 43 Vlassiouk, I. *et al.* Versatile ultrathin nanoporous silicon nitride membranes. *Proc. Natl. Acad. Sci. USA*. **106**, 21039-21044 (2009).
 - 44 Savariar, E. N. *et al.* Molecular discrimination inside polymer nanotubules. *Nature Nanotechnology* **3**, 112-117 (2008).
 - 45 Lee, S. B. *et al.* pH-Switchable, Ion-Permselective Gold Nanotubule Membranes Based on Chemisorbed Cysteine. *Anal. Chem.* **73**, 768-775 (2001).
 - 46 Hou, Z. Z. *et al.* Self-Assembled Monolayers on Electroless Gold Impart pH-Responsive Transport of Ions in Porous Membranes. *Langmuir* **16**, 2401-2404 (2000).
 - 47 Song, L. *et al.* Structure of staphylococcal alpha-hemolysin, a heptameric transmembrane pore. *Science* **274**, 1859-1865 (1996).
 - 48 Kasianowicz, J. J. *et al.* Characterization of individual polynucleotide molecules using a membrane channel. *Proc. Natl. Acad. Sci. USA*. **93**, 13770-13773 (1996).
 - 49 Branton, D. *et al.* The potential and challenges of nanopore sequencing. *Nature Biotechnology* **26**, 1146-1153 (2008).
 - 50 Akeson, M. *et al.* Microsecond time-scale discrimination among polycytidylic acid, polyadenylic acid, and polyuridylic acid as homopolymers or as segments within single RNA molecules. *Biophys. J.* **77**, 3227-3233 (1999).
 - 51 Bayley, H, and Jayasinghe, L. Functional engineered channels and pores. *Mol. Membr. Biol.* **21**, 209-220 (2004).
 - 52 Bayley, H. *et al.* Engineered Nanopores in NanoBiotechnology (eds Niemeyer, C. M. and Mirkin, C. A.), Wiley-VCH, Weinheim (2005).
 - 53 Maglia, G. Enhanced translocation of single DNA molecules through alpha-hemolysin nanopores by manipulation of internal charge. *Proc. Natl. Acad. Sci. USA*. **105**, 19720-19725 (2008).
 - 54 Rincon-Restrepo, M. *et al.* Controlled Translocation of Individual DNA Molecules through Protein Nanopores with Engineered Molecular Brakes. *Nano Letters* **11**, 746-750 (2011).
-

-
- 55 Movileanu, L. *et al.* Detecting protein analytes that modulate transmembrane movement of a polymer chain within a single protein pore. *Nature Biotechnology* **18**, 1091-1095 (2000).
- 56 Gu, L. Q. *et al.* Stochastic sensing of organic analytes by a pore-forming protein containing a molecular adapter. *Nature* **398**, 686-690 (1999).
- 57 Kang, X. *et al.* Stochastic Detection of Enantiomers, *J. Am. Chem. Soc.* **128**, 10684-10685 (2006).
- 58 Howorka, S. and Siwy, Z. Nanopore analytics: sensing of single molecules. *Chem. Soc. Rev.* **38**, 2360-2384 (2009).
- 59 Halverson, K. M. *et al.* Anthrax biosensor, protective antigen ion channel asymmetric blockade. *J. Biol. Chem.* **280**, 34056-34062 (2005).
- 60 Nestrorovich, E. M. *et al.* Designed to penetrate: Time-resolved interaction of single antibiotic molecules with bacterial pores. *Proc. Natl. Acad. Sci. USA.* **99**, 9789-9794 (2002).
- 61 Butler, T. Z. *et al.* Single-molecule DNA detection with an engineered MspA protein nanopore. *Proc. Natl. Acad. Sci. USA.* **105**, 20647-20652 (2008).
- 62 Derrington, I. M. *et al.* Nanopore DNA sequencing with MspA. *Proc. Natl. Acad. Sci. USA.* **107**, 16060-16065 (2010).
- 63 Schneider, G. F. *et al.* DNA translocation through graphene nanopores. *Nano Lett.* **10**, 3163-3167 (2010).
- 64 Merchant, C. A. *et al.* DNA translocation through graphene nanopores. *Nano Lett.* **10**, 2915-2921.
- 65 Garaj, S. *et al.* Graphene as a subnanometre trans-electrode membrane. *Nature* **467**, 190-193 (2010).
- 66 Koçer, A. *et al.* Synthesis and utilization of reversible and irreversible light-activated nanovalves derived from the channel protein MscL. *Nature Protocols* **2**, 1426-1437 (2007).
- 67 Koçer, A. *et al.* A Light-Actuated Nanovalve Derived from a Channel Protein. *Science* **309**, 755-758 (2005).
- 68 Majd, S. *et al.* Applications of biological pores in nanomedicine, sensing, and nanoelectronics. *Current Opinion in Biotechnology* **31**, 439-476 (2010).
- 69 Balme, S. *et al.* New Bioinspired Membrane Made of a Biological Ion Channel Confined into the Cylindrical Nanopore of a Solid-State Polymer. *Nano Letters* **11**, 712-716 (2011).
- 70 Hall, A. R. *et al.* Hybrid pore formation by directed insertion of alpha-haemolysin into solid-state nanopores. *Nature Nanotechnology* **5**, 874-877 (2010).
- 71 Clarke, J. *et al.* Continuous base identification for single-molecule nanopore DNA sequencing. *Nature Nanotechnology* **4**, 265-270 (2009).
-

-
- 72 Jovanovic-Talisman, T. *et al.* Artificial nanopores that mimic the transport selectivity of the nuclear pore complex. *Nature* **457**, 1023-1027 (2009).
- 73 Kowalczyk, S. W. *et al.* Single-molecule transport across an individual biomimetic nuclear pore complex. *Nature Nanotechnology*, accepted (2011).
- 74 Alberts, B. *et al.* *Molecular Biology of the Cell* (5th ed.). New York: Garland Science (2008).
- 75 Alber, F. *et al.* The molecular architecture of the nuclear pore complex. *Nature* **450**, 695-701 (2007).
- 76 Denning, D. P. *et al.* Disorder in the nuclear pore complex: The FG repeat regions of nucleoporins are natively unfolded. *Proc. Natl. Acad. Sci. USA*. **100**, 2450-2455 (2003).
- 77 Strawn, L. A. *et al.* Minimal nuclear pore complex define FG repeat domains essential for transport. *Nature Cell Biology* **6**, 197-206 (2004).
- 78 Soni, G. V. *et al.* Synchronous optical and electrical detection of biomolecules traversing through solid-state nanopores. *Rev. Sci. Instrum.* **81**, 014301 (2010).
- 79 Keyser, U. F. *et al.* Direct force measurements on DNA in a solid-state nanopore. *Nature Physics* **2**, 473-477 (2006).
- 80 Ma, J. and Yang, W. Three-dimensional distribution of transient interactions in the nuclear pore complex obtained from single-molecule snapshots. *Proc. Natl. Acad. Sci. USA*. **107**, 7305-7310 (2010).
- 81 Yamada, J. *et al.* A bimodal distribution of two distinct categories of intrinsically-disordered structures with separate functions in FG nucleoporins. *Mol. Cell. Proteomics* **9**, 2205-2224 (2010).
- 82 D. Deamer. Nanopore Analysis of Nucleic Acids Bound to Exonucleases and Polymerases. *Annu. Rev. Biophys.* **39**, 79-90 (2010).
- 83 Illustrations used in Figures 5a and 5b (left) are taken from: <http://newswire.rockefeller.edu/?page=engine&id=870>
-

Chapter 9

Single-molecule transport across an individual biomimetic nuclear pore complex

Nuclear pore complexes (NPC) regulate the selective exchange of RNA and proteins across the nuclear envelope in eukaryotic cells [1]. Biomimetic strategies offer new opportunities to investigate this remarkable transport phenomenon [2]. Here we show selective transport of proteins across individual biomimetic NPCs at the single molecule level. Each biomimetic NPC is constructed by covalently tethering the natively unfolded phenylalanine-glycine rich (FG) domains of human nucleoporins (Nups), the key component of NPCs, to a solid-state nanopore [3]. Individual translocation events are monitored using ionic current measurements with sub-millisecond temporal resolution. Transport receptors (Imp β) proceed with a dwell time of ~ 2.5 milliseconds for both Nup98- and Nup153-coated pores whereas the passage of non-specific proteins is strongly inhibited with different degrees of selectivity. For pores up to ~ 25 nm in diameter, Nups form a dense and lowly conducting barrier whereas Nups in larger pores adopt a more open structure. Our biomimetic NPC provides a quantitative platform for studying nucleocytoplasmic transport phenomena at the single-molecule level *in vitro*.

This chapter has been published as S.W. Kowalczyk, L. Kapinos, T. R. Blosser, T. Magalhães, P. van Nies, R.Y.H. Lim, and C. Dekker, *Nature Nanotechnology* **6**, 433–438 (2011).

9.1 Introduction

The nuclear pore complex (NPC) is the sole connection between the nucleus and the cytosol of eukaryotic cells. By connecting the genetic material and the protein-synthesizing apparatus, this remarkable ‘gatekeeper’ [4] controls all nucleocytoplasmic transport. The NPC acts as a selective sieve which is permeable to ions and small solutes (up to ~40 kD), while macromolecular access is reserved for transport receptors (karyopherins) that ferry cargo. Vertebrate NPCs have a total mass of ~120 MDa and are composed of ~30 distinct protein subunits (nucleoporins or Nups) [5]. Roughly one third of these Nups contain natively unfolded FG domains [6] that are rich in mainly FxFG or GLFG repeat motifs (F-Phe; G-Gly; L-Leu; x-any amino acid). Importantly, the FG-domains are believed to constitute the key NPC components that regulate the selective access of receptor-cargo complexes across the NPC channel [7].

There is a need to test the various models that have been proposed for the mechanism of transport. Current NPC transport models include the ‘virtual-gate’ [8, 9], the ‘polymer-brush’ [10], the ‘selective-phase’ [11, 12], and the ‘reduction-of-dimensionality’ [13] models. It has been argued that both brush-like (less cohesive FxFG domains) and meshwork-like (more cohesive GLFG domains) Nup conformations are present in the NPC [14]. Despite recent experimental efforts [15], it remains a challenge to discriminate between NPC models due to the complexity of the cellular environment. It would be useful to reconstitute the large NPC *in vitro*, where conditions and parameters can be changed systematically, but this has proven impossible. It has thus remained a challenge to probe selective transport at the relevant length and time scales.

9.2 Biomimetic nuclear pore complex

In this work, we take a bottom-up approach that enables single-molecule transport studies on a biomimetic ‘minimalist NPC’ *in vitro*. We construct biomimetic NPCs by tethering FG Nups to individual solid-state nanopores. This follows bulk selective transport experiments through parallel (~10⁸) artificial NPCs constructed from polymeric membranes [2] and functionalized long nanochannels [16–19]. The first step in our bottom-up approach [20] involves drilling a small hole (nanopore) in a thin freestanding silicon nitride (SiN) membrane with a focused transmission electron microscope (TEM) beam (see Figure 9.1a and Methods) [3, 21]. Subsequently, Nup

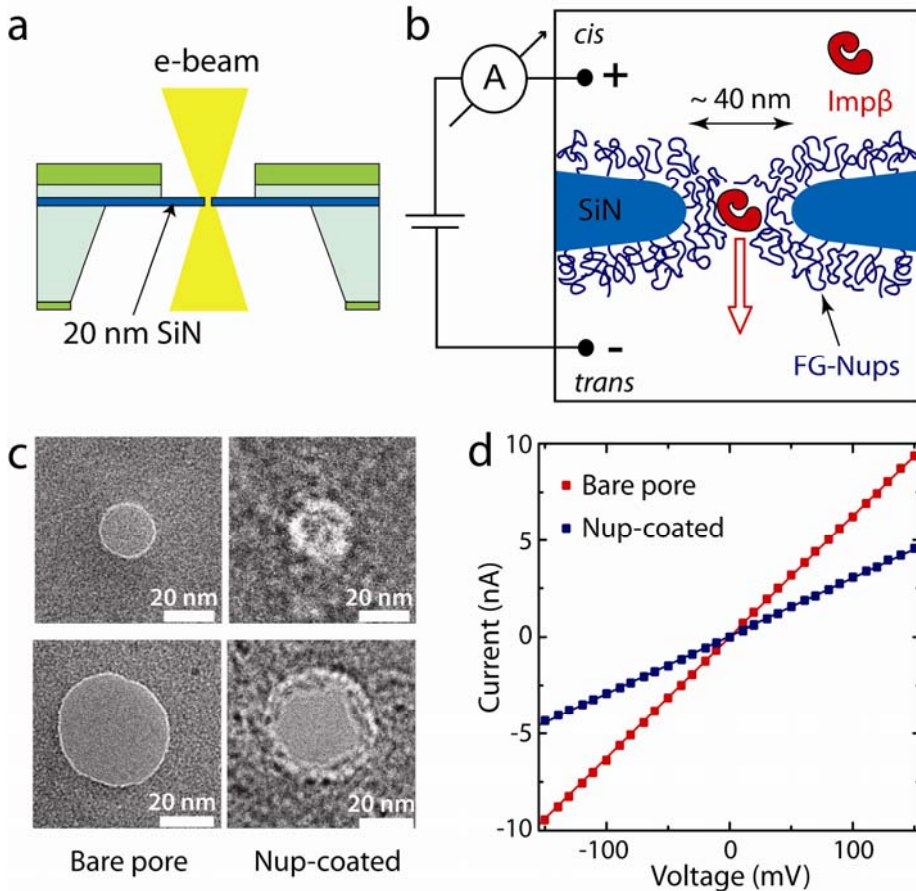


Figure 9.1 Biomimetic nuclear pore complex. (a) Side-view schematic showing the device consisting of a 20 nm thin free-standing silicon nitride window (blue layer) embedded in a silicon wafer (light green). A nanopore is drilled using a highly focused electron beam (yellow). (b) A sketch showing the concept of the experiment. The biomimetic NPC is engineered by attaching FG-Nups to a solid-state nanopore and transport of Imp β is measured by monitoring the trans-pore current. (c) TEM images of the same nanopore with a diameter of 20 nm (top) or 40 nm (bottom) before (left) and after (right) coating with Nup98. (d) Example of a current-voltage (I-V) curve before (red) and after (blue) coating a 40 nm nanopore with Nup98, showing an increased resistance due to the coating.

functionalization of the nanopore is performed in a three-step process similar to the immobilization of DNA to silicon surfaces [22] (see SI for details). Representative

TEM images (Figure 9.1c) confirm the presence of organic material after coating a nanopore with Nups. Note that we work with truncated versions of Nup98 and Nup153 which are limited to the relevant FG-domains (see Materials and Methods). The SiN membrane is placed in a microfluidic flow cell where a single nanopore forms the only connection between two compartments (Figure 9.1b). Subsequently we measure the transport properties of our biomimetic NPC. Electrical measurements were previously performed on the nuclear envelope [23, 24] but these remain in dispute in the light of technical issues with sealing of the nuclear membrane.

Ion current measurements through a 40-nm pore in near-physiological salt conditions (Figure 9.1d) shows an increased resistance (decreased conductance) upon coating the pore with Nup98, which partially blocks the ion conductance in comparison to a bare pore. The strictly linear current-voltage (I-V) characteristics indicate that the Nups are not aligned by the applied electric field (i.e. in accordance to their low charge; see Table T9.1 and SI-9.5), which merely acts as a noninvasive probe. We estimate the Nup density to be ~ 1 Nup per 50 nm^2 along the pore's circumference (see SI-9.3). Given the hydrodynamic diameter of these proteins ($\sim 11 \text{ nm}$) this is a very high density, close to monolayer coverage. Current power spectral densities [25] show comparable noise levels at high frequencies with an increased $1/f$ -type low-frequency noise for the NPC mimics compared to the bare pores (see SI-6). This can likely be attributed to the dynamic fluctuations of Nups, similar to reports for the motion of polymeric subunits in a nanopore [26].

Figure 9.2a compares the measured conductance for bare (black squares), Nup98- (green circles), and Nup153-coated pores (inset; red triangles) over a wide range of pore diameters. Three observations stand out. First, the conductance decreases in the presence of Nups regardless of pore size. Second, Nup98 has a stronger effect at lowering the conductance than Nup153. Third, surprisingly, the pore conductance remains almost negligible up to about 25 nm, followed by a rise with a slope that is roughly similar to that of bare pores.

We discuss two simple models that may potentially account for these data. In model 1, the pore is filled with a Nup meshwork with multiple channels of some characteristic size, corresponding to the selective-phase model [11, 12] (Figure 9.2c). This gives rise to a finite ionic permeability, which is a material parameter that is independent of nanopore diameter. Accordingly, model 1 exhibits a linear conductance [27] as a function of pore diameter (Figure 9.2a, dashed line) as given by $G(r) = \gamma G_0(r)$, where G_0 is the bare pore conductance, γ is a fraction that denotes the reduction of the conduction, and r is the pore radius. This yields an effective ion

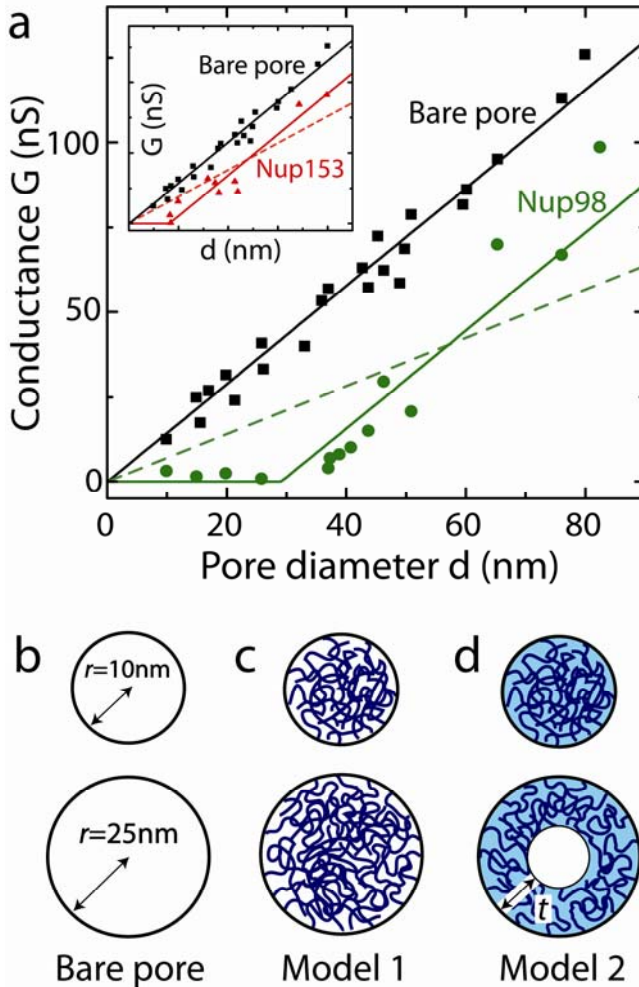


Figure 9.2 Conductance measurements and models. (a) Measured conductances versus pore diameter for bare pores (black points), Nup98-coated (green), and in the inset for Nup153-coated (red) pores. For all pores, the pore conductance decreases upon coating. Colored lines are linear fits of two models, see text. Model 2 (solid lines) is found to fit the data much better than model 1 (dashed lines). (b–d) Schematics showing the small- and large-pore regimes for models 1 and 2, as discussed in the text. Fitting to model 2 yields a Nup layer thickness $t_{\text{Nup98}} = 15 \pm 1$ nm and $t_{\text{Nup153}} = 8 \pm 1$ nm along the outer circumference of the pore for Nup98 and Nup153, respectively.

permeability of $\gamma = 50\%$ for Nup98 and $\gamma = 67\%$ for Nup153 (defining the permeability of a bare pore as 100%). However, this provides a very poor fit to the data with a normalized reduced sum of squared residuals $\chi^2 = 16.7$ and 8.1 for Nup98 and Nup153, respectively.

In model 2, the Nups coat the circumference of a pore with a dense layer of thickness t (that we assume to first order to not significantly conduct ions), leaving an open channel through the central pore axis that is available for ion conduction (Figure 9.2d). For small pores ($r < t$), the high density of Nups occludes the entire channel thereby blocking ion conduction ($G \approx 0$). For large pores ($r > t$), a more open central channel is formed based on the difficulty for opposing Nups to stretch and cross-link each other across the pore. This conductance is given by $G(r) = G_0(r-t)$, i.e., a linear dependence on pore diameter beyond an offset of 29 ± 2 nm for Nup98- and 16 ± 2 nm for Nup153-coated pores (solid lines in Figure 9.2a and inset). Model 2 fits the data much better, with $\chi^2 = 3.8$ and 3.6 for Nup98 and Nup153, respectively. The horizontal offsets correspond to $t_{\text{Nup98}} = 15 \pm 1$ nm and $t_{\text{Nup153}} = 8 \pm 1$ nm along the pore circumference. Note that these two models are limiting cases only. Other Nup arrangements with equal excluded conducting areas are possible as well (Figure S9.8). Indeed, the Nups could resemble some subtle mixture of model 1 and 2 where some low density of dynamic Nups is present at the pore center. Nevertheless, model 2 is close to recent descriptions of Nups within the NPC [28, 29].

9.3 Protein translocation through a biomimetic nuclear pore complex

An important question is whether these minimal hybrid nanopores indeed mimic NPCs. In order to test for the most discriminating characteristic, viz. selectivity, we compare the transport properties of Imp β (97 kDa) and bovine serum albumin (BSA; a 66 kDa protein with similar charge and isoelectric point, see SI) through 40 nm-diameter pores. Using first a *bare* pore as a control, we observe downward spike-like changes in the open-pore conductance after adding either Imp β or BSA to the *cis* side (Figure 9.3a). Each spike signals the translocation of an individual protein [3, 30]. Subsequently, we repeated these experiments on Nup-modified pores. Figure 9.3b shows representative traces of Imp β translocations through Nup98-coated pores (and similarly, Figure S9.9 for Nup153-coated pores). Short temporal depressions in the current again appear after adding Imp β . To our knowledge, these are the first single-molecule measurements of protein transport across individual biomimetic NPCs. An analysis of inter-event times (see SI-9) indicates that about $86 \pm 4\%$ of the observed

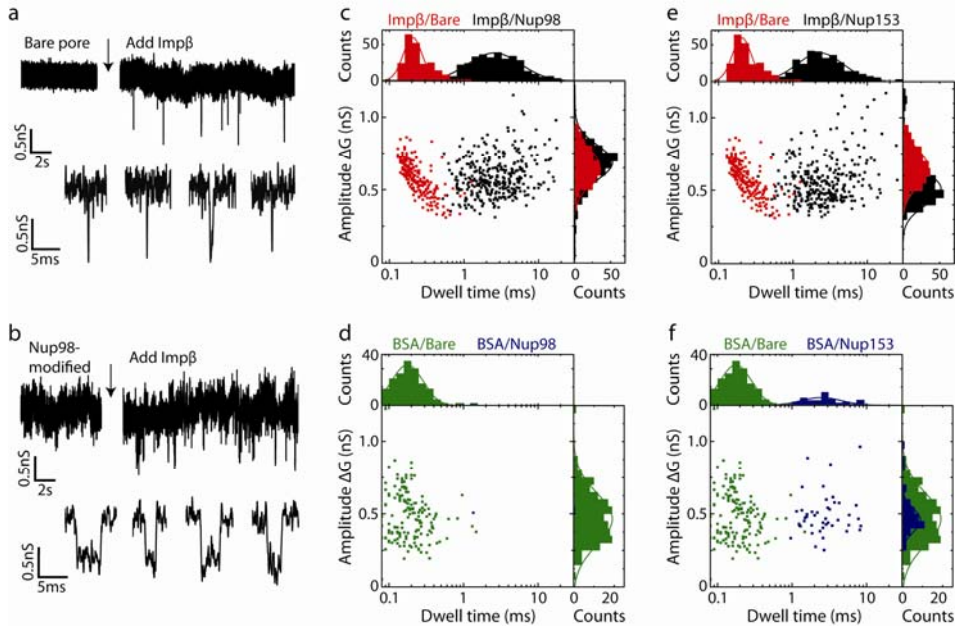


Figure 9.3 Single-molecule translocation events. (a) Representative ion current trace before and after addition of Imp β in a bare pore. Downward spikes appear in the current trace upon addition of Imp β . Each spike is a single-molecule event. The lower panel shows zoom-ins on a number of events. (b) Same for a Nup98-coated pore. (c) Scatter diagram for Imp β translocation in a bare (red) and Nup98-modified (black) pore, where each point represents an individual event. Event amplitudes are similar (~ 0.6 nS), while the dwell times differ by more than an order of magnitude (~ 200 μ s versus ~ 3 ms). (d) Scatter diagram for BSA translocation through a bare (green), and Nup98 pore (black). (e) Same as c, but for a Nup153 pore. (f) Same as d, but for a Nup153-modified pore.

events (spikes) are indeed translocations rather than binding events where the protein does return to the *cis* chamber. This corresponds well with single-molecule fluorescence studies that showed that $\sim 20\%$ of Imp β translocations were aborted after entering into the NPC [31].

We continue with a detailed quantification of the amplitudes and dwell times of these translocation events, using a standard event-fitting algorithm described before [32] (Table T9.2). Each event is plotted in a scatter diagram of ΔG versus τ , where ΔG is the conductance blockade amplitude and τ the dwell time (Figure 9.3c–f). Note that the average ΔG for Imp β is similar for a bare (0.59 ± 0.12 nS), a Nup98-coated

(0.56 ± 0.12 nS) and a Nup153-coated pore (0.50 ± 0.10 nS). This is expected since ΔG is a measure of the size of the translocating object. The Imp β dwell time through a bare pore is short: a log-normal fit to the data gives 190 ± 40 μ s (Figure 9.3e, top histogram), in good agreement with previous reports of translocations of similar-sized proteins through solid-state nanopores [30]. As expected, comparable values (0.47 ± 0.19 nS; 170 ± 70 μ s) were obtained for BSA translocation through a bare pore (Figure 9.3d).

Interestingly, we measure much longer dwell times for the passage of Imp β through Nup-coated pores: 2.7 ± 0.3 ms (average value from independent measurements on three different pores, $N=3$) for a Nup98-coated pore (Figure 9.3e) and 2.2 ± 0.3 ms (also $N=3$) for a Nup153-coated pore (Figure 9.3f). This is more than a 10-fold increase in dwell time compared to the bare pore. Remarkably, these values are in close agreement with the ~ 5 ms dwell time of Imp β in NPCs obtained by single molecule fluorescence *in vivo* [33] and in permeabilized cells [28, 34, 35] (Figure S9.12). This indicates that Imp β interacts with the Nups for a substantial amount of time before exiting the pore. An important control is our observation that the dwell time is independent of the applied voltage (Figure S9.5b). This contrasts conventional biomolecular transport through bare pores where the dwell time is inversely proportional to the applied voltage [36], and it shows that the ~ 2.5 ms time is intrinsically due to the Imp β -Nup interaction.

9.4 Selectivity

It is noteworthy that our simple biomimetic NPCs display the exclusive selectivity of native NPCs. A comparison of the event rates of BSA and Imp β translocation through a 46 nm pore before and after Nup98 modification is shown in Figure 9.4. Most strikingly, the passage of BSA shows a dramatic 60-fold reduction in event rate yielding 0.21 events s^{-1} in a bare pore but only 0.0035 events s^{-1} in the Nup98-coated pore. In contrast, the event rate for Imp β is similar in bare pores and Nup98-coated pores (0.27 versus 0.21 events s^{-1}). The biomimetic Nup98-coated pore thus very effectively blocks the passage of BSA, while the event frequency for Imp β is not significantly affected. For a 42 nm-diameter Nup153-coated pore, translocation of BSA and Imp β yielded rates of 0.05 and 0.25 events s^{-1} , respectively. This indicates that Nup98 hinders BSA transport more strongly than Nup153, although both Nup support similar Imp β event rates. Indeed, sequence analysis [14] indicates that Nup98 is more cohesive than Nup153 (Table T9.3), providing for a more effective physical

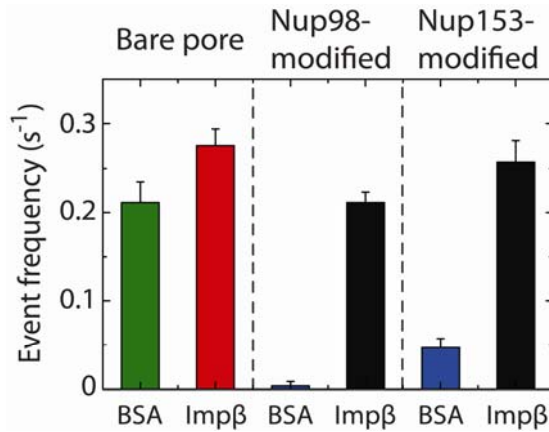


Figure 9.4 Event frequencies through bare and Nup-modified pores, showing NPC-like selectivity. Average number of events per second for BSA through a bare pore (green), Impβ through a bare pore (red), BSA through a Nup98-coated pore (blue), Impβ through a Nup98-coated pore (black), and finally BSA through a Nup153-coated pore (blue) and Impβ through a Nup153-coated pore. Pore diameter was 42–46 nm in all cases. The passage of BSA through the Nup-modified pore is significantly inhibited in Nup-coated pores, whereas that of Impβ is not, i.e., these pores display the hallmark of NPC selectivity.

barrier. The reduced selectivity is also consistent with our finding (Figure 9.2d) that the layer of Nup 153 was thinner than that for the Nup98-coated pore. Our findings indicate that a single Nup is enough to form a barrier, and that intrinsic differences between Nups result in varying barrier effectiveness. Additional enhancement of transport selectivity might be achieved through competition of transport receptors and non-specific cargo [2, 37, 38].

Finally, we used Alexa488-labeled Impβ to verify that Impβ proteins actually translocate through our Nup-coated pores to the *trans* chamber. Here we translocated proteins for 20 hours through an array of 61 parallel Nup98-coated nanopores with diameters of 43 ± 3 nm (Figure 9.5a and S9.14) to maximize the amount of translocated Impβ in the *trans* chamber. Subsequently, buffer from the 20 μL *trans* chamber was deposited on a cover slide for total-internal-reflection-fluorescence (TIRF) imaging (see Methods). Fluorescent proteins are clearly observed (Figure 9.5b), corresponding to an amount of ~1 pM of Impβ that translocated to the *trans* chamber based, in good agreement with the expected value of about 2 pM (SI-14).

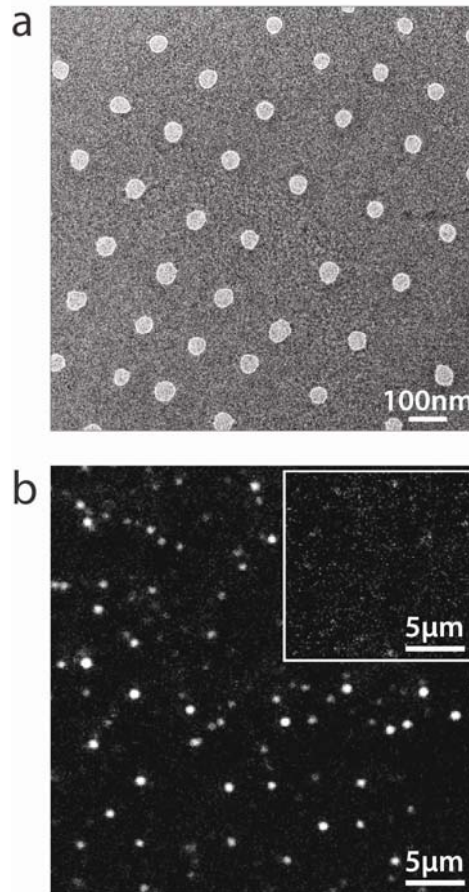


Figure 9.5 Nanopore array. a, TEM image of a nanopore array consisting 61 pores of 43 ± 3 nm in diameter. b, TIRF image of individual Alexa488-labeled fluorescent Imp β proteins that were translocated through the Nup98-coated nanopore array of panel a to the *trans* chamber and subsequently immobilized onto a cover slide (see text). The inset shows a control image of buffer only, for exactly similar TIRF conditions.

To conclude, we have built a *de novo* designed ‘minimalist NPC’ that faithfully reproduces the essential feature of selectivity of the NPC. We have used electrophysiology as a new technique to measure ion and protein transport across the biomimetic pore at single-molecule resolution. We have found that translocation events through such biomimetic NPCs are indeed observed for transport receptors

(Imp β) whereas the passage of non-specific proteins (BSA) is strongly inhibited. Importantly, our approach has the advantage of revealing intrinsic differences between Nups that can determine the selectivity barrier. Future work may encompass a step-wise expansion of the complexity of the system, as well as measurement of forces on transport factors during translocation using an integrated nanopore-optical tweezers setup [39].

9.5 Materials and Methods

Cloning and expression of recombinant Nup153 and Nup98

The 601aa C-terminal FG-repeat domain of human Nup153 (aa 874–1475, Nup153-C) was PCR-cloned into the bacterial expression vector pGEX 6P-1 (GE Healthcare, UK) which contains a N-terminal glutathione-*S*-transferase (GST) and C-terminal His-tag. The nucleotide sequence encoding the FG-domains of human nucleoporin Nup98 (aa 1-505) was cloned into pPEP-TEV vector at the *Bam*HI and *Eco*RI restriction sites employing the prokaryotic expression vector pPEP-TEV [40]. This construct contains a N-terminal His-tag followed by 36 residues of a short laminin linker and a TEV protease cleavage site. To allow attachment of the recombinant Nup153 or Nup98 fragments to the Au surfaces, three cysteines were added to the N-terminus in both cases. The recombinant Cys-Nup153 and Cys-Nup98 were expressed in *Escherichia coli* BL21 (DE3) competent cells (Novagen). The expressed FG-domains were purified under denaturing conditions (8 M urea, 100 mM Na₂HPO₄, 10 mM DTT, and 10 mM Tris-HCl, pH 8.5) using a Ni-NTA column. A PreScission protease (GE Healthcare, UK) was used to cleave both the N-terminal glutathione-*S*-transferase (GST) and C-terminal His-tag from Cys-Nup153-C after purification. TEV protease was used to remove the His-tag from Cys-Nup98. After cleavage, the recombinant fragments of Nup98 carry a pre-sequence of GlyGlySer before the three cysteines at the N-terminus. Some additional residues were also present in the Cys-Nup153-C construct at both termini after cleavage. Subsequently, all FG-domains were purified under denaturing conditions as it was already done previously [11]. The His-tag-free protein fragments were then eluted with a buffer containing 8 M urea, 100 mM Na₂HPO₄, 10 mM DTT, and 10 mM Tris-HCl, pH 8.5. The final protein purity was analyzed by 12% PAGE at 0.1% SDS. The protein concentration was determined by Bradford assay and verified by estimation of protein amounts on Commassie Brilliant Blue-stained SDS-PAGE (12% acryl amide), see also Figure S9.2. Alternatively, the protein concentration was also calculated from the

absorption at 280 nm. An extinction coefficient of the protein fragment was calculated using the ProtParam program available at ExPaSy homepage (<http://us.expasy.org/sprot/>).

Cloning and expression of Importin- β (Imp β)

Full-length human Imp β was amplified by PCR and inserted into a *NcoI*–*Bam*HI digested pETM-11 expression vector (EMBL Protein Expression and Purification Facility). N-terminal His₆-tagged Imp β was expressed in *E. coli* BL21 (DE3) cells at 30 °C overnight and purified on a Ni-NTA column (50 mM TrisHCl, pH 8, 100 mM NaCl, 1 mM DTT; eluted with 80-300 mM imidazole) followed by gel-filtration using Superdex 200 column (GE Healthcare). Purified protein was analyzed by SDS–PAGE (see also Figure S9.2) and selected fractions containing Imp β were pooled, dialyzed against PBS and concentrated. Imp β was also labeled with Alexa Fluor488 sulfodichlorophenol esters (Alexa Fluor488-5-SDP ester) using a standard labeling procedure of Invitrogen Protocols for amine-reactive probes (<http://products.invitrogen.com/ivgn/product/A30052>). The labeling was carried out in PBS buffer with pH 7.2. Under these conditions dye molecules couple mainly to the N terminus (primary amine) of Imp β and the amine groups of the side chains remain mainly unlabeled. This minimizes any effects that might alter the biochemical properties and structure of Imp β . The degree of labeling was 2.8 dyes per Imp β .

Fabrication of solid-state nanopores

Our devices consist of a nanometer-sized hole in a thin silicon nitride (SiN) membrane [3, 21]. Briefly, thin free-standing membrane of low-stress SiN. The free-standing membrane is then placed in a transmission electron microscope (TEM) operated at 300 kV. Formation of a nanopore results from the exposure of the membrane to a tightly focused electron beam. The diameter of the pore can be tuned with sub-nanometer accuracy with direct visual feedback [21]. For this study, we used pores ranging in diameter from 10 to 85 nm. After drilling, the pores are stored in a solution containing 50% ethanol and 50% ddH₂O. A more detailed description of the nanopore fabrication process is given elsewhere [41].

Chemical modification of solid-state nanopores

The surface treatment used to immobilize Nups at the pore is schematically depicted Figure S9.1. First both sides of the sample are subjected to oxygen plasma for about

30 s. This process removes any organic contaminants and results in the oxidation of the surface, yielding it SiO₂. The membranes are then (step 1) immersed into a 5% solution of (aminopropyl)triethoxysilane (APTES; obtained from Pierce (Lausanne, Switzerland)) in pure Methanol for 3-6 hours, followed by rinsing for 10-15 min in pure Methanol, drying under N₂, and baking at 100°C for 30 min. This leaves exposed amine groups [42]. Subsequently (step 2), the amine groups are activated with a water-soluble, non-cleavable heterobifunctional crosslinker Sulfosuccinimidyl-4-(*N*-maleimidomethyl)cyclohexane-1-carboxylate (Sulfo-SMCC; 2 mg powder tablets were obtained from Pierce (Lausanne, Switzerland)) to introduce maleimide groups (step 2). The crosslinkers bear an amine-reactive NHS-ester (NHS esters react with primary amines at pH 7-9 to form stable amide bonds), in addition to a thiol-reactive maleimide (maleimides react with sulfhydryl groups at pH 6.5-7.5 to form stable thioether bonds). 2 mg “no-weigh” powder tablets of Sulfo-SMCC are dissolved in 1.5 ml phosphate-buffered saline (PBS), pH = 7.2. Membranes are then immersed overnight in the resulting solution. Afterwards they are rinsed with Milli-Q filtered water (Millipore, USA), acetone, ethanol, 2-isopropanol, and again Milli-Q. In parallel, Nup98 and Nup153 are dialyzed from buffer containing 8M urea into PBS and 1mM of TCEP is added into their solutions for 30 min to reactivate the SH-groups. Finally, each membrane is incubated for 3 h in solutions containing 3 µg of Nup98 or Nup153 (step 3), which attach to the pore via the maleimide moieties. Ellipsometry on coated SiN membranes confirms the presence of the three layers.

Data acquisition and analysis

Ionic currents are detected by Ag/AgCl electrodes, connected to an amplifier operating in resistive feedback mode (Axopatch 200B, Axon Instruments). All ion current measurements are performed at 150 mM KCL and 10 mM Tris-HCl, pH 8.0. Current traces are measured at 100 kHz bandwidth and digitized at 500 kHz. When necessary, low-pass filtering is applied: bare pore data was low-pass filtered at 5 kHz, Nup-coated pore data at 2 kHz. The upper trace in Figure 9.3b was low-pass filtered at 0.5 kHz for display-purposes. The concentrations used in the nanopore experiment are 4.2 µM for BSA and 2.9 µM for Impβ (13 µM for the experiment with the array). The selectivity measurements were all performed with pores of 44 ± 2 nm size. The event-fitting algorithm used to analyze and label the translocation events was the same as the one described by Storm *et al* [32]. Error bars mentioned in the text denote the standard deviation of the distribution. Only events exceeding 6 times the standard deviation of the open-pore root-mean-square noise are considered. To avoid the

effects of possible baseline fluctuations, we also limited ourselves to events for which the current before and after the event does not change more than 10% of the event amplitude.

Importin- β TIRF imaging

Glass microscope cover slips (22 x 22 mm, number one) were incubated with Poly-L-lysine solution (0.1% (w/v), Sigma-Aldrich) for 5 minutes and washed with PBS. A solution with Alexa-Fluor488-labeled Importin- β (Imp β -Alexa488), extracted from a diluted solution or from the trans chamber in the translocation experiment, was then added at indicated concentrations and allowed to non-specifically adhere to the coated cover slips for 30 minutes. Following this, the fluorescence from individual molecules was detected by a TIRF microscope. The fluorescence signals from these surface-anchored Imp β were excited with a 491 nm diode-pumped solid-state laser (Cobolt) in a total internal reflection geometry, and fluorescence emission from Alexa-488 was detected with a 60x, 1.45 NA, oil immersion objective (Olympus), filtered with a 525/50 filter (Chroma Technology) and imaged onto a CCD camera (Andor iXon 897). Custom-written software was then used to identify single Imp β proteins on the cover slip and to monitor the Alexa-488 fluorescence at these positions.

Acknowledgements. We thank K. A. Williams for suggestions on the chemistry, A.R. Hall, M. van den Hout and X. Janssen for membrane fabrication and discussions, D. Grünwald and G.V. Soni for help with TIRF measurements, Y. Rabin and A. Y. Grosberg for help with theoretical work, and T. Dange, N.H. Dekker, D. Grünwald, P.L. Hagedoorn, G.F. Schneider, and G.M. Skinner for discussions. This research was funded by the “Nederlandse Organisatie voor Wetenschappelijk Onderzoek (NWO)”, the program NanoSci E+ of the European Commission, and the READNA (REvolutionary Approaches and Devices for Nucleic Acid analysis) project of the European Commission. L. Kapinos and R.Y.H. Lim are supported by the National Center of Competence in Research “Nanoscale Science” (NCCR-Nano), the Swiss National Science Foundation, the Biozentrum and the Swiss Nanoscience Institute.

References

- 1 Alberts, B. *et al.*, Molecular Biology of the Cell (5th ed.). New York: Garland Science (2008).
 - 2 Jovanovic-Talisman, T. *et al.* Artificial nanopores that mimic the transport selectivity of the nuclear pore complex. *Nature*, **457**, 1023-1027 (2009).
 - 3 Dekker, C., Solid-state nanopores. *Nature Nanotech.* **2**, 209-215 (2007).
 - 4 Wentz, S.R. Gatekeepers of the nucleus. *Science*. **288**, 1374-1377 (2000).
 - 5 Alber, F. *et al.* The molecular architecture of the nuclear pore complex. *Nature*. **450**, 695-701 (2007).
 - 6 Denning, D.P., Patel, S.S., Uversky, V., Fink, A.L., and Rexach, M.. Disorder in the nuclear pore complex: The FG repeat regions of nucleoporins are natively unfolded. *Proc. Natl. Acad. Sci. USA*. **100**, 2450-2455 (2003).
 - 7 Strawn, L.A., Shen, T., Shulga, N., Goldfarb, D.S., and Wentz, S.R. Minimal nuclear pore complexes define FG repeat domains essential for transport. *Nature Cell Biol.* **6**, 197-206 (2004).
 - 8 Rout, M.P. *et al.* The yeast nuclear pore complex: composition, architecture and transport mechanism. *J. Cell Biol.* **148**, 635-651 (2000).
 - 9 Rout, M.P., Aitchison, J.D., Magnasco, M.O., and Chait, B.T. Virtual gating and nuclear transport: the hole picture. *Trends Cell Biol.* **13**, 622-628 (2003).
 - 10 Lim, R.Y.H. *et al.* Nanomechanical basis of selective gating by the nuclear pore complex. *Science*. **318**, 640-643 (2007).
 - 11 Frey, S., Richter, R.P., and Görlich, D. FG-rich repeats of nuclear pore proteins form a three-dimensional meshwork with hydrogel-like properties. *Science*. **314**, 815-817 (2006).
 - 12 Frey, S. and Görlich, D. A saturated FG-repeat hydrogel can reproduce the permeability properties of nuclear pore complexes. *Cell*. **130**, 512-523 (2007).
 - 13 Peters, R. Translocation Through the Nuclear Pore Complex: Selectivity and Speed by Reduction-of-Dimensionality. *Traffic*. **6**, 421-427 (2005).
 - 14 Yamada, J. *et al.* A Bimodal Distribution of Two Distinct Categories of Intrinsically Disordered Structures with Separate Functions in FG Nucleoporins. *Mol. Cell. Proteomics*. **9**, 2205-2224 (2010).
 - 15 Lowe, A.R. *et al.*, Selectivity mechanism of the nuclear pore complex characterized by single cargo tracking. *Nature*. **467**, 600-603 (2010).
 - 16 Caspi, Y., Zbaida, D., Cohen, H., and Elbaum, M. Synthetic Mimic of Selective Transport Through the Nuclear Pore Complex. *Nano Lett.* **8**, 3728-3724 (2008).
 - 17 Lakshmi, B. and Martin, C.R. Enantioseparation Using Apoenzymes Immobilized in a Porous Polymeric Membrane. *Nature*. **388**, 758-760 (1997).
-

- 18 Lee, S.B. *et al.* Antibody-Based Bio-Nanotube Membranes for Enantiomeric Drug Separations. *Science*. **296**, 2198-2200 (2002).
 - 19 Kohli, P. *et al.* DNA-Functionalized Nanotube Membranes with Single-Base Mismatch Selectivity. *Science*. **305**, 984-986 (2004).
 - 20 Lim, R.Y.H., Aebi, U., and Stoffer, D. From the trap to the basket: getting to the bottom of the nuclear pore complex. *Chromosoma*. **115**, 15-26 (2006).
 - 21 Storm, A.J., Chen, J.H., Ling, X.S., Zandbergen, H.W., and Dekker, C. Fabrication of solid-state nanopores with single-nanometre precision. *Nature Mater.* **2**, 537-540 (2003).
 - 22 Jin, L., Horgan, A., and Levicky, R. Preparation of end-tethered DNA monolayers on siliceous surfaces using heterobifunctional cross-linkers. *Langmuir*. **19**, 6968-6975 (2003).
 - 23 Bustamante, J.O., Liepnis, A., Prendergast, R.A., Hanover, J.A., and Oberleithner, H. Patch clamp and atomic force microscopy demonstrate TATA-binding protein(TBP) interactions with the nuclear pore complex. *J. Membr. Biol.* **146**, 263-272 (1995).
 - 24 Danker, T. *et al.* Nuclear hourglass technique: An approach that detects electrically open nuclear pores in *Xenopus laevis* oocytes. *Proc. Natl. Acad. Sci. USA*. **96**, 13530-13535 (1999).
 - 25 Smeets, R.M.M., Keyser, U.F., Dekker, N.H., and Dekker, C. Noise in solid-state nanopores. *Proc. Natl. Acad. Sci. USA*. **105**, 417-421 (2008).
 - 26 Siwy, Z. and Fulinski, A. Fabrication of a synthetic nanopore ion pump. *Phys. Rev. Lett.* **89**, 198103 (2002).
 - 27 Hall, J.E. Access resistance of a small circular pore. *J. Gen. Physiol.* **66**, 531-532 (1975).
 - 28 Ma, J. and Yang, W. Three-dimensional distribution of transient interactions in the nuclear pore complex obtained from single-molecule snapshots. *Proc. Natl. Acad. Sci. USA*. **107**, 7305-7310 (2010).
 - 29 Moussavi-Baygi, R. Jamali, Y., Karimi, R., and Mofrad, M.R.K. Biophysical Coarse-Grained Modeling Provides Insights into Transport through the Nuclear Pore Complex. *Biophys. J.* **100**, 1410-1419 (2011).
 - 30 Fologea, D., Ledden, B., McNabb, D.S., and Li, J. Electrical characterization of protein molecules by a solid-state nanopore. *Appl. Phys. Lett.* **91**, 053901 (2007).
 - 31 Yang, W. and Musser, S.M. Nuclear import time and transport efficiency depend on importin β concentration. *J. Cell. Biol.* **174**, 951-961 (2006).
 - 32 Storm, A.J., Chen, J.H., Zandbergen, H.W., and Dekker, C. Translocation of double-strand DNA through a silicon oxide nanopore. *Phys. Rev. E*. **71**, 051903 (2005).
-

- 33 Dange, T., Grünwald, D., Grünwald, A., Peters, R., and Kubitscheck, U. Autonomy and robustness of translocation through the nuclear pore complex: a single-molecule study. *J. Cell Biol.* **183**, 77-86 (2008).
- 34 Yang, W.D., Gelles, J., and Musser, S.M. Imaging of single-molecule translocation through nuclear pore complexes. *Proc. Natl. Acad. Sci. USA.* **101**, 12887-12892 (2004).
- 35 Kubitscheck, U. *et al.* Nuclear transport of single molecules: dwell times at the nuclear pore complex. *J. Cell Biol.* **168**, 233-243 (2005).
- 36 Kowalczyk, S.W., Hall, A.R., and Dekker, C. Detection of local protein structures along DNA using solid-state nanopores. *Nano Lett.* **10**, 324-328 (2010).
- 37 Zilman, A., Di Talia, S., Chait, B., Rout, M., and Magnasco, M. Efficiency, selectivity and robustness of the transport through the nuclear pore complex. *PLoS Comput. Biol.* **3**:e125 (2007).
- 38 Zilman, A. *et al.* Enhancement of transport selectivity through nano-channels by non-specific competition. *PLoS Comput. Biol.* **6**:e1000804 (2010).
- 39 Keyser, U.F. *et al.* Direct force measurements on DNA in a solid-state nanopore. *Nature Phys.* **2**, 473-477 (2006).
- 40 Strelkov, S.V., Kreplak, L., Herrmann, H., and Aebi, U. Intermediate filament protein structure determination. *Meth. Cell Biol.* **78**, 25-43 (2004).
- 41 Krapf, D. *et al.* Fabrication and characterization of nanopore-based electrodes with radii down to 2 nm. *Nano Lett.* **6**, 105-109 (2006).
- 42 Wanunu, M. and Meller, A. Chemically modified solid-state nanopores. *Nano Lett.* **7**, 1580-1585 (2007).

9.6 Supplementary Information

Schematic of the chemistry used for Nup-binding

The chemistry used to attach the Nups to the surface consists of three steps. Figure S9.1 shows a schematic. We first coat the pores with APTES, leaving amine groups exposed (step 1 in Figure S9.1). Next, we covalently bind the amines to cross linker Sulfo-SMCC leaving the surface terminated with thiol-reactive maleimides (step 2). We then bind the C-terminal FG-domains of the Nups (98 or 153) via terminal thiols (step 3).

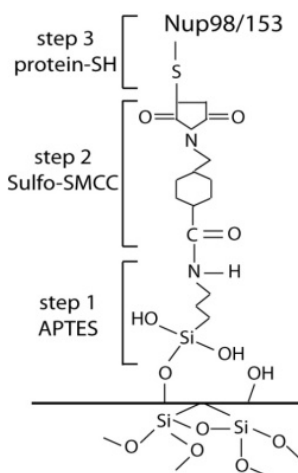


Figure S9.1 Schematic of the chemistry used to covalently bind Nups to the nanopore.

Protein gels

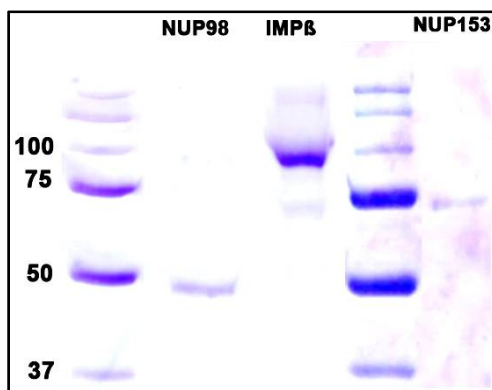


Figure S9.2 Comassie Brilliant Blue-stained SDS-PAGE (12% acrylamide) of Impβ (97 kDa), Nup98 (50 kDa) and Nup153 (62 kDa).

Estimate of the Nup density in the pore

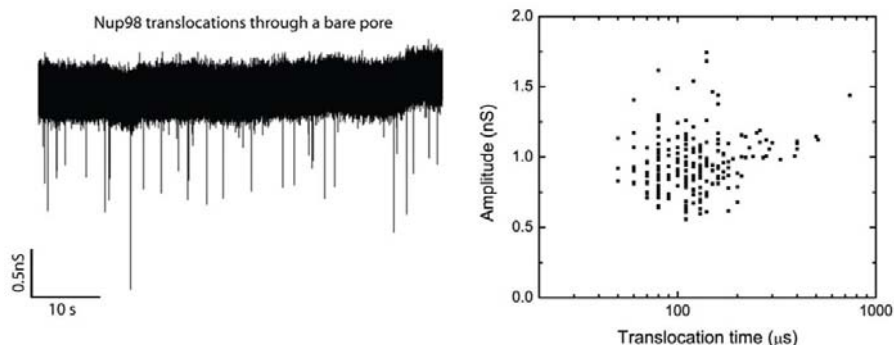


Figure S9.3 Nup98 translocation through a bare pore. (left) Example trace after addition of Nup98 in a bare pore. Downward spikes appear in the current trace upon addition of Nup98. Each spike is a single-molecule event. (right) Scatter diagram for Nup98 translocations. We find that one Nup molecule reduces the open-pore conductance by 0.92 ± 0.18 nS. The average dwell time is 107 ± 30 μ s.

The Nup density in the pore can be estimated as follows: We translocate Nups through a bare pore and quantify the reduction of conductance caused by its presence in the pore. We find that a single translocating Nup98 molecule reduces the open-pore conductance by 0.92 nS (see Figure S9.3). This means that a typical pore of 40 nm in diameter, where the conductance reduces from 58 nS to 16 nS upon coating with Nup98, contains approximately 46 Nups. Given that the surface area of the pore is $2 \cdot \pi \cdot 20 \cdot 20 \approx 2500$ nm², this means that the Nup density is of the order of 1 Nup per 54 nm² at the pore wall surface, i.e., each Nup occupies an area of $\sim 7 \times 7$ nm². Given the hydrodynamic diameter of these proteins (~ 11 nm, as measured from dynamic light scattering (unpublished data); similar values for other Nups were reported in Ref. S1), this is a very high density.

Charge and isoelectric points of BSA, Imp β , Nup98, and Nup153

The theoretical pIs (based on using their amino acid composition) of BSA and Imp β are slightly different (5.6-5.8 and 4.7, respectively, see Table T9.1). However, both values are clearly below pH=8, which will yield the same sign for both proteins in our experimental conditions. Furthermore, the experimental pIs of native (folded) BSA

Protein (total aa)	pI		# of neg. aa	# of pos. aa	Net charge at pH=7	Stokes diameter, nm (d_h)
	Theor. pI	Measured pI, IEF				
BSA (607 aa)	5.6-5.8	4.6-4.9 ^{S2}	99	86	13 -	7.4
Imp β (876 aa)	4.68	5.3	124	75	49 -	12
Nup98 (498 aa)	8.89		12	16	4 +	11.2
Nup153 (602 aa)	8.85		37	43	6 +	11.3

Table T9.1 Theoretical pI values and charges of various proteins (based on its sequence) and experimentally deduced pI values of the native (folded) protein as measured by isoelectric focusing.

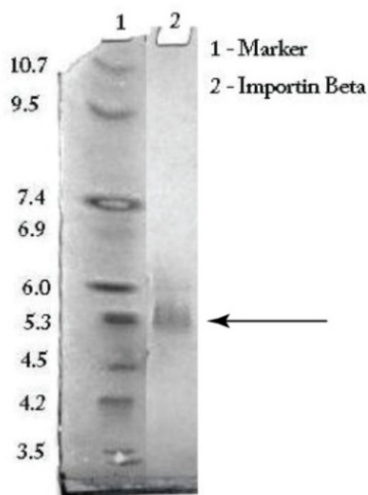


Figure S9.4 Isoelectric focusing gel, showing a pI of about 5.3 for native (folded) Imp β . The 5% polyacrylamide isoelectric gel (Novex IEF Gel from Invitrogen) consist of high-purity acrylamide, bisacrylamide, TEMED, APS, ultrapure water, and 2% ampholytes. It does not contain denaturing reagents.

and Imp β can be different from the theoretical estimates, and indeed they are. For BSA, isoelectric focusing experiments give values of pI=4.6-4.9 [S2]. For Imp β such measurements had not been performed yet, and hence we performed such measurements ourselves, and found an experimental pI of 5.3 for the native (folded) Imp β (data shown in Figure S9.4). We thus find that the experimental values for BSA range from 4.6 to 4.9 versus 5.3 for Imp β , which is not a great difference. Table T9.1

lists the charges of these two proteins. These values are not very different for BSA and Imp β . The size of both proteins is somewhat different. In fact, this further enhances our observations: based on size, the observation of a much lower permeability of BSA through the Nup-coated pores versus Imp β (which is bigger) makes this control only stronger.

Voltage (non-)dependence for Imp β translocations through a Nup-coated pore

As mentioned in the manuscript, the fact that we measure linear I-V relations (Figure 9.1d) up to an applied voltage of at least 200 mV indicates that the Nups in the nanopore are not significantly influenced by the applied electric field. We measured the voltage dependence of translocation times and amplitudes for Imp β translocation through a 35 nm diameter Nup-coated pore. Event amplitudes for Imp β translocations are found to be constant as a function of voltage (Figure S9.5a), similar to the observations for bare pores. However, the behavior of translocation time versus voltage is different between bare and Nup-coated pores. The translocation times for bare pores scale inversely proportional with voltage, $\tau \sim 1/V$ (see for example Ref. 36 in the main text), which appears *not* to be the case for Nup-coated pores. As presented in Figure S9.5b, the dwell times for Imp β through a Nup-98 coated pore are constant within experimental error in the range probed (25-175 mV).

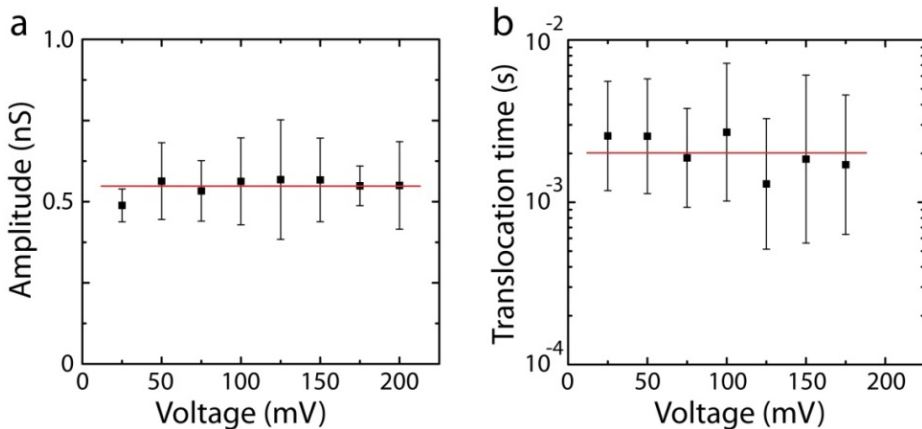


Figure S9.5 Voltage dependence of (a) amplitude and (b) translocation time for Imp β translocations through a Nup98-coated pore. We observe no dependence of amplitude and translocation time on voltage.

This is strong evidence showing that the dominant effect determining the translocation time is not set by the applied voltage, but by the interaction of the Imp β with the FG-domain Nups. We find values of 0.55 ± 0.01 nS for the amplitudes, and 2.0 ± 0.2 ms for the translocation times over the entire range of voltages probed here, where the error bars denote the standard deviation due to the variation of points. Note that the error bars in Figure S9.5 indicate the width of the Gaussian fits to the data at each voltage.

Noise in bare and coated pores

A direct probe to study the properties of a nanopore is to examine its ionic current signature. In addition to the average current, the noise characteristics can provide nanoscopic information about the state of a nanopore. As mentioned in the manuscript, we see an increase in low-frequency noise upon coating of a nanopore with Nups, as presented in Figure S9.6. Importantly, the additional noise for the Nup-coated pores does not significantly decrease the signal-to-noise ratio in our single-molecule translocation measurements because typical transport events occur in the millisecond range (indicated in green in Figure S9.6), where the noise level is similar to that of bare pores.

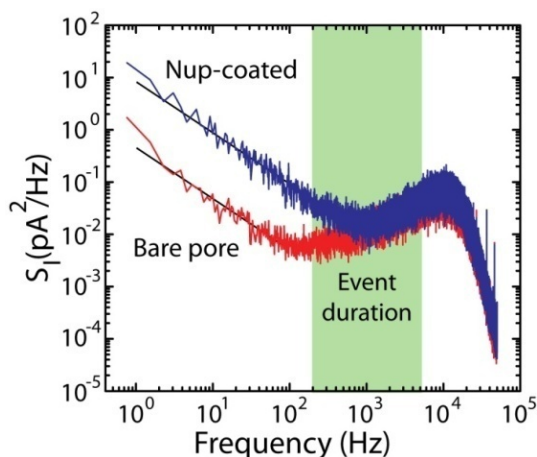


Figure S9.6 Noise characterizations shows characteristic $1/f$ -type (black solid lines) low-frequency noise of different magnitude, and a comparable noise level at high-frequencies for both a bare (red) and a Nup98-coated pore (blue). The range in which typical translocation events occur (roughly, 0.2 – 5 ms) is indicated in green.

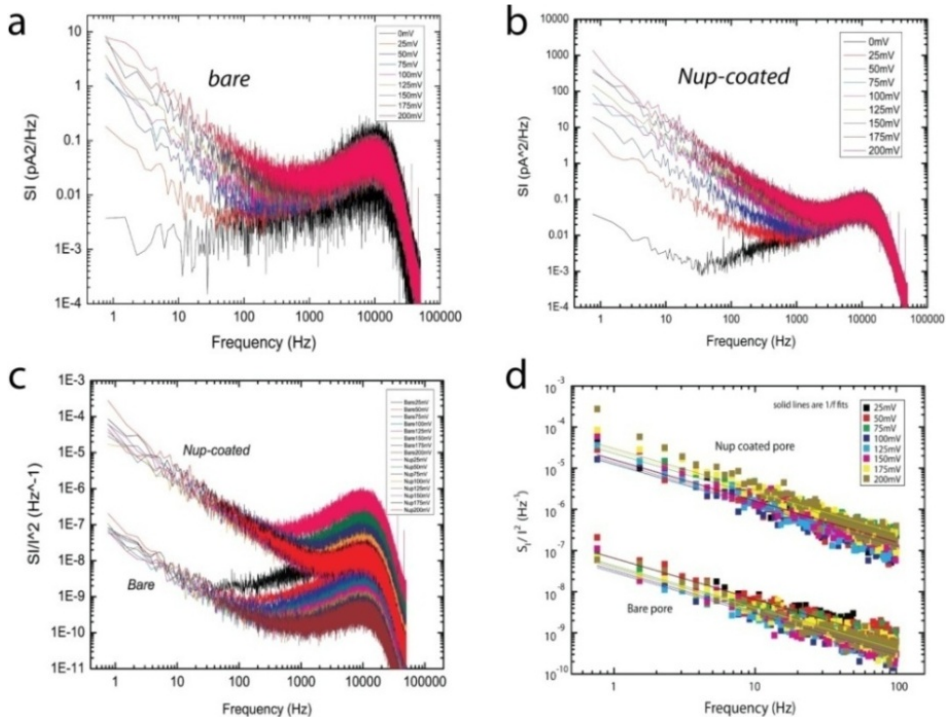


Figure S9.7 (a) Current power spectral densities of a bare nanopore at a range of voltages (25-200 mV). (b) Current power spectral densities of a Nup98-coated nanopore using a similar voltage range. The low-frequency noise increased for all applied voltages, while the high-frequency noise stays constant. (c) Normalized current power spectral density S_I/I^2 for a bare and a Nup98-coated pore for voltages in the range 25-200 mV. (d) Low-frequency normalized current power spectral density S_I/I^2 for a bare and a Nup98-coated pore. In both cases we observe a $1/f$ -type of dependence for all voltages probed. The solid-lines are fits to $S_I/I^2 = A/f$.

Additionally we studied the noise in a range of voltages (25-200 mV). For the current power spectra S_I (Figure S9.7a and Figure S9.7b), we find that low-frequency noise increases with the applied voltage, for both bare and Nup98-coated pores, as expected for resistance fluctuations. By contrast, the high-frequency noise is independent of voltage, as expected, because this noise derives from the SiN membrane. The low-frequency noise in the normalized current power spectra (S_I/I^2) is independent of applied voltage for both a bare and a Nup98-coated pore (Figure S9.7c), and both display a typical $1/f$ -type character (Figure S9.7d).

Alternative exclusion structures

As mentioned in the main text, in our measurements of ionic current what we measure is the “free” conducting volume of the pore and not a particular configuration of Nups in the pore. While there are several good reasons to regard our model 2 with an open channel in the middle of the pore as the natural choice for interpreting the striking data of a cutoff in the conductance versus diameter (Figure 9.2a), there are different possible geometrical models that can explain our data. Figure S9.8 shows some possible alternative exclusion structures.

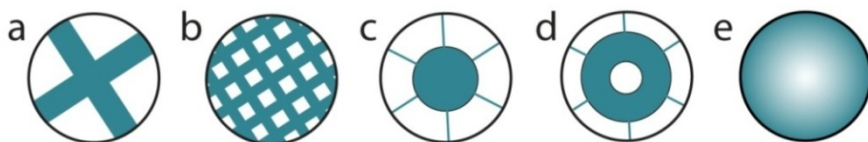


Figure S9.8 Alternative exclusion structures (representations of the reduction of the pore volume induced by the Nup coating, with dark referring to higher Nup density) to models 1 and 2 presented in Figure 9.2. Based on the current data, which essentially measures the excluded volume in the pore, it is not possible to discriminate between these more complicated models.

In reality the situation will likely be some subtle mixture of different models, with for example a low density of (likely dynamic) Nups with a certain mesh size in the middle of the pore. This could also explain why BSA transport is inhibited (if the mesh size is approximately smaller than the size of BSA) even though the time-averaged density of Nups in the center of the channel is lower than at the edges.

Example events of Imp β translocations through a Nup153-modified pore



Figure S9.9 Example ion current traces for Imp β translocation through a Nup153-modified pore. The data was filtered at 2 kHz for display purposes.

Analysis of re-entry events of Imp β

From an analysis of the electrical signals, viz., the times between Imp β events, we can obtain additional evidence that Imp β is indeed translocating and not merely binding at the pore. Events are defined as temporal excursions from the baseline current. Because of the applied electric field, in the bare pore there is no reason to suspect proteins will not translocate through the pore once they entered the pore. However, in the Nup-modified pore, there is a barrier to translocate and hence, in principle, Imp β might bind to the Nup-modified pore and exit at the “wrong” side, namely the entry side instead of the exit. In this case, however, it will be driven back into the pore again by the electric field. This would yield a second event in the current signal that quickly follows the first event, see Figure S9.10.

Remarkably, for Nup-coated pores, we indeed find a clear overrepresentation (see Figure S9.11) of such what we term “re-entry events” compared to bare pores: a second current dip following a previous current dip within a few ms (in contrast to the typical event separation which is a few seconds). The occurrence of these events indicates that about 90% of the events signal a normal translocation event, whereas in about 10% of the occasions Imp β proteins exit at the entry side and re-enter the pore, as we discuss in more detail below.

The re-entry process can be modeled quantitatively (A. Y. Grosberg and Y. Rabin, “Correlations between translocation events: possibility of re-entrance”, unpublished) which allows to extract the ratio of translocation events versus re-entry events from the times between events. In this model, we assume that diffusively moving particles attempt passing through the pore completely independently from one another. Let us call the refusal probability p . We can calculate the probability that no blockage event of any kind happens before time t after an initial event as:

$$w(t) = e^{-\pi} - p e^{-\pi} (R_{\text{access}}/R_{\text{total}}) [1 - (2/d) \cdot (\tau/t)^{d/2} / \Gamma(d/2)],$$

with $\tau = a^2/D$ (where a is the pore radius and D the diffusion coefficient), d , the number of dimensions, R_{access} the access resistance to the pore from infinity, and R_{total} the total resistance across the pore including the access resistance. Note that $w(0)$ equals $1 - P(t)$ in the limit for $t \rightarrow 0$, with $P(t)$ the relative fraction of events occurring within time t after the previous event, as plotted in Figure S9.11. The second term in square brackets becomes negligible because in practice always $t \gg \tau \sim 10 \mu\text{s}$.

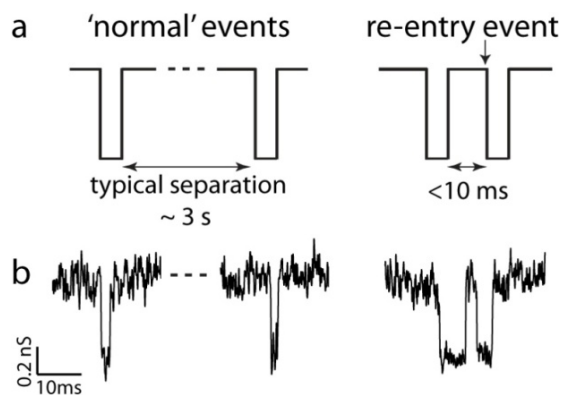


Figure S9.10 (a) For ‘normal’ events the typical separation between events is a few seconds. For what we term “re-entry events” (a second current dip rapidly following a previous current dip), the time separation is very short (<10 ms). (b) Experimental data (filtered at 2kHz) showing example events corresponding to the cartoon in a.

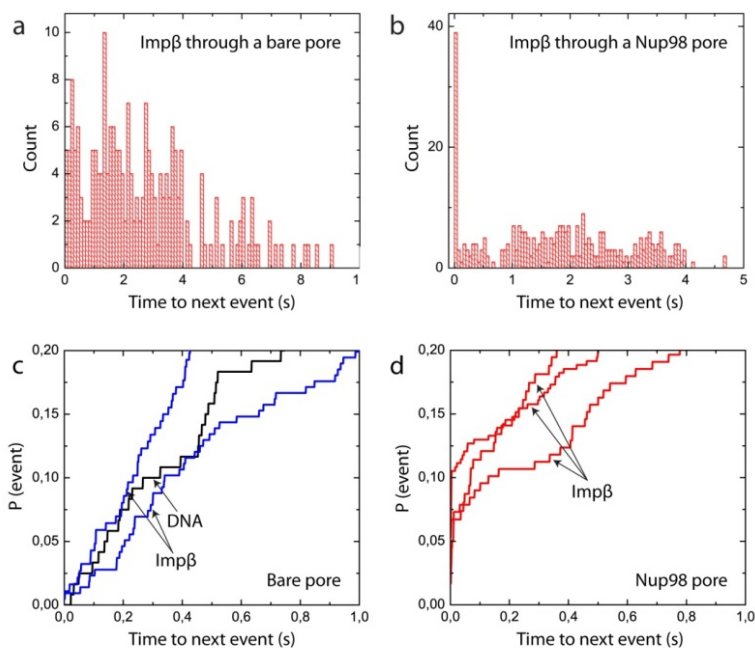


Figure S9.11 Re-entry analysis. (a, b) Distributions of times between Imp β events in a bare and Nup98-modified pore, respectively. (c, d) Relative fraction, P , of events occurring within a time, t , after the previous event, in a bare and Nup98-modified

pore, respectively. The data extrapolate to $P(0)=0$ for the bare pore (both for DNA or Imp β translocation), whereas a finite $P(0)$ is obtained for Imp β in Nup-coated pores.

For a 40 nm pore, the access resistance is roughly equal to the pore resistance, hence the expression simplifies to:

$$w(t) = e^{-t/\tau} (1 - p/2).$$

Experimentally, we measure $w(0) = 0.93 \pm 0.02$ for Imp β translocation through a Nup98-modified pore (Figure S9.11d). This gives a value of $p = 0.14 \pm 0.04$ for the refusal probability. Note that in the case of a bare pore there is simply no barrier for entry since the hole is essentially an open space that is much larger than the size of a protein. The theory thus predicts a negligible amount of re-entry events for such bare pores. This is consistent with our measurements. (Figure S9.11c) where for bare pores we measure $w(0) = 1$, and hence $p = 0$.

Overview of event amplitudes, translocation times, and event rates

AMPLITUDE ΔG (nS)	BSA	Imp β
bare pore	0.47 \pm 0.19	0.59 \pm 0.12
Nup98-coated pore	-	0.56 \pm 0.12
Nup153-coated pore	0.46 \pm 0.08	0.50 \pm 0.10

TIME τ (ms)	BSA	Imp β
bare pore	0.17 \pm 0.07	0.19 \pm 0.04
Nup98-coated pore	-	2.7 \pm 0.3
Nup153-coated pore	2.5 \pm 0.3	2.2 \pm 0.3

EVENT RATE (s^{-1})	BSA	Imp β
bare pore	0.21 \pm 0.02	0.27 \pm 0.02
Nup98-coated pore	0.0035 \pm 0.003	0.21 \pm 0.01
Nup153-coated pore	0.05 \pm 0.01	0.25 \pm 0.02

Table T9.2 Overview of measured event amplitudes, translocation times, and event rates at 50 mV through pores of 46 nm (Nup98) and 42 nm (Nup153) in diameter. The concentrations used are: [BSA] = 4.2 μ M; [Imp β] = 2.9 μ M. The measured

rates for BSA are rescaled by a factor of 29/42 to accommodate for this difference in concentrations.

Dwell time histograms on linear scale

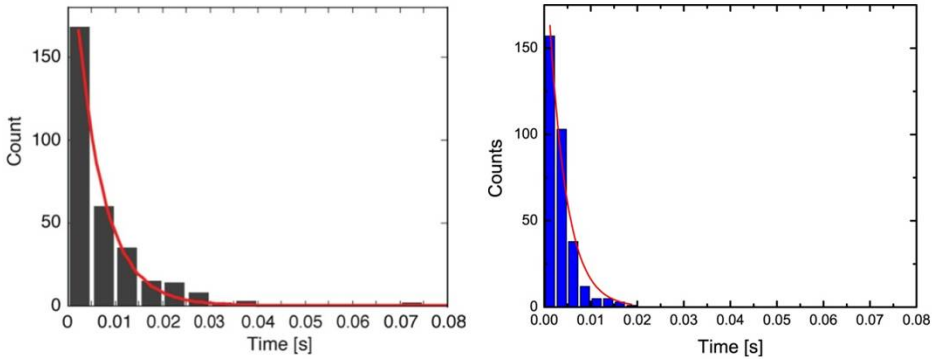


Figure S9.12 Comparison of the exponential distributions of dwell times. Left: data from Ref. S3 on permeabilized cells, with an exponential decay time constant of 5.8 ± 0.2 ms. Right: our data on biomimetic NPCs, the exponential fit gives $\tau = 3.8 \pm 0.2$ ms.

Event frequency versus voltage

It is useful to comment once more on the role of the applied electric field in our experiments. We find the event rate for Imp β to be exponentially dependent on the applied voltage (Figure S9.13). This indicates [S4] that the delivery of new Imp β proteins to the pore entrance occurs through electrophoretic transport from bulk solution, rather than, for example, by lateral diffusion along the top membrane. Furthermore, during the time that the Imp β interacts with the Nups in the pore, the field exerts a small electrophoretic force (likely of order a few pN) to the Imp β protein which biases it toward the pore exit, thus favoring the protein to leave the exit into the *trans* chamber rather than to return to the *cis* chamber. Such a directional bias has also been suggested for NPCs in vivo, for example due to an affinity gradient along the NPC channel [S5] or simply by the ratcheting effect of the RanGTP unloading of Imp β from the nuclear side of the NPC [S6].

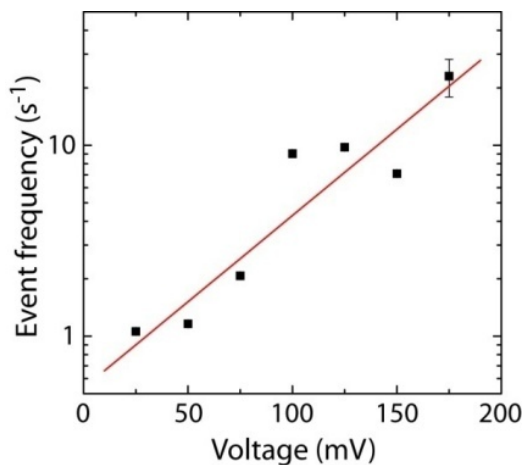


Figure S9.13 We find that the event rate Γ for Imp β translocations through a Nup98-coated pore increases exponentially with voltage. We fit an exponential function $\ln \Gamma = c_1 + c_2 V$ to the data as shown by the red line, yielding $c_2 = 0.009 \pm 0.002 \text{ mV}^{-1}$. Imp β concentration used for this data set was $4.5 \text{ }\mu\text{M}$; pore diameter was 35 nm .

Nanopore array

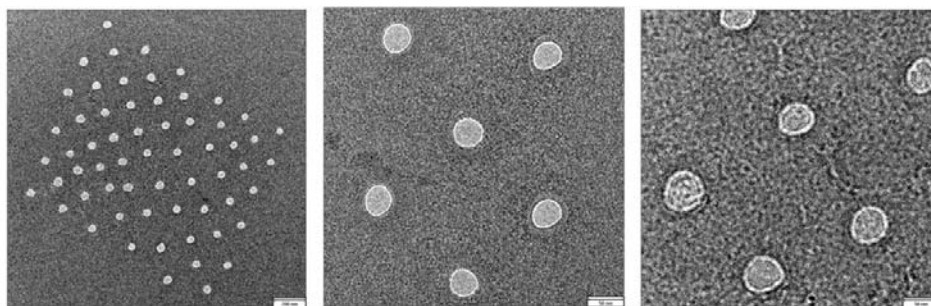


Figure S9.14 TEM image of nanopore array (left and middle) before coating and (right) after coating. The array consists of 61 nanopores with diameters of $43 \pm 3 \text{ nm}$. The measured ionic conductance was stable over time, and decreased from 1840 nS before coating to 257 nS after coating, as expected from Figure 9.2.

TIRF measurements

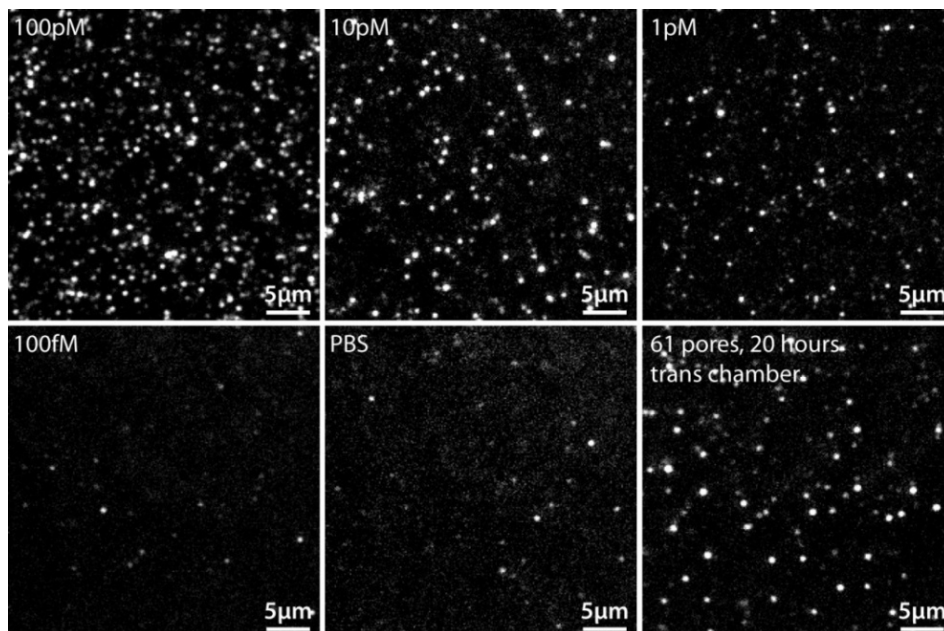


Figure S9.15 TIRF data. Dilution series of Imp β -Alexa488 (100pM, 10pM, 1pM, 100fM), buffer only (PBS), and the contents of the experimental result with Imp β -Alexa488 from the *trans* chamber (see manuscript).

To rigorously prove that the Imp β proteins have translocated is a challenging effort because the amount of protein that is translocated to the *trans* chamber is very small (low attomolar) and no PCR analogue exists for proteins. Nonetheless, we have performed experiments where we optically imaged the proteins that translocated to the *trans* chamber. Specifically, we have labeled Imp β with a fluorescent dye (Alexa488) and collected all the proteins that translocated to the *trans* chamber after a measurement to subsequently visualize these translocated proteins. The collected material was deposited on a microscope glass cover slip and imaged using TIRF. Because the expected number of molecules in the *trans* chamber is very small in a typical experiment, we made an array of nanopores consisting of 61 Nup-98 coated nanopores of 43 ± 3 nm in diameter (Figure 9.5a) and ran the experiment overnight to maximize the number of molecules in the *trans* chamber. Figure S9.15 shows a dilution series, as well as the material collected from the *trans* chamber. The signal is clearly above background.

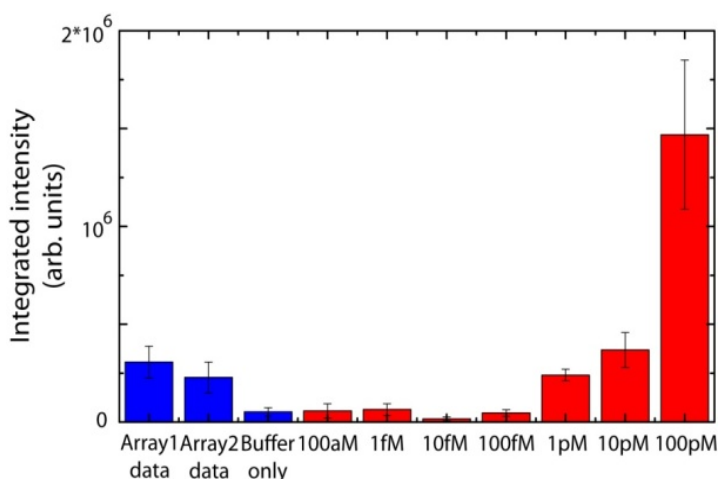


Figure S9.16 Analysis of the integrated intensity in the TIRF images, including a number of controls (buffer only and a dilution series). See also Materials and Methods in the manuscript.

Figure S9.16 shows the results of the analysis of the integrated intensity for the two arrays, a buffer only control where buffer was taken out of the flow cell, and a dilution series. The predicted concentration in the *trans* chamber of the array (total volume 20 μL) after 20 hours (for array2; 15 hours for array1) at 100 mV applied voltage with an $\text{Imp}\beta$ concentration of 13 μM in the *cis* chamber is given by: $c_{\text{trans}} \approx 61 \cdot (1/\text{s} \cdot 13\mu\text{M}/3\mu\text{M}) \cdot (20 \cdot 60 \cdot 60\text{s}) / (6 \cdot 10^{23} \cdot 2 \cdot 10^{-5} \text{M}^{-1}) = 2 \text{ pM}$, in good agreement with the TIRF data.

SPR measurements

Traditionally, measurements on NPCs are performed at pH 7.2. Our measurements were done at pH 8.0. To evaluate how this might affect $\text{Imp}\beta$ binding interactions, we performed additional surface plasmon resonance (SPR) measurements at both pH 8.0 (Tris) and pH 7.2 (PBS) to compare the binding between $\text{Imp}\beta$ and Nup153 at these two conditions (see Figure S9.17). The equilibrium K_D constants are evaluated using the Langmuir isotherm, which shows that $\text{Imp}\beta$ binding at pH 8 that is only slightly weaker than at pH 7.2, giving 431 nM and 387 nM, respectively. This shows conclusively that the slight change in pH does not have a large influence on the binding affinities.

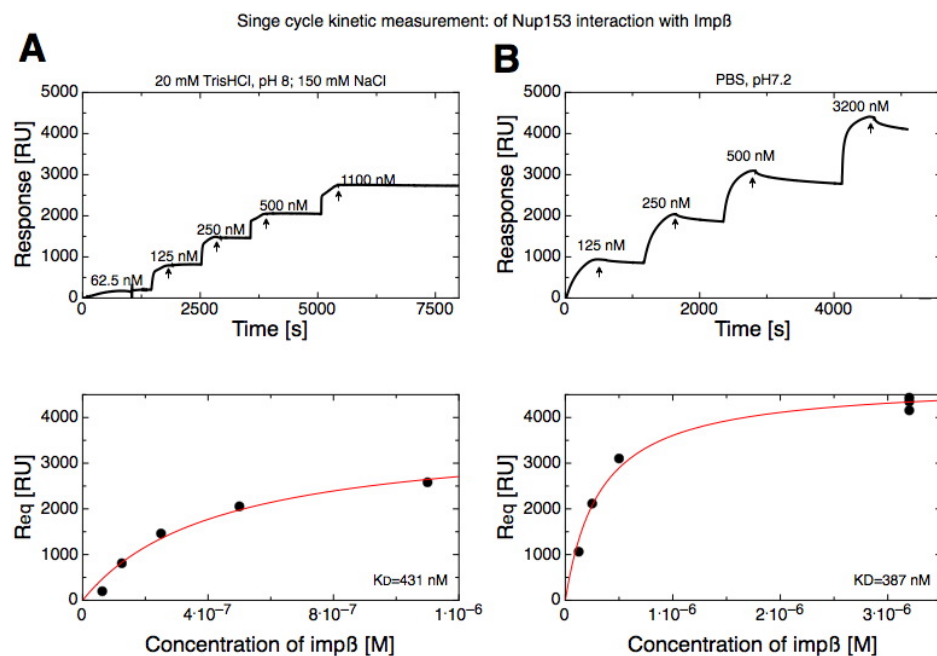


Figure S9.17 SPR sensograms for Imp β binding to the FG-domain (874-1475) of Nup153 at increasing concentrations (62.5 / 125 / 250 / 500 / 1100 or 3200 nM) in 20 mM TrisHCl, pH 8 buffer with 150 mM NaCl (top, A) and in PBS, pH 7.2 buffer (Invitrogen) (top, B). The arrows (top, A and B) signify to the end of Imp β binding followed by dissociation (rinsing with buffer). The binding responses at steady state (R_{eq}) are obtained by fitting the association parts of the sensogram obtained at each respective Imp β concentration to the equation: $R_t = R_{eq}(1 - e^{-k_{obs}(t-t_0)})$, where k_{obs} is an observed rate constant and R_t is a binding response at time t . Then R_{eq} (black points) is plotted versus the corresponding Imp β concentration at pH=8 (A lower panel) and pH=7.2 (B lower panel). Each red line shows a best fit with a Langmuir absorption isotherm, $R_{eq} = (R_{max} * C_{Imp\beta}) / (C_{Imp\beta} + K_D)$, where R_{max} is a maximal binding capacity and $C_{Imp\beta}$ is a concentration of Imp β . The obtained equilibrium constants are as follows: $K_D = 431$ nM and $K_D = 387$ nM for pH8 and pH7.2, respectively.

Conformational characteristics of Nup98 and Nup153

Protein (total # of amino acids (aa))	aa range:	Charged/ Hydrophobic	% of length	Conformation
Nup98 (498 aa) (FG-domain: 1-498)	1-160	0.081	32	cohesive
	161-226	1.066	13	repulsive
	227-498	0.117	55	cohesive
Nup153 (602 aa) (FG-domain: 874-1475)	874-1270	0.681	66	repulsive
	1270-1475	0.005	34	cohesive

Table T9.3 Conformational characteristics of human Nup98 and Nup153 based on charge to hydrophobic ratio (in accordance with Ref. S7).

SI References

- S1. Denning, D.P., Patel, S.S., Uversky, V., Fink, A.L., and Rexach, M.. Disorderin the nuclear pore complex: The FG repeat regions of nucleoporins are natively unfolded. *Proc. Natl. Acad. Sci. USA*. **100**, 2450-2455 (2003).
- S2. Malamud, D. and Drysdale, J.W., Isoelectric points of proteins: A table. *Anal. Biochem.* **86**, 620 (1978).
- S3. Kubitscheck, U. *et al.* Nuclear transport of single molecules: dwell times at the nuclear pore complex. *J. Cell Biol.* **168**, 233-243 (2005).
- S4. Smeets, R.M.M. *et al.* Translocation of RecA-coated double-stranded DNA through solid-state nanopores. *Nano Lett.* **9**, 3089-3095 (2009).
- S5. Ben-Efraim, I. and Gerace, L. Gradient of increasing affinity of importin beta for nucleoporins along the pathway of nuclear import. *J. Cell Biol.* **152**, 411-417 (2001).
- S6. Stewart, M. Molecular mechanism of the nuclear protein import cycle. *Nature Rev. Mol. Cell Biol.* **8**, 195-208 (2007).
- S7. Yamada, J. *et al.* A Bimodal Distribution of Two Distinct Categories of Intrinsically Disordered Structures with Separate Functions in FG Nucleoporins. *Mol. Cell. Proteomics.* **9**, 2205 (2010).

Chapter 10

Outlook

In this outlook we discuss (i) alternative nanopore detection schemes; (ii) nanopores for epigenetics; and (iii) biomimetic and hybrid approaches. The topics discussed here are not meant as a comprehensive list of ideas, but rather as a personal view on the upcoming development of the field of solid-state nanopores.

10.1 Introduction

Over the course of the last decade, the nanopore community has grown from just a few research groups into a mature field generating nearly a thousand new publications each year on the topic (see Figure 10.1). There are now over 50 research groups worldwide that carry out nanopore-related research (for a partial list, see [1]), the first nanopore textbook has been written [2], and solid-state nanopores are now also available commercially [3]. Additionally, several companies including IBM, PacBio, Nabsys, Genia, and most notably Oxford Nanopore, are investing heavily in nanopore research. It is clear that the future is bright for nanopore research. In this outlook we discuss (i) alternative nanopore detection schemes; (ii) nanopores for epigenetics; and (iii) biomimetic and hybrid approaches. The topics discussed here are not meant as a comprehensive list of ideas, but rather as a personal view on the upcoming development of the field of solid-state nanopores.

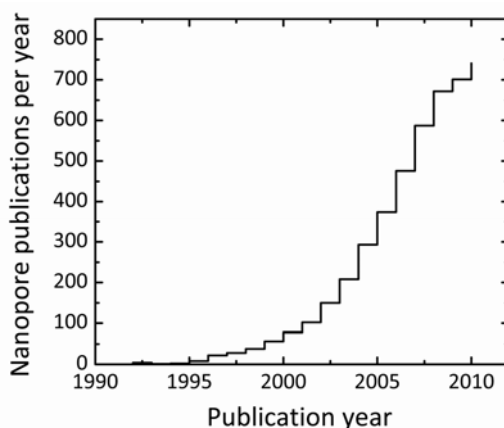


Figure 10.1 Number of publications per year from 1990 to 2010 with “nanopore” or “nanopores” as topic, as obtained from ISI Web of Knowledge.

10.2 Alternative nanopore detection schemes

Sequencing of DNA by simply monitoring the ionic current as DNA passes through the nanopore remains a challenge. Even in a graphene pore the electric field will extend for approximately one channel diameter in the direction perpendicular to the

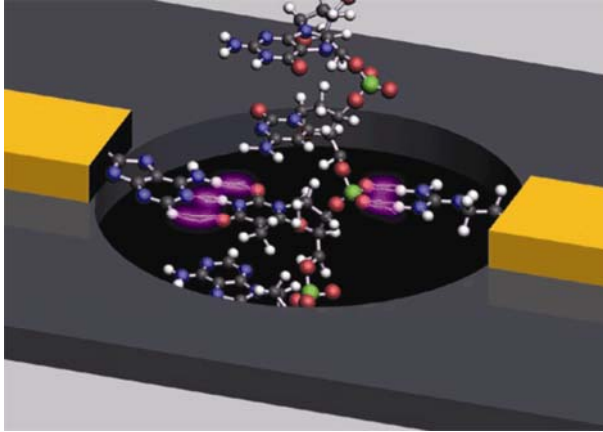


Figure 10.2 Alternative detection scheme that makes use of transverse electrodes, as well as conventional ionic current measurement. Adapted from [4].

pore (see chapter 2), setting a restriction on the spatial resolution that can be achieved. A different means for base identification therefore seems necessary. Here, we discuss a few possible alternative detection schemes, including trans-electrode tunneling, and plasmonic nanopores.

Several groups (see for example, [5]) are now pursuing fabrication of nanopore devices that enable measurement of trans-electrode tunneling-current through a nanometer-sized electrode gap (Figure 10.2). This approach is powerful because the tunneling current forms a very sensitive local probe right at the pore. Recent tunneling experiments could identify differences in tunneling current of three of the four DNA nucleotides [6], and all four DNA nucleosides (i.e., a base joined to a sugar, without phosphate groups) [7]. Very recently similar tunneling experiments detected methylcytosines in a DNA oligomer [8], see also section 10.2. A different approach, one that does not require fabrication of additional electrodes on top of a membrane, is to use the excellent in-plane conductivity of graphene to perform tunneling measurements across a graphene gap [9, 10]. But many hurdles need to be taken before these proof-of-principle experiments could become a mainstream sequencing technique. As of yet, only individual nucleotides have been distinguished from one another, but detecting individual nucleotides within a long DNA molecule as it translocates through the pore remains elusive.

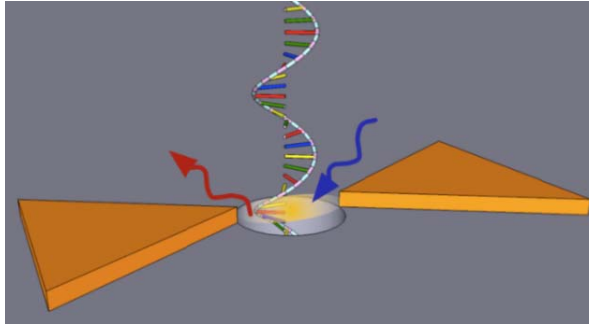


Figure 10.3 Alternative detection scheme that makes use of antenna structures (orange) where excited surface plasmons create a high field enhancement right at the nanopore. Credits: Magnus Jonsson.

An alternative detection scheme is to use fluorescence in combination with ion current measurements. An instrument that demonstrated synchronous optical (by means of total internal reflection fluorescence, or TIRF) and electrical (by means of ionic current) detection of biomolecules traversing solid-state nanopores was recently realized [11] and might be used for visualizing sequence-dependent optical probes that can be attached to the DNA [12]. Yet another promising scheme is to use excitation of surface plasmons that locally at the pore (or slit) can result in extremely strong enhancement of the electromagnetic field (many orders of magnitude, even up to 10^{11} in some cases) (Figure 10.3) [13, 14]. This is useful for applications such as surface enhanced Raman scattering (SERS), and can potentially be used to get sequence-dependent light signatures out of a label-free DNA molecule that is translocating through a nanopore.

10.3 Nanopores for epigenetics

Nanopores may be used as a new tool to study epigenetic modifications. The fact that our genomes are written in the 4-character language of DNA that is passed on from generation to generation, is not the full story of life. Epigenetics, the study of potentially heritable changes in gene expression that are not accompanied by changes in DNA sequence, is one of the most rapidly expanding fields of biology [15]. Local DNA methylation plays a predominant role in epigenetics, with the conversion of the

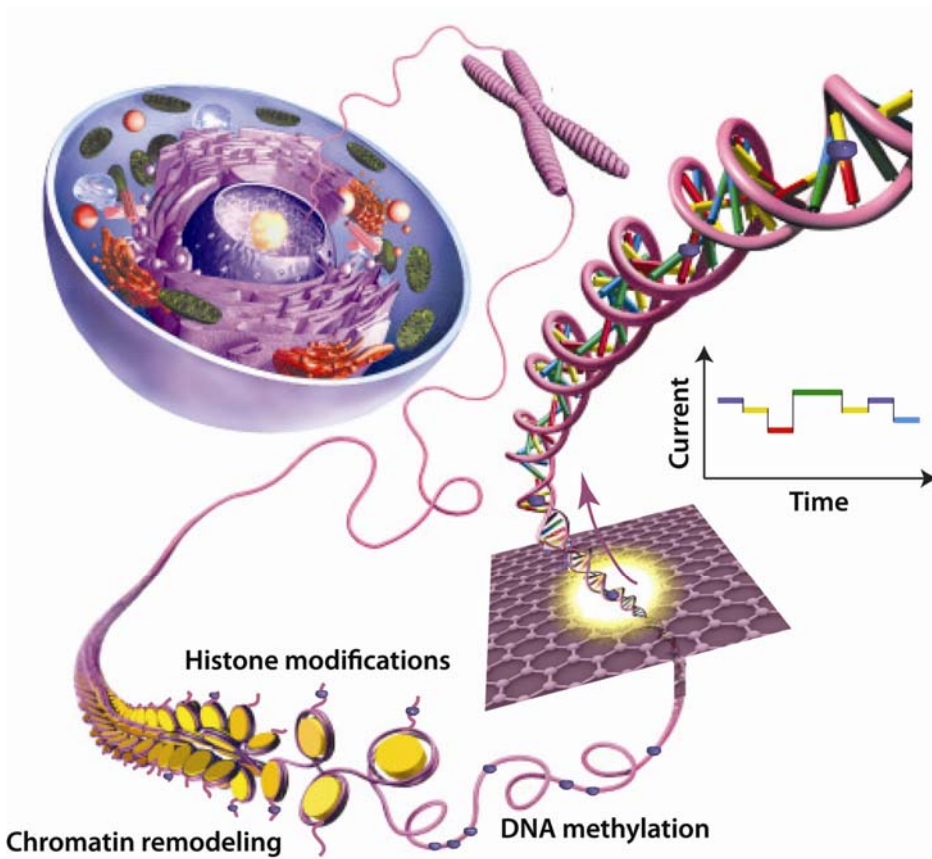


Figure 10.4 Schematic of a DNA strand that is pulled out of a cell and translocates through a graphene nanopore. Information, including sequence and epigenetic modifications, is read off as the DNA treads through a nanopore. Interestingly, nanopores seem well suited to probe all three categories of epigenetic modifications, i.e., DNA methylation, histone modifications, and nucleosome positioning. Image modified from [24].

cytosine base (C) into 5-methylcytosine (5-mC), sometimes referred to as “the fifth base”, as the most studied epigenetic variation [16]. Such heritable changes are common (roughly 5% of cytosines in the human genome are methylated [17]), and are involved in gene regulation, development, aging, cancer, and disease [18–20]. For example, a connection between DNA (hyper)methylation and cancer was found [21].

two years ago a rarer “sixth base”, 5-hydroxymethylcytosine (5-hmC), was identified in Purkinje neurons and the brain [22] and later in stem cells [23].

Histone modifications and nucleosome positioning are other important epigenetic markers (see Figure 10.4). In the cell, DNA is wrapped around histone proteins. These units, called nucleosomes, are then folded in a series of ordered structures into a chromosome. Nucleosomes efficiently package DNA into a small volume, as well as form a barrier to transcription by blocking access for transcription factors to the DNA. Nucleosome positioning plays an important role in determining DNA methylation locations [25]. On the other hand, nucleosome remodelers are influenced by DNA methylation [26, 27]. Furthermore, different histone variants influence the function on nucleosomes. For example, histone variant H2A.Z protects DNA against methylation [28]. As all of this makes clear, the all-important (non-)expression of genes is a complex interplay between many different (epigenetic) factors.

What can nanopores teach us about epigenetics? Using a (modified) α -hemolysin pore, 5-mC could already be clearly discriminated from C, as well as from the other bases [29]. Last year, it was shown that using a solid-state nanopore [30], as well as using α -hemolysin [31], different current signatures can be measured for 5-mC and 5-hmC. Such a single-molecule method (for a different single-molecule method that can directly detect DNA methylation see [32]) has many advantages over conventional biochemical “bisulfite sequencing” (for example used in the *Human Epigenome Project*), which relies on conversion of (unmethylated) cytosine to uracil. Such biochemical conversion has the disadvantage that, among other limitations, under conditions necessary for complete conversion (such as long incubation times, elevated temperature, and high bisulfite concentration) as much as about 90% of the DNA can be degraded. Furthermore, bisulfate sequencing cannot distinguish between 5-mC and 5-hmC modifications as both protect the cytosine from bisulfite-mediated oxidation to uracil.

Future experiments aimed at reading the locations of methylation along DNA, much like the mapping of local proteins structures as discussed in chapter 4, will have to proof the validity of this approach for direct single-molecule detection of DNA methylation. Also other main epigenetic categories (Figure 10.4), such as nucleosome positioning, could be addressed using nanopores. In particular, in a hybrid setup with

a nanopore and an optical tweezer [33], where the DNA is pulled taut and kept inside the nanopore, may allow observing nucleosomes moving along the DNA. In this way nucleosome dynamics can be studied on different DNA sequences, with and without methylated bases, with and without the presence of nucleosome remodelers, etc. Such experiments are technically challenging, but do not seem impossible. Ideally, the DNA would be pulled out of a cell and information, including epigenetic modifications, would be read off as it threads through a nanopore.

10.4 Biomimetic and hybrid strategies

Biomimetic and hybrid nanopores (reviewed in chapter 8) also provide excellent new research opportunities: Natural pores can be studied through a bottom-up approach, whereas the functionalization of artificial pores can be inspired by nature. Here we discuss a few ideas for future work in this direction. As already mentioned in chapter 8, an instrument that synchronously detects fluorescence in combination conductance [11] could be used for biomimetic nanopores, for example, in imaging the diffusion of transport receptors in nucleoporin-coated nanochannels. In simple ionic current measurements, proteins of similar charge and mass cannot be discriminated by their current signature. However, by attaching differently-colored fluorescent probes to the proteins, they could be distinguished. Alternatively, an integrated nanopore-optical tweezer setup [33] could allow measurement of the force on transport factors during the translocation process. These types of experiments may yield new information about the forces governing the translocation process, and accordingly shed new light on the mechanism of translocation. Furthermore, many follow-up studies building on the work presented in chapter 9 could be done, with or without the above mentioned additions to the experimental layout. This includes studies with Imp β -cargo complexes and RanGTP/RanGDP [34], attachment of fusions of nucleoporins, mixtures of different types of nucleoporins, effect of the orientation and concentration of Nups in the pore, effect of channel length on dwell time, etc. Another important question that might be addressed is which route transporters and cargo take through the NPC [35].

Furthermore, transport of DNA and RNA through biomimetic nuclear pores might provide interesting insights into the transport process. Here, for example the effects of

an RNA cap and poly(A) tail could be studied [36], as well as import of DNA into the nucleus which might give useful insights for gene therapy. Gene therapy is a promising technology in which modified genes are inserted into the cell nucleus. According to NIH director Francis Collins [37] gene therapy is, along with stem cell research, one of the two most promising developments in medicine at the moment. One of the key challenges here is that the DNA – a large, charged molecule – has to travel across the cell and the nuclear membrane. Biomimetic pores might provide insight into this last step. Viruses provide one efficient means of DNA delivery [38], and biomimetic nanopores might test the docking of viruses on nanopores and the release of DNA (Figure 10.5).

Other ways of functionalizing nanopores might be useful for recognition of particular molecules. For examples, by functionalizing nanochannels with antibodies, enatiomeric selectivity was achieved [40]. A similar approach works for complementary DNA pieces [41, 42] (more examples of nanopore functionalizations are listed in chapter 8). An interesting idea [43] is to functionalize an array of thousands of nanopores and to spot different SNP-specific DNA (or synthetic DNA-analogs) probes on each nanopore. In this way DNA (or RNA) molecules might be quickly scanned for particular single-nucleotide polymorphisms (SNPs). Parallelization in itself is under investigation: see for example [44–46]. A different type of promising biomimetic nanopore functionalization is to cover solid-state nanopores with lipid bilayers. This has already been proven to be very useful for reducing protein sticking, as well as to slow down translocation speed [47].

Recently, hybrid biological/artificial pores, which bring together the best of both worlds, have been demonstrated. In particular, controlled and oriented insertion of an individual α -hemolysin protein into a narrow solid-state nanopore was achieved, combining the two most experimentally studied nanopores [48]. Such hybrid approaches have the great advantage of combining a biological, atomically precise, structure that can be genetically engineered with the robustness, sustainability and potential for parallelization and device-integration of solid-state nanopores. Future work in this direction should focus on reducing noise levels to enable full advantage of this approach. A new appealing idea would be to use the newly developed graphene nanopores (chapter 7) instead of the silicon nitride ones, and to do tunneling

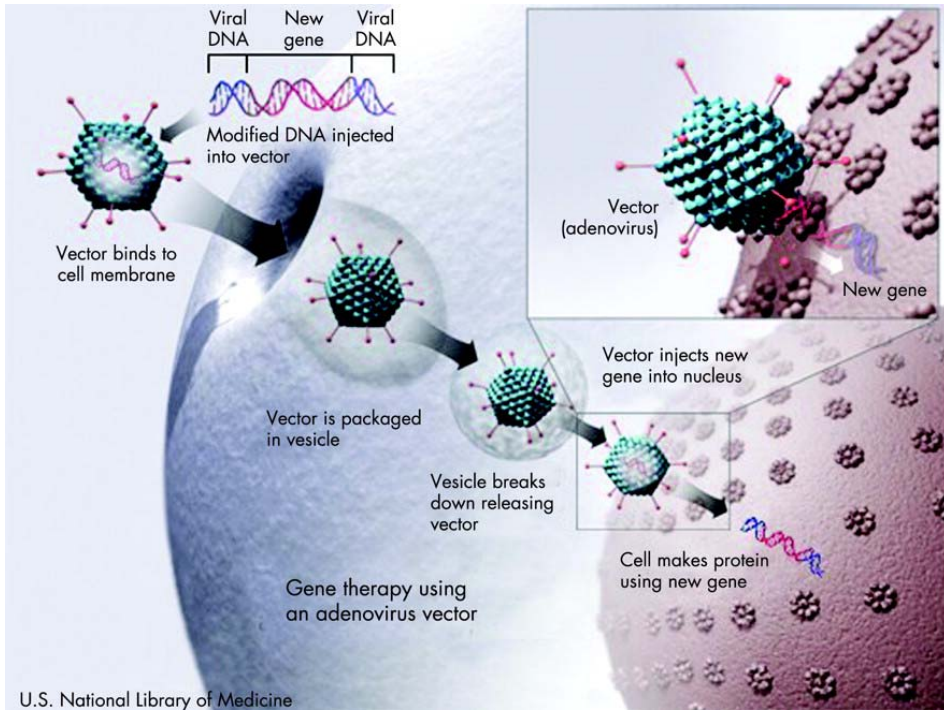


Figure 10.5 Gene therapy using an adenovirus vector. A new gene is inserted into an adenovirus vector, which is used to introduce the modified DNA into the cell nucleus through a nuclear pore complex. Image taken from [39].

measurements (see earlier in this chapter) across the α -hemolysin stem. Alternatively, MspA [49], which has a tighter central channel than α -hemolysin, might be used for this purpose.

Other exciting ideas for future nanopore research include using nanopores to determine RNA secondary structure, sequencing RNA and proteins, and so on. Furthermore, now that nanopore methods have been relatively well developed, the road is open for applying nanopores in clinical applications. For example, very recently nanopores have been applied to detect levels of cancer-associated microRNAs in the bloodstream of lung cancer patients [50], which may lead to non-invasive early diagnosis of cancer. In the past few years, nanopore research has

already been proven to be very fruitful, but with so many new research directions and potential real-life applications opening up, the best is surely yet to come.

References

- 1 <http://www.thenanoporesite.com/>
 - 2 Iqbal, S. W. and Bashir, R. (Eds.) Nanopores – Sensing and Fundamental Biological Interactions. Springer (2011).
 - 3 <http://www.nanoporesolutions.com>
 - 4 Branton, D. *et al.*, The potential and challenges of nanopore sequencing. *Nat. Biotechnol.* **26**: 1146–1153 (2008).
 - 5 Ivanov, A. P. *et al.*, DNA Tunneling Detector Embedded in a Nanopore, *Nano Lett.* **11**: 279–285 (2011).
 - 6 Tsutsui, M. *et al.*, Identifying single nucleotides by tunnelling current, *Nat. Nanotechnol.* **5**: 286–290 (2010).
 - 7 Shuai, C. *et al.*, Electronic Signatures of all Four DNA Nucleosides in a Tunneling Gap, *Nano Lett.* **10**: 1070–1075 (2010).
 - 8 Tsutsui, M. *et al.*, Electrical detection of single methylcytosines in a DNA oligomer, *J. Am. Chem. Soc.* **133**(23): 9124–9128 (2011).
 - 9 Postma, H. W., Rapid sequencing of individual DNA molecules in graphene nanogaps, *Nano Lett.* **10**(2): 420–425.
 - 10 Wang, X. and Dai, H., Etching and narrowing of graphene from the edges, *Nat. Chem.* **2**(8): 661–665 (2010).
 - 11 Soni, G. V. *et al.*, Synchronous optical and electrical detection of biomolecules traversing through solid-state nanopores. *Rev. Sci. Instrum.* **81**: 014301 (2010).
 - 12 McNally, B. *et al.*, Optical recognition of converted DNA nucleotides for single-molecule DNA sequencing using nanopore arrays, *Nano Lett.* **10**(6): 2237–2244 (2010).
 - 13 Genet, C. and Ebbesen, T. W., Light in tiny holes, *Nature* **445**: 39–46 (2007).
 - 14 Chen, C. *et al.*, Highly confined surface plasmon polariton resonances in rectangular nanopore cavities, *Physica Status Solidi* **4**(10): 247–249 (2010).
 - 15 Portela, A. and Esteller, M., Epigenetic modifications and human disease, *Nat Biotechnol.* **28**(10): 1057–1068 (2010).
 - 16 J. Klose, R. J. and Bird, A. P., Genomic DNA methylation: the mark and its mediators, *Trends Biochem Sci.* **31**(2): 89–97 (2006).
 - 17 Beck, S. and Rakyán, V. K., The methylome: approaches for global DNA methylation profiling, *Trends Genet.* **24**(5): 231–237 (2008).
-

- 18 Reik, W., Stability and flexibility of epigenetic gene regulation in mammalian development, *Nature* **447**: 425–32 (2007).
 - 19 Portela, A. and Esteller, M., Epigenetic modifications and human disease, *Nat. Biotechnol.* **28**(10): 1057–68 (2010).
 - 20 Gal-Yam, E. N. *et al.*, Cancer epigenetics: modifications, screening, and therapy, *Annu. Rev. Med.* **59**: 267–80 (2008).
 - 21 Esteller, M., Cancer epigenomics: DNA methylomes and histone-modification maps, *Nat Rev Genet.* **8**(4): 286–98 (2007).
 - 22 Kriaucionis, S. and Heintz, N., The nuclear DNA base 5-hydroxymethylcytosine is present in Purkinje neurons and the brain, *Science* **324**: 929–930 (2009)
 - 23 Ito, S. *et al.*, Role of Tet proteins in 5mC to 5hmC conversion, ES-cell self-renewal and inner cell mass specification, *Nature* **466**: 1129–1133 (2010).
 - 24 Image modified from <http://www.rikenresearch.riken.jp/eng/frontline/5514>.
 - 25 Chodavarapu, R. K. *et al.*, Relationship between nucleosome positioning and DNA methylation, *Nature* **466**: 388–92 (2010).
 - 26 Harikrishnan, K. N. *et al.*, Brahma links the SWI/SNF chromatin-remodeling complex with MeCP2-dependent transcriptional silencing, *Nat. Genet.* **37**(3): 254–64 (2005).
 - 27 Wysocka, J. *et al.*, A PHD finger of NURF couples histone H3 lysine 4 trimethylation with chromatin remodelling, *Nature* **442**: 86–90 (2006).
 - 28 Zilberman, D. *et al.*, Histone H2A.Z and DNA methylation are mutually antagonistic chromatin marks, *Nature* **456**: 125–129 (2008).
 - 29 Clarke, J. *et al.*, Continuous base identification for single-molecule nanopore DNA sequencing. *Nat. Nanotech.* **4**: 265–270 (2009).
 - 30 Wanunu, M. *et al.*, Discrimination of Methylcytosine from Hydroxymethylcytosine in DNA Molecules. *J. Am. Chem. Soc.* **133**: 486–492 (2010).
 - 31 Wallace, E. V. *et al.*, Identification of epigenetic DNA modifications with a protein nanopore, *Chem Commun.* **46**: 8195–8197 (2010).
 - 32 Flusberg, B. A. *et al.*, Direct detection of DNA methylation during single-molecule, real-time sequencing, *Nat. Meth.* **7**: 461–465 (2010).
 - 33 Keyser, U. F. *et al.*, Direct force measurements on DNA in a solid-state nanopore, *Nat. Phys.* **2**, 473–477 (2006).
 - 34 Görlich D, *et al.*, Identification of different roles for RanGDP and RanGTP in nuclear protein import, *EMBO J.* **15**: 5584–5594 (1996).
 - 35 Yamada, J. *et al.* A bimodal distribution of two distinct categories of intrinsically-disordered structures with separate functions in FG nucleoporins. *Mol. Cell. Proteomics* **9**: 2205–2224 (2010).
-

-
- 36 Alberts, B. *et al.*, Molecular biology of the cell (5th ed.), New York: Garland Science (2008).
 - 37 Collins, F., The language of life: DNA and the revolution in personalized medicine, New York: HarperCollins (2010).
 - 38 Graham, F. L. and van der Eb, A. J. A new technique for the assay of infectivity of human adenovirus 5 DNA, *Virology* **52**: 456–467 (1973).
 - 39 Lyon, A. R. Gene therapy: targeting the myocardium, *Heart* **94**, 89-99 (2008).
 - 40 Lee, S. B. *et al.* Antibody-Based Bio-Nanotube Membranes for Enantiomeric Drug Separations. *Science* **296**: 2198–2200 (2002).
 - 41 Kohli, P. *et al.* DNA-Functionalized Nanotube Membranes with Single-Base Mismatch Selectivity. *Science* **305**: 984–986 (2004).
 - 42 Iqbal, S. M. *et al.* Solid-state nanopore channels with DNA selectivity. *Nat. Nanotechnol.* **2**: 243–248 (2007).
 - 43 Personal communication with Cees Dekker.
 - 44 Osaki, T. *et al.*, Multichannel simultaneous measurements of single-molecule translocation in alpha-hemolysin nanopore array, *Anal Chem.* **81**(24): 9866–9870 (2009)
 - 45 Kleefen, A. *et al.*, Multiplexed Parallel Single Transport Recordings on Nanopore Arrays, *Nano Lett.* **10**: 5080–5087 (2010).
 - 46 GridION system from Oxford Nanopore Technologies, <http://www.nanoporetech.com/gridion>
 - 47 Yusko, E. C. *et al.*, Controlling protein translocation through nanopores with bio-inspired fluid walls, *Nat. Nanotechnol.* **6**: 253–260 (2011).
 - 48 Hall, A. R. *et al.* Hybrid pore formation by directed insertion of alpha-haemolysin into solid-state nanopores. *Nat. Nanotechnol.* **5**, 874–877 (2010).
 - 49 Derrington, I. M. *et al.* Nanopore DNA sequencing with MspA. *Proc. Natl. Acad. Sci. USA.* **107**: 16060–16065 (2010).
 - 50 Wang, Y. *et al.*, Nanopore-based detection of circulating microRNAs in lung cancer patients, *Nat Nanotechnol.* 2011 Sep 4. doi: 10.1038/nnano.2011.147.
-

Summary

Solid-state nanopores, nanometer-size holes in a thin synthetic membrane, are a versatile tool for the detection and manipulation of charged biomolecules. When a molecule is driven through a nanopore by an externally applied electric field, it causes a characteristic temporary change in the trans-pore current. This signal can be used for sensitive single-molecule biosensing platforms. Much current research is, for example, directed towards nanopore sequencing of DNA.

This thesis describes mostly experimental work on solid-state nanopores. First, we present theoretical modeling and measurements of ionic conductance of nanopores, with and without double-stranded DNA (dsDNA) inserted into the pore (**chapter 2**). Next, we demonstrate that it is possible to distinguish bare DNA from protein-coated DNA in a nanopore, based on their respective conductance blockade signal (**chapter 3**). Building on this work, we probe local protein structures on DNA and show that it is possible to obtain length-wise ‘topographic reading’ of proteins along a single unstained DNA molecule at high speed and high resolution using a solid-state nanopore (**chapter 4**). Furthermore, we investigate the partial reduction of the DNA charge due to counterion binding by means of nanopore translocation experiments and all-atom molecular dynamics (MD) simulations, which leads to the discovery of a new practical method for achieving at least a ten-fold enhanced resolution in nanopore applications (**chapter 5**). Next, we study the unraveling of single-stranded DNA (ssDNA) in a nanopore, where we measure blockade amplitudes and translocation times as a function of voltage for both ssDNA and dsDNA (**chapter 6**). We then fabricate nanopores in graphene, a carbon sheet that is only one atom thin, and demonstrate dsDNA translocation through such graphene nanopores, and find similar folding behavior as was measured with conventional silicon nitride nanopores (**chapter 7**). Finally, we mimick the nuclear pore complexes of the cells in our bodies by attaching nuclear pore proteins to a nanopore and we study protein transport across this selective biomimetic pore at the single-molecule level (**chapter 8 and 9**). In the following, we give a short summary for each chapter.

In **chapter 2** we present theoretical modeling and measurements of the conductance G of solid-state nanopores with 5–100 nm diameters, with and without DNA inserted into the pore. We show that it is essential to include both the access and the geometrical pore resistance to describe the open-pore conductance. We present an exact solution for G of an hourglass-shaped pore, which agrees very well with our measurements without any adjustable parameters. Additionally, we discuss the conductance blockade ΔG due to the insertion of a DNA molecule into the pore. We find that ΔG strongly decreases with pore diameter, contrary to the predictions of earlier models that forecasted a constant ΔG .

In the biological cell, DNA is continually acted upon by proteins. RecA protein is an example: it plays a central role in DNA repair in prokaryotes, where it catalyzes the pairing of broken DNA with complementary regions of undamaged DNA. In **chapter 3**, we show that nanopores can probe DNA-RecA structures. We report translocation measurements of dsDNA molecules that are fully coated with RecA protein. Because of its thicker size than DNA, as expected, we find that translocation of RecA-coated DNA leads to an order of magnitude larger blockades as compared to bare dsDNA. We furthermore distinguish two different regimes of translocation: a low-voltage regime (< 150 mV) in which the event rate increases exponentially with voltage, and a high-voltage regime in which it remains constant.

Building on this work, we examine the translocation of dsDNA with discrete patches of the RecA protein attached along its length (**chapter 4**). First, we develop a protocol to partially coat DNA molecules with RecA protein. We image the resultant molecules using atomic force microscopy to confirm the formation of discrete RecA patches of variable length, ranging from a few monomers to filaments of several micrometers long. Using the fact that RecA-coated DNA and bare DNA yield very different current-blockade signatures (as found in chapter 3), we demonstrate for the first time that it is possible to obtain length-wise ‘topographic reading’ of proteins along a single, unstained DNA molecule at high speed and high resolution using a solid-state nanopore. We show a voltage-dependent resolution of these structures, reaching dimensions as small as 8 nm. Given the possibilities to further slow down the pace of DNA translocation as described in chapter 5, it seems feasible to extend these measurements to detect a single RecA protein on DNA.

Next, we investigate the partial reduction of the DNA charge due to counterion binding by means of nanopore translocation experiments and all-atom molecular dynamics (MD) simulations (**chapter 5**). Surprisingly, we find that DNA in a lithium chloride (LiCl) solution has a much lower effective charge than in the traditionally used ionic solutions like potassium chloride (KCl). Both in experiments and simulations, we find that the translocation time of a DNA molecule through a solid-state nanopore strongly increases as the counterions decrease in size from K^+ to Na^+ to Li^+ . MD simulations elucidate the origin of this effect: Li^+ can approach the charged phosphate groups on the DNA more closely than Na^+ and K^+ and transiently bind up to a thousand-fold longer. Hence, DNA in a LiCl solution has a low effective charge, and thus experiences a low electrophoretic force and slow translocation. These insights also provide a practical method for achieving at least ten-fold enhanced resolution in nanopore applications.

Subsequently, we investigate the translocation of long random-sequence single-stranded DNA (ssDNA) through a solid-state nanopore (**chapter 6**). Using atomic force microscopy, we observe the ssDNA to hybridize into large random coils. These entangled structures have to unravel when they arrive at the pore entrance. Indeed, we observe strong blockade events with a translocation time that is exponentially dependent on voltage, $\tau \sim e^{-V/V_0}$. Interestingly, this is very different than for dsDNA, for which $\tau \sim 1/V$. Surprisingly, we find larger current blockades for ssDNA than for dsDNA, which we account for by an increased resistance due to a large random-coiled blob of hybridized ssDNA at the pore entrance.

In **chapter 7** we provide proof of concept that it is possible to realize and use ultrathin nanopores fabricated in graphene monolayers for single-molecule DNA translocation. Graphene is a carbon sheet that is only one atom thin. This presents substantial advantages over much thicker (~ 20 nm) conventional silicon nitride (SiN) nanopores, where the pore channel is relatively long and the signal from a passing DNA molecule is averaged out over tens of bases. We realize a graphene nanopore by placing a graphene flake over a micro-sized hole in a silicon nitride membrane. A nanosized hole is drilled in the graphene using a highly focused electron beam. Subsequently we translocate dsDNA through the graphene nanopore, and find similar folding behavior as was measured with conventional SiN nanopores.

Finally, we explore biomimetic nanopores. Biomimetics – the development of synthetic systems that imitate biological structures and processes – is now feasible at the nanoscale. Biological nano-scale channels and pores have inspired researchers to devise artificial pores that demonstrate molecular selectivity or other functional advantages. Such pores can be used in an array of applications in biotechnology, notably as biosensors and separation filters. But the biomimetic approach can also yielded new knowledge about biological pores, in particular, the nuclear pore complex (NPC). We review the developments in this emerging research field (**chapter 8**).

We built a *de novo* designed ‘minimalist nuclear pore complex’ that faithfully reproduces the essential feature of selectivity of the natural NPC (**chapter 9**). Nuclear pore complexes regulate the selective exchange of RNA and proteins across the nuclear envelope in eukaryotic cells. We show selective transport of proteins across a biomimetic NPC at the single-molecule level. The biomimetic NPC is constructed by covalently tethering the natively unfolded phenylalanine-glycine rich (FG) domains of human nucleoporins (Nups), the key component of NPCs, to a solid-state nanopore. For pores up to ~25 nm in diameter, Nups form a dense and lowly conducting barrier whereas Nups in larger pores adopt a more open structure. Individual translocation events are monitored using ionic current measurements with sub-millisecond temporal resolution. Transport receptors (Imp β) proceed with a dwell time of ~2.5 milliseconds for both Nup98- and Nup153-coated pores whereas the passage of non-specific proteins (BSA) is strongly inhibited with different degrees of selectivity. This biomimetic NPC provides a quantitative platform for studying nucleocytoplasmic transport phenomena at the single-molecule level *in vitro*, which may be useful for studying, for example, drug delivery to the cell nucleus.

In **chapter 10**, we provide an outlook of where developments in the nanopore field may be going in the near future.

Stefan Kowalczyk,
September 2011

Samenvatting

Nanogaatjes, gaatjes van enkele nanometers doorsnee in een dun membraan, kunnen gebruikt worden om DNA te screenen op het niveau van enkele moleculen. Met een elektrisch veld worden DNA-moleculen van kop tot staart door een nanogaatje getrokken. Uit de daaruit voortkomende verandering in de ionenstroom die door het gaatje loopt, kan essentiële informatie verkregen worden over het passerende molecuul. Veel van het huidige onderzoek is er bijvoorbeeld op gericht om te pogen de DNA sequentie uit te lezen met behulp van nanogaatjes.

Dit proefschrift beschrijft grotendeels experimenteel werk aan nanogaatjes. We starten met enkele theoretische modellen en metingen van de ionengeleiding van nanogaatjes, zowel met als zonder dubbelstrengs DNA (dsDNA) in het nanogaatje (**hoofdstuk 2**). Vervolgens laten we zien dat het mogelijk is om kaal DNA te onderscheiden van DNA dat volledig met eiwitten is bedekt op basis van verschillende stroomveranderingen (**hoofdstuk 3**). Hierop voortbordurend laten we zien dat het mogelijk is om snel en nauwkeurig de positie van eiwitten op een enkel DNA molecuul te bepalen met een nanogaatje (**hoofdstuk 4**). Voorts onderzoeken we de gedeeltelijke reductie van de DNA lading als gevolg van kortstondige binding van positief geladen ionen. Zo ontdekken we een nieuwe praktische methode voor het behalen van een sterk verbeterde resolutie in nanogaatjes-toepassingen (**hoofdstuk 5**). Hierna bestuderen we het ontrafelen van enkelstrengs DNA (ssDNA) in een nanogaatje (**hoofdstuk 6**). Aansluitend demonstreren we dat het mogelijk is om nanogaatjes te maken in grafeen, een koolstoflaag van slechts één atoom dik. We meten het transport van dsDNA door zulke grafeen nanogaatjes, waarbij we vinden dat DNA soms gevouwen door het nanogaatje gaat (**hoofdstuk 7**). Ten slotte bootsen we biologisch nanogaatjes die in het kernmembraan van een cel zitten na door kernporie-eiwitten te bevestigen aan een kunstmatig nanogaatje. We bestuderen transport van enkele eiwitten door dit selectieve, biomimetische, nanogaatje (**hoofdstuk 8 en 9**). Hieronder geven we per hoofdstuk een korte samenvatting.

In **hoofdstuk 2** presenteren we enkele theoretische modellen en metingen van de geleiding G van nanogaatjes met diameters van 5–100 nm, zowel met als zonder DNA in het nanogaatje. We laten zien dat het essentieel is om zowel de toegangsweerstand als de geometrische weerstand te beschouwen om de geleiding te beschrijven. We presenteren een exacte oplossing zonder vrije parameters voor G van een nanogaatje in een zandlopervorm. Deze is in goede overeenstemming met onze metingen. Aansluitend bespreken we de verandering in geleiding ΔG ten gevolge van de aanwezigheid van een DNA molecuul in het gaatje. We vinden dat ΔG sterk afneemt met de diameter van het gat, in tegenstelling tot de constante waarde voor ΔG die eerdere modellen voorspelden.

In de biologische cel heeft DNA continue interacties met eiwitten. RecA eiwit is een voorbeeld: het speelt een centrale rol in DNA reparatie in prokaryotische cellen, waar het de paring van beschadigd DNA met complementaire gebieden van intact DNA katalyseert. In **hoofdstuk 3** tonen we aan dat een nanogaatje zulke DNA-RecA structuren kan detecteren. We meten translocatie van dsDNA moleculen die volledig met RecA eiwit zijn bedekt. We vinden dat translocatie van DNA bedekt met RecA eiwit tien maal zo sterke blokkades geeft dan voor kaal DNA, zoals verwacht is omdat deze eiwitfilamenten dikker zijn dan kaal DNA. Bovendien bepalen we twee verschillende regimes voor translocatie: een laag-voltage regime (< 150 mV) waarin het aantal events per seconde exponentieel toeneemt met voltage, en een hoog-voltage regime waarin deze constant blijft.

Hierop voortbordurend, onderzoeken we translocatie van DNA moleculen die slechts gedeeltelijk met RecA zijn bedekt (**hoofdstuk 4**). We ontwikkelen eerst een protocol om DNA moleculen alleen lokaal met RecA eiwit te bedekken. We bekijken de resulterende moleculen met een tastmicroscop (AFM) om zeker te zijn van de vorming van discrete RecA stukken van variabele lengte. Deze lengte varieert van enkele monomeren tot filamenten van enkele micrometers lang. Gebruikmakend van het feit dat kaal DNA en RecA-DNA heel verschillende stroomblokkades geven (hoofdstuk 3), demonstreren we dat het mogelijk is om de locatie van eiwitten op een enkel DNA-molecuul middels een nanogaatje te bepalen. We laten zien dat de resolutie afhangt van voltage, waarbij eiwitfilamenten kleiner dan 8 nanometer kunnen worden gemeten, ofwel 5 RecA monomeren naast elkaar die aan 15

baseparen van DNA binden. Gegeven de mogelijkheden om DNA te vertragen, zoals beschreven in hoofdstuk 5, lijkt het binnen de mogelijkheden te liggen deze metingen door te voeren tot het detecteren van een enkel RecA eiwit op DNA.

Vervolgens onderzoeken we de gedeeltelijke reductie van DNA lading als gevolg van binding van positieve ionen door middel van translocatie metingen in nanogaatjes en moleculaire dynamica (MD) simulaties (**hoofdstuk 5**). Hierbij vinden we een onverwacht resultaat, namelijk dat DNA in een lithiumchloride (LiCl) oplossing een veel lagere effectieve lading heeft dan in traditioneel gebuikte oplossingen zoals kaliumchloride (KCl). Zowel in de experimenten als in de simulaties, vinden we dat de translocatietijd van een DNA molecuul door een nanogaatje sterk toeneemt als de grootte van de positieve ionen afneemt van K^+ naar Na^+ naar Li^+ . De MD simulaties wijzen op de oorsprong van dit effect: Li^+ kan dichter naderen tot de geladen fosfaatgroepen op het DNA dan Na^+ en/of K^+ en bindt tot duizend keer langer. DNA in een LiCl heeft dus een lagere effectieve lading, wat leidt tot een lagere electroforetische kracht en langzame translocatie. Deze inzichten bieden ook een praktische methode voor het behalen van een tenminste tienvoudig verbeterde resolutie in nanogaatjestoepassingen.

Vervolgens onderzoeken we de translocatie van lang enkelstrengs DNA door een nanogaatje (**hoofdstuk 6**). Tot dusver onderzochten de meeste studies van nanogaatjes translocatie van dsDNA, maar ssDNA is ook van groot belang, bijvoorbeeld om zulke nanogaatjes in te zetten om de DNA sequentie uit te lezen. Gebruikmakend van een tastmicroscop (AFM) observeren we dat het ssDNA plaatselijk hybridiseert. Deze grote structuren moeten ontrafelen om een nanogaatje te kunnen passeren. We observeren dat de translocatietijd exponentieel afhangt van de aangelegde spanning, $\tau \sim e^{-V/V_0}$. Dit is heel anders dan voor dsDNA, waarvoor de translocatietijd schaalt als $\tau \sim 1/V$. We vinden, onverwachts, dat het blokkadeniveau voor ssDNA veel groter is dan door dsDNA. Dit schrijven we toe aan een verhoogde weerstand doordat de grote kluwen van ssDNA bij het ingang van het gaatje blijft steken en moet ontrafelen alvorens het door het gaatje past.

In **hoofdstuk 7** demonstreren we dat het mogelijk is om nanogaatjes te maken in grafeen, een koolstoflaag van slechts één atoom dik. Deze grafeen nanogaatjes gebruiken we vervolgens om DNA-transport door zulke gaatjes te meten. De

bijzondere eigenschap van grafeen dat het slechts één atoom dik is, heeft het voordeel dat het stroomsignaal niet wordt uitgemiddeld over een groot aantal basen die tegelijk in het gaatje zitten. Dat is wel het geval voor conventionele nanogaatjes in siliciumnitride (typisch ~20 nm dik). We maken grafeen nanogaatjes door een stuk grafeen op een groot (~micrometerschaal) gat in een siliciumnitride membraan te leggen. Vervolgens schieten we er een klein (~nanometerschaal) gaatje in met een sterk gefocuseerde elektronenbundel. We meten het transport van dsDNA door zo'n grafeen nanogaatje, waarbij we vinden dat DNA soms gevouwen door het nanogaatje gaat, vergelijkbaar met wat er gebeurt in siliciumnitride nanogaatjes. Dit werk is een belangrijke eerste stap om de resolutielimiet te verlagen tot subnanometer nauwkeurigheid.

Tot slot bespreken we biomimetische nanogaatjes. Biomimetica – de ontwikkeling van kunstmatige systemen die biologische structuren en processen nabootsen – wordt nu ook mogelijk op de nanoschaal. Biologische nanokanaaltjes en nanogaatjes hebben onderzoekers geïnspireerd om kunstmatige nanogaatjes te ontwikkelen die als een moleculair filter werken en andere functionele voordelen hebben. Zulke gaatjes kunnen voor verschillende biotechnologische toepassingen worden gebruikt, in het bijzonder als biosensoren en scheidingsfilters. Maar een biomimetische aanpak kan ook leiden tot nieuwe kennis over biologische gaatjes – in het bijzonder, over het kernporie-complex (NPC). In **hoofdstuk 8** bespreken we recente ontwikkelingen in dit opkomend onderzoeksgebied.

In **hoofdstuk 9** bouwen we een *de novo* ontworpen 'minimaal kernporie-complex' dat getrouw de essentiële eigenschap van selectiviteit van de natuurlijke NPC reproduceert. Kernporie-complexen reguleren de uitwisseling van RNA en eiwitten door het kernmembraan in eukaryotische cellen. We laten selectief transport van eiwitten door een biomimetisch NPC zien op het niveau van enkele moleculen. Het biomimetische NPC wordt gemaakt door de belangrijkste eiwitten van het NPC – namelijk diegene die voor selectiviteit verantwoordelijk zijn – te bevestigen in een kunstmatig nanogaatje. We vinden dat voor gaatjes tot ~ 25 nm in diameter de kernporie-eiwitten een dichte en weinig geleidende barrière vormen, terwijl kernporie-eiwitten in grotere gaatjes een meer open structuur aannemen. In stroommetingen nemen we individuele translocatie events waar met sub-milliseconde

tijdresolutie. Transport receptoren (Imp β) passeren met een translocatietijd van ~ 2.5 milliseconde voor zowel Nup98- als Nup153-gefunctionaliseerde nanogaatjes, terwijl de passage van niet-specifieke eiwitten (BSA) sterk wordt gehinderd, met een verschillende mate van selectiviteit. Deze biomimetische NPC verschaft een testplatform voor het bestuderen van transport tussen de celkern en het cytoplasma op het niveau van enkele moleculen *in vitro*, hetgeen bruikbaar kan zijn voor het bestuderen van bijvoorbeeld afgifte van medicijnen in de celkern.

In **hoofdstuk 10** blikken we vooruit op waar de ontwikkelingen op het gebied van nanogaatjes in de nabije toekomst mogelijk heen gaan.

Stefan Kowalczyk,

September 2011

Curriculum Vitae

Stefan Kowalczyk



- 15-06-1983 Born in Warsaw, Poland
- 1995-2001 Secondary school
Vossius Gymnasium, Amsterdam
- 2001-2004 B.Sc. Physics and Astronomy
and B.Sc. Mathematics and Statistics
University of Amsterdam
- 2004-2006 M.Sc. Mathematical Physics
University of Amsterdam
- 2006-2007 Graduate student and teaching assistant
State University of New York, Stony Brook, NY, USA
- 2007-2011 Ph.D. research under supervision of Prof. dr. C. Dekker
Delft University of Technology

List of Publications

1. *Charge reduction of DNA by transient binding of counter ions*
S.W. Kowalczyk*, D.B. Wells*, A. Aksimentiev, and C. Dekker.
In preparation. *equal contribution.
2. *Biomimetic nanopores: learning from and about nature*
S.W. Kowalczyk, T.R. Blosser, and C. Dekker.
Trends in Biotechnology, December 2011 issue.
3. *Modeling the conductance and DNA blockade of solid-state nanopores*
S.W. Kowalczyk, A.Y. Grosberg, Y. Rabin, and C. Dekker.
Nanotechnology **22**, 315101 (2011).
4. *Single-molecule transport across an individual biomimetic nuclear pore complex*
S.W. Kowalczyk, L. Kapinos, T.R. Blosser, T. Magalhães, P. van Nies, R.Y.H. Lim, and C. Dekker.
Nature Nanotechnology **6**, 433–438 (2011).
5. *Nanogaatjes voor DNA analyse*
S.W. Kowalczyk and C. Dekker.
Nederlands Tijdschrift voor Natuurkunde **77/5** (2011).
6. *DNA translocation through graphene nanopores*
G.F. Schneider, S.W. Kowalczyk, V.E. Calado, G. Pandraud, H.W. Zandbergen, L. M. K. Vandersypen, and C. Dekker.
Nano Letters **10**, 3163–3167 (2010).
7. *Unraveling single-stranded DNA in a solid-state nanopore*
S.W. Kowalczyk, M.W. Tuijtel, S.P. Donkers, and C. Dekker.
Nano Letters **10**, 1414–1420 (2010).

-
8. *Detection of local protein structures along DNA using solid-state nanopores*
S.W. Kowalczyk, A.R. Hall, and C. Dekker.
Nano Letters **10**, 324–328 (2010).
 9. *Translocation of RecA-coated double-stranded DNA through solid-state nanopores*
R.M.M. Smeets*, S.W. Kowalczyk*, A.R. Hall, N.H. Dekker, and C. Dekker.
Nano Letters **9**, 3089–3095 (2009). *equal contribution.
-

Solid-state nanopores, nanometer-size holes in a thin synthetic membrane, are a versatile tool for the detection and manipulation of charged biomolecules. This thesis describes mostly experimental work on DNA translocation through solid-state nanopores, which we study at the single-molecule level. In particular, we demonstrate length-wise 'topographic reading' of proteins along a single DNA molecule, we realize ultrathin nanopores fabricated in graphene monolayers, and, finally, we mimic the nuclear pore complexes of human cells by attaching key nuclear pore proteins to a nanopore.



Casimir PhD Series 2011-22
ISBN: 978-90-8593-109-6

Stellingen

behorende bij het proefschrift
“Solid-state nanopores for scanning single molecules and mimicking biology”
door Szczepan W. Kowalczyk

1. Nanogaatjes kunnen worden gebruikt om de positie van eiwitten op een enkel DNA molecuul te bepalen.
[Hoofdstuk 4 van dit proefschrift]
2. Het is mogelijk om een selectief filter te maken van een nanogaatje door er kernporie-eiwitten aan te bevestigen.
[Hoofdstuk 9 van dit proefschrift]
3. Meten aan nanogaatjes is als schaken: gemakkelijk om te leren, maar moeilijk om meester in te worden.
4. De revolutie op het gebied van DNA uitleestechnieken zal de gezondheidszorg transformeren door de nadruk te verschuiven van het behandelen van symptomen naar het anticiperen op ziektes.
5. DNA informatie behoort te worden gebruikt voor ongelijke behandeling van mensen, maar niet om het waardevolle gelijkwaardigheidprincipe te ondermijnen dat ten grondslag ligt aan het zorgstelsel.
6. Evolutie valt goed te integreren in een christelijk wereldbeeld.
7. Het feit dat uitbuiting van Polen in Nederland economisch voordeel oplevert voor beide partijen is geen reden om het niet af te keuren.
8. De gehele Zuidpool zou kunnen worden samengeperst tot een zwart gat ter grootte van een nanometer. Zo'n “nanogat in de ruimtetijd” zal niet verdampen omdat het meer kosmische achtergrondstraling zal absorberen dan uitzenden, gegeven de lage Hawking-Unruh temperatuur.
9. Een eigen bedrijf beginnen maakt je voor eeuwig tot werkzoekende.
10. 0,5 is niet noodzakelijkerwijs gelijk aan $\frac{1}{2}$; het verschil tussen beide is hoogstens $\frac{1}{20}$.
11. Als je teveel bezig bent om alle noten goed te spelen, verlies je de muziek.

Deze stellingen worden opponeerbaar en verdedigbaar geacht en zijn als zodanig goedgekeurd door de promotor, Prof. dr. C. Dekker.

Propositions

accompanying the thesis
“Solid-state nanopores for scanning single molecules and mimicking biology”
by Szczepan W. Kowalczyk

1. Nanopores can be employed to map the location of proteins along a single DNA molecule.
[Chapter 4 of this thesis]
2. A nanopore can be engineered into a selective filter by binding nuclear pore proteins to it.
[Chapter 9 of this thesis]
3. Measuring on nanopores is like playing chess: easy to learn, but hard to master.
4. The DNA sequencing revolution will transform health care by shifting the focus from treating symptoms to anticipating disease.
5. DNA information ought to be used for unequal treatment of people, but not to break down the valuable egalitarian principle that underlies the health care system.
6. Evolution can be well integrated in a Christian worldview.
7. The fact that exploitation of Polish people in the Netherlands provides economic profit for both parties is no good reason not to condemn it.
8. The entire South Pole could be squeezed into a black hole of the size of a nanometer. Such a “nanohole in the fabric of space-time” would not evaporate because it would absorb more cosmic background radiation than it would emit, given its low Hawking-Unruh temperature.
9. Starting your own business induces a perpetual search for work.
10. 0.5 does not necessarily equal $\frac{1}{2}$; the difference between the two is at most $\frac{1}{20}$.
11. If you are too eager to play all the notes just right, you will lose the music.

These propositions are considered opposable and defensible and as such have been approved by the supervisor, Prof. dr. C. Dekker.